U.S. Department of Energy
FreedomCAR and Vehicle Technologies, EE-2G
1000 Independence Avenue, S.W.
Washington, D.C. 20585-0121

FY 2005

Annual Progress Report for the Advanced Power Electronics and Electric Machinery Program

Energy Efficiency and Renewable Energy
FreedomCAR and Vehicle Technologies
Vehicle Systems Team

Susan A. Rogers, Technology Development Manager

November 2005

Contents

Acronyms and Abbreviations

AC	air-conditioning
ac	alternating current
AIPM	automotive integrated power module
ANL	Argonne National Laboratory
BDCM	brushless direct current motor
BFE	brushless field excitation
CAN	controller area network
CFC	chlorofluorocarbon
COP	coefficient of performance
CPA	conventional phase advance
CPSR	constant power speed range
CSI	current-source inverter
DAC	data acquisition system
d-axis	direct-axis
DMIC	dual-mode inverter control
DOE	U.S. Department of Energy
DSP	digital signal processor
EERE	Energy Efficiency and Renewable Energy
emf	electromotive force
EMI	electromagnetic interference
ESR	equivalent series resistance
FC	fuel cell
FCV	fuel cell vehicle
FEA	finite-element analysis
FVCT	FreedomCAR and Vehicle Technologies
GaN	gallium nitride
GT	Georgia Institute of Technology
GWP	global warming potential
HC	hydrocarbon
HCFC	hydrochlorofluorocarbon
HEV	hybrid electric vehicle
HFC	hydrofluorocarbon
HFE	hydrofluoroether
HSUPM	hybrid-secondary-uncluttered permanent magnet
HVAC	heating, ventilating, and air-conditioning
ICE	internal combustion engine
IGBT	insulated gate bipolar transistor
IM	induction motor
IPM	integrated power module
IPM	interior permanent magnet
I-source	current-source
ISR	Isothermal Systems Research
JFET	junction field-effect transistor
JIC	jet impingement cooling
mmf	magneto-motive
MOSFET	metal oxide semiconductor field-effect transistor
MS	methylsiloxane
MSU	Michigan State University

NASA	National Aeronautics and Space Adminstration
NTRC	National Transportation Research Center
ODP	ozone-depleting potential
OFCVTs	Office of FreedomCAR and Vehicle Technologies
ORNL	Oak Ridge National Laboratory
PEEM	Power Electronics and Electric Machines
PEEMRC	Power Electronics and Electric Machinery Research Center
PFC	perfluorocarbon
PMDC	permanent magnet direct current
PMSM	permanent magnet synchronous motor
PWM	pulse-width modulation
q-axis	quadrature-axis
R&D	research and development
rad/s	rotational speed
RFP	request for proposals
RIPM	reluctance interior permanent magnet
rms	root-mean-square
RSC	Rockwell Scientific Company
RTFC	real time flux control
SDPR	switching device power rating
Si	silicon
SiC	silicon carbide
SKAI	Semikron Advanced Integration
SMPM	surface mounted permanent magnet
SOC	state-of-charge
SPM	surface-mounted PM motor
THS II	Toyota hybrid system (2004)
toff	turn-off times
ton	turn-on
UWM	University of Wisconsin, Madison
VIBE	vibration-induced bubble ejection
V-source	voltage-source
VSI	voltage source inverter
WBG	wide bandgap
WEG	water–ethylene glycol
ZSC	zero-sequence circuit
ZVS	zero-voltage-switching

Executive Summary

The U.S. Department of Energy (DOE) and the U.S. Council for Automotive Research (composed of automakers Ford, General Motors, and DaimlerChrysler) announced in January 2002 a new cooperative research effort. Known as FreedomCAR (derived from "Freedom" and "Cooperative Automotive Research"), it represents DOE's commitment to developing public/private partnerships to fund high-risk, high-payoff research into advanced automotive technologies. Efficient fuel cell technology, which uses hydrogen to power automobiles without air pollution, is a very promising pathway to achieve the ultimate vision. The new partnership replaces and builds upon the Partnership for a New Generation of Vehicles initiative that ran from 1993 through 2001.

The Vehicle Systems subprogram within the FreedomCAR and Vehicle Technologies Program provides support and guidance for many cutting-edge automotive and heavy truck technologies now under development.

Research is focused on understanding and improving the way the various new components of tomorrow's automobiles and heavy trucks will function as a unified system to improve fuel efficiency. This work also supports the development of advanced automotive accessories and the reduction of parasitic losses (e.g., aerodynamic drag, thermal management, friction and wear, and rolling resistance).

In supporting the development of hybrid propulsion systems, the Vehicle Systems subprogram has enabled the development of technologies that will significantly improve fuel economy, comply with projected emissions and safety regulations, and use fuels produced domestically.

The Vehicle Systems subprogram supports the efforts of the FreedomCAR and Fuel and the 21st Century Truck Partnerships through a three-phase approach intended to

- Identify overall propulsion and vehicle-related needs by analyzing programmatic goals and reviewing industry's recommendations and requirements, then develop the appropriate technical targets for systems, subsystems, and component research and development activities;
- Develop and validate individual subsystems and components, including electric motors, emission control devices, battery systems, power electronics, accessories, and devices to reduce parasitic losses; and
- Determine how well the components and subsystems work together in a vehicle environment or as a complete propulsion system and whether the efficiency and performance targets at the vehicle level have been achieved.

The research performed under the Vehicle Systems subprogram will help remove technical and cost barriers to enable technology for use in such advanced vehicles as hybrid and fuel-cell-powered automobiles that meet the goals of the FreedomCAR Program.

A key element in making hybrid electric vehicles practical is providing an affordable electric traction drive system. This will require attaining weight, volume, and cost targets for the power electronics and electrical machines subsystems of the traction drive system. Areas of development include

- Novel traction motor designs that result in increased power density and lower cost;
- Inverter technologies involving new topologies to achieve higher efficiency and the ability to accommodate higher-temperature environments;
- Converter concepts that employ means of reducing the component count and integrating functionality to decrease size, weight, and cost;
- More effective thermal control and packaging technologies; and
- Integrated motor/inverter concepts.

The following report discusses those projects carried out in FY 2005 and conveys highlights of their accomplishments. Numerous project reviews, technical reports, and papers have been published for these efforts, if the reader is interested in pursuing details of the work.

1. Technical Support

1.1 Power Electronics Crosscut Analysis

Principal Investigator: Sam Nelson
Oak Ridge National Laboratory
National Transportation Research Center
2360 Cherahala Boulevard
Knoxville, TN 37932
Voice: 865-946-1327; Fax: 865-946-1262; E-mail: neslonsscjr@ornl.gov

DOE Technology Development Manager: Susan A. Rogers
Voice: 202-586-8997; Fax: 202-586-1600; E-mail: Susan.Rogers@ee.doe.gov

ORNL Program Manager: Mitch Olszewski
Voice: 865-946-1350; Fax: 865-946-1262; E-mail: olszewskim@ornl.gov

---

Objectives

The objective of the Energy Efficiency and Renewable Energy (EERE) Power Electronics Crosscut task is to organize and implement technology cross-cutting research tasks in power electronics. Potential areas of research will be identified that will be jointly funded by two or more offices within EERE leveraging PEEM research funds. Power electronics and electric machinery applications span many areas of research currently being funded by a number of agencies of the federal government.

Approach

The approach for this effort is to bring together Power Electronics and Electric Machines (PEEM) program managers and researchers from within FreedomCAR and Vehicle Technologies (FVCT) sub-programs, other DOE programs and offices, government agencies, and industry partners who are interested in pursuing a common goal. The common goal is to improve the performance and reduce the cost, weight, and volume of PEEM components and systems. Strategic collaboration will be needed to identify key areas of expertise, gain insights for developing research goals and technical targets, and establish projects of mutual benefit.

To successfully complete the objectives of this task, several subtasks that define the overall approach to this task must be accomplished. They include

- identifying potential areas of focus
- selecting research and development (R&D) projects
- identifying funding partners
- identifying a potential research organization to perform the R&D
- establishing an agreement
- monitoring the R&D

Major Accomplishments

During FY 2005, the Advanced Power Electronics and Electric Machines technology development manager funded the tasks required to forge partnerships within EERE, and the FVCT program manager funded the R&D activity. A crosscut task was identified in silicon carbide (SiC) research to prepare a comprehensive study and report on the state-of-the-art technology in SiC power electronics and to assess R&D needs so that full advantage may be taken of this new material for power electronics devices.

A workshop was held June 8, 2005, with a National Aeronautics and Space Adminstration (NASA) representative to present an overview of power research and technology at NASA's Glenn Research Center.

Technical Discussion

Discussions and interactions occurred among FCVT, Solar Energy Technology, Hydrogen Fuel Cells and Infrastructure Technology, Distributed Energy and Energy Reliability, Building Technologies, and other offices about common areas of R&D in PEEM. Several projects were considered, and the SiC assessment task was selected as a task to be funded in FY 2006.

A workshop was held on June 8, 2005, in Washington, D.C. James F. Soeder, Chief of the Advanced Electrical Systems Branch at NASA Glenn Research Center, made a presentation to DOE entitled "Exploration and Power Systems at NASA." The presentation provided an overview of power research and technology at Glenn Research Center. NASA's traditional space power systems (i.e., space station, satellites, and shuttle) are low-power units (i.e., less than 10 kW) and operate at low voltages (i.e., less than 160 V) in an environment with moderate temperatures. Traditional space power systems are created from one-of-a-kind components and have limited growth potential. NASA's power systems for exploration distribute high power (i.e., 10 to 1000 kW) and operate in harsh environments with wide temperature ranges. These systems present many challenges, but they represent growth opportunities for power electronics. Some technology areas in power electronics might present opportunities for cooperation in R&D between NASA and DOE. In addition to advanced inverter/converter R&D, SiC components and high-temperature capacitors are areas of focus for both agencies.

Conclusion

Evaluations have shown a potential for duplication of effort among the various agencies with an interest in power electronics research. Collaboration among organizations with high-risk, long-range PEEM projects is highly desired to maximize the leverage gained from working with other organizations pursuing similar research goals and objectives. The funding of research tasks by multiple funding sources will result in more effective utilization of research funds. Power electronics crosscut analysis has an objective of reducing the duplication of effort by identifying PEEM R&D tasks of mutual interest that can be jointly funded by organizations with common research interests.

Future Direction

The R&D areas of focus for this task will be identified by the interaction between the program managers, PEEM researchers, and other interested parties. Discussions and interaction will continue with DOE programs and offices to identify and fund PEEM research that will advance knowledge and capability in power electronics technologies.

Some potential candidate tasks for power electronics crosscut research are

- Z-source inverters
- high-temperature packaging for electronics
- dc/dc converters
- enhanced inverter control techniques
- electric machines with brushless field excitation
- permanent magnet R&D
- compressed powdered material for stator cores
- finite element analysis characterization of motor parameters
- improved cooling techniques for inverters and motors
- high-dielectric-strength capacitors

This list is not all-inclusive, and there are additional areas of PEEM R&D that should receive consideration for future research funds.

References

1. R. L. Smith and R. J. Kevala, *Power Electronics Crosscut Activities for EERE and OETD*, Final Report, U.S. Department of Energy, Washington, D.C., September 30, 2004.

1.2 Development of a Novel Bi-Directional Isolated Multiple-Input dc-dc Converter

Principal Investigator:Laura Marlino
Oak Ridge National Laboratory
National Transportation Research Center
2360 Cherahala Boulevard
Knoxville, TN 37932
Voice: 865-946-1245; Fax: 865-946-1262; E-mail:marlinold@ornl.gov

DOE Technology Development Manager: Susan A. Rogers
Voice: 202-586-8997; Fax: 202-586-1600; E-mail: Susan.Rogers@ee.doe.gov

ORNL Program Manager: Mitch Olszewski
Voice: 865-946-1350; Fax: 865-946-1262; E-mail: olszewskim@ornl.gov

---

Objectives

The objective is to develop a *low-cost, lightweight, high-power-density* bi-directional dc-dc converter to interface multilevel energy storage elements for fuel cell vehicles (FCVs) in order to optimize the power flow between the fuel cell and on board energy storage elements such as the battery and ultracapacitors. This topology will result in a system with an increased life cycle, optimized size and weight for fuel cell and energy storage elements, and improved vehicle system dynamic behavior and efficiency.

Approach

The proposed converter technology utilizes magnetic flux linkage to provide a controllable way to combine energy from different input sources, and the transformer makes the converter capable of connecting three ports: the battery, the ultracapacitor, and the load, with galvanic isolation between the load and sources. The converter can also be viewed as an extension of a single-input soft-switched bi-directional dc-dc converter, and so maintains the advantages of soft-switching technologies, along with requiring a minimum number of devices, and a simple control methodology.

Major Accomplishments

- Analyzed the operating principles of the proposed converter and verified them with simulation results.
- Derived the design guidelines of the converter for fuel cell vehicle applications.
- Developed the computer software to design and size the proposed converter.
- Constructed the 5-kW hardware prototype of the proposed dc-dc converter.
- Tested the hardware prototype of the proposed dc-dc converter and derived experimental results to verify the steady-state power flow control.

Technical Discussion

The proposed converter has the following advantages:

- Electrical isolation can be achieved naturally.
- The magnitude of dc input voltages may be low and similar or dissimilar.
- The dc sources can deliver power individually, simultaneously, and bi-directionally.
- The soft-switching technology is achievable in a wide operating range.

- The number of devices is minimal, and control is simple.
- It is light in weight and has high power density.

The size of this converter is 12×15×7 in. The converter is operated at a switching frequency of 20 kHz or higher. The transformer-turns ratio is 1:12. The current implementation cost of this converter is $1,950. The power density of the prototype reaches 4 W/in.^{3} (continuous).

Conclusion

A low-cost multiple-input dc-dc converter has been proposed, analyzed, designed, built, and tested. It uses only six switching devices, leading to significant cost savings and high power density. It requires no auxiliary circuits or complex control to achieve soft switching. Flexible power flow is obtained by controllable leakage inductance and a phase shift angle control scheme. The analysis, simulation, and experimental results confirmed the operating principles of the proposed converter.

Future Direction

- The power flow from the high-voltage to the low-voltage side needs to be experimentally verified.
- The power flow control scheme during transients—including start-up, acceleration, and deceleration—needs to be developed to optimize the operation of the energy storage elements.
- The weight and power density can be further improved by advanced power electronics technology.

Publications

Danwei Liu and Hui Li, "A Novel Multiple-Input ZVS Bidirectional dc- dc Converter," to be presented at IECON 2005.

Patents

To be filed soon.

References

1. Yaow-Ming Chen, "Multiple-input dc/dc Converter Based on the Multiwinding Transformer for Renewable Energy Application," in IEEE Trans. on Industry Applications, 38(4), 1096–1103 (July/August 2002),.
2. L. Solero, A. Lidozzi, and J.A. Pomilio, "Design of Multiple-Input Power Converter for Hybrid Vehicles," pp. 1145-1151 in Proc. IEEE APEC'04, 2004.
3. Fang Z. Peng, Hui Li, Gui-jia Su, and J. Lawler, "A New ZVS Bi-directional dc-dc Converter for Fuel Cell and Battery Applications," *IEEE Transaction on Power Electronics*, **19**(1), 54–65 (January 2004).

2. Thermal Management and Systems

2.1 Thermal Control

Principal Investigator: John S. Hsu
Team Members: Curtis Ayers, Steven Campbell, Jim Conklin, Chester Coomer, Michael Jenkins, Kirk Lowe, Marshall McFee, Larry Seiber, Michael Starke, Randy Wiles
Oak Ridge National Laboratory
National Transportation Research Center
2360 Cherahala Boulevard
Knoxville, TN 37932
Voice: 865-946-1325; Fax: 865-946-1262 ; E-mail: hsujs@ornl.gov

DOE Technology Development Manager: Susan A. Rogers
Voice: 202-586-8997; Fax: 202-586-1600; E-mail: Susan.Rogers@ee.doe.gov

ORNL Program Manager: Mitch Olszewski
Voice: 865-946-1350; Fax: 865-946-1262; E-mail: olszewskim@ornl.gov

---

Objectives

The goal of this effort is to prove the effectiveness of using thermal methods to reduce the size of the current 600-V Semikron SKAI inverter by 50% of its current size in 2006, and then reduce it to one-third of the original size in 2008 without negatively impacting power density, cost, life expectancy, and performance of the entire system. This should result in a cost savings for the production of the overall system.

The objectives for FY 2005 included

- assessment of emerging two-phase cooling technologies,
- development of floating-loop technologies using high- or low-pressure refrigerants that can be operated independently without a compressor,
- development of methods of die mounting for better heat transfer and to reduce the inverter size
- develoopment of means of capacitor cooling,
- development of inverter/converter packaging techniques, and
- development of motor cooling techniques.

Approach

During FY 2005, Oak Ridge National Laboratory (ORNL) assessed three cooling techniques to determine if they could be beneficial for power electronics in hybrid electric vehicles (HEVs). The technologies were vibration-induced bubble ejection (VIBE) cooling from Innovative Fluidics/Georgia Institute of Technology (GT), a jet impingement system from Rockwell Scientific Company (RSC), and a spray cooling system from Isothermal Systems Research (ISR).

A floating-loop cooling system for automotive applications was developed, and a prototype system was incorporated into an automotive AC system. This system has the capability of using high- or low-pressure refrigerants to cool motors, insulated gate bipolar transistors (IGBTs), diodes, and capacitors independently of the compressor.

Major Accomplishments

- The floating-loop concept for cooling inverters and motors of HEVs and electric vehicles was validated through tests.
- ORNL's novel silicon die mounting and cooling techniques were prototyped and evaluated. These innovations will allow for potential cost and size reductions in the inverter. The heat flux of the copper-foam die mounting structure cooled by R134A refrigerant reached 170 W/cm².
- The work on a new direct cooling method for film capacitors was begun. It offers the possibility of a significant reduction in capacitor size required.
- The interim report on the evaluation of emerging two-phase cooling technologies was completed.
- The coolant fluid study (including dielectric strength) was completed.

Technical Discussion

1. Floating Refrigerant Loop Based on R-134a Refrigerant Cooling of High-Heat-Flux Electronics

The proof-of-concept work conducted on the floating loop is detailed in the report, *Floating Refrigerant Loop Based on R-134a Refrigerant Cooling of High Heat Flux Electronics*, ORNL/TM-2005/223. The concept was successfully proved. This loop (based on R-134a) is integrated with a vehicle's existing AC condenser, which dissipates waste heat to the ambient air. Because the temperature requirements for power electronics and electric machines are not as low as that required for passenger compartment air, this adjoining loop can operate on the high-pressure side of the existing AC system. This arrangement also allows the floating loop to run without the compressor and only needs a small pump to move the liquid refrigerant. For the design to be viable, the loop must not adversely affect the existing system. The loop should also provide a high coefficient of performance (COP), a flat-temperature profile, and low-pressure drop.

Proof-of-concept

To demonstrate the refrigerant cooling concept for power electronics, three main project goals were set. The first step was to show that a significant heat load could be removed with no compressor, and the refrigerant could be moved through the system with a liquid pump or vapor blower, requiring minimal input power. This would prove that a low-pressure drop, high-temperature, two-phase coolant loop would remove sufficient heat by itself.

The second step was to attach a similar loop to an automotive AC system where the loop and AC system would share the condenser. The objective of the second goal was to prove that the loop could share the condenser without adversely affecting the inventory behavior or performance of the automotive AC. In a full hybrid setup, the loop would operate constantly. The second configuration would realistically only come into question if the loop was used on an assist motor where the internal combustion engine runs all the time, and the electric assist is more intermittent.

The last goal was to operate the floating loop and AC simultaneously. This test would be indicative of normal operation of the floating loop in a full hybrid configuration. The loop would be cooling a waste-heat load from the power electronic components, while the AC system satisfied the passengers' compartment air temperature requirements.

Prototype results

The first goal was met with a bench-top setup consisting of a variable-speed pump, heat source, and condenser (Figures 1a and 1b). This cooling loop removed more than 2.1 kW of heat load with minimal input power. A vapor blower and pump were both tried with input power of 210 and 48 W, respectively.

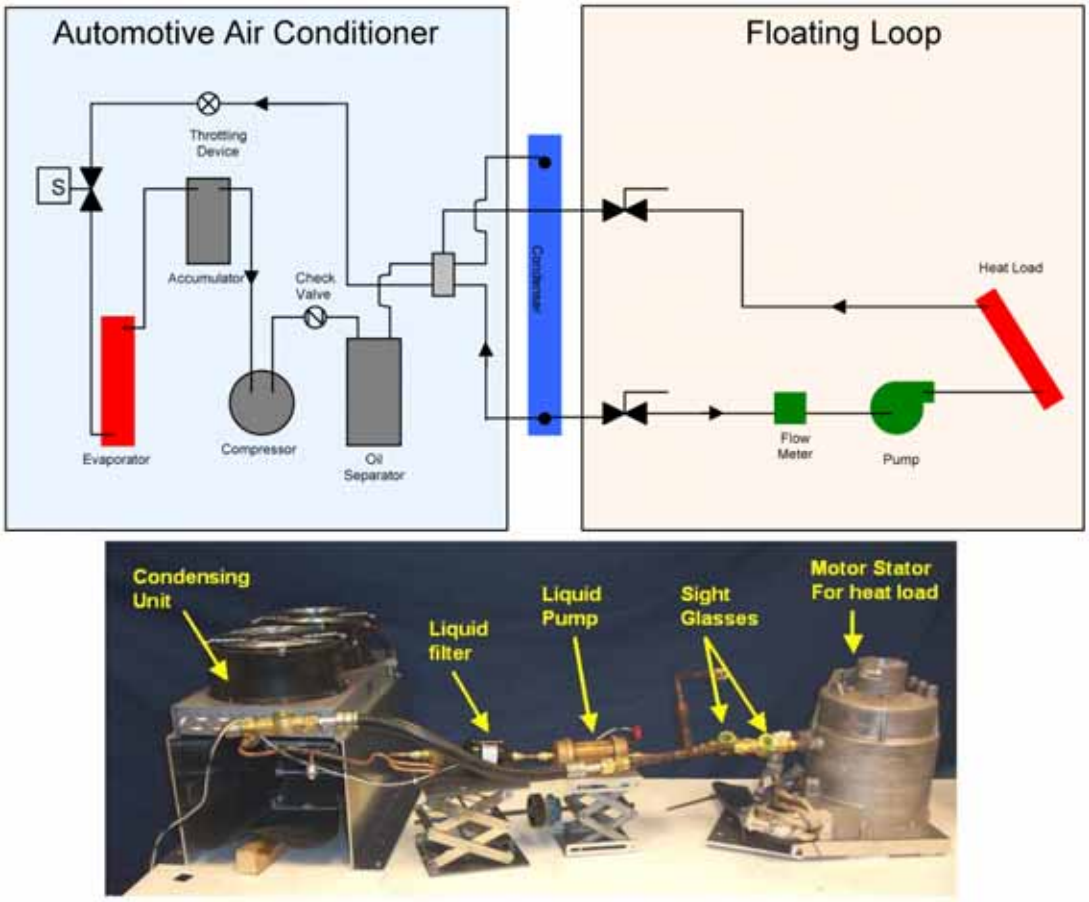

Figure 1. Floating loop diagram (a); floating loop bench top apparatus with pump (b).

Both components managed similar loads, but the pump did so with less input power, as expected. The cooling loop resulted in a COP of 44 with this configuration.

Another advantage of the pump was its compact size compared with the cumbersome fan housing. Limiting components on this bench-top setup included the size of the condenser and air flow across the condenser. Other broader issues that became apparent with this test were the flow passages through the motor housing and conduction-heat transfer from the motor windings to the refrigerant passages. These issues would need to be given consideration during motor-design stages when the R-134a loop-cooling method is being implemented.

For the second setup, a loop was attached to the high-pressure condenser section of a commercially available automotive AC system from a full-size sedan with a 9-kW capacity. The loop-inlet line was placed at the lowest elevation possible to ensure the pump inlet would remain flooded with liquid without undue increases in system inventory. A 1-kW test load was initially used to prove loop operation. The loop maintained the test load near 30°C. This specific system could also have handled a larger load, but these tests were not necessary for the proof-of-concept prototype.

After running, the loop was isolated from the stock AC system. The AC system produced adequate cooling after this test, which showed the loop had no adverse effect on AC system refrigerant-inventory behavior or refrigerant migration.

The final test involved operation of both systems simultaneously. The loop cooled the 1-kW test load and maintained it near 40°C. This increase in temperature, as compared to the loop-only scenario, is a result of the increase in condenser-heat load when the compressor is running.

When the loop runs by itself, the condenser pressure is around 650-720 kPa. When the AC system and loop are running simultaneously, the condenser pressure is ~1 MPa. One key element in obtaining these stable results was to provide increased air flow across the condenser. For all tests, the condenser inlet air temperature was ambient laboratory temperature, ~25°C.

Overall, the floating-loop system met the initial design goals; however, these tests revealed several issues with the loop/AC dynamics. Oil traps and liquid refrigerant traps had been unintentionally created during the integration of the loop into the automotive AC system. Liquid migration and flash boiling during the cycling of the compressor was also discovered to be a problem. Dry-out of the load is considered to be a major issue when designing for direct cooling of power electronics. If the liquid level drops significantly in the load or dry-out occurs, loss of two-phase cooling occurs, and superheated vapor is produced, which results in significantly reduced heat transfer and rapidly increasing junction temperatures.

To correct these problems, four major revisions were implemented:

- Move the check valve downstream of the oil separator in a horizontal position.
- Move the solenoid valve closer to the condenser outlet.
- Move the evaporator fan to blow out of the case instead of through the condenser. Add dedicated condenser fans (Figure 2).
- Move the pump position within the loop to upstream of the filter and flow meter.

Figure 2. Revised floating loop attached to full-size sedan AC system in a cabinet.

During these changes, the original pump performance dropped due to unrelated pump motor electrical issues. One major design challenge had also been the electrical connections to the pump. A new pump was installed with commercially available high-pressure electrical terminals.

Results

After these changes were implemented, the loop shown in Figures 2 and 3 was retested at 1 kW, 1.5 kW, and ~2 kW. The 1-kW load had similar results as previous tests. Repeated tests of the cooling loop by itself resulted in maintaining the load temperature around 35°C with ~1.5 kW of heat.

The AC unit was incorporated with the loop-test load at 1 kW and at 1.5 kW, and the load was maintained at 37 and 41°C, respectively. This slightly higher temperature was expected because of the increase in operating pressure and, thus, higher saturation temperature. The flash-boiling effects were minimal during these tests, and no risk of load dry-out was obvious. The pump was at full power during these operations. When the l.5-kW load was decoupled from the AC system, the floating-cooling loop returned to 34°C.

For test runs at up to 1960 W, the floating-cooling loop maintained the load near 38°C. When the AC was coupled to the loop, the system continued to run well with the load surface temperature at 49°C with full pump power. When the AC was turned off, the flash-boiling effects appeared to be minimal.

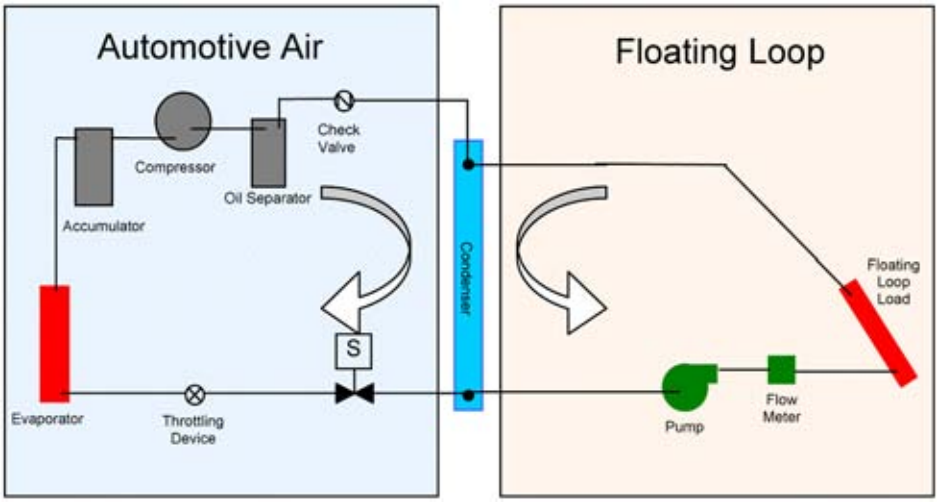

Figure 3. Floating loop/AC schematic with revisions.

System dynamics

To ensure a more robust design, the system instabilities previously mentioned were examined. When the pump was not at full power, several modes of system failure could arise: the pump would not supply enough liquid refrigerant to the loop in order to keep it wet, the differential pressure across the loop would collapse and cause backflow, or the cycling of the compressor would cause dry-out. During typical operation at 22°C, four operating scenarios were encountered.

The four operating scenarios are steady operation of floating loop, steady operation with automotive AC, transient start-up of automotive AC with loop, and the cycling off of the automotive air while maintaining loop operation. Each case presents unique operating requirements for which control methods are proposed and future design issues are discussed in the ORNL report.

2. ORNL's Novel Silicon Die Mounting and New Capacitor Design

The current status of the technology of conventional die mounting of the inverter is shown in Figure 4. This technology was chosen as the baseline for the development comparison. The heat flux path of the conventional die-mounted inverter is indicated by the arrow shown in Figure 5. There are multiple layers of thermal resistance in a conventional die-mounted inverter.

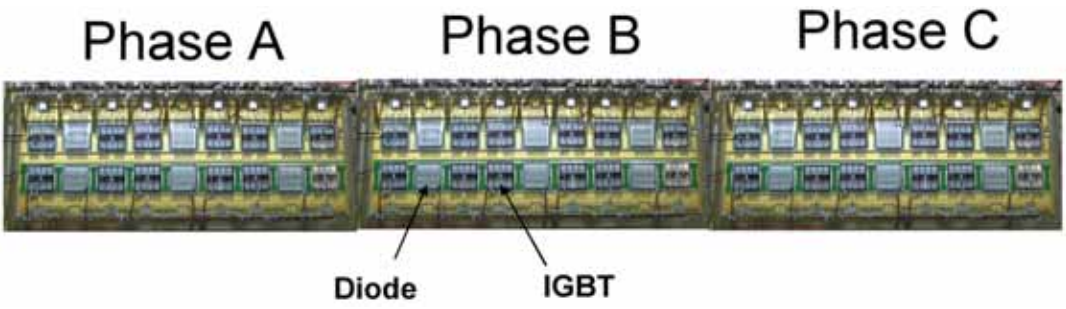

Figure 4. Conventional die mounting of inverter.

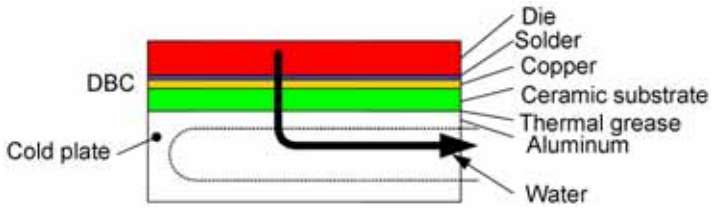

Figure 5. Arrow indicates the conventional heat flux path of the conventional die-mounting inverter.

The specific technical problem(s) addressed at ORNL for improving die cooling is to change the inverter packaging design for direct-contact, two-phase cooling and implement the design in the floating loop. The specific measurement at the end of the project is to reduce the inverter size to one-third of the 2005 Semikron inverter size with the same power rating.

The cascaded die mounting invented by ORNL is shown conceptually in Figure 6.

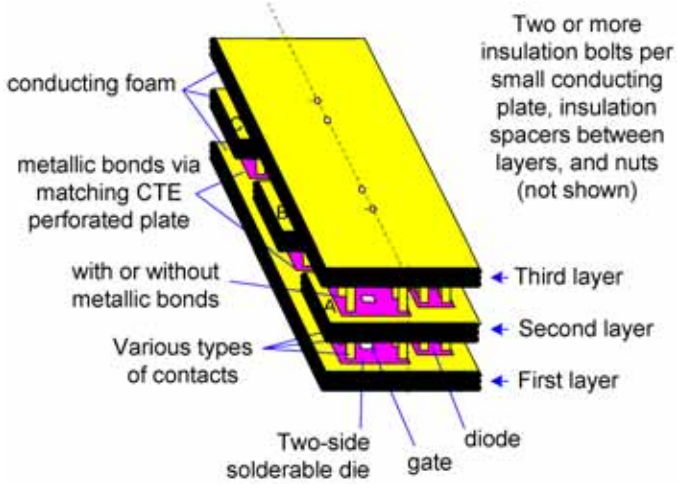

Figure 6. ORNL's cascaded die mounting concept.

Figure 7 shows copper foams used in the mounting. The reasons to use copper foam for the first prototype are (1) copper foam is a conductor without the need for heavy current wire bonds, (2) the dielectric cooling fluid can contact the die and the copper foam directly for two-phase heat transfer, and (3) it provides possibilities for thermal expansion control. This sample uses 25% density foam with 49 pores/in.

For the copper foam preliminary prototype, Figure 8 shows a two-side solderable silicon die (IXGD9265) obtained from IXYS Company. Its dimensions are 0.012 × 0.284 × 0.375 in. A larger die obtained from Rockwell Scientific, shown in Figure 9, was also used for the copper foam die mounting.

Figure 10(a) shows the copper-foam cascaded die mounting inside a glass test tube filled with R134a refrigerant. Figure 10(b) shows that when the die is conducting electric current, two-phase cooling occurs. The heat flux of ORNL's preliminary copper-foam die mounting reaches 170 W/cm².

Figure 11 shows the ORNL 20% density copper foam die cooling tests, and Figure 12 shows similar tests with 25% foam density. The heat flux reaches about 170 W/cm² in continuous operation.

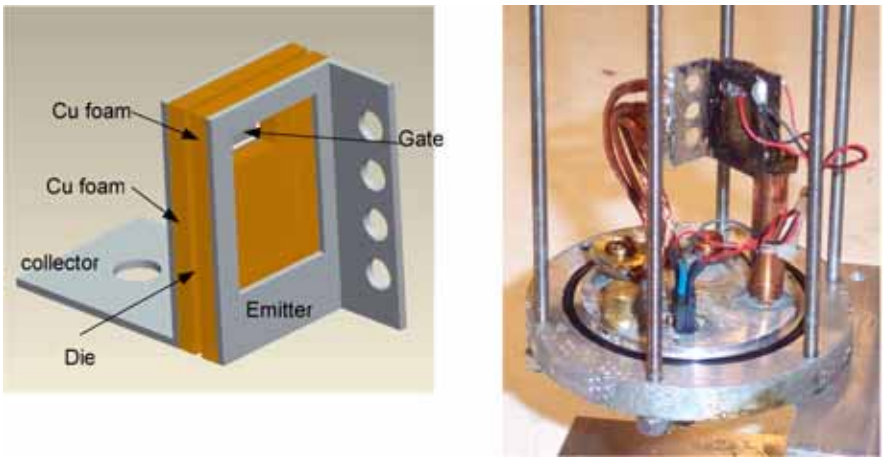

Figure 7. Copper foam is used as an example for cascaded die mounting.

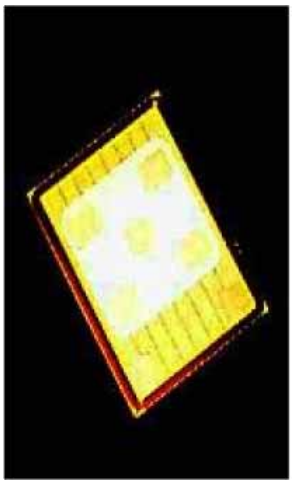

Figure 8. An IXYS two-side solderable die.

Figure 9. A two-side solderable die obtained from Rockwell Scientific.

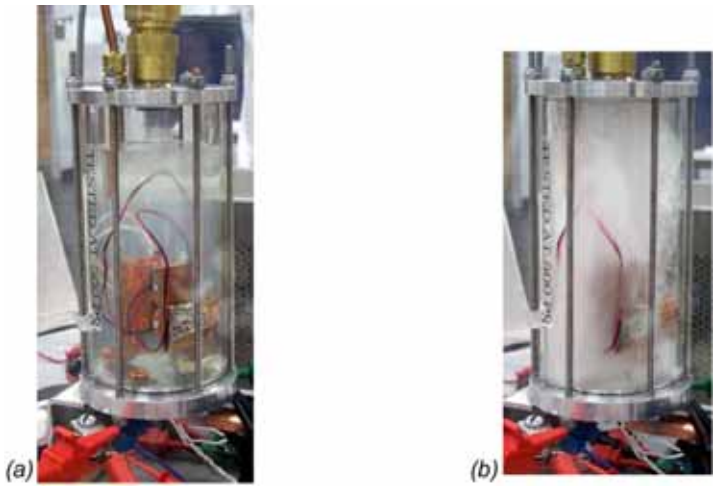

Figure 10. Prototype of copper-foam cascade die mounting (a). Two-phase cooling occurs when the die is loaded (b).

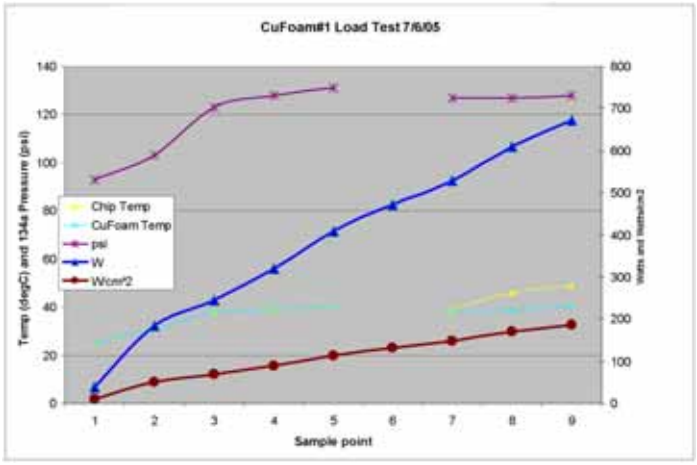

Figure 11. ORNL 20% density copper foam die cooling tests.

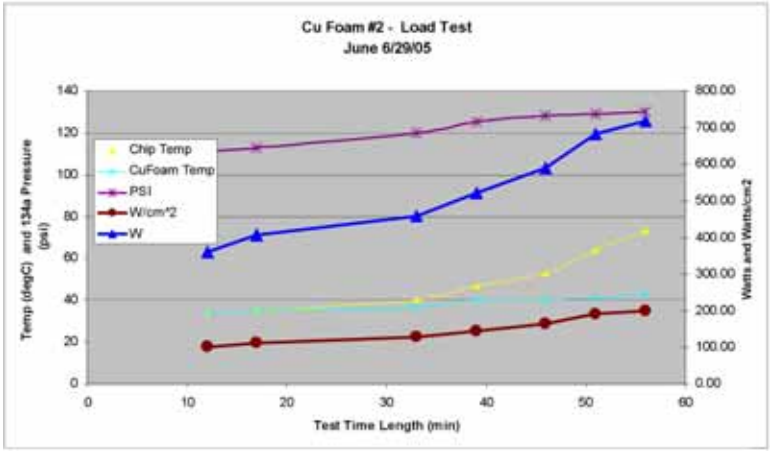

Figure 12. 25% foam density test.

3. Film Capacitor Cooling

It is known that the permissible ripple current of a film capacitor goes down when the ambient temperature of the capacitor goes up. Reducing the capacitor size cooling of the capacitor is important. ORNL has a patent pending on the direct cooling of film capacitors with refrigerants. The design of a new film capacitor prototype is shown in Figure 13.

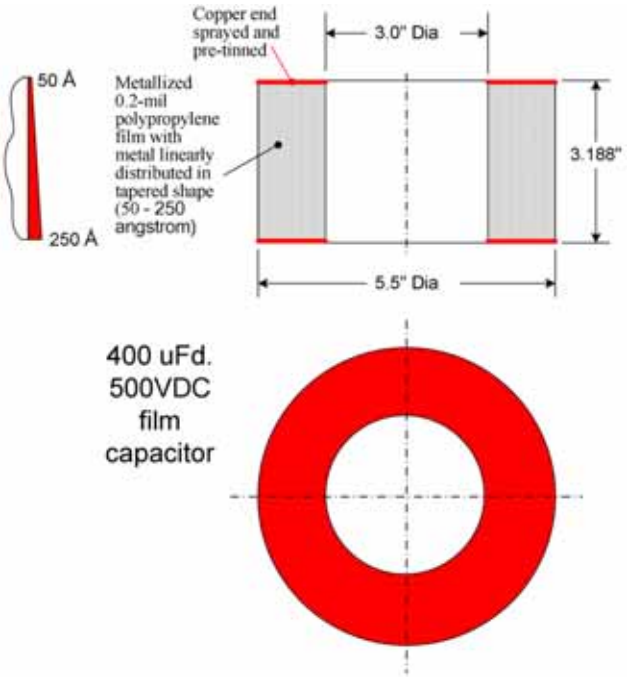

Figure 13. Example of an ORNL directly cooled film capacitor.

In this concept, the hollow center of the capacitor is the space available for the power electronic dies. The inverter assembly consisting of the capacitor, the dies, and other components are housed in a container allowing for direct refrigerant cooling. Figure 14 shows how the metal thickness on the film is linearly tapered with the thicker side positioned for external connections. Because the current is accumulating when it goes toward the connection side, this helps to make the current density more uniform in the metal.

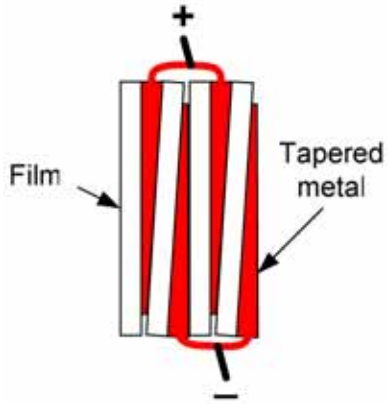

Figure 14. Tapered metal thickness on film.

4. Assessment of Emerging Two-Phase Cooling Technologies for Power Electronic Inverters

Details of the assessment are presented in the *Emerging Two-Phase Cooling Technologies for Power Electronic Inverters (Interim Report)*, ORNL/TM-2005/156. The report presents the findings of two single-loop, two-phase, water-ethylene-glycol (WEG) cooling systems and a double-loop, two-phase, transmission oil/dielectric fluid system through the tests of prototypes built by three subcontractors. The subcontractors are GT/Innovative Fluidics, RSC, and ISR. All three prototype cooling systems were implemented on a modified WEG coolant, single-phase, single-loop Semikron inverter. The 105ºC WEG coolant was used in GT's VIBE system and in RSC's jet impingement cooling (JIC) system for their two-phase, single-loop systems. ISR used 85ºC transmission oil to cool a second-dielectric fluid loop for direct-die spray cooling. All three subcontractors' systems operate below 30-psi pressure.

In this investigation, the potentials and problems of different two-phase technologies proposed by the three subcontractors can be clearly seen. All test results presented in the report were witnessed by ORNL.

ORNL's assessment of GT/Innovative Fluidics, single-loop, two-phase JIC system

The prototype required roughly 760 VA (720 VA plus fan motor) of apparent power to cool a 380-W loss during a dc test. Figure 15 shows severe erosion that appeared on the surfaces of the piezoelectric vibrators and on the metal-cooling chamber of the inverter after an hour of testing. Very little vaporization occurred due to the high-boiling temperature of the WEG and the low permissible junction temperature (125ºC) of the Si dies. The WEG boils at 106ºC at atmosphere pressure. The boiling temperature increases as the pressure increases.

Although the VIBE technology failed to show its effectiveness from the tests, it may still be worth revisiting when the permissible junction temperature of the dies can be raised to allow more vaporization. However, to use this technology, the input power to the piezoelectric vibrators and the cooling fan would have to be reduced and the erosion problem solved.

ORNL's assessment of RSC single-loop, two-phase JIC system

RSC developed a closed-loop jet-impingement cooling (JIC) technique with 105ºC WEG temperature. The targeted micro-jet array-impingement technique was implemented on a 450-V (dc link voltage) 400-A (rms current) Semikron module. Figure 16 shows the schematic of the closed-loop WEG micro-jet array impingement cooling system for the Semikron inverter.

Figure 15. Photograph of Array B—2.4-MHz actuators.

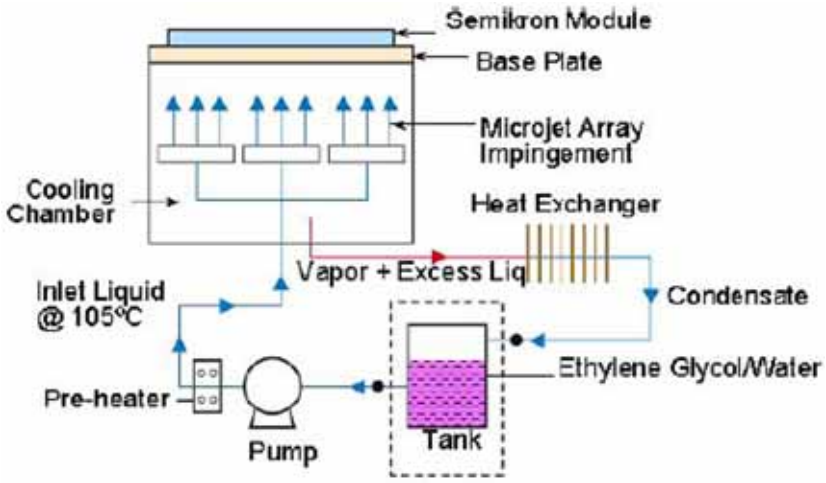

Figure 16. A schematic of the closed-loop WEG micro-jet array impingement cooling system for the Semikron inverter.

The dc testing of the module with ~105°C coolant at 2.25-gpm flow rate (corresponding pressure drop 24 psi) demonstrated 1623 W of heat dissipation at an allowable 20°C device temperature rise. This translates to a chip-level power dissipation density of 56 W/cm^2, an estimated 1.8× improvement over the state-of-the-art Semikron cold-plate thermal control scheme prorated to the same 105°C coolant temperature for comparison.

RSC also estimated that by cutting off part of the heat sink to expose the direct-bonded copper (DBC) underneath the die to the jets, the heat flux might potentially reach 90 W/cm^2.

ORNL's assessment of ISR double-loop, two-phase spray cooling system

Figure 17 shows the ISR double-loop, two-phase spray cooling system. It is designed to use an 85ºC transmission oil loop to cool a second loop containing a dielectric liquid for spray cooling. The final ISR report and ORNL's assessment will be completed upon final testing of the ISR modules in early 2006

.

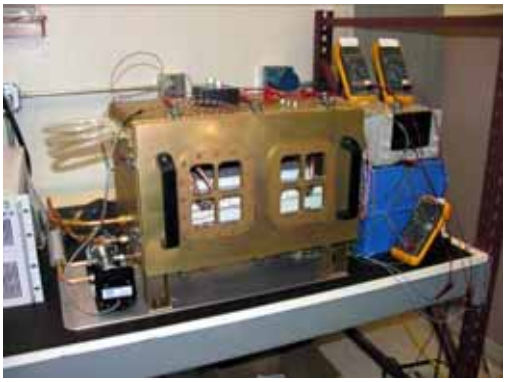

Figure 17. ISR spray cooling system for the Semikron inverter.

5. Refrigerant Properties

Detailed basic refrigerant properties are included in the report *Potential Refrigerants for Power Electronics Cooling*, ORNL/TM-2005/219.

Cooling power electronic components in a refrigerant requires that the refrigerant meet certain constraints. First, the refrigerant must be environmentally friendly. Second, the refrigerant must be effective at two-phase cooling. This implies that the refrigerant has appropriate thermo-physical properties. Finally, the refrigerant must have high-dielectric strength. The major conclusions are outlined by the following tables.

A major issue with cooling power electronics directly with refrigerant is the dielectric strength. High-dielectric strength of a fluid enables it to resist current under high-voltage potential. Because power electronics are completely exposed in the refrigerant, the fluid must not permit the flow of current to short-circuit and damage power electronics and other components, or to cause malfunction of power electronics control circuits.

Environmental impact

Table 1 depicts data concerning environmental, flammability, and health concerns of the refrigerants under investigation. Chlorofluorocarbons (CFCs) have the worst environmental impact with a large ozone-depleting potential (ODP) and global-warming potential (GWP) (100 years), and has been eliminated from use through the Montreal Protocol. The only other refrigerants to have ODP are the hydrochlorofluorocarbons (HCFCs). Although HCFCs have a much lower ODP value, the Copenhagen Amendments to the Montreal Protocol call for ending production of ozone-depleting compounds by 2010 [1], eliminating the use of HCFCs in the future.

Figure 18 graphically represents the GWP of different refrigerants in reducing order. Clearly from Figure 18, CFCs and perfluorocarbons (PFCs) are undesirable refrigerants in terms of the environment with significantly larger GWP values compared with other refrigerants. A noteworthy observation is the low GWP values of hydrofluoroether (HFE), hydrocarbons (HC), and methylsiloxane (MS) refrigerants. Along with low values of GWP, these refrigerants have no ODP and low environmental impact. Still, water is the optimum refrigerant with no harmful effects to the environment.

Two-phase cooling

Figure 19 depicts the latent-heat values of the refrigerants in reducing order. These and other important physical properties of the refrigerants being examined are listed in Table 2. Based on observation of Figure 19, water has the highest two-phase heat-transfer potential, by more than a factor of 6. For this reason, water is often used in indirect cooling because the water does not come in contact with the electronics. The next highest refrigerants with the greatest two-phase heat-transfer potential are the HC blends of Table 2. The lowest potential heat-transfer refrigerants are the HFE and PFC of Table 2 with latent-heat values smaller than 1/23 that of water.

In terms of the normal-boiling point, the refrigerants most suited for cooling electronics are those with boiling-point temperatures in the range 20–80°C. From Table 2, these refrigerants include PFCs and HFE type refrigerants. HCFC, hydrofluorocarbon (HFC), CFC, and HC refrigerants require a medium-pressure container to have both liquid and vapor phases due to the low values of the normal-boiling points. The MS refrigerants have high normal-boiling point temperatures requiring a slightly subatmospheric pressure on the container. This gives PFC and HFE refrigerants an advantage in terms of safety, operation, and cost.

Table 1. Environmental, ignitability, and health data

Cooling Fluid Description			Flammable ?	Auto Ignition	Lower Expl. Limit	Enviornmental		NFPA	HMIS
	Company	Product Name	Yes/No	Point (°C)	LEL (%)	ODP (R11=1)	GWP (100yr)	health/ flamability	health/ flamability
1,1,1,2 tetra fluorethane	Various	HFC-134a	No	750	NA	0	1300	1/0	1/0
1,1-dichloro-1-fluoroethane	Various	HCFC-141b	Yes	325	6	0.086	700	1/0	1/0
1-chloro-1,1-difluoroethane	various	HCFC-142b	Yes	632	9	0.043	2300	1/0	1/0
Dichlorodifluoro methane	Various	CFC-12	No	>750	NA	0.82	10600	2/4	2/4
Chlorodifluoro methane	Various	HCFC-22	No	NA	NA	0.034	1700	2/1	2/1
perfluorocarbon	3M	Fluoroinert FC-87	No	NA	NA	0	8900	3/0	0/0
perfluorocarbon	3M	Fluoroinert FC-72	No	NA	NA	0	9000	3/0	1/0
perfluorocarbon	3M	Fluoroinert FC-77	No	NA	NA	0	9000	3/0	1/0
hydrofluoroether	3M	Novec HFE-7000	No	415	NA	0	400	3/1	0/1
hydrofluoroether	3M	Novec HFE-7100	No	405	NA	0	320	3/1	0/1
hydrofluoroether	3M	Novec HFE-7200	No	375	2.4	0	55	3/0	1/0
methylsiloxane	Dow Corning	Cleaning Agent 1	Yes	341.1	1.25	0	<10 est	1/3	
methylsiloxane 60% w/alcohol	Dow Corning	Cleaning Agent 2	Yes	365	1.3	0	<10 est	1/3	
De-Ionized Water		H_2O	No	NA	NA	0	<1 est		
(butane/isobutane/propane)	Duracool	Duracool 12a	Yes	891	1.95	0	~20	1/4	1/4
hydrocarbon blend (propane/butane)	Enviro-safe	ES-12	Yes	863	1.9	0	~20	1/4	1/4
fluorocarbon blend (HFC-134a/HCFC-142b)	Technical Chemical	Freeze 12	No	>150	not determined	0.01	1500	2/2	2/2

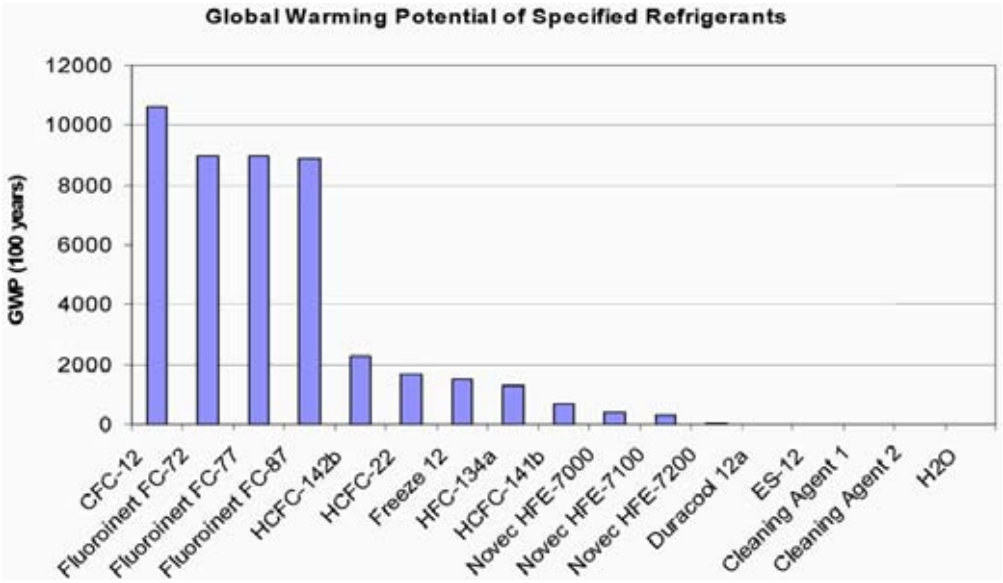

Figure 18. Refrigerant global warming potential.

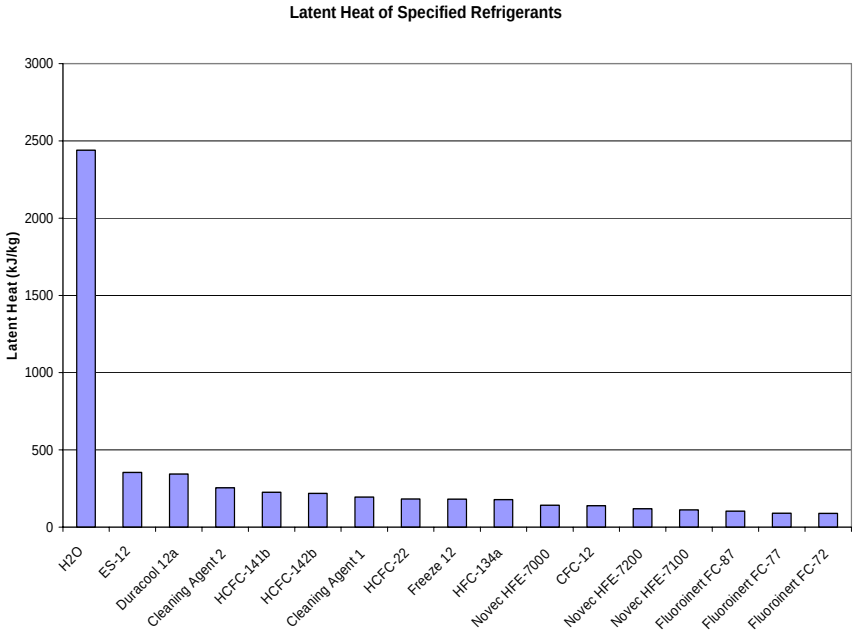

Figure 19. Latent heat at normal boiling point.

Table 2. Physical properties

Cooling fluid description			Latent heat @ 25°C	Specific heat @ 25°C	Density @ 25°C	Normal boiling point
	Company	Product name	kJ/kg	Liquid (kJ/kg/K)	liquid kg/m³	°C
1,1,1,2 tetra fluorethane	Various	HFC-134a	178	1.4	1210	–26
1,1-dichloro-1-fluoroethane	Various	HCFC-141b	226	1.15	1234	32
1-chloro-1,1-difluoroethane	various	HCFC-142b	217.8	1.3	1.12	–10
Dichlorodifluoro methane	Various	CFC-12	139	1	1311	–29.8
Chlorodifluoro methane	Various	HCFC-22	182.7	1.26	1191	–40.8
perfluorocarbon	3M	Fluoroinert FC-87	103	1.1	1650	30
perfluorocarbon	3M	Fluoroinert FC-72	88	1.1	1700	56
perfluorocarbon	3M	Fluoroinert FC-77	89	1.1	1780	97
hydrofluoroether	3M	Novec HFE-7000	142	1.3	1400	34
hydrofluoroether	3M	Novec HFE-7100	112	1.17	1520	61
hydrofluoroether	3M	Novec HFE-7200	119	1.22	1420	76
methylsiloxane	Dow Corning	Cleaing Agent 1	194	1.72	850	100
methylsiloxane 60% w/alcohol	Dow Corning	Cleaning Agent 2	255		770	98
De-Ionized Water		H_2O	2440	4.13	1002	100
hydrocarbon blend (butane/isobutane/propane)	Duracool	Duracool 12a	343.5	2.56	526	–31.5
hydrocarbon blend (propane/butane)	Enviro-safe	ES-12	354.2	2.574	530	–30.4
fluorocarbon blend (HFC-134a/HCFC-142b)	Technical Chemical	Freeze 12	180.7	1.4	1189	–25

Dielectric Strength

Because power electronics are to be cooled using two phases, both the liquid and vapor phases require dielectric-strength testing. The testing temperatures are based on the expected operating temperature of the two-phase mixtures. Saturated liquid and vapor denote the test pressure of the mixtures. To replicate the actual placement of power electronics in the mixtures, sharp electrodes are used in the dielectric-strength test. The dielectric strengths of the refrigerants are given in Table 3.

Table 3. Dielectric strength table

		Dielectric Strength	Dielectric Strength
		Liquid (kV/mil)	Vapor (kV/mil)
Products	Product Name	50 °C/Saturated Liquid	50 °C/Saturated Vapor
1,1,1,2 tetra fluorethane	HFC-134a	**7.2**	**6.7**
		50 °C/Saturated Liquid	50 °C/Saturated Vapor
1-chloro-1,1-difluoroethane	HCFC-142b	**5.9**	**5.4**
		50 °C/Saturated Liquid	50 °C/Saturated Vapor
1,1 - dichloro -1-fluoroethane	HCFC-141b	**6.1**	**4.4**
		50 °C/Saturated Liquid	50 °C/Saturated Vapor
hydrofluoroether	Novec HFE-7000	**8.0**	**6.0**
		80 °C/Saturated Liquid	
hydrofluoroether	Novec HFE-7100	**8.1**	**7.1**
		80 °C/Saturated Liquid	80 °C/Saturated Vapor
hydrofluoroether	Novec HFE-7200	**7.7**	**3.8**
		100 °C/Saturated Liquid	100 °C/Saturated Vapor
methylsiloxane	Cleaning Agent 1	**7.6**	**5.4**
		100 °C/Saturated Liquid	100 °C/Saturated Vapor
methylsiloxane 60% w/alcohol	Cleaning Agent 2	**6.3**	**4.4**

Conclusions

The concept of the floating refrigerant loop based on R-134a refrigerant cooling of high-heat-flux electronics was proved through experimental tests. For operation as part of a 9-kW automobile cooling system, the ORNL floating-loop system has been proven to function well at 2 kW, with a very attractive COP of >40. The system capacity is easily scalable for larger loads. The operation of the floating cooling loop results in four major running scenarios. Each one has the potential to run stably and reliably, subject to appropriate component sizing and controls. A solenoid valve located close to the loop supply/condenser outlet to isolate the passenger AC components is crucial to the stable operation of the floating-cooling loop during AC compressor shutoff. Methods of increasing liquid inventory in the condenser and floating loop are required to maintain a wet load during compressor transients.

The ORNL cascaded die mounting that uses copper foam can achieve 170-W/cm² heat flux value.

The work on direct cooling of film capacitors began, and a design for incorporation into the reduced size inverter was developed.

The assessment of emerging two-phase cooling technologies for power electronic inverters gave objective conclusions through test data. Comparing with pure water, it is relatively harder to cool an inverter with WEG. The 105°C WEG was used for the GT's VIBE system as well RSC's JIC system for their two-phase, single-loop systems. The 85ºC transmission oil was used by ISR to cool a second-dielectric fluid loop for direct-die spray cooling. All three subcontractors' systems operate below 30-psi pressure. The VIBE prototype took more energy to cool than its ability to extract. The JIC prototype reached 55 W/cm² heat flux. The ISR spray system will be tested in 2006.

The refrigerant property study indicates that the HFC (R134-a) remains a good candidate for hybrid power electronics cooling with good mechanical properties, strong dielectric strength, nonflammability, and wide acceptance in the auto industry. The HFE (Novec) fluids show good general properties for power electronics cooling, but are not presently used in automotive applications. The MS materials show excellent mechanical properties, but exhibit high flammability in conjunction with a high normal-boiling point at low system pressure and moderate dielectric strength. This creates the need for care in designing a safe oxygen-free system. The HCFC materials show moderate to poor dielectric strengths and are slated to be removed from production in the near future due to significant ODP and GWP.

Future Direction

The engineering improvements on the floating loop technology will be conducted for dynamic conditions as issues arise. The Venturi effect will be introduced into the cascaded die mounting for further increase of the heat flux. The specially made film capacitor will be tested with the reduced-size inverter. The ISR spray cooling prototype will be tested.

Publications

*Floating Refrigerant Loop Based on R-134a Refrigerant Cooling of High Heat Flux Electronic*s, ORNL/TM-2005/223.

Report On Toyota Prius Motor Thermal Management, ORNL/TM-2005/33.

Patents

The available ORNL patents on thermal control are as follows:

- "Cascaded Die Mountings with Spring-Loaded Contact-bond Options," U.S. Patent 6,930,385, August 16, 2005.
- "Total Thermal Management System for Hybrid and Full Electric Vehicles," U.S. Patent 6,772,603, August 10, 2004.
- "Refrigerant Directly Cooled Capacitors," Patent pending No. 11/166,502.
- "Floating Loop System for Cooling Integrated Motors and Inverters," Patent pending No. 10/926,205.
- "Motor Frame and Cooling with Refrigerant and Liquid," Patent pending No. 60/565,461.

Reference

1. *The Challenge: Moving Away From HCFC Refrigerants*, HRAI, The Heating, Refrigerating, and Air Conditioning Institute of Canada, 2005 (http://www.hrai.ca/hcfcphaseout/).

2.2 Component Characterization

Principal Investigator: Larry Seiber
Oak Ridge National Laboratory
National Transportation Research Center
2360 Cherahala Boulevard
Knoxville, TN 37932
Voice: 865-946-1334; Fax: 865-946-1400; E-mail: seiberle@ornl.gov

DOE Technology Development Manager: Susan A. Rogers
Voice: 202-586-8997; Fax: 202-586-1600; E-mail: Susan.Rogers@ee.doe.gov

ORNL Program Manager: Mitch Olszewski
Voice: 865-946-1350; Fax: 865-946-1262; E-mail: olszewskim@ornl.gov

---

Objective

As capacitor and magnet technologies mature, it is important to ascertain their limitations by subjecting the components to standardized tests to evaluate their capabilities. This testing will determine their reliability, degradation tendencies, and level of robustness when subjected to accelerated life testing conditions. Test results will help to predict whether the components are capable of meeting the 15-year service life requirement and help determine their ability to provide improvements in power electronics and motor designs to meet FreedomCAR goals.

Approach

In order to record and plot capacitor performance data, it has been necessary to develop a test stand that logs data at predetermined temperature extremes and controls thermal cycling between these extremes. This test stand includes an automated data acquisition system, an environmental chamber, and the necessary measuring instrumentation.

To understand how the new magnet technologies respond to thermal cycling, a hysteresis graph and BH curves of new magnet materials over the full range of temperatures from –40°C to 140°C will be plotted.

Major Accomplishments

To obtain temperature cycling data, the thermal cycling process must continue uninterrupted for extended periods of time. To accomplish this long-term testing, an automated data acquisition system (DAC) using LABView was developed to control the environmental chamber and record data from the measuring instruments. The DAC will allow the operator to input upper and lower temperature limits as well as temperature increments to be used during the testing. The program will command a temperature to the environmental chamber; when that temperature has been reached, it will then monitor a capacitor parameter for stability. After this parameter is stable, the program will record the capacitor data from the measuring instruments at each of seven frequencies before another temperature step is commanded.

Technical Discussion

Capacitor Evaluation

In FY 2005, the capacitor testing was limited to thermal cycling. Future testing will be done by applying a ripple current and bias voltage to the capacitors in the environmental chamber. The parameters recorded during the thermal cycling tests were capacitance value, dissipation factor, and equivalent series

resistance (ESR). The temperature extremes for all tests were –40 and 140°C. The typical increment for a temperature step was 20°C. At each temperature increment, the parameters were measured at seven different frequencies: 1, 5, 10, 15, 20, 25, and 30 kHz. All capacitors were tested in an ESPEC environmental chamber, and their parameters were measured by an Agilent 4284A LCR meter.

Data acquisition system

The data acquisition system consists of a Dell Precision 380 Workstation running LABView 7.1. At the beginning of the thermal cycling test, the program turns on the environmental chamber, commands a temperature, and begins monitoring the chamber temperature to determine when that temperature has been reached. After the target temperature has been reached and a pre-programmed delay time has been met, the program sends a command to the LCR meter to output the first test frequency and monitors the ESR from the capacitor under test. When that value is stable, the data point is recorded and the next parameter is monitored and recorded.

After all parameters—ESR, dissipation factor, and capacitance value—are recorded at the first test frequency, the command is given to the LCR meter to output the next test frequency; and the monitoring and recording process is repeated. After data are recorded at all seven frequencies, the next temperature step is commanded to the environmental chamber, the frequencies are scanned again, and the parameters are recorded. The number of temperature steps that can be entered into the LABView program is, for all practical purposes, unlimited. The only test limitation is imposed by the LCR meter, which allows only certain test frequencies to be used.

The pre-programmed delay discussed earlier is to ensure that the temperature of the dielectric has equalized once the target temperature of the environmental chamber has been reached. When the difference between the ambient temperature and the target temperature of the chamber is 40° or greater, the delay is invoked when the target temperature is reached. This delay value is entered before the program starts monitoring the temperature. The value is determined by the operator and is based on the size of the capacitor. A larger capacitor requires a larger delay to ensure that the temperature of the dielectric is uniform. After this delay time has expired, the program monitors the ESR for a stable reading before the value is recorded to ensure the ESR readings are accurate.

Five types of capacitors were tested and will be reported on here. Pennsylvania State University supplied a multilayer glass ceramic capacitor. Sandi National Laboratories supplied a commercial polyester film and a commercial Teflon film, both manufactured by ASC. The commercial capacitors were tested, and Sandia will use the data to aid in the development of its new technologies. The fourth capacitor tested was a metallized proprietary experimental film capacitor supplied by Dearborn Electronics. The fifth was a module consisting of 16 capacitors in parallel. This capacitor module was manufactured by Electronics Concepts, Inc., and supplied by Semikron. It is currently in use in the Semikron 600-V SKAI inverter.

Multilayer glass ceramic

The multilayer glass ceramic capacitor is a 1-μF, 500-Vdc capacitor. It was tested from –40 to 140°C at 20° increments. Figures 1 and 2 show the data at the temperature extremes. The capacitance value and ESR decrease as frequency increases at the temperature extremes, but the dissipation factor increases with frequency at the temperature extremes. The dissipation factor and ESR values are much lower at the higher temperature, but the capacitance value is higher at the higher temperature.

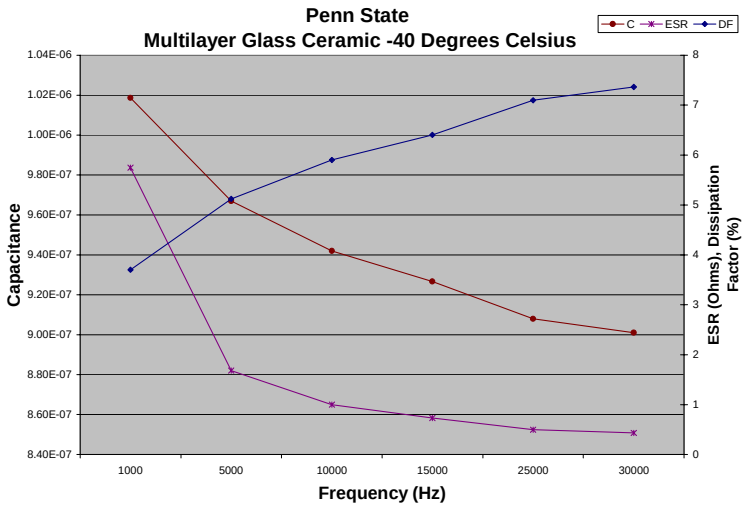

Figure 1. Multilayer glass ceramic at –40°C.

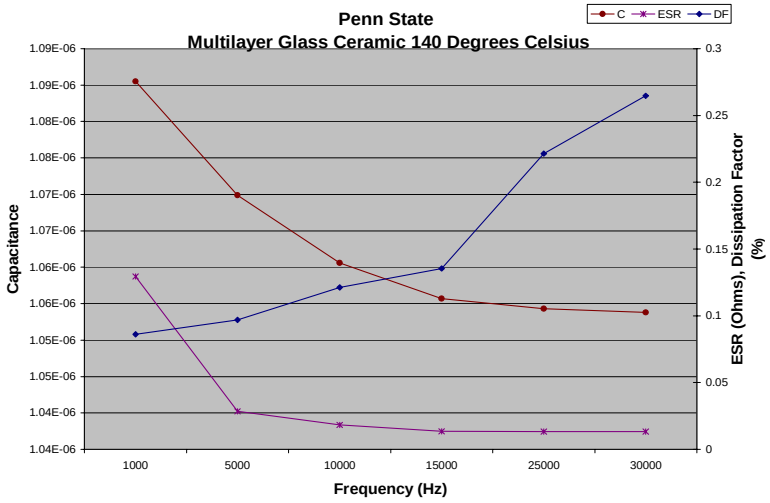

Figure 2. Multilayer glass ceramic at 140°C.

Commercial polyester film

The polyester film capacitor is a 2-µF, 600-Vdc capacitor manufactured by ASC. It was tested from –40°C to 140°C at 20° increments between the extremes. Figures 3 and 4 show the data at the temperature limits. The dissipation factor and capacitance value increase with frequency at the temperature limits, but the ESR decreases as the frequency increases at both temperature limits.

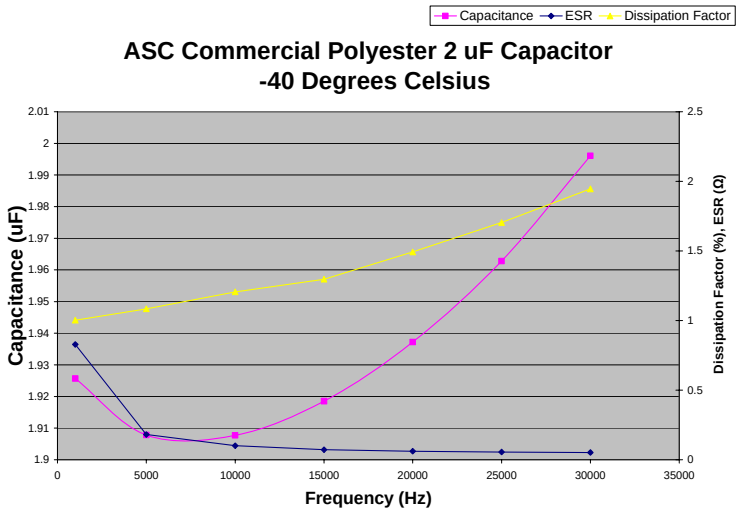

Figure 3. ASC commercial polyester capacitor at –40°C.

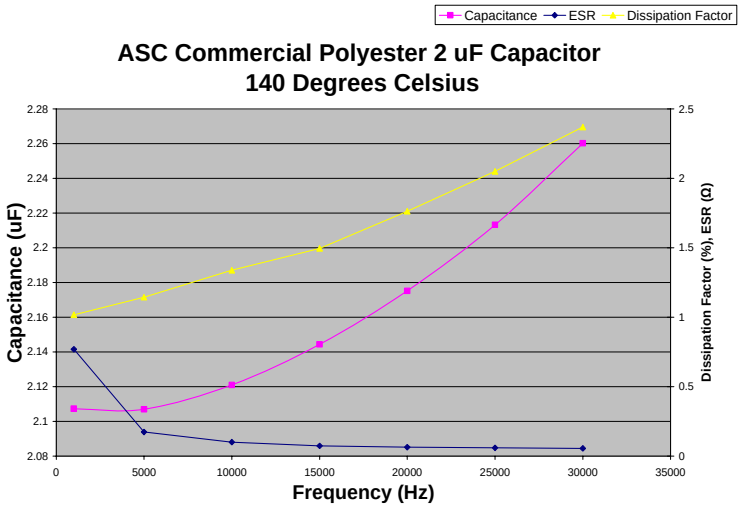

Figure 4. ASC commercial polyester capacitor at 140°C.

Commercial Teflon film

The Teflon film capacitor tested is a 0.1-µF, 600-Vdc capacitor, also manufactured by ASC. It was also tested from –40 to 140°C at 20° increments. The ESR and dissipation factor are very low on this capacitor at both temperature limits. The ESR decreases as frequency increases, but the capacitance value and dissipation factor both increase with frequency (Figures 5 and 6).

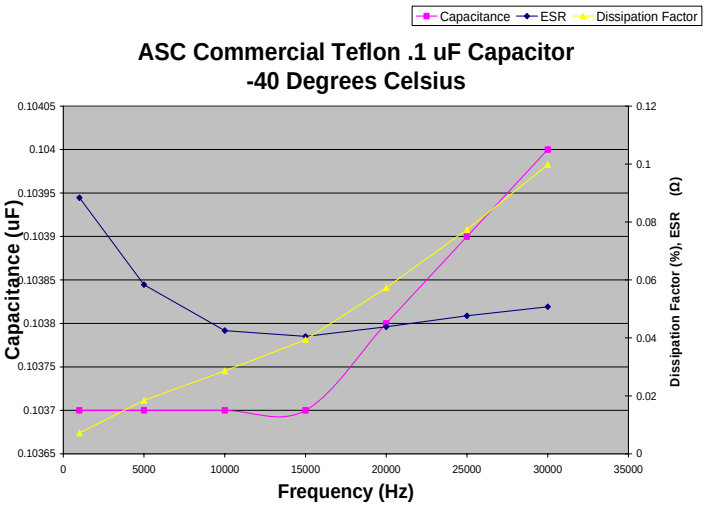

Figure 5. Commercial Teflon film capacitor at –40° C.

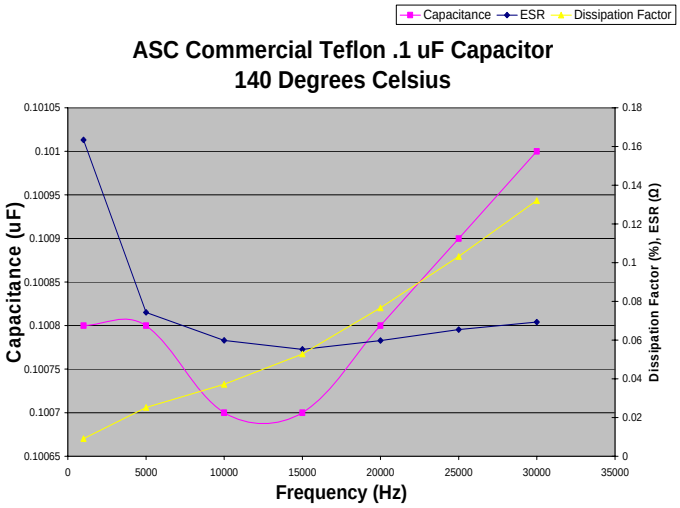

Figure 6. Commercial Teflon film capacitor at 140° C.

Dearborn 200° C capacitor

The Dearborn high-temperature capacitor is a metallized proprietary experimental film 13-µF, 250-Vdc capacitor. It was tested from –40 to 140° C at 20° increments. The ESR on this capacitor is low at both temperature limits and decreases as frequency increases. Both the dissipation factor and capacitance value increase with frequency at both temperature limits.

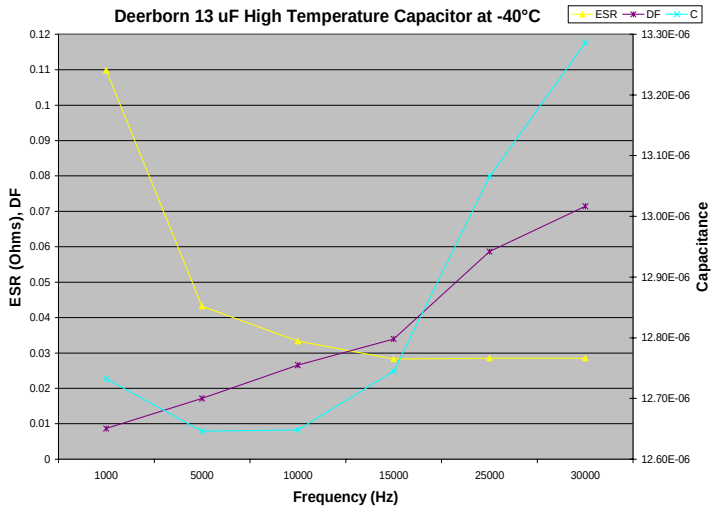

Figure 7. Dearborn metallized proprietary film capacitor at –40°C.

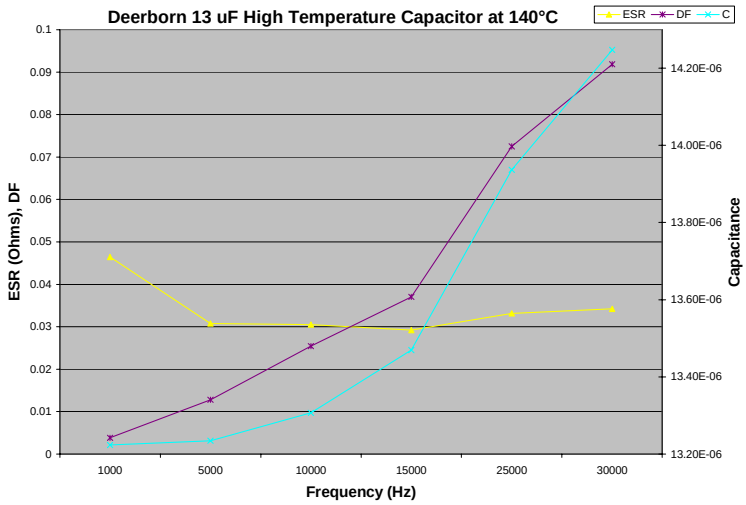

Figure 8. Dearborn metallized proprietary film capacitor at 140°C.

Semikron capacitor module (electronic concepts)

The Semikron capacitor bank is 1000 µF and consists of sixteen 62.5-µF, 900-Vdc capacitors in parallel. The capacitors are metallized polypropylene with a polyester wrap and epoxy end fill. The capacitor module was being tested at this writing.

ESR Thermal Evaluation

In an effort to accurately evaluate the data from these capacitor components, an independent method of measuring ESR is being developed. These tests are designed to validate the ESR for capacitors by quantifying the amount of heat released from the capacitor to its environment. A test stand has been developed consisting of a thermal chamber filled with oil, thermometers to monitor temperatures, a stirring method to keep the oil bath mixed, and insulation to maintain the temperature inside the container.

The test is accomplished by measuring the mass of the oil bath, capturing the initial conditions for the oil (specific heat, temperatures), and operating the test specimen for a period of time. The bath heats up as

a result of the test specimen's waste heat. This waste heat in joules is calculated and related to the test time length, allowing the heat loss rate to be calculated.

Figure 9 shows the test setup. A LabView virtual instrument program has been written to capture all the critical data during the extended test period.

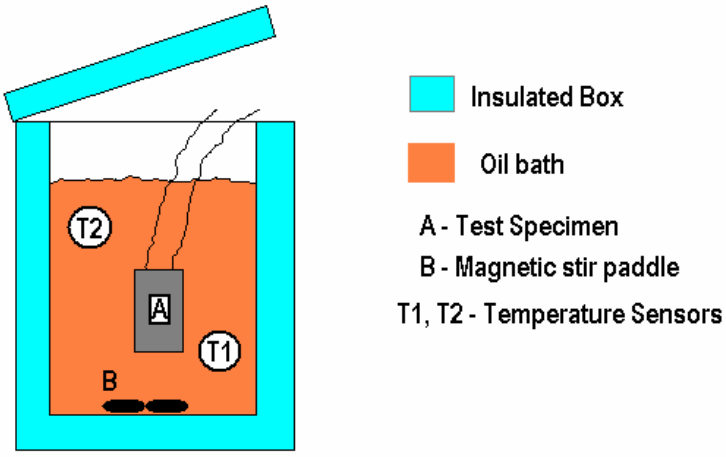

Figure 9. ESR validation oil bath test setup.

The heat captured in the oil bath is calculated using the following relationship:

$$Q = m_{oil} * C_p * \Delta temp$$

where
Q = Heat captured in the oil
m_{oil} = mass of the test oil in the bath
C_p = specific heat of the oil
$\Delta temp$ = change in temperature of the oil (ºC) during the test

The bath is being calibrated by supplying a known amount of current into a known resistive load, measuring the voltage drop across the test resistor, and calculating the power in watts. The program inputs are then calibrated to produce sound thermal measurements. The thermal results can then be compared to the capacitor's electrical data, including ESR, to show that the electrical parameters measured (which would result in a certain amount of heat) match what is measured in the thermal bath.

Magnet Evaluation

Three types of new magnet technologies were evaluated and are reported here. Ames Laboratory provided a sample of 2205 MQP-O in a PPS binder; Argonne National Laboratory (ANL) provided a sintered NdFeB magnet; and Shin-Etsu Magnetics Inc. provided two samples of NdFeB (N43TS and N41TU). The magnet evaluations reported here are not at elevated temperatures.

The Ames and Argonne magnets were tested using a Walker Scientific AMH-40 Automatic Hysteresisgraph (Figure 10). This computer-controlled system is used to test, analyze, and evaluate the hysteresis properties of hard and very hard magnetic materials. The system consists of a PC-based control consol; two computer-interfaced integrating flux meters; a gauss meter; B and B-H coil sets; two 7-in.-diameter, variable-gap, water-cooled electromagnets with cobalt-iron tipped poles; and a 5-kW, 50-A programmable power supply. The 1200-lb electromagnets are capable of generating demagnetizing forces

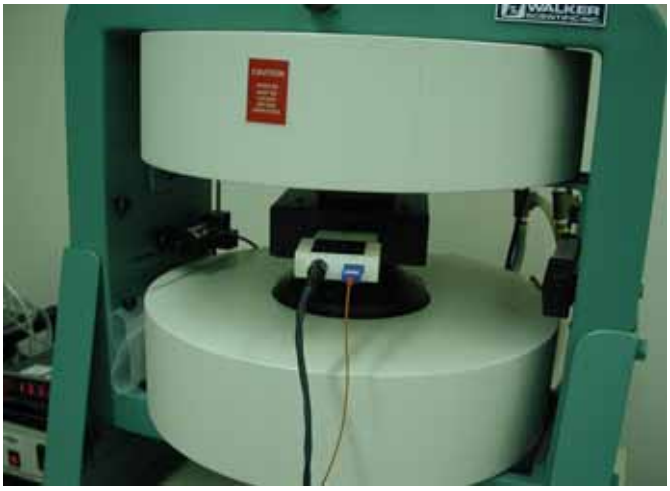

Figure 10. Walker Scientific AMH-40 Automatic Hysteresisgraph.

of up to 30,000 Orsteads. This system allows the operator to perform five different types of tests: manual H-field sweep, second-quadrant demagnetization curves, complete four-quadrant full hysteresis loops, recoil minor loops after saturation in the first quadrant, and first-quadrant saturation or demagnetization of the samples. Also complementing the system is a pulse charger capable of saturating very hard magnetic materials and a Model TCS2 temperature-controlled water-cooled fixture for testing materials at temperatures ranging from −100 to +300° C. This fixture is used with a compatible thermocoupled high-temperature coil set.

Ames Laboratory

Two samples were tested from Ames Laboratory. The sample of 2205 bonded magnet material was tested using the Walker Hysteresisgraph. The de-magnetization curves were plotted at ambient temperature and are shown in Figure 11. The sample of 60% MPQ-O and 40% PPS bonded magnet material from Ames was also tested using the Hysteresisgraph. The de-magnetization curves were plotted at ambient temperature (Figure 12).

Argonne National Laboratory

A sample of NdFeB sintered magnet material was received from Dr. Cha at Argonne National Laboratory. This sample was tested in the Hysteresisgraph at ambient temperature. The hysteresis graph obtained from that test is shown in Figure 13.

Shin-Etsu Magnetics

Two samples of NdFeB (N43TS and N41TU) sintered magnets were obtained from Shin-Etsu Magnetics for testing on the Hysteresisgraph machine. These magnets were not magnetized when received. After the first hysteresis graph was conducted, it was apparent that the magnets were anisotropic across the diameter. This presented a problem in testing the magnet using the Hysteresisgraph machine. The geometry of the coil will not allow the magnet to be placed in the machine so that the magnetization and demagnetization process can produce the hysteresis graph. At this writing, the problem is being discussed with Shin-Etsu Magnetics.

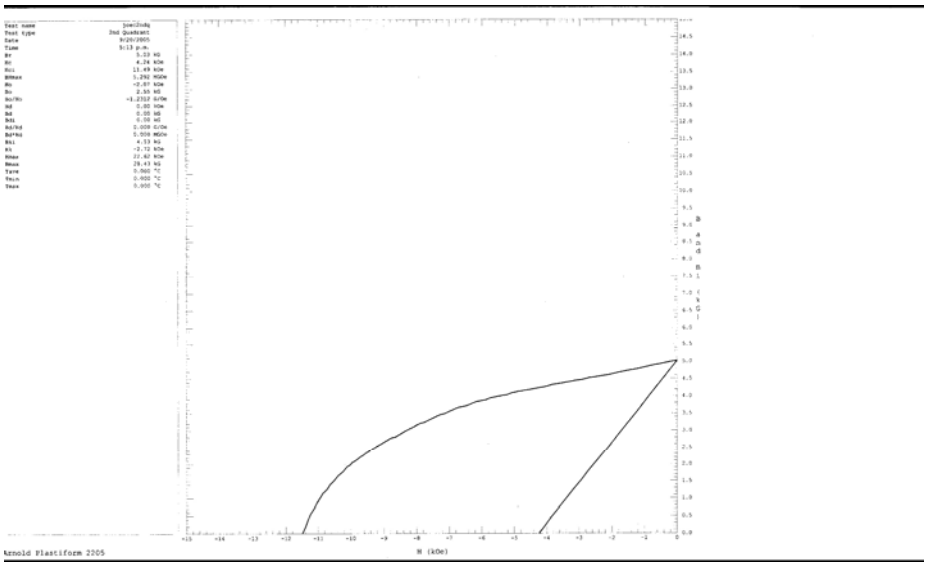

Br	5.03 kG
BHmax	5.29 MGOe
HC	4.24 kOe
HCi	11.49 kOe
Hmax	22.62 kOe

Figure 11. Ames 2205 bonded magnet demagnetization curves.

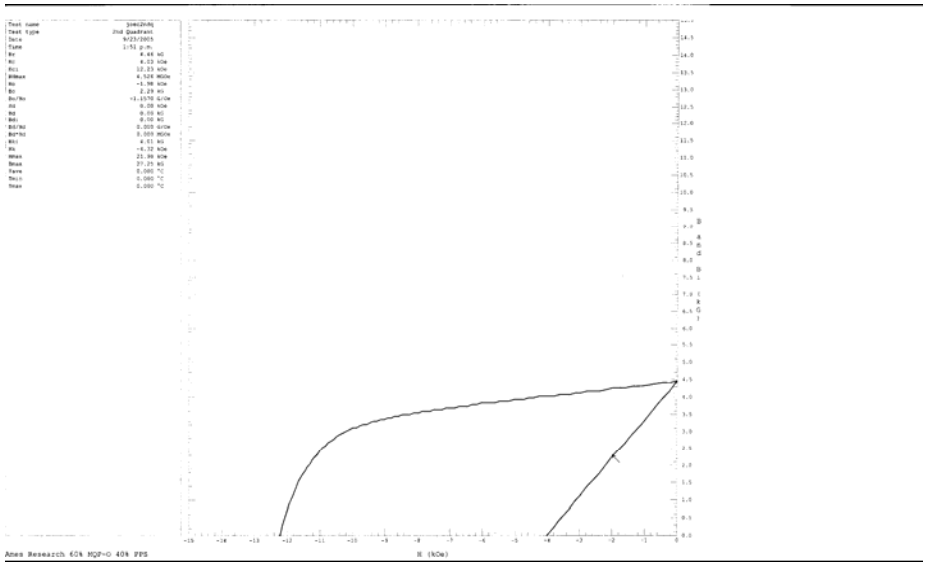

Br	4.46 kG
BHmax	4.53 MGOe
Hc	4.03 kOe
Hci	12.23 kOe
Hmax	21.98 kOe
Bmax	27.25 kG

Figure 12. Ames 60% MPQ-O and 40% PPS bonded magnet demagnetization curves.

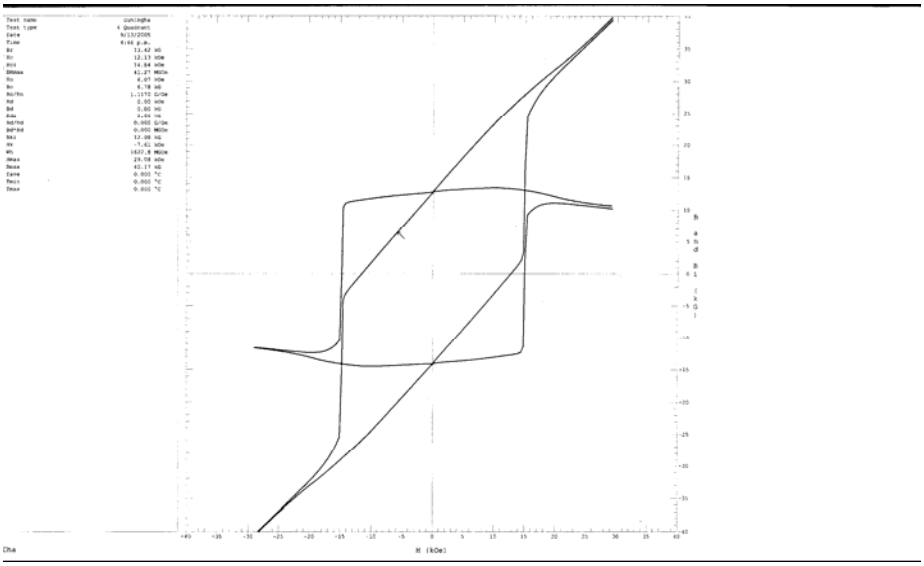

Br	13.42 kG
BHmax	41.27 MGOe
HC	12.13 kOe
HCi	14.84 kOe
Hmax	29.08 kOe
Bmax	40.17 kG

Figure 13. Argonne sintered magnet hysteresis graph.

Future Direction

The testing and characterization of magnets and capacitors will continue in FY 2006 as samples become available. Dynamic testing will be done on samples received in FY 2005. Temperature cycling and dynamic testing will be done on samples received in FY 2006. Thermal ESR evaluation will continue as an independent method of verifying ESR values that are questionable. Alternative methods of measuring ESL will also be explored.

2.3 Benchmarking of Competitive Technologies

Principal Investigator: Robert Staunton
Oak Ridge National Laboratory
National Transportation Research Center
2360 Cherahala Boulevard
Knoxville, TN 37932
Voice: 865-946-1351 ; Fax: 865-946-1262 ; E-mail:stauntonrh@ornl.gov

DOE Technology Development Manager: Susan A. Rogers
Voice: 202-586-8997; Fax: 202-586-1600; E-mail: Susan.Rogers@ee.doe.gov

ORNL Program Manager: Mitch Olszewski
Voice: 865-946-1350; Fax: 865-946-1262; E-mail: olszewskim@ornl.gov

---

Objectives

The Benchmarking of Competitive Technologies project conducts electrical and thermal studies of hybrid electric vehicle (HEV) systems most recently introduced into the automotive market by non-U.S. companies. This produces data on efficiency, torque, speed, and voltage-current relationships. The full inspection and characterization of the electric motors and inverters also defines their thermal system performance in terms of temperature and corresponding sustainable power levels. Testing of these systems helps to rapidly advance the domestic technology base relative to electric traction drive systems suitable for HEV applications.

The FY 2005 accomplishments have made it possible to combine test data with design, packaging, and fabrication assessments to enable analysts to determine how various commercial HEV traction systems, such as the Accord and the Prius, compare with system and program technology targets (peak-power-to-weight and volume ratios).

Approach

As domestic vehicle manufacturers develop HEV systems, they are conducting periodic assessments of the HEV market dynamics, competitive HEV products, and production cost estimates for their own near-term products. Crucial information for the assessments can be obtained only through detailed evaluations of competitive HEV systems. Oak Ridge National Laboratory's (ORNL's) proposed testing program will reveal how the HEV systems contribute to vehicle performance, how the systems are manufactured and packaged, and what performance limitations exist.

Benchmarking of HEV traction drive systems provides detailed electrical and mechanical data from known permanent magnet synchronous motors (PMSMs) and inverters and yields information concerning their thermal performance. The ORNL testing program reveals how the systems are manufactured and packaged and what performance limitations exist. Data were obtained by instrumenting the HEV motor/inverter system and conducting locked-rotor, back–electromotive force (emf), mechanical and electrical loss, and broad-based thermal and performance tests over the entire design envelope. In essence, the overall approach of this project was to thoroughly define the systems and then perform a detailed evaluation of their performance in a controlled laboratory environment. This approach proved to be technically sound and successful.

Other facets of ORNL's technical approach include the following tasks:

- Provide the auto company partners with a consistent, open-literature source for complete characterization of HEV technology recently introduced in the marketplace.

- Continue to use benchmarking information to assist in program planning, developing and executing specific projects, and supporting the partnership with original equipment manufacturers at the U.S. Council for Automotive Research.
- Confirm the realism of performance goals for the technologies and components and identify technology gaps.
- Query DOE and industry partners regarding emerging technology issues and the competitive technologies that hold the greatest technical interest.
- Use benchmarking data to validate multi-project R&D modeling efforts, thus confirming that the validated modeling methods can be used appropriately to develop new technologies.
- Confirm the validity of the project technology thrust and avoid duplication of existing efforts.
- Based on resources, complete limited benchmarking of emerging hybrids or other subassembles and components selected by DOE, EE/TT, and/or industry partners.
- Provide technical insights that can be used to guide research efforts.

From ORNL's own technical perspective, there is an ongoing need for detailed electrical and mechanical data from known PMSMs and inverter designs to feed into analytical models and to support parametric studies. Data from successfully marketed HEV system designs are of special interest. These data can be obtained by instrumenting the HEV motor/inverter system and conducting locked-rotor, back-emf, loss, and broad-based thermal, and performance tests over the entire design envelope. The results of these tests will be shared with other ORNL programs, documented, and transmitted to DOE and domestic vehicle manufacturers on the EE/TT. The motor controller that was developed during the course of this project will be a valuable tool for future ORNL projects.

Controller Development

In order to operate the Prius motor outside the vehicle, a controller system had to be developed. The following provide examples of the technical hurdles and accomplishments related to this effort:

— Since differentiating the position signal produced spiking, the approach was modified to measure the frequency of the sinusoidal signal from the resolver—with improved results. It was also necessary to reduce noise in the current, frequency, and position feedback signals.

— Because of a glitch in Opal-RT program, controller developers began to perform the triangle-to-sine-wave comparison in an external circuit; this made a dramatic improvement in the stability of the motor speed.

— Programmers introduced an enhanced model for motor/inverter control that considers three ranges of speed based on actual operating constraints—each range is rigorously defined by comprehensive equations that are designed to maximize torque per current.

— A new code for a motor/inverter controller was completed and verified against a motor simulation with excellent agreement. (However, the model did **not** have acceptable agreement with the locked-rotor testing data, likely

Major Accomplishments

The following summarizes the main accomplishments for FY 2005 in approximate chronological order:

- The Prius motor was prepared for testing on the dynamometer. To ensure full motor loading capability, machining was required to attain direct coupling to the motor (bypassing the axle gears).
- The report *Evaluation of 2004 Toyota Prius Hybrid Electric Drive System Interim Report*, ORNL/TN-2004/247, was issued early in December.
- Partially funded by the benchmarking project, fixed-speed thermal testing of the Prius motor (using the dynamometer) was completed early in November. The data proved to be of high quality and were documented in *Report on Toyota Prius Motor Thermal Management*, ORNL/TM-2005/33, issued in February 2005.
- ORNL completed an analysis of Prius motor and inverter packaging, which provided estimates of peak-power-to-weight and -volume ratios

- The code for a motor/inverter controller (see the text box) was completed in July, and it successfully ran the Prius motor to full speed and demonstrated full torque capability at all speeds. This allowed final preparation to begin for testing of the Prius system.
- ORNL completed an evaluation of Prius boost converter design and packaging.
- The data acquisition system was enhanced to write data from the Yokogawa PZ4000 power meter and numerous other sources to a single spreadsheet.
- ORNL began final performance testing of the Prius in July and August that led to the identification of hardware and EMI-related issues that were resolved in a timely fashion (see Technical Discussion).
- All required hybrid Accord HEV drive system components/assemblies were purchased during June/July; other parts required a 3-dimensional design process and fabrication (in FY 2006).

Much of the year was devoted to various aspects of preparing the test cell for comprehensive testing under controlled and verified conditions. This included ensuring (1) versatile control of the inverter/PMSM system, (2) precise electrical measurements amid high levels of EMI, (3) calibration of all critical instruments, and (4) the acquisition of approximately 50 channels of data. The test cell block diagram and corresponding layout are shown in Figure 1.

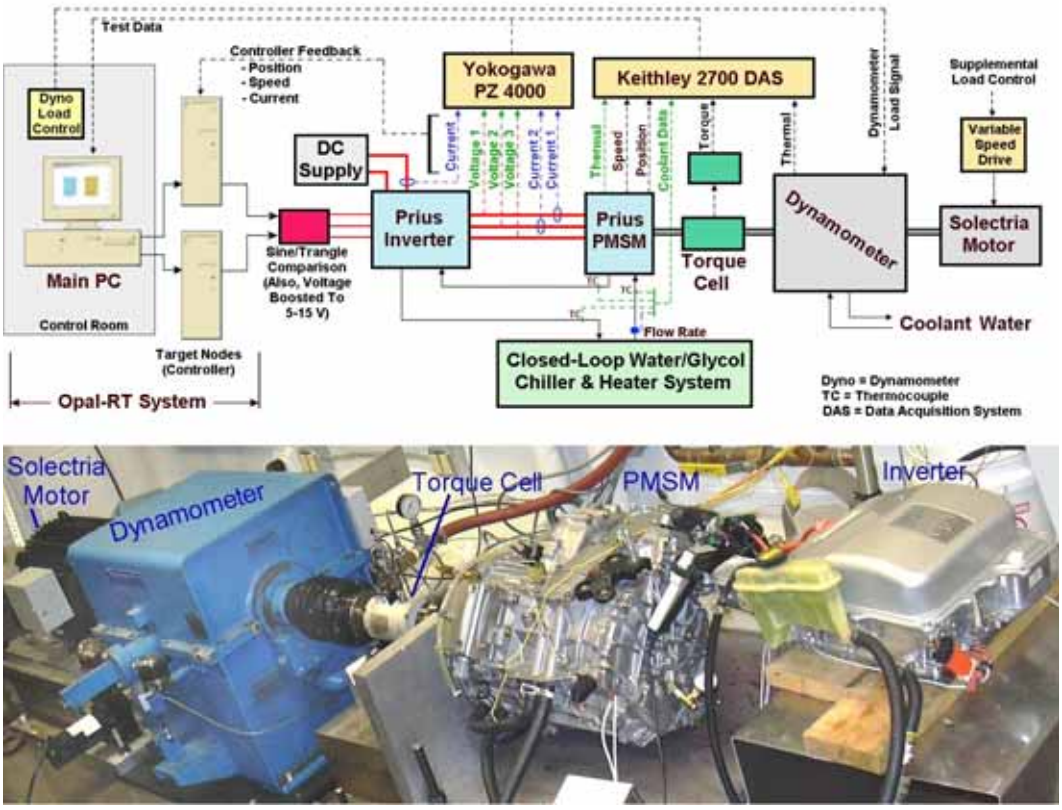

Figure 1. Test cell design, configuration, and actual layout.

Technical Discussion

The performance benchmarking of the 2004 Prius PMSM and inverter systems was accomplished through subassembly inspections/evaluations, a review of manufacturing and packaging, controller development in preparation for full design envelope testing, and laboratory evaluations.

Specifically, the subassembly-level performance testing involved

- Collecting back-emf voltage waveforms for both the PMSM and generator
- Performing locked-rotor tests at varying torque angles (over the range of 90 to 134°)
- Determining gear, bearing, and other friction losses for various operating speeds and lubricating oil temperatures
- Thermal testing at fixed speed (see Thermal Control Studies)
- Mapping motor/inverter performance over the full speed and shaft loading ranges using 50 and 90°C motor/inverter coolant temperatures (in progress).

Controller Algorithm

The algorithm for the controller was divided into three speed regimes: (1) a low-speed regime where operation is limited by current, (2) a mid-speed regime where operation is limited by voltage and current, and (3) a high-speed regime where operation is limited by voltage. In each case, the code was designed to maximize torque per current in a salient PMSM over a wide speed range with an adjustable level of field weakening.

First, a model of a salient PMSM was set up and simulated in Simulink/Opal. This was developed to help in verifying the controller algorithm. The machine model in the direct/quadrature coordinate system, as indicated by d and q subscripts, is given by

$$L_d \frac{di_d}{dt} = -R_S i_d + n_p \omega L_q i_q + u_d \ , \tag{1}$$

$$L_q \frac{di_q}{dt} = -R_S i_q - n_p \omega L_d i_d - K_m n_p \omega + u_q \ , \tag{2}$$

$$J \frac{d\omega}{dt} = n_p K_m i_q + n_p \left(L_d - L_q\right) i_d i_q - \tau_L \ , \tag{3}$$

where R_S = stator resistance, n_p = number of pole pairs, ω = rotational speed (rad/s), L = inductance, J = the energy in joules, i = current, u = voltage, K_m = the torque constant in the dq frame, and τ_L = load torque.

The field weakening problem is to maximize the torque, that is,

$$n_p K_m i_q + n_p \left(L_d - L_q\right) i_d i_q \ ,$$

subject to the following constraints:

$$V = \sqrt{u_d^2 + u_q^2} \le V_{max} \ . \tag{4}$$

$$I = \sqrt{i_d^2 + i_q^2} \le I_{max} \ . \tag{5}$$

A controller algorithm was developed that, for any fixed speed, ω, derives the values of $i_d(\omega)$, $i_q(\omega)$, $u_d(\omega)$, and $u_q(\omega)$ that maximize torque for motoring, and minimize the torque for braking.

This is broken down into three cases:

1. $$\sqrt{i_d^2 + i_q^2} = I_{max}, \sqrt{u_d^2 + u_q^2} \le V_{max}$$
2. $$\sqrt{i_d^2 + i_q^2} \le I_{max}, \sqrt{u_d^2 + u_q^2} = V_{max}$$
3. $$\sqrt{i_d^2 + i_q^2} = I_{max}, \sqrt{u_d^2 + u_q^2} = V_{max}$$

This was further developed in a Matlab™ program that solves a static optimization problem. The control algorithm was used on the simulated PMSM with excellent agreement. This essentially verified the control algorithm. The next step was to validate the simulation model with data from the Prius machine.

Having a very high power density, the Prius motor operates well into the saturation régime. This has added complexity to the motor modeling and controller development efforts. Furthermore, the agreement between the model and motor operation data has not been as good as expected. Recent research papers [1,2] indicate that the flux linkage in the *q* axis depends on *both* the *d* and *q* currents. This also appears true for the *d* axis flux linkage. Late in the year, the model was being revised accordingly so that it corresponds better with flux saturation levels and the locked-rotor data. This is expected to lead to an improved understanding of how an interior permanent magnet (IPM) motor such as the Prius should be modeled.

Controller Hardware

The RT-LAB real-time computing platform from OPAL-RT Technologies was used to model and replace the Prius control system. The RT-LAB system interfaces with the MATLAB SIMULINK software for quick controller development without tedious programming. The system consists of a host PC running a user-selected operating system and two target PCs running the QNX Neutrino operating system. One of the PCs is a dual-processor computer with additional counter, encoder, and analog/digital I/O PCI boards.

The model of the Prius controller and a user interface was built in MATLAB SIMULINK using both built-in SIMULINK blocks and RT-LAB blocks, as illustrated in Figure 2. This figure is an upper-level representation; most blocks can be opened for additional levels of detail. Using the Real-Time Workshop Toolbox of SIMULINK, the model was converted to C-source code and the executable uploaded to the target PCs. The controller software runs on two target PCs that communicate with each other through a Firewire connection, while the host computer is used to command the controller through an ethernet connection. The software allows the controller development to be flexible and versatile with the capability of quickly making required development changes. This approach bypasses some of the more difficult hardware development efforts required to allow the inverter to be controlled outside the vehicle. It also enhances the ability to make changes during testing, if required.

dc Converter Assessment

With planning under way for detailed performance testing at ORNL, it was necessary to review data that made clear the operation of the voltage boost circuit in the Prius. In addition, there was considerable technical interest in boost converters, including both their packaging and operation. In the Prius HEV system, the PMSM obtains most of its power from the generator and the rest from the high-voltage-battery–converter system. Thus the converter's power rating is less than half of the PMSM's rating.

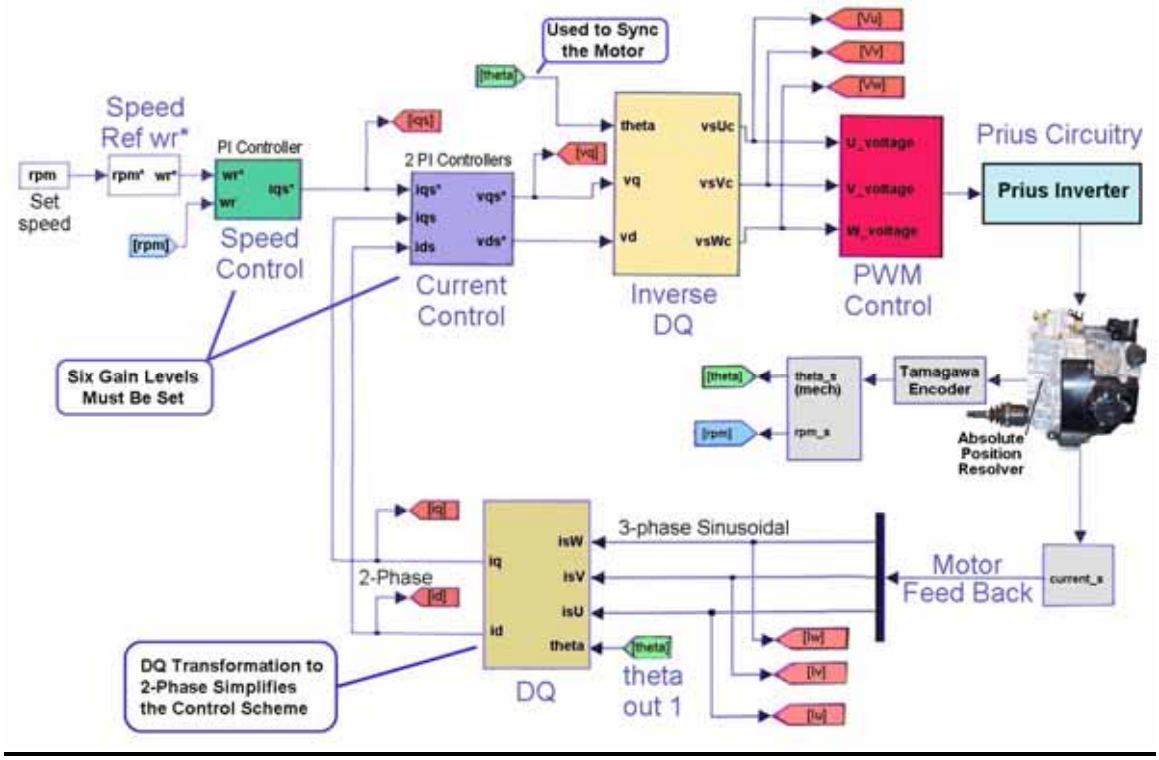

Figure 2. Upper-level flow diagram of Prius controller system.

The converter consists of three main components: an Intelligent Power Module, an auto-transformer, and a water-filled heat sink on which the first two are mounted. The module, simplified schematic, and transformer are shown in Figure 3. The figure indicates the mass and volume of the components and the total silicon area of the insulated gate bipolar transistors (IGBTs) and diodes. The boost converter is unusual in that two IGBTs are used instead of one so that two-way power flow can take place—the powering of the PMSM and the recharging of the high-voltage battery.

Of high interest is how the generator voltage, which increases with vehicle speed, compares with the voltage that the ECU directs the converter to produce. In order to determine this, the generator back-emf data plot was modified as shown in Figure 4 to show, by extrapolation, the voltage-speed relationship at speeds of up to 10,000 rpm. Also, the vehicle speed is included in the plot so that the data can be compared with vehicle operation data provided by Argonne National Laboratory (ANL). Note that the peak voltage developed in the generator is in the variable range of the dc converter when the vehicle is traveling 25–65 mph. This relationship will prove useful in the discussion below.

ANL generated vehicle drive cycle test data and, at ORNL's request, transmitted converter-related data to ORNL in April 2005. These data helped to characterize the operation of the voltage boost converter relative to acceleration and vehicle speed.

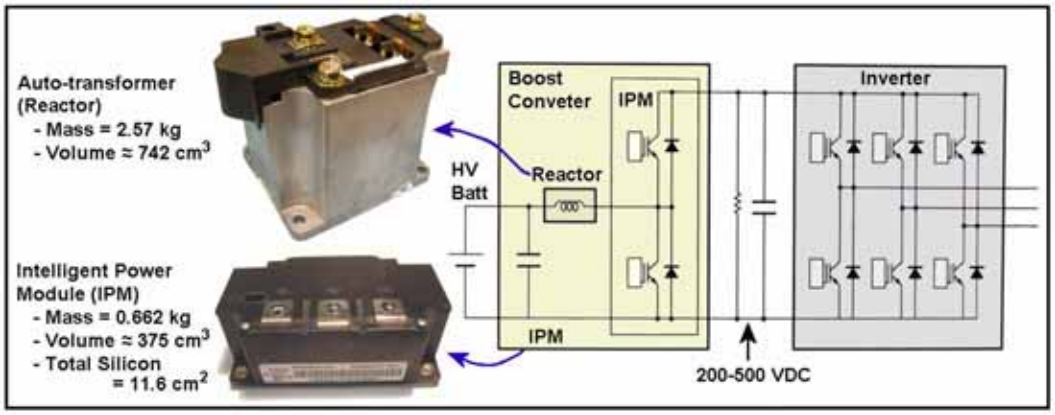

Figure 3. Voltage boost converter components and simplified schematic.

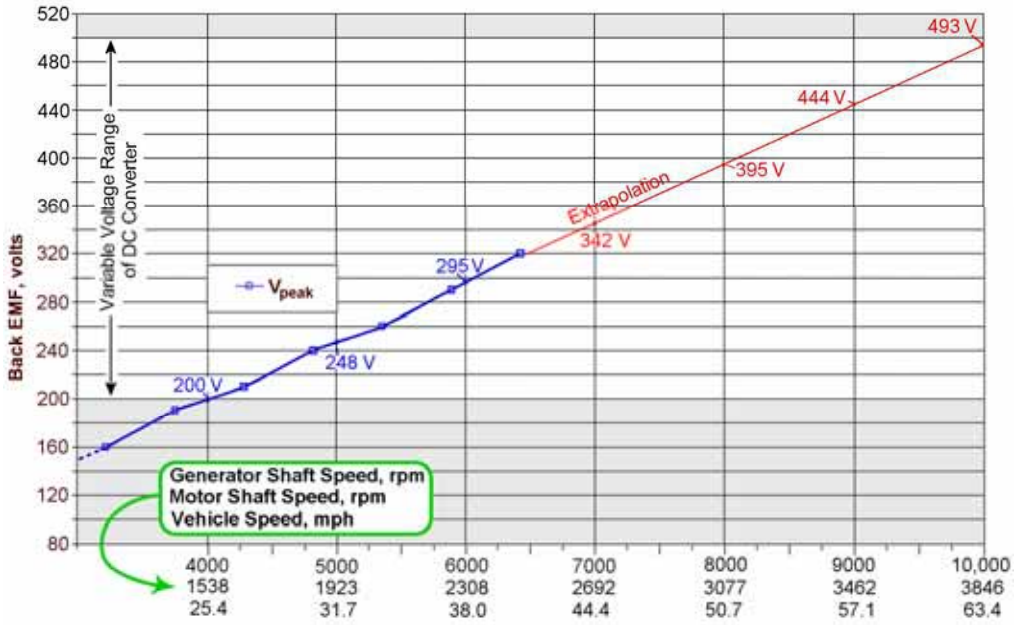

Figure 4. Extrapolation of generator back-emf data for generator speeds of up to 10,000 rpm.

Figure 5 shows data from a drive cycle where the vehicle was accelerated to about 31.5 mph, based on chassis-dyne data, followed by braking. The plot includes voltage and current output from the converter, accelerator pedal position output, brake pedal position output, and vehicle speed. A portion of the y-axis scale is expanded to enlarge/clarify the plots at the bottom of the chart (also making the depiction qualitative). As indicated in the figure, there are three instances where a current spike from the output of the voltage boost circuit preceded or accompanied a rise in the output voltage from the boost circuit. The voltage then remained elevated for different periods and then fell. Two instances occurred during acceleration and one at the end of the acceleration period. Note that braking causes a maximum boost to 500 V to support the regeneration battery-charging mode. The data do not appear to provide a full picture of what is happening; this is not surprising, since the ECU algorithm is unknown.

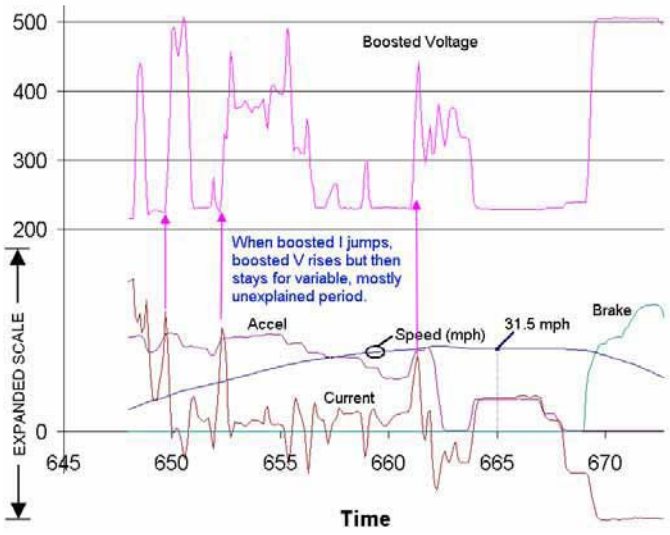

Figure 5. Drive cycle data from ANL showing voltage boost converter response.

The operation of the converter is further defined in the drive cycle plot in Figure 6. In this case, the vehicle is accelerated to about 68 mph. Because the level of acceleration is varied, the voltage boost swings between min and max several times. From 28.1 mph to 49.8 mph, maximum voltage results from both the acceleration process and the increasing speed. Between 49.8 mph and 59.7 mph, there is minimal tendency for voltage to drop below the max level. Above 59.7 mph, voltage remains at the max level. Notice that the plot also specifies the rotational speed of the PMSM[1] at specified points.

Figure 6 also shows the peak back-emf from the generator based on ORNL testing as presented above. The points are plotted at the calculated equivalent vehicle speeds, and then approximate interconnecting lines are added for clarity. The data show how the boosted voltage rarely falls below the generator's peak voltage. Although the actual ECU algorithm for controlling the voltage boost is unknown, this plot and the preceding plot create a partial concept of how voltage is generally controlled during acceleration, high speeds, and braking. Because the rating of the converter prevents it from providing full power to the Prius motor, the converter was not used in performance characterization testing at ORNL.

Subassembly Testing

Motor and generator testing yielded back-emf voltage and frequency data. During the tests, a dynamometer drive was used to control motor speed and generator speed. Results of the back-emf testing are summarized in Table 1. These tests were repeated later in the year to verify that no measurable rotor demagnetization occurred as a result of prior thermal testing at elevated temperatures. It was found that the data agreed quite well (within instrument error).

[1] The rotational speed of the PMSM (rpm) is 60.66 times the vehicle speed in mph. This is based on the constant gear ratio of the Prius, wheel/tire diameter, and conversion of units.

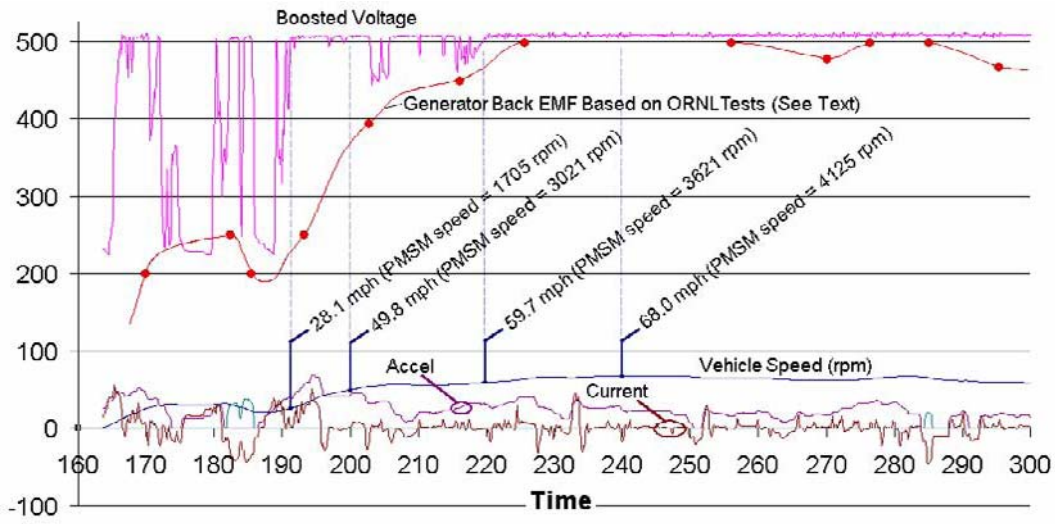

Figure 6. Drive cycle data set showing voltage boost at high speeds (ANL/ORNL data).

Table 1. Summary of back-emf test results

Test conditions	Results
Motor back-emf (6000 rpm)	540 Vrms
Motor Volts/Hertz	1.33 Vrms/Hz
Generator back-emf (6420 rpm)	195 Vrms
Generator Volts/Hertz	0.46 Vrms/Hz

A series of locked-rotor tests was performed to determine the general operating capabilities of the traction motor. In particular, the torque and current were studied during the locked-rotor tests to characterize the startup torque capability of the motor. This test was repeated later in the year using improved methodology and equipment, since the prior data did not agree well with the Prius motor model. Figure 7 shows the torque vs rotor position plots for seven different current levels. Based on the plots, current and corresponding maximum torque values are summarized in Table 2. The new data are more extensive and of higher quality; however, because the model does not fully account for magnetic saturation, some discrepancy remains. Finite-element analysis (FEA) studies are ongoing that may help to improve the model's handling of saturation.

Motor Testing

The benchmarking project partially supported and funded the thermal testing of the Prius motor. These tests were successful in determining the continuous ratings of the Prius motor design at coolant temperatures ranging from 35 to 105°C. This information has not been released by the Toyota Motor Company. The ratings at base speed (1200 rpm) were projected from test data at 900 rpm. The continuous ratings were determined to be 15 kW using 105°C coolant and 21 kW using 35°C coolant. These ratings are well below the 30-kW target of the DOE FreedomCAR Program (see the Thermal Control Studies section for further discussion).

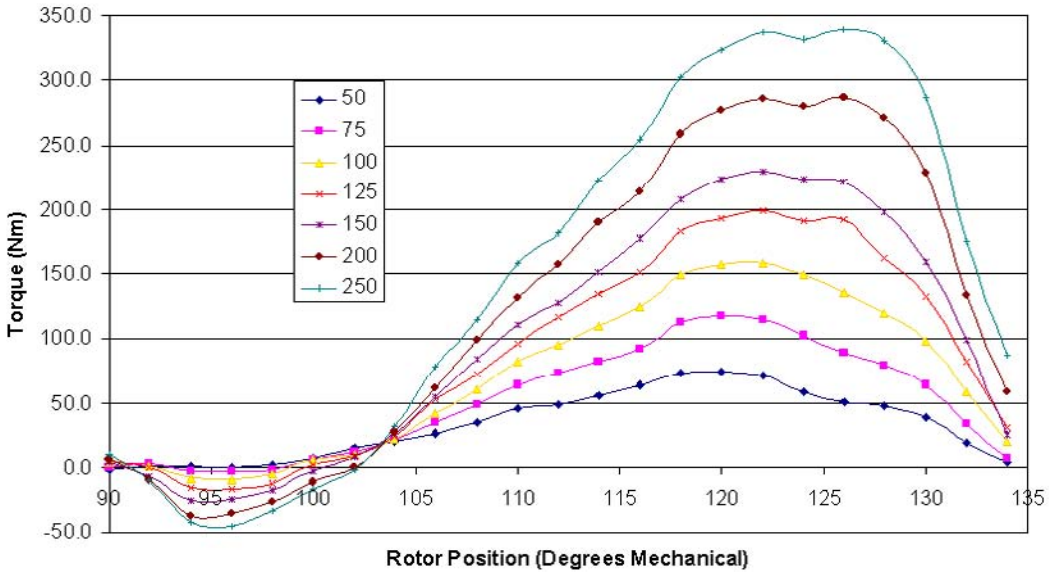

Figure 7. Prius locked-rotor data showing torque vs rotor position.

Table 2. Summary of motor current and torque test results

Current, A	Maximum torque, Nm
50	74
75	118
100	154
125	199
150	221
200	286
250	337

The final testing of the Prius was the mapping of motor/inverter performance over the full speed and shaft loading ranges using 50 and 90°C motor/inverter coolant temperatures. Successive attempts at accomplishing this test during July and August were useful in identifying and ultimately resolving lingering barriers. In summary, excessive vibration was resolved by shaft realignment, a data-related discrepancy was resolved with a recalibration of the torque cell, and higher-than-expected temperatures led to a review of the test plan and modifications to allow safe testing at a higher temperature limit (200°C). In the most recent test run, data showed unrealistically high 99% inverter efficiency (however, the error may be as small as one percentage point). This led to an investigation that ultimately pointed to EMI-induced noise introduced in the CT output circuitry as the most likely cause. Preliminary testing using fully shielded CTs indicated a significant improvement—a potentially complete resolution of this problem. Further testing in FY 2006 is required to verify these findings.

Conclusion

The Prius HEV system was fully evaluated by design inspection, disassembly, physical and electrical measurements, fabrication and packaging studies, and a series of laboratory spin and loss tests. In addition, thermal testing over a broad temperature range proved to be effective in determining the limitations of the continuous and peak power operation of the PMSM.

The importance of having developed a fully functional controller algorithm/code during the year cannot be overemphasized. ORNL now has a highly versatile tool that will enable laboratory testing of essentially any PMSM as long as position and speed sensors exist. The controller can adjust and explore

varying levels of field weakening to determine the most efficient operating point. As shown in Figure 8, this controller system has already been put to use in another project to operate an experimental IPM motor even *before* completion of Prius testing. It is highly likely that this code will be used to operate a variety of motor designs for many years to come.

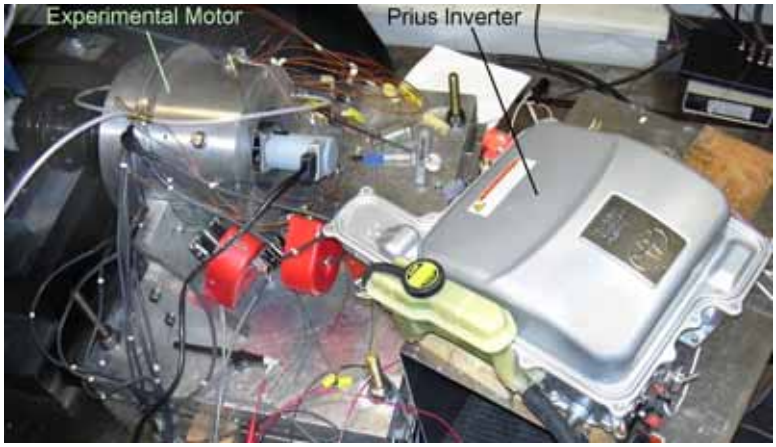

Figure 8. Prius controller/inverter system operating an IPM-reluctance motor with brushless field excitation.

It is estimated that 1–2 more weeks of testing in the test cell will produce all the data needed to map the entire speed vs torque range (full design envelope) of the Prius. Since the final Prius report draft is lacking only these data (and discussion), the data/report will be published early in FY 2006 and immediately disseminated.

Future Direction

During FY 2006, ORNL will perform benchmark testing of the hybrid Accord traction drive system. The test data and design, packaging, and fabrication assessment will be combined to enable analysts to determine how the Accord system compares with the Prius system and program technology targets (peak-power-to-weight and -volume ratios). Other hybrid systems will be considered for limited analysis based on resources and DOE/EETT interest. A decision will then be made by DOE in concert with the original equipment manufacturer partners regarding the need for further benchmarking.

Hybrid SUVs are emerging on the market and may represent significant deviations from existing hybrid technology. There may be some innovations in the drive system that merit benchmarking studies.

Publications

Evaluation of 2004 Toyota Prius Hybrid Electric Drive System Interim Report, ORNL/TM-2004/247, Oak Ridge National Laboratory, December 2004.

Report on Toyota Prius Motor Thermal Management, ORNL/TM-2005/33, Oak Ridge National Laboratory, February 2005

References

1. N. Bianchi, S. Bolognani, and B. J. Chalmers, "Salient-Rotor PM Synchronous Motors for an Extended Flux-Weakening Operation Range," *IEEE Transactions on Industry Applications*, **36**(4) (July/August 2000).
2. S. D. Rubira and M. D. McCulloch, "Control Method Comparison of Doubly Fed Wind Generators Connected to the Grid by Asymmetric Transmission Lines," *IEEE Transactions on Industry Applications*, **36**(4) (July/August 2000).

2.4 Jet Impingement for Cooling Power Electronics Components

Dr. Sreekant Narumanchi, Dr.Vahab Hassani, Dr. Desikan Bharathan
National Renewable Energy Laboratory
1617 Cole Boulevard
Golden, Colorado 80401
Voice: (303)-275-4062; Fax: (303) 275-4415; E-mail:Sreekant_Narumanchi@nrel.gov

DOE Program Manager: Susan Rogers
Voice: (202) 586-8997; Fax: (202) 586-4403; E-mail: Susan.Rogers@EE.DOE.GOV

NREL Task Leader & Technical Advisor: Dr. Vahab Hassani
Voice: (303) 275-4427; Fax: (303) 275-4415; E-mail: vahab_hassani@nrel.gov

---

Objectives

Jet impingement has been an attractive cooling option in a number of industries over the past few decades. Over the past 15 years, jet impingement has been explored as a cooling option in microelectronics. Recently, interest has been expressed by the automotive industry in exploring jet impingement for cooling power electronics components. The main purpose of this technical report is to explore from a modeling perspective both single-phase and boiling jet impingement cooling in power electronics, primarily from a heat transfer viewpoint. The discussion is from the viewpoint of the cooling of IGBTs (insulated-gate bipolar transistors), which are found in hybrid automobile inverters.

Approach

First, single-phase jets are examined. In the literature, single and multiple submerged, confined as well as free-surface jets have been investigated. Empirical correlations for heat transfer from the simulated chip surface have been presented. For single-phase liquid jets, non-dimensional correlations have been fairly well established in the literature.

In this report, we discuss in detail these correlations, as well as the heat transfer results from them, using water as a fluid. Computational fluid dynamics (CFD) modeling is also performed, within the framework of the code FLUENT. The CFD results are compared with experimental data from the literature to validate the numerical results and gain confidence in the CFD predictions. Simulations for the IGBT package are then performed. One of the FreedomCAR goals is to use glycol-water mixture at 105°C inlet temperature and also to dissipate close to 200 W/cm^2 from the silicon die of the IGBT package. CFD simulations are presented that demonstrate conditions under which it may be possible to achieve these goals using glycol-water mixture. For comparison, results are also presented with water. Some aspects related to the practical implementation—such as pressure drop, erosion, and corrosion associated with impinging jets—are also discussed briefly.

Second, jets that involve nucleate boiling are examined. Typically, for electronic cooling applications, nucleate boiling is the preferred regime of operation because it involves the lowest wall superheats. As is the case with the single-phase jets, a number of experimental studies have been reported in the literature with submerged and free-surface jets that involve boiling. In the boiling literature, because of the difficult nature of the problem, the correlations are typically all dimensional.

In this report, we present CFD modeling of jets involving nucleate boiling. It is not possible to model boiling jets in the commercially available version of FLUENT, so a user-defined function (UDF) was used to perform these simulations. All the simulations relating to boiling jets are performed in close collaboration with the staff at Fluent, Inc. For nucleate boiling, the Eulerian multiphase model is used. A mechanistic model of nucleate boiling is implemented in a UDF in FLUENT. The numerical predictions

are validated against experimental studies on submerged jets involving nucleate boiling. These experimental studies involve water and R-113 as the fluids. After this, IGBT package simulations are reported with a submerged boiling jet of water. To the best of our knowledge, these validations and IGBT package simulations with boiling jets are being reported for the first time. A comparison between single-phase and boiling jets from the heat transfer viewpoint and in the context of cooling the IGBT package is also presented.

Accomplishments

A survey of the nucleate jet impingement boiling literature indicates substantial experimental nucleate boiling data. There is considerable scatter in the data: uncertainties on the order of 40% are quite common. The nature of the target surface and the fluid-surface interaction is critical in determining the bubble nucleation process. The important CHF correlations in the literature yield results that agree with one another. Saturated fluorinerts (FC72, 77, 84) and OS-10 yield low CHFs on the order of 50 W/cm^2, even with velocities as high as 8 m/s. Fluids such as water, ammonia, and R-134a have much superior heat transfer characteristics than fluorinerts. Several jet parameters—such as diameter, nozzle-to-target separation, velocity, number of jets, and orientation—do not have much of an impact on the nucleate boiling phenomenon.

We have observed some of these effects in our CFD simulations also. The CFD model and code are validated against two experimental studies involving submerged jets. To the best of our knowledge, this is the first time such validations are being reported. A reasonable match is found between the experimental boiling curves and those obtained by CFD. IGBT package simulations suggest that for the limited number of cases examined here, boiling jets are not providing any significant benefits over non-boiling jets. It is not entirely clear under what conditions boiling jets would be more beneficial than single-phase jets in the context of IGBT package cooling.

Regarding practical implementation with boiling jets, a separate loop would be necessary. Water is eliminated from the picture owing to freezing problems. Similar problems eliminate having boiling with the glycol-water mixture. Perhaps R-134a could be used, but this must be investigated further.

Overall, it appears the single-phase glycol-water jets in the single-phase regime should be investigated further. Glycol-water is likely to be readily accepted as a working fluid by the automotive industry. If practical concerns relating to reliability, erosion, corrosion, and package stresses are addressed, glycol-water jets can be implemented realistically. With further heat transfer enhancements, they can remove high heat fluxes of up to 200 W/cm^2. In this first part of the report, we have demonstrated baseline conditions under which it may be possible to dissipate such heat fluxes using glycol-water jets in the single-phase regime.

Future Direction

The future direction of research in this area is to enhance the heat transfer coefficients that can be obtained with steady single-phase circular liquid jets by 70% to 100%. The goal is to achieve this enhancement by inducing pulsations in the flow path of the jets and also by modifying the surface of the impingement surface. Basically the pulsed jet corresponds to an on-off configuration, where the liquid jet is prevented from coming in contact with the target at certain intervals due to an impediment in its path. Increasing the heat transfer coefficients due to jet pulsations and impingement surface modifications may enable removal of heat fluxes of up to 150-170 W/cm^2 with jet velocities equal to or less than 8 m/s while maintaining a low temperature difference of about 20 ^oC.

Outcome and Results

The outcome of this research will be a prototype inverter that will demonstrate the capability of pulsating jets coupled with surface modifications in cooling the low resistance IGBT structure. The results will

show that this configuration will be able to operate at 125°C die temperatures while being cooled by 105°C coolant inlet temperature and removing heat fluxes on the order of 150 W/cm^2. This heat flux level is more than 2 times the heat flux compared to the existing technology.

2.5 Low Thermal Resistance IGBT Structure

Dr. Vahab Hassani, Daniel Benhammou
National Renewable Energy Laboratory
1617 Cole Boulevard
Golden, Colorado 80401
Voice: (303)-275-4427; Fax: (303) 275-4415; E-mail:Vahab_Hassani@nrel.gov

DOE Program Manager: Susan Rogers
Voice: (202) 586-8997; Fax: (202) 586-4403; E-mail: Susan.Rogers@EE.DOE.GOV

NREL Task Leader & Technical Advisor: Dr. Vahab Hassani
Voice: (303) 275-4427; Fax: (303) 275-4415; E-mail: vahab_hassani@nrel.gov

---

Objectives

Develop advanced thermal management methods and systems that will allow next-generation power electronics to operate at high heat fluxes and high temperatures in a compact (low-volume), lightweight power electronics package.

- To reduce thermal resistance between insulated gate bipolar transistor (IGBT) and coolant
- To enable use of 105°C inlet coolant
- To reduce the size and cost of the thermal management unit.

The limiting factor in current designs of IGBT cooling structures is the thermal resistance caused by the multiple layers of poor thermal conductors. By reducing the total number of layers, the resistor network is truncated, which allows increased heat transfer. Achieving this will lead to the implementation of a heat exchanger that can expel the heat generated by the power electronics with a small temperature gradient. By reducing this difference to 20°C, a coolant with an inlet temperature of 105°C can be used to maintain the power electronics within the acceptable temperature range. This allows the heat exchanger to be integrated with the cooling loop of the engine and reduce the size and cost of the thermal management unit by eliminating the infrastructure of a separate cooling process.

Approach

- Model conventional IGBT structure.
- Model low thermal resistance structure.
- Verify structural integrity.
- Collaborate with industry for hardware application and testing.

The approach used to develop this low thermal resistance IGBT structure begins with modeling the conventional IGBT structure and then the new low thermal resistance structure to compare and contrast the performance with finite element analysis (FEA). FEA can also be used to verify structural integrity. Prototype fabrication can begin when this verification is complete. Using industry partnerships, the prototypes are then sent for hardware integration so that we can then corroborate the numerical simulations with experiments.

Accomplishments

- Project started in FY 2005.
- Initial modeling of conventional and new low thermal resistance architecture is complete.
- A patent for the new structure was filed.
- Results indicate 64% less thermal resistance than the conventional configuration.
- Next-generation design considerations were proposed.
- Results indicate viability of 105°C inlet coolant temperature.

This project commenced in FY 2005 with a timeline of two years. Detailed structural and thermal analysis of conventional and low thermal resistance IGBT structures have been performed with the FEA package ANSYS and show a reduction of thermal resistance of at least 64%. These successful results have led to a patent being filed for the cut-through IGBT structure invention while modeling design refinement continue as subtleties are optimized. Results also indicate that the high heat transfer available through jet impingement cooling can sustain the 125°C maximum operating temperature of the electronics with an inlet temperature of 105°C given power densities as high as 100 W/cm^2. This is 66% higher than what conventional IGBT structure can handle with a 75 C coolant.

Future Direction

The idea of low thermal resistance IGBT structure has been extensively examined using ANSYS and other thermal and structural modeling tools. However, the actual hardware testing and evaluation is needed for proof of concept. Therefore it is proposed here that at first stage a simple small scale low thermal resistance IGBT module be prepared for laboratory testing and evaluation. In the proposed laboratory tests, a set four IGBTs with low thermal resistance structure will be constructed and tested in the laboratory environment with die temperature of 125 C and the inlet coolant temperature of 105 C. Water/Glycol mixture will be used as working fluid and the back of the DBC will be cooled by single phase jet impingement technique. These tests will be simulating the exact structure of the Semikron inverter that has been used in our modeling activities.

At the second phase of this work, NREL will work with Semikron to build a prototype of the proposed structure in an actual inverter and the whole unit will be tested for various operating conditions and proof of concept.

This project is very important and it is in line with DOE's FreedomCAR objectives. This project responds to a major issue that is facing the industry now which is the utilization of 105 C inlet coolant temperature. Our analysis show that temperature differences as low as 21 C for a heat flux of 90 W/cm2 is feasible. This is more than what the current technology can do which is to remove about 60 W/cm2 at a temperature difference of about 50 C.

Outcome and Results

The outcome of this research will be a prototype inverter that will demonstrate applicability of the low thermal resistance IGBT structure. The results will include performance of the new structure under various operating conditions. The results will address fatigue, thermal stress, and thermal fluctuation results. The results will also show that the new structure will be able to operate at 125 C die temperature while being cooled by 105 C inlet coolant temperature. It will also show that the new structure will be able to remove 50% more heat flux compared to the existing technology.

Design and Analysis

Conventional IGBT Structure

The conventional design of an IGBT structure consists of : silicon die, a solder layer, a direct bond copper layer (which consists of a layer of ceramic sandwiched between two thin layers of copper), and a layer of thermal interface material (TIM) that is used to facilitate heat transfer between the DBC and the base plate where the cooling medium flows through. This structure is depicted in Figure 1. Based on existing thermal data and a numerical analysis done in this work, TIM constitutes a significant portion of the total thermal resistance between the silicon die and the coolant.

In order to reduce this thermal resistance, NREL researchers have come up with a novel idea of eliminating those layers that cause the most resistance; namely the base plate and TIM. To eliminate those resistances, we propose to cut through those layers and cool the bottom surface of the DBC layer directly. We propose to provide a good seal between the DBC layer and the base plate in the remaining surfaces to prevent the coolant from penetrating into the electronics side. This idea is depicted in Figure 1 where a conventional structure is shown next to the cut through structure for comparison.

Figure 1 illustrates the two principal differences between the two cases being considered. Case A is the conventional design currently in use. The IGBT (top green rectangle) is soldered directly to the top layer of the Direct Bond Copper (DBC) (top red layer). The copper is brazed at high temperature to aluminum nitride (AlN), which is also brazed to a bottom copper layer. The copper is then set on a thick heat spreader plate/base plate with a thin layer of thermal paste to bridge the air gap between the two layers.

The concept behind Case B eliminates the thermal paste and most of the base plate to allow direct cooling of the DBC. In this first generation design we propose to solder the DBC to the cut-through base plate with holes of various shape depending on the geometry of the silicon die. The holes can be square, circular, etc.

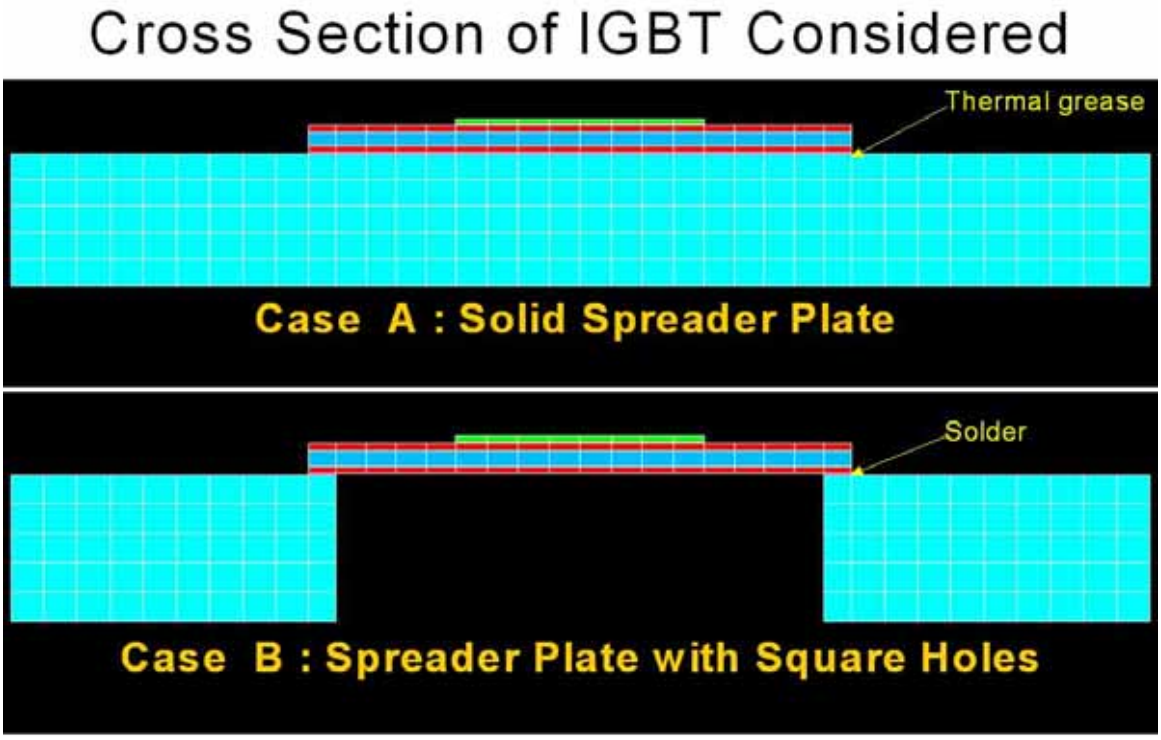

Figure 1 Contrasting the conventional IGBT design with a thick heat spreader plate to the proposed design with a cut-through

In order to show the significant impact of the new design on thermal performance of the IGBT structure, we performed a thorough thermal analysis of the conventional structure followed by the similar analysis for the cut through design. This analysis showed that the new structure has more than 64% lower thermal resistance compared to the conventional design.

To further investigate the performance of the conventional IGBT structure under thermal loads, we analyzed a single phase of an inverter consisting of 12 IGBTs and 6 diodes. We assumed a heat flux of 90 W/cm2 for the IGBTs and 60 W/cm2 for the diodes. The remaining boundary conditions where the same as those used above for single IGBT analysis.

Figure 2 shows a detailed thermal profile over the entire length of the single phase of an inverter. Note that the plate shown in blue color is the heat sink plate where the DBC layer is resting on. This figure clearly shows temperatures in excess of 150°C for the IGBT chips. The power diodes maintain a temperature of around 130°C because they generate less heat, even though this exceeds the maximum operating temperature of 125°C. This analysis shows a maximum temperature difference between the silicon die and the coolant to be 57°C. It is clear from both analyses performed here that the presence of TIM hinders the flow of heat. The TIM layer has a conductivity of about 1 W/m K and is usually applied at a thickness of 20 microns. The conventional structure is only suitable for low heat fluxes and or for conditions where the coolant enters the base plate at very low temperatures.

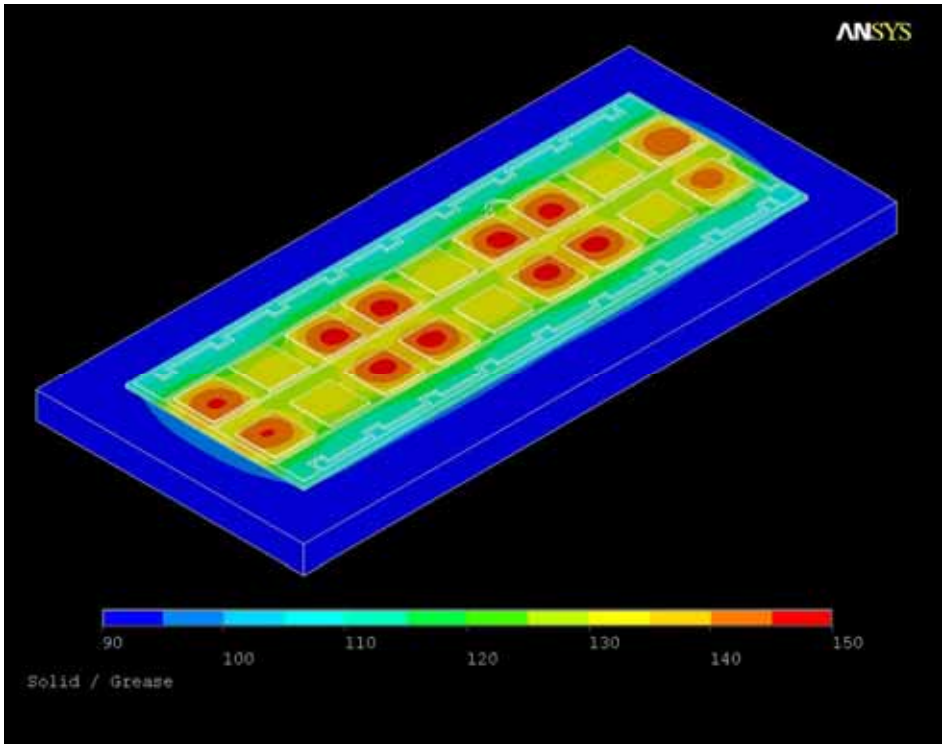

Figure 2 Thermal contours single phase of an inverter with thermal paste interface

Cut-Through IGBT Structure

A similar thermal analysis performed on the first-generation design of the cut-through IGBT structure shows much more promising results.
Figure 3 shows a detailed view of the first-generation cut-through structure for a single IGBT while Figure 4 shows the cut through design for one phase of an inverter. In this design, the TIM has been completely removed and the bottom copper layer of the DBC is directly soldered to the base plate/heat sink. A circular, tapered hole cuts through the entire thickness of the heat sink under an IGBT to provide the coolant direct access to the bottom of the DBC. The taper allows the spent cooling fluid an exit path that limits the re-entrainment of the flow, which would heat the incoming coolant and reduce the efficiency of the heat exchanger. Figure 4 shows a plurality of holes that are cut through the heat sink under each IGBT.

A thermal analysis was carried out for the single phase of an inverter with holes cut through under each IGBT as shown in Figure 4. The DBC layer was assumed to connect to the heat sink by soldering process.
Figure **5** shows the temperature distribution for this configuration. For this particular analysis, the holes are tapered to reduce entrainment of the spent coolant into the incoming coolant path and have a top diameter of 9 mm and a lower diameter of 12 mm.

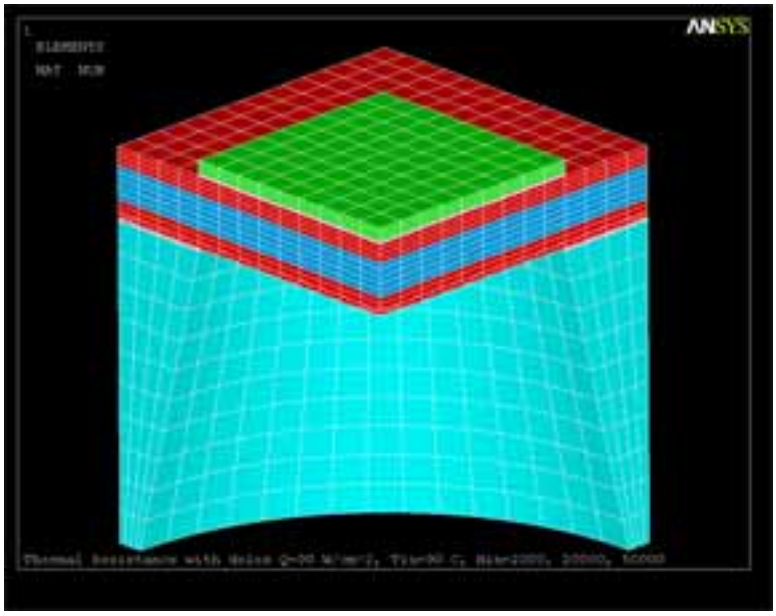

Figure 3 Close-in view of low thermal resistance structure with a round hole

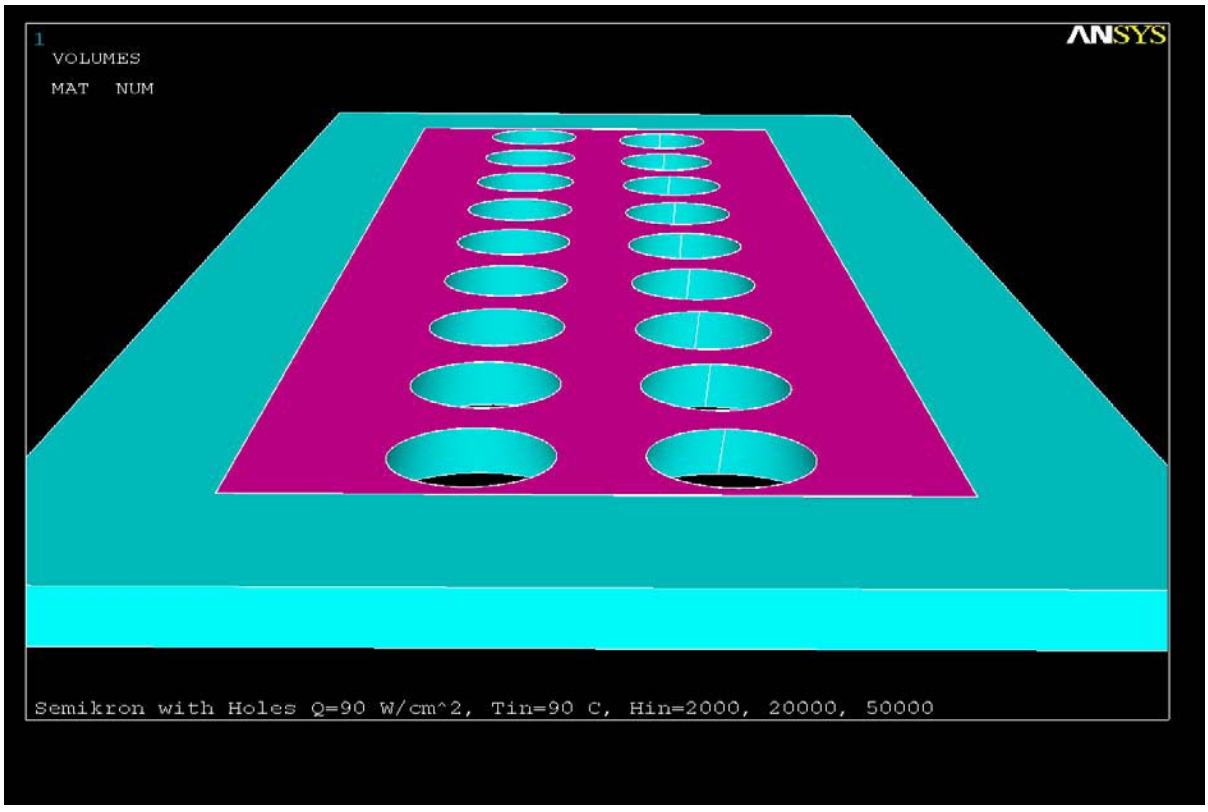

Figure 4 Close-in view of heat sink for the low thermal resistance structure with round holes

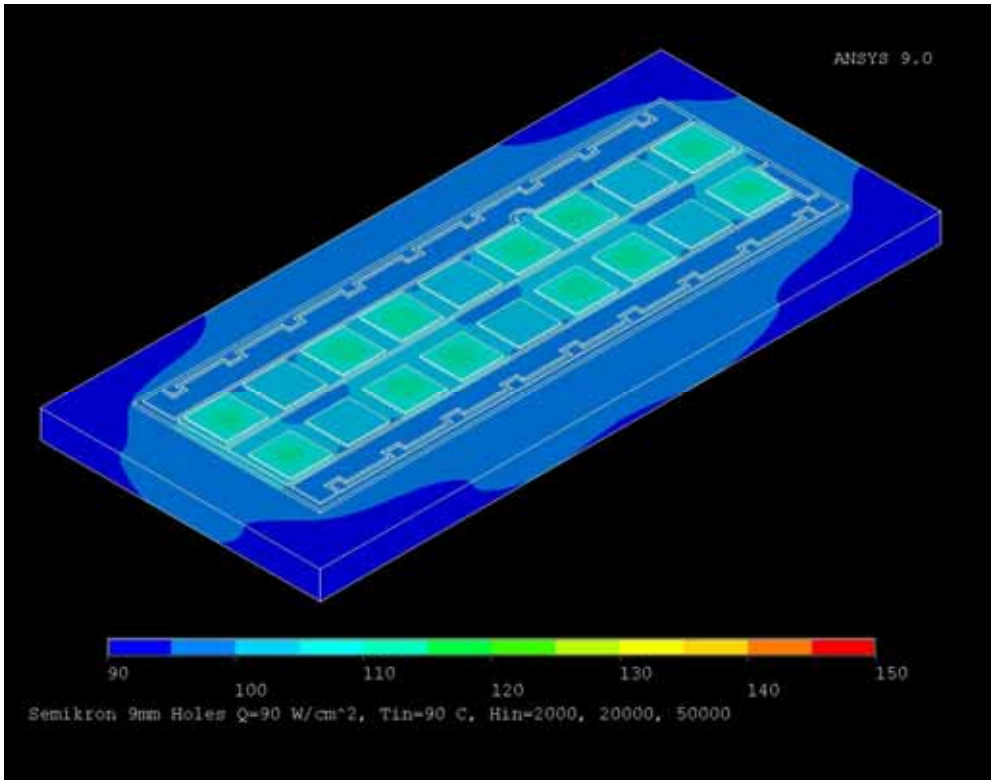

Figure 5 Thermal contours for a single phase of an inverter with cut-through holes for enhanced cooling and solder interface

The performance of the cut-through design with the solder interface was a great improvement over the previous layouts. The use of solder as an interface material substantially reduces the thermal resistance of the entire structure.

Enhanced Low Thermal Resistance IGBT Structure

The alternative to using a solder layer with intricate topology (which can be both expensive and difficult) is to forgo bonding of the DBC to the heat sink altogether. Instead, we propose to provide a seal between the heat sink and the DBC without a rigid physical bond. We propose to achieve the tight seal by providing a flexible sealing member, such as a gasket, O-ring or the like, between the heat sink and the DBC and then, forcing the heat sink and the DBC together by applying a force to the DBC at one or more points proximal to the location of the sealing member. If this o-ring could adequately seal the coolant from leaking into the power electronics, the mismatch in the CTE between the DBC and the heat sink would not be an issue because the strains would not be coupled. The two layers would be able to slide independently and expand freely when going through temperature swings.
Figure 6 shows a conceptual illustration of the cut through IGBT structure connected to the heat sink via an o-ring that is installed inside a groove cut out around each IGBT or a group of IGBTs. .

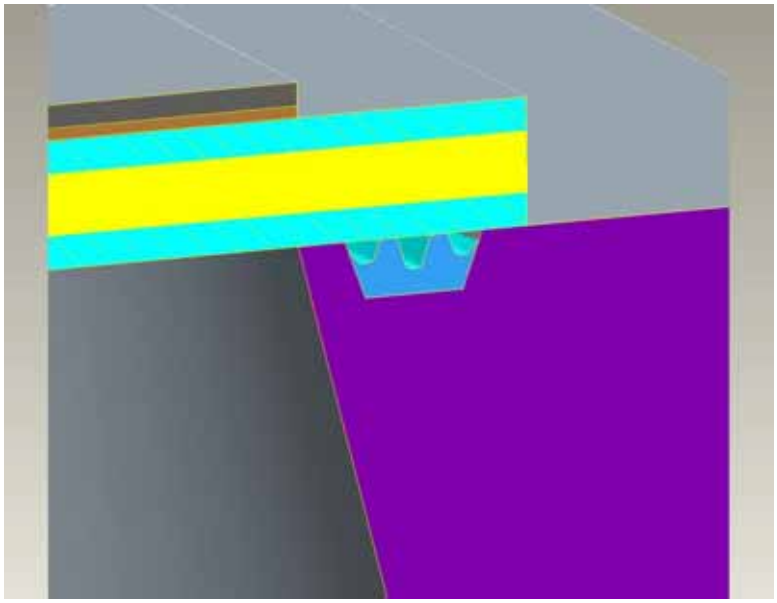

Figure 6 Close-up of o-ring between aluminum heat spreader and DBC

Implementing this new concept required redesigning the cooling plate to maximize the area exposed to the impinging jets and designing the hardware required to provide the coolant impinging jets. The result of this design iteration can be seen exploded in
Figure **7**.

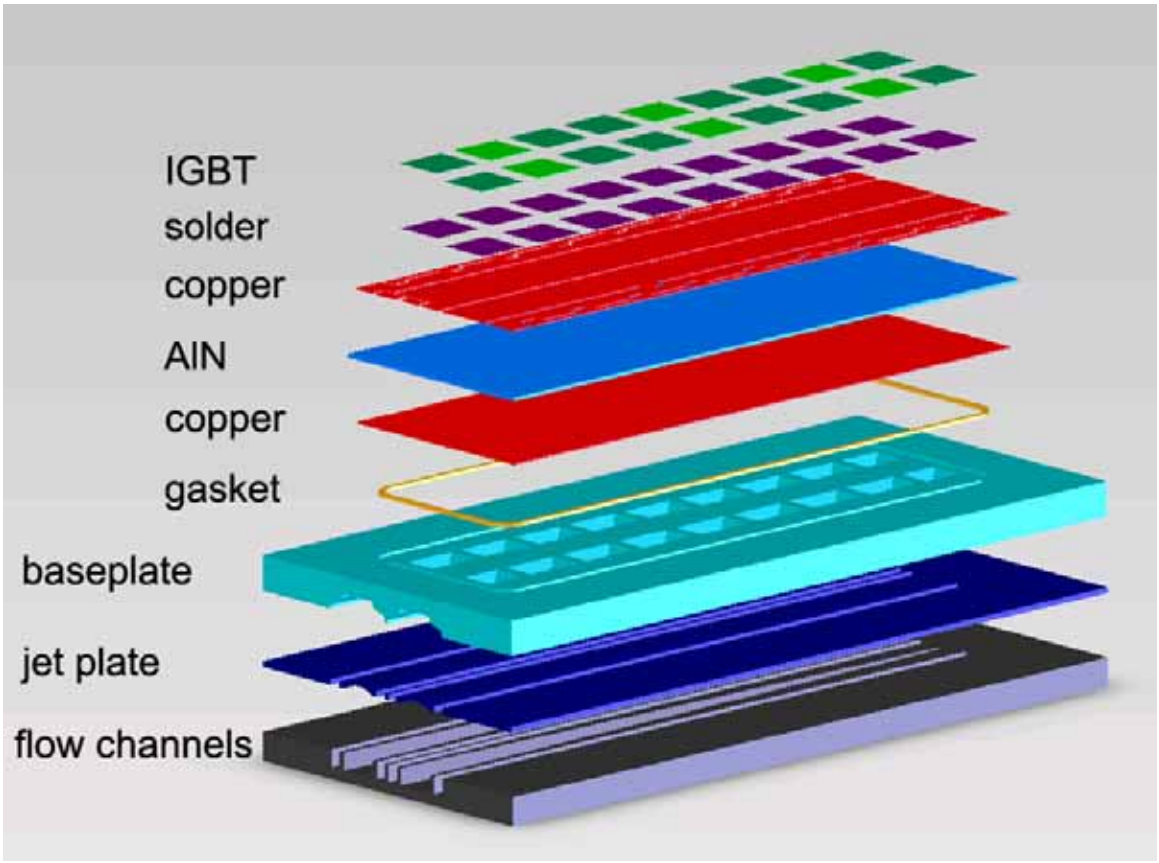

Figure 7 Exploded view of IGBT structure including o-ring

Thermal Analysis

To compare the utility and effectiveness of this new design, we performed similar thermal analyses on earlier design iterations. Each IGBT and power diode was assigned an internal heat generation of 90 watts and 60 watts, respectively. Since the dimensions of the silicon dies are 9 mm on a side, this heat generation rate is equivalent to 111 W/cm^2 and 74 W/cm^2, respectively.
Figure 8 and 9 show the thermal contours of the top and bottom for one phase of the modified Semikron inverter with o-ring and cut-through structure. The maximum temperature can be seen at the extremities in the lateral direction at the two extreme IGBTs. The temperature anomalies appear because the o-ring, which is close to the edge of the DBC, lies under the edge of the IGBT. The area exposed to the impinging jets is thus limited and the temperature increases dramatically. The results of this analysis are very promising.

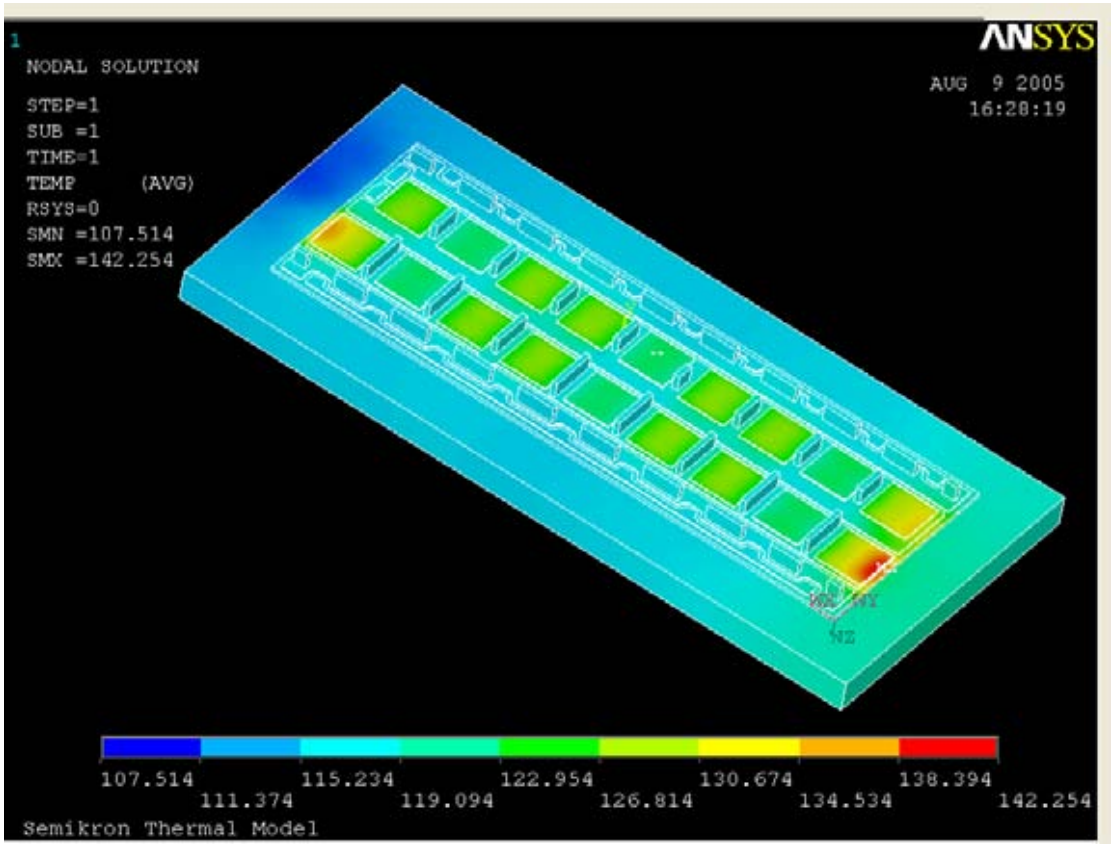

Figure 8 Top view of IGBT structure with enhanced cooling plate

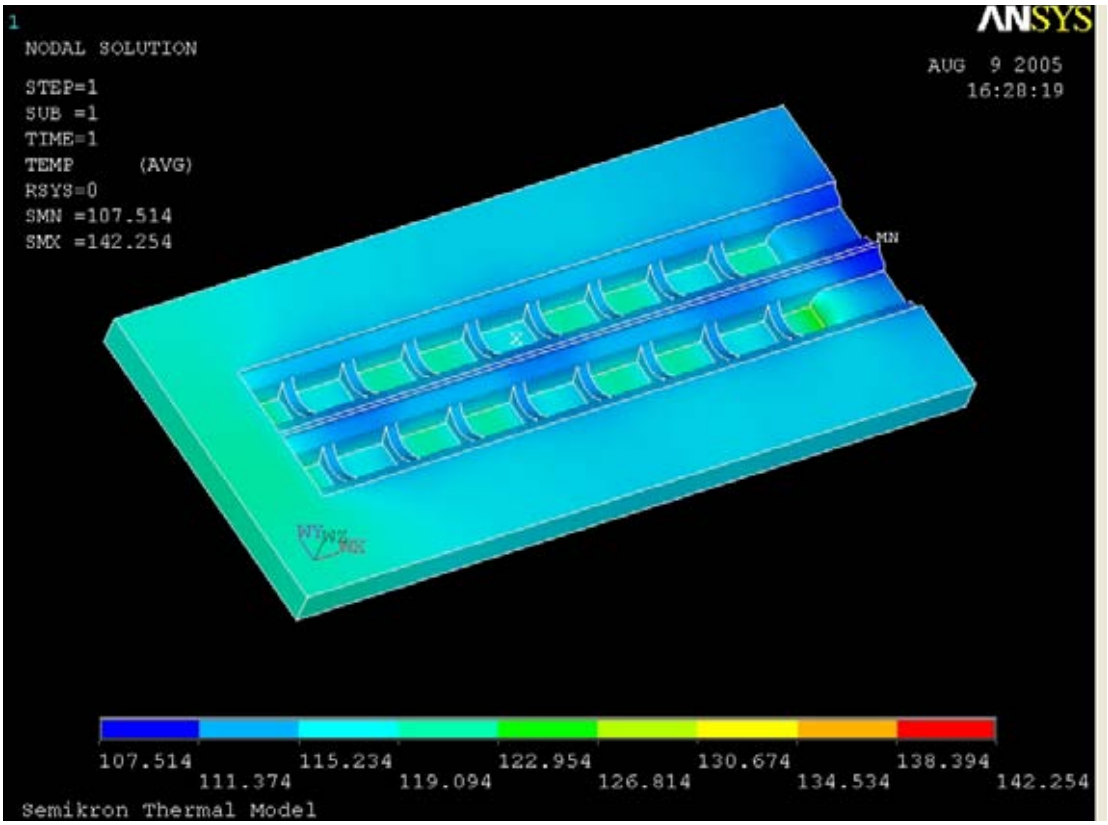

Figure 9 Bottom view of IGBT structure with enhanced cooling plate

2.6 Spray Cooling: An assessment for use with automotive power electronics applications

Dr. Desikan Bharathan, Dr. Vahab Hassani
National Renewable Energy Laboratory
1617 Cole Boulevard
Golden, Colorado 80401
Voice: (303)-275-4427; Fax: (303) 275-4613; E-mail:Desikan_bharathan@nrel.gov

DOE Program Manager: Susan Rogers
Voice: (202) 586-8997; Fax: (202) 586-4403; E-mail: Susan.Rogers@EE.DOE.GOV

NREL Task Leader & Technical Advisor: Dr. Vahab Hassani
Voice: (303) 275-4427; Fax: (303) 275-4415; E-mail: vahab_hassani@nrel.gov

---

Objectives

The overall objective is to assess the suitability of spray cooling for heat removal from power electronic components being developed as part of the FreedomCAR effort under DOE.

The overall mission of the FreedomCAR program addresses many components of the vehicle. Achieving the FreedomCAR goals will require the development of new technologies for power electronics and electric machinery. The new technologies must be compatible with high-volume manufacturing; must ensure high reliability, efficiency, and ruggedness; and simultaneously reduce cost, weight, and volume. Key components for fuel cell and hybrid-electric vehicles include motors, inverters/converters, sensors, control systems, and other interface electronics.

One of the specific objectives related to power electronics is to develop automotive integrated modular power modules for power conversion and control. Building blocks to be developed include power switch stages optimized to run newly developed motors, drives, DC/DC converters, advanced controllers and sensors.

Of specific interest to this study is the inverter/converter where the electronic chips are expected to generate heat fluxes of up to 250 W per square centimeter of the silicon-based external chip contact surface. Current technology based on silicon chips requires that the chip maximum temperature not exceed 125^{o}C to assure their reliable performance over the required life of 15 years. To reduce the complexity and perhaps the overall cost for the electronic cooling system, the technology team also set other system requirements such as - the coolant to be used will be the same water-ethylene glycol mixture (WEG) that cools the internal combustion engine, and that - this coolant will be available at a return temperature of 105^{o}C.

These requirements as set by the EE Tech team dictate the use of a particular fluid and limit the choices of methods that can be adopted to achieve high heat removal capabilities. However, parallel activities within the APEEM program generated additional tasks to look into technologies that might have the potential to yield substantially higher heat removal capabilities.

Spray cooling and two-phase heat removal methods fall under this category of technologies that could potentially meet the heat removal requirements with greater ease and lower cost.

Approach

Our initial approach was to attempt to model the spray heat transfer using the commercially available code Fluent. However, we quickly realized that there were severe uncertainties in the specifications for various parameters for simulating such sprays. These begin with 1) the instabilities of the flow and nature of the spray formation, 2) the uncertainty with which the fresh liquid-vapor interface is formed at the spray outlet, and 3) the transient condensation heat transfer that occurs at those surfaces from the vapor that was generated else where in the domain. The fresh interfaces are quickly covered by a shell of hot liquid on account of the high rate of condensation. Such details dominate the heat transfer and the fluid flow induced within the domain. It is in general difficult to assess the flow and the accompanying heat transfer in the spray formation region. A second area of difficulty arises at the contact zone where the liquid droplets impinge on the hot surface. Depending on the wall superheat, the liquid undergoes a wide variety of behaviors, with large spreading or bouncing and break up. One may have to assume that there is a thin film of liquid that remains in contact with the hot surface on account of the intermittent arrival of spray droplets. In case of high superheat, vapor blankets the hot surfaces once again on an intermittent basis.

At present, there are no adequate models to capture the complexity of spray heat transfer for the present application.

On account of this realization, we confined our efforts to looking into experimental results only. These experiments focus on arriving at the effective heat transfer coefficient for sprays of different liquids aimed at a hot plate of sizes similar to the electronic chips. Of high importance are the variations of the heat transfer coefficient as functions of the liquid spray flow, geometry, and subcooling, and the critical heat flux at which the temperature of the wall rises sharply with increasing heat flux.

We examined the literature to arrive at key results that are most relevant to the present application. Based on those results, we modeled the electronic board assemblies to assess the suitability of sprays for removing high heat fluxes.

.

Accomplishments

Spray cooling with FC-72 sprays is unlikely to meet the program goal for heat flux removal at a rate of 200 to 250 W/cm^2.

Higher potential exists for the use of R-134a as the coolant, based on projected critical heat fluxes. However we lack data on spray cooling heat transfer for this liquid.

One drawback for use of this liquid is that the chamber pressures are likely to be high at high ambient temperatures. Pool boiling data reported by Hseih [2004] suggest a maximum heat transfer coefficient of only about 0.5 W/cm^2K. Data using sprays and liquid films are likely to be substantially higher and are needed for assessing their improved performance with R-134a.

Surface enhancements such as micro grooves and grids have been shown in the literature to enhance spray heat fluxes substantially. Such enhancements may be usable on the board side, but unlikely to be used on the chip surfaces.

Surface modifying agents in the liquid have also been reported to enhance spray heat removal capacity, but are not likely to be put in everyday use in consumer maintained items.

Future Direction

Considering that R-134a is already in use automotive air conditioning systems, we recommend that we continue to investigate the use this liquid for electronic cooling. Spray heat transfer using this fluid must be experimentally evaluated. Experiments should be carried out to assess the limits for heat fluxes and effective heat transfer coefficients using sprays directed at hot spots simulating the electronic chips and boards.

Outcome and Results

The outcome of this research will be a cooling technique that will help cool the IGBTs directly.

3. Electric Machinery Research and Technology Development

3.1 Field Weakening and CPSR Enhancement Techniques

Principal Investigator: John W. McKeever
Oak Ridge National Laboratory
National Transportation Research Center
2360 Cherahala Boulevard
Knoxville, TN 37932
Voice: 865-946-1316; Fax: 865-946-1262; E-mail: mckeeverjw@ornl.gov

DOE Technology Development Manager: Susan A. Rogers
Voice: 202-586-8997; Fax: 202-586-1600; E-mail: Susan.Rogers@ee.doe.gov

ORNL Program Manager: Mitch Olszewski
Voice: 865-946-1350; Fax: 865-946-1262; E-mail: olszewskim@ornl.gov

---

Objectives

- To review, study, and evaluate recent progress in methods of flux control, both flux strengthening to increase torque at low speeds and flux weakening to extend the constant power speed range (CPSR). These features are being explored to extend motor design capability in order to develop motors that can meet torque/power/speed requirements without a gearbox. Success can result in a motor with higher power density (>10%) at lower initial cost (80%) than existing integral slot motors.
- To determine the conditions for maximum benefit using Oak Ridge National Laboratory's (ORNL's) dual mode inverter control (DMIC) to minimize current at high speeds under partial load and to quantify that benefit.

Approach

For this task, the research areas of field weakening and extending the CPSR were subdivided into (1) voltage control, (2) flux control, (3) inductance control, (4) inverter control, and (5) reluctance control.

- **Voltage control.** As an example of benefits derived from voltage control, the Toyota Prius has cornered the HEV market with its THS II model by adding a boost converter to the earlier THS model, to deliver 50% more power from the electric motor [1]. The increased voltage delivers more power with the original current so that the motor did not require redesign. The Z-source inverter [2] was developed to provide the voltage boost required by the fuel cell in an HEV. The Z-source inverter eliminates the shoot-through problem in transistors, which can destroy them in traditional inverters, and actually uses what formerly was dead time to boost the voltage. It makes better use of the inverter's pulse-width modulation (PWM) circuitry. The use of this inverter was explored and found to be inappropriate for an HEV powered by an internal combustion engine (ICE) because of the voltage drop across the diode. The same is true for its use with all electric vehicles.
- **Flux control.** Several methods of real-time flux control were explored, including traditional vector control [3], flux weakening in a consequent pole generator [4], flux control using an external coil [5], magnetic polarization variation (memory motors) [6], magnetic strength variation by thermal field weakening [7], actively switching the number of turns per coil while in operation [8], and gap control [9].
- **Inductance control.** Some earlier motor design experience implied that it is difficult to design sufficiently high inductance in integral-slot surface-mounted permanent magnet (SPM) motors to allow high-CPSR operation. Motor designers such as Toyota have focused their design on internal

PM motors, which bury the magnet in the silicon steel rotor to increase their saliency [10]. ORNL teamed with the University of Wisconsin, Madison (UWM) to look at opportunities for PM synchronous motor (PMSM) cost reduction. Their report highlighted some significant benefits associated with fractional-slot PM motors with concentrated windings [11]. In particular, its inductance would be high because of the concentrated windings, and its structure could lead to material savings and ease of assembly. Because this design could achieve increased inductance along with other benefits, ORNL entered into collaboration with the University of Wisconsin to build and test a 6-kW fractional-slot PM motor with concentrated windings [12, 13]. The measured inductance of the windings is as high as the analysis had predicted. The structure of the motors facilitated low-cost assembly with high slot utilization. ORNL has collaborated with UWM by modeling the 6-kW motor and by preparing preliminary models of a 30/55-kW motor that meets FreedomCAR specifications. The notation 30/55 refers to continuous and intermittent power delivery. UWM has successfully tested the 6-kW motor to 4000 rpm. ORNL will receive the motor in FY 2005 to test a control scheme that promises a 7–8% increase in efficiency at partial load [14]

- **Inverter control.** It is well known that the ability of the PMSM to operate over a wide CPSR depends upon the motor's inductance. Early approaches to extending the CPSR included adding inductances in each phase [15] and using anti-parallel thyristors in each phase [16]. The motor control method that requires increased inductance is compatible with a voltage source inverter controlled by PWM and is called conventional phase advance (CPA). The thyristor method is called DMIC. The fractional-slot motor with concentrated windings, which is being explored as part of this task, has the potential to make the PMSM motor compatible with CPA without external inductance and, if successful, will make the PMSM an attractive option for applications requiring high CPSR. The approach of this task was to model two PMSMs, one with the characteristic inductance that would allow operation at infinite CPSR and a second with a higher value of inductance equal to the value that was measured on the 6-kW fractional-slot motor with concentrated windings. Following this, integration of the motor model with models of the CPA and DMIC inverters was performed to explore their performance and find regions of performance where the cost-to-benefit ratio would justify the additional cost of the thyristors required by DMIC.
- **Reluctance control.** When vector control is applied to field-weaken a motor for operation at high CPSR the power and torque equations have two terms. The prominent term involves the interaction of the PM's flux linkages with the current in the coils and is the PM torque. A second term involves the difference between the stator inductance along an axis through the magnet, L_d, and the stator inductance along an axis displaced 90 electrical degrees, L_q, and is the reluctance torque. Rotors for which L_q/L_d is greater than 1 are salient rotors, and the ratio is the saliency ratio. PMSMs with surface-mounted motors have uniform inductance around their periphery, so the saliency ratio is 1, which means they are non-salient. Laboratory measurements have indicated that the reluctance torque for non-zero saliency motors can be significant. This task was initiated to see if additional torque could be obtained with a reluctance-assisted PM motor at low speeds while extending the CPSR without sacrificing performance. If it is successful, less magnet material would be required, which would lower the cost of the motor. The type of motor used in the study was an inset PM motor, which embeds the magnets in the rotor's silicon steel core so they are flush with the rotor surface. The magnet fraction is the ratio of the magnet pitch to the pole pitch. An early plot for a four-pole inset PM exhibited a magnet fraction at which the reluctance torque passed through a maximum, which was very close to where the total torque passed through a maximum. Encouraged by that result, this task was initiated to examine the performance response of the reluctance-assisted inset PM motor as the magnet fraction is varied.

Major Accomplishments

- **Voltage Control**
  - — Reviewed the technology of boost converters with emphasis on the Z-source inverter, finding that it is excellent fuel cell vehicle (FCV) technology, whose present configuration does not migrate naturally into conventional ICE-powered HEV configurations.
  - — Presented the review and evaluation of the Z-source inverter in report ORNL/TM-2005/531.
- **Flux Control**
  - — Reviewed seven methods, two originating at ORNL and five presented in open literature, that may be used to increase the CPSR of PMSM motors while they are in operation without reducing their efficiency.
  - — Presented the results in report ORNL/TM-2005/175.
- **Inductance Control**
  - — Collaborated with UWM in designing 6-kW and 30/55-kW fractional-slot PMSMs with concentrated windings, which have potential to reduce material and assembly costs, increase slot utilization, and increase inductance for optimal CPSR.
  - — Built a 6-kW motor with concentrated windings and tested it at UWM to 4000 rpm.
  - — Compared analytical and measured results, which agreed reasonably well.
  - — UWM prepared preliminary 30/55-kW motor designs with fractional-slot concentrated windings.
  - — ORNL prepared preliminary 30/55-kW motor designs with integral slot windings, which will be compared with UMW's fractional-slot designs.
  - — Summarized and revised results in report ORNL/TM-2005/183.
- **Inverter Control**
  - — Developed an analytical per-phase fundamental frequency phasor model of a PMSM driven by CPA, including winding resistance and rotational losses.
  - — Developed an analytical per-phase fundamental frequency phasor model of a PMSM driven by DMIC, including winding resistance and rotational losses.
  - — Developed an analytical model for blocking losses and conduction losses in transistors, thyristors, and diodes; for switching losses in transistors; and for reverse recovery losses in diodes and thyristors.
  - — Affirmed the analytical model with a detailed PSPICE time domain simulation showing that results from the analytical model are sufficiently accurate for comparing the performance of different motor/inverter combinations.
  - — Applied the analytical model to two PMSMs, one with characteristic inductance, the lowest value that allows infinite CPSR, and one with the much higher inductance equal to the value measured on the 6-kW PMSM with fractional-slot concentrated windings to search for performance regions at partial load and to quantify the improved efficiency.
  - — Detailed results in report ORNL/TM-2005/184.
- **Reluctance Control**
  - — Completed a preliminary analysis to show the benefits derived from controlling reluctance in PMSMs.
  - — Applied SPEED software to analyze three configurations of interior PM motors (IPMs) to explore the impact on the performance of varying the magnet fraction. The configurations included an inset PM motor, an embedded V-shaped PM motor (type 4), and an embedded layered U-shaped PM motor (type 6).
  - — Applied the design equations of a reluctance motor to explore relations between variables and to develop a methodology for determining values of parameters that would result in optimum performance.
    - o The optimum number of turns per coil for maximum power delivery as a function of speed.
    - o The optimum magnet fraction for power delivery as a function of speed.
  - — Summarized results in report ORNL/TM-2005-185.

Technical Discussion

1. Voltage Control

HEVs are driven by at least two prime energy sources, such as an ICE and propulsion battery. For a series HEV configuration, the ICE drives only a generator, which maintains the state-of-charge (SOC) of propulsion and accessory batteries and drives the electric traction motor. For a parallel HEV configuration, the ICE is mechanically connected to directly drive the wheels as well as the generator, which likewise maintains the SOC of propulsion and accessory batteries and drives the electric traction motor. Today the prime energy source is an ICE; tomorrow it may be a fuel cell (FC). Use of the FC eliminates a direct-drive capability, accentuating the importance of the battery charge and discharge systems. In both systems, the electric traction motor may use the voltage directly from the batteries or from a boost converter that raises the voltage. If low battery voltage is used directly, some special control circuitry, such as DMIC, which adds a small cost, is necessary to drive the electric motor above base speed. If high voltage is chosen for more efficient motor operation or for high-speed operation, the propulsion battery voltage must be raised, which would require some type of two-quadrant bi-directional chopper with an additional cost.

Two common dc-to-dc converters are (1) the transformer-based boost or buck converter, which inverts a dc voltage, feeds the resulting ac into a transformer to raise or lower the voltage, and rectifies it to complete the conversion; and (2) the inductor-based switch-mode boost or buck converter [17]. A benefit of the transformer-based boost converter is that it isolates the high voltage from the low voltage. Usually the transformer is large, further increasing the cost. A useful feature of the switch-mode boost converter is its simplicity. Its inductor, which is responsible for its main cost, must handle the entire current. The new Z-source inverter technology [18, 19] boosts voltage directly by actively using the zero state time to boost the voltage. In the traditional PWM inverter, this time is used only to control the average voltage by disconnecting the supply voltage from the motor. The purpose of this study is to examine the Z-source's potential for reducing the cost and improving the reliability of FC HEVs.

The additional cost of a boost converter adds a significant cost penalty to the control system. Apparently this penalty has not discouraged the engineers at the Toyota Motor Corporation, because in September 2003 Toyota introduced a second generation of the Toyota Hybrid System (THS II), which boasted a 50% improvement in motor power output [20], enabled by the use of a two-quadrant bi-directional chopper placed between the inverter's system voltage and the batteries' output voltage.

Recently, a new power converter topology was introduced that modifies a standard voltage-fed or current-fed PWM inverter and may be controlled to buck or boost not only dc-to-dc, but also dc-to-ac, ac-to-dc, and ac-to-ac. It is called a Z-source inverter [18, 19], and it adds a network of impedance to eliminate the problem of shoot-through. Shoot-through, which shoots the supply voltage through an inverter's upper and lower semiconductor switches, destroys the switches. It must be prevented by time delays in the control circuit. The Z-source inverter actually uses shoot-through to boost the voltage.

The research objective of the Z-source inverter was to provide a monolithic inverter to connect an FC with the traction drive of an HEV. The boost feature is essential for FC operation because the static characteristics of FCs exhibit more than a 30% reduction in the output voltage between no-load and full-load current draw [21]. The buck feature in the opposite direction is needed because the storage batteries' SOC must be maintained.

Technology for the two traditional inverters, which are voltage-source inverters (VSIs) and current-source inverters (CSIs), has been advanced by the invention of the Z-source inverter, which employs an impedance circuit to couple a power source to the input of an inverter [18, 19]. The Z-source inverter provides a power conversion process that may be used to synthesize waveforms with voltages above and below the source voltage. Its use eliminates the switch or switches required by a boost converter. It can be applied to all dc-to-ac, ac-to-dc, ac-to-ac, and dc-to-dc power conversions.

Traditional VSIs and CSIs have certain limitations not exhibited by the Z-source inverter. First, they may either boost or buck the voltage, but not both. Second, false gating, which can be induced by

electromagnetic interference (EMI), may cause shoot-through in a VSI or may cause an open inductor circuit in a CSI, which will destroy the switches. Dead time for the VSI and overlap time for the CSI causes waveform distortion.

Figure 1 shows a schematic of the basic Z-source converter. If an FC is used, the blocking diode has the additional task of preventing current flow back into the FC in addition to its boosting function.

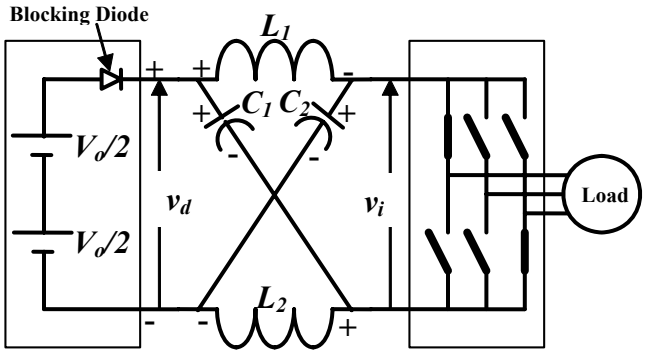

Figure 1. Field weakening and CPSR enhancement techniques.

As already mentioned, the Z-source inverter makes more complete use of the available operating time of a PWM inverter. During traditional PWM, an active semiconductor switch is turned off to disconnect the voltage source from the motor each time the magnitude of the triangular carrier voltage exceeds the magnitude of the modulating wave. It is not turned back on until the carrier wave falls back below the modulating wave. That time period is used by the traditional PWM inverter to synthesize the average voltage and may only allow the three upper switches or the three lower switches to be closed simultaneously to synthesize the average voltage. If an upper and lower switch in the same phase are closed, shoot-through occurs, which could destroy the switches in that phase. These two permitted states, one with three upper switches on or one with three lower switches on, are called zero states and all they do is create a path for the motor current when the supply is disconnected. Because of the two inductances and two capacitors in the Z-source circuit, shoot-through is permitted, allowing double use of what was formerly the zero vector time. This time is used not only to control the average voltage but also to boost the voltage.

There are two possible places to insert a propulsion battery in an FC-powered HEV driven by a Z-source inverter. The configuration shown in Figure 2 has been studied and reported [22]. In it, a battery is inserted in parallel with either one of the two Z-circuit capacitors because of circuit symmetry. The capacitor must remain across the battery terminals to absorb ripple currents, which shorten the battery life. Thus the battery must be a high-voltage battery whose voltage exceeds the FC voltage. The inverter module may be operated in the same way as traditional inverters to maintain the battery SOC with excess power from the FC and from regenerative braking. Furthermore, the high voltage across the propulsion battery is sufficient to operate the compressor motor expansion unit, thereby eliminating the dc-dc boost converter.

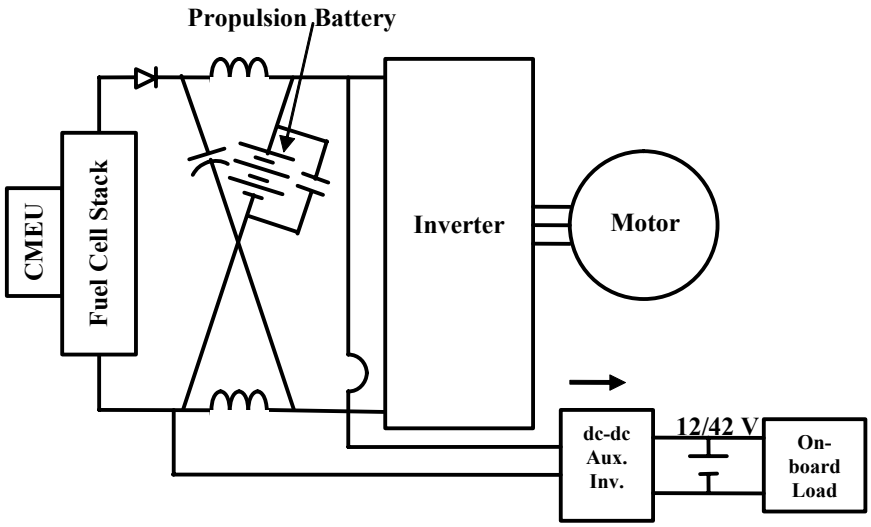

Figure 2. Configuration of a Z-source inverter-driven FCV.

Although the Z-source inverter was developed in the search for a better FC drive system, it poses questions when an attempt is made to apply its boost feature to a traditional ICE-powered HEV. Figure 3 shows one such configuration. Attempts to apply the Z-source inverter to an ICE-powered HEV revealed that Z-source technology does not migrate naturally into conventional ICE-powered HEV configurations. First, the FC is replaced by a low-voltage propulsion battery, which does not have the dramatic voltage drop exhibited by the FC as the load increases. Although the 200-V low-voltage propulsion battery in Figure 3 can provide a secondary source of power, it cannot receive regenerated braking power from the motor because of the intervening blocking diode required to isolate the 500-V link from the 200-V battery. In this configuration, the only available regenerated power to maintain the battery SOC must pass through the generator. Further, since the generator is connected to maintain the SOC on the secondary energy propulsion battery, it incurs additional losses when in drive mode because current must pass through the Z-source inverter's blocking diode. If the generator were connected directly to the high-voltage link, there would be no way to maintain the SOC on the propulsion battery, again because of the intervening diode. This might be accommodated by switching the generator connection between the low-voltage and high-voltage buses, depending upon whether it is charging or driving; however, this adds a significant control complication and more hardware.

Further, as we explored the potential to replace the two-quadrant bi-directional chopper with the boost technology of a Z-source inverter, we found a straightforward modular replacement is complicated by the Z-circuit's integration requirements. The problem is that the connecting lines must be very short to prevent unacceptable inductance because the inductance cannot be easily compensated by snubber caps without affecting shoot-through operation of the Z-source inverter. Consequently, we conclude that, based on today's understanding, a new bi-directional configuration of the Z-source inverter will be required for use in ICE-powered HEVs.

One may compare the costs of the power build sections of each configuration. The power build section contains the semiconductors in the inverters that drive the motor and the generator; the semiconductors in the boost converter or in the chopper; and the inductances needed by the chopper, traditional boost converter, and Z-source inverter. These numbers are based on vendor quotes for 1000–1999 units for three levels of semiconductor packs [23]. Current in conventional PWM motor inverters and in traditional boost converters that feed PWM inverters requires 600-V/400-A dual packs at $269.60 each. Current in the starter/generator inverter drives and in the PWM inverter fed by a traditional boost converter require only 600-V/200-A six packs at $240 each. Current in the Z-source inverters employed 600-V/300-A six packs at $308.88 each.

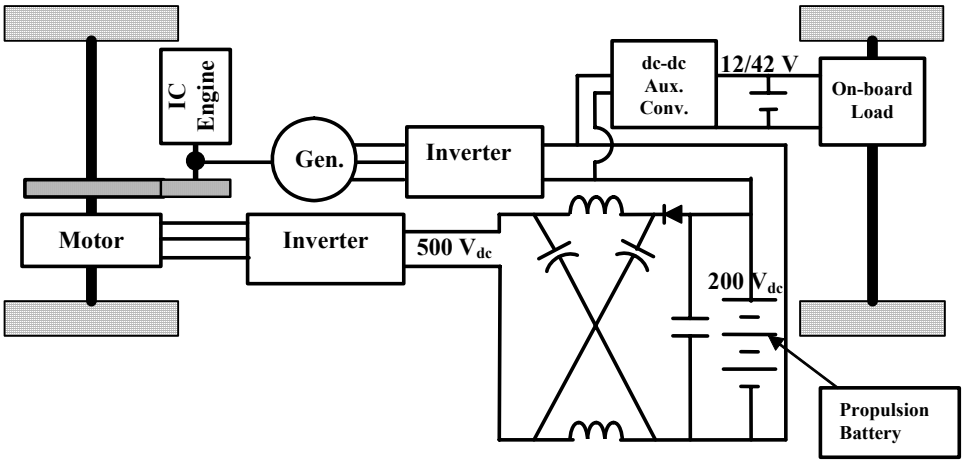

Figure 3. A configuration of an ICE-powered HEV driven by a Z-source inverter.

Now we shall look at some cost comparisons for different power build sections. There is general consensus among those who have studied the TH SII that it is the current baseline with the most desirable features. Its power build section estimated cost is $1392. The power build section's estimated cost difference between THS I and THS II is $343, which is an estimate of what Toyota was willing to pay to improve reliability and to deliver 50% more power without changing the motor/drive size. What stands out is the drop in cost of the power build section when FCs replace the ICE as the primary energy source. The power build section of the FC-powered HEV with a traditional boost converter and a bi-directional chopper, which is comparable to Toyota's THS II in function, costs about $996, which is $396 less than the THS II. Most notable, however, is the dramatic reduction of the power build section cost to $383 for the FC-powered Z-source inverter with a high-voltage battery as a secondary energy source in parallel with one of the two capacitors. This power build section cost is $666 below the THS I cost and $1009 below the THS II cost. Furthermore, it is $201 less than the power build section cost of the conventional FC inverter, which is fed by a traditional boost converter.

The recent invention of the Z-source inverter provides a new technology that can eliminate the switch in the traditional boost converter between the FC and the high-voltage dc link. It can also eliminate the two additional switches between a moderate 200-V secondary energy storage voltage and a high 500-V traction motor voltage similar to that used in the THS II system. It eliminates all danger from shoot-through, which short circuits the supply voltage through the inverter switches, destroying switches in a traditional inverter. Instead, it makes double use of the zero-state time to boost the voltage as well as control the average voltage. Components introduced by the FC-powered Z-source inverter with a battery replacing one of the capacitors over the traditional boost converter are two small inductors to replace one large inductor with little cost difference. One less capacitor and one less switch are required.

The ICE or the FC must supply power to more than the traction motor. Hybrid ICEs and FCVs must supply power to charge a 12/42-V auxiliary storage battery and a 200-V or 500-V secondary energy storage system. The energy storage system supplements the power from the ICE or FC, allowing the vehicle to deliver rated power during high-load conditions. If the Z-source inverter is applied to both hybrid ICEs and FCVs, the challenge is to connect it to the power source without interfering with its shoot-through boost operation.

2. Flux Control

Significant research at the ORNL Power Electronics and Electric Machinery Research Center (PEEMRC) is being conducted to develop ways to increase (1) torque, (2) speed range, and (3) efficiency of traction electric motors for HEVs and FCVs within existing current and voltage bounds. Current is limited by the inverter semiconductor devices' capability; and voltage is limited by the stator wire insulation's ability to withstand the maximum back-electromotive force (emf), which occurs at the upper end of the speed range.

One research track has been to explore ways to control the path and magnitude of magnetic flux while the motor is operating. The phrase "real time flux control" (RTFC), refers to this mode of operation in which system parameters are changed while the motor is operating to improve its performance and speed range. RTFC has the potential to meet an increased torque demand by introducing additional flux through the main air gap from an external source. It can augment the speed range by diverting flux away from the main air gap to reduce back-emf at high speeds. Conventional RTFC technology is known as vector control [3, 24]. Vector control decomposes the stator current into two components; one that produces torque and a second that opposes (weakens) the magnetic field generated by the rotor, thereby requiring more overall stator current and reducing the efficiency. Efficiency can be improved by selecting an RTFC method that reduces the back-emf without increasing the average current. This favors methods that use pulse currents or very low currents to achieve field weakening.

Foremost in ORNL's effort to develop flux control is the work of J. S. Hsu. Early research [4] introduced direct control of air-gap flux in PMSMs and demonstrated it with a flux-controlled generator. The configuration eliminates the problem of demagnetization because it diverts all the flux from the magnets instead of trying to oppose it. It is robust and could be particularly useful for PM generators and electric vehicle drives. Recent efforts have introduced a brushless machine that transfers a magneto-motive (mmf) force generated by a stationary excitation coil to the rotor [5]. Although a conventional PM machine may be field-weakened using vector control, the air-gap flux density cannot be effectively enhanced. In Hsu's new machine, the magnetic field generated by the rotor's PM may be augmented by the field from the stationery excitation coil and channeled with flux guides to its desired destination to enhance the air-gap flux that produces torque. The magnetic field can also be weakened by reversing the current in the stationary excitation winding. A patent for advanced technology in this area is pending.

Several additional RTFC methods have been discussed in open literature. These include methods of changing the number of poles by magnetizing and demagnetizing the magnets' poles with pulses of current corresponding to direct-axis (d-axis) current of vector control [6], changing the number of stator coils [8], and controlling the air gap [9]. Test experience has shown that the magnet strengths may vary and weaken naturally as rotor temperature increases, suggesting that careful control of the rotor temperature, which is no easy task, could yield another method of RTFC.

The purpose of this research was (1) to examine the interaction of rotor and stator flux with regard to RTFC, (2) to review and summarize the status of RTFC technology, and (3) to compare and evaluate methods for RTFC with respect to maturity, advantages and limitations, deployment difficulty, and relative complexity.

Most approaches to extend the speed range of operation of PM motors focus on weakening the rotor's magnetic flux in order to decrease its contribution to the magnitude of the back-emf and thus allow for power input and generation of stator magnetic field at higher speeds. This weakening may be accomplished in several ways, as discussed in the following paragraphs.

Vector control

The traditional approach to field weakening is vector control, in which the effective rotor magnetic flux is suppressed by controlling d-axis stator current to generate a magnetic field that directly opposes and thereby weakens each PM's field. When this approach is used, one must be careful not to demagnetize the PMs. If, in addition, higher torque must be maintained at high speed, extra quadrature-

axis (q-axis) stator current must be supplied besides the current invested to suppress the rotor's magnetic field, which results in higher resistance losses and lower efficiency.

Flux weakening in consequent pole generator

Research at ORNL [4] has produced a consequent pole generator with an external coil connected to the stator. A schematic is shown in Figure 4. A consequent pole device replaces alternate magnetic poles with ferromagnetic poles and doubles the thickness of the remaining magnets. The alternate pole is induced in the ferromagnetic material as a consequence of the magnet. Current in the external coil controls flux, allowing the consequent pole to aid, to do nothing, or to oppose the magnet flux during generation of a back-emf. In Figure 4(b), flux in the external coil forces the magnet flux into the consequent pole to aid the magnet as it generates the largest back-emf. In Figure 4(c), the external-flux path accommodates the entire magnet flux, thus removing the consequent pole as the magnet generates a back-emf of its traditional equivalent. In Figure 4(d), the external path provides flux to oppose the magnet, thereby reducing the back-emf to a low value. The external coil requires a small amount of additional current, but it may be used with a conventional PWM inverter and it eliminates completely the danger of demagnetizing the magnets. The only increase in complexity is a controller for the auxiliary stator coil current.

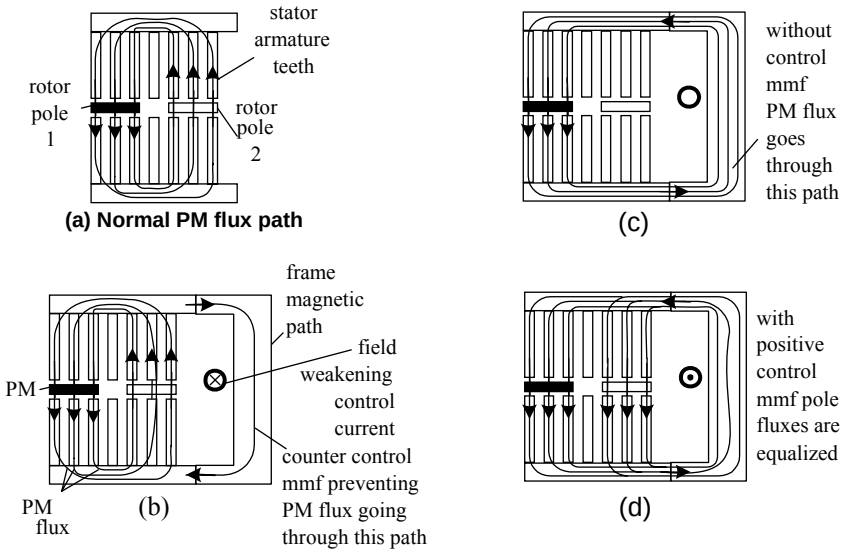

Figure 4. Axial-gap consequent pole generator weakened and strengthened by external coil.

High-strength undiffused brushless PM motor.

Another innovative approach at ORNL [5] employs an external-flux control coil that boosts the magnetic flux at low speeds and weakens it at high speeds. For a conventional PM motor, the air-gap flux density cannot be enhanced effectively, but it can be weakened; consequently, this approach addresses the problem of reduced back-emf at low speeds as well as the problem of excessive back-emf at high speeds. A schematic is shown in Figure 5.

The new machine is brushless because it transfers the mmf from the stationary excitation coil to the rotor through two secondary air gaps, identified as "air gap" in Figure 5. In the new machine, the PM in the rotor prevents magnetic-flux diffusion between the poles and guides the reluctance-flux path. The pole-flux density in the air gap can be higher than what the PM alone can produce, thus resulting in a machine with high magnetic strength. The higher magnetic strength manifests itself in higher torque.

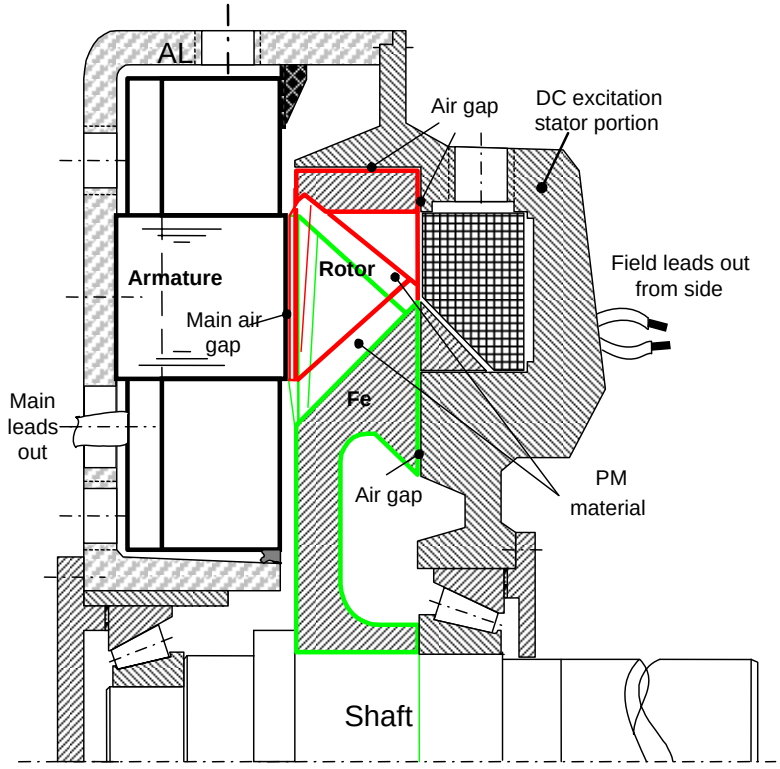

Figure 5. High-strength (magnetic) undiffused brushless axial-gap PM motor.

The axial flux produced by the dc excitation stator coil passes across the secondary air gap into the center part of the rotor (green), into the pole face (green), across the main air gap into a stator tooth, through the stator yoke to the adjacent tooth, back through the main gap into the rotor pole face (red), radially outward through the secondary air gap, and back through the external coil housing to close the flux path.

Magnetic polarization variation—memory motors

A fourth approach is to change the magnetization of the PMs by means of mmf pulses [6] so that the strength of the rotor poles is changed at will while the motor is operating. This type of motor is a variable-flux motor. If the magnets are demagnetized completely, the result is to decrease the number of poles. This second type of motor is a pole-changing motor. Ostovic calls this motor a "memory motor" because of its ability to memorize the flux-density level in the rotor magnets.

Figure 6 is a schematic of the memory motor. The magnets are polarized circumferentially and placed in a consequent pole configuration. The magnetization of the PMs can be varied by a short-current pulse and does not require a steady demagnetization current characteristic of vector control; consequently, its efficiency is higher. The demagnetizing current flows through the stator windings, requiring no special current source. The memory motor combines the advantages of a wound rotor, with its variable flux, and a PM motor with no excitation losses, whose benefits suggest it may be a candidate for an HEV traction drive.

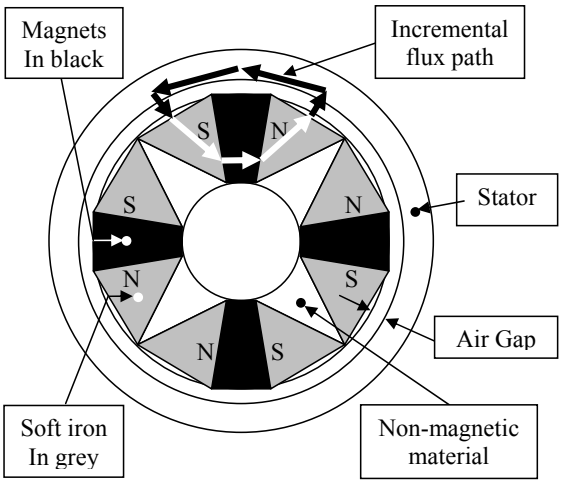

Figure 6. Variable flux PM motor—memory motor.

Magnetic strength variation—thermal field weakening

A fifth approach could be to control the strength of the PMs by actively or passively regulating their temperature below the material's maximum service temperature so that permanent demagnetization will not occur [7]. The effect of thermal field weakening has been observed during PM motor testing by a reduction in the field weakening current required to maintain operation as the speed increases. The total current is the square root of the d-axis (field weakening) current squared plus q-axis current squared. The reduction in total current observed during the test is a result of the lower d-axis current. The anticipated result is higher efficiency.

Changing number of stator turns per coil

Relationships between stator current and stator-magnetic flux, as well as between rotor flux and back-emf, are usually considered fixed by construction; but this is an unnecessary constraint. A reduction in back-emf reduces the wasted current required to weaken the rotor magnet's field; consequently, another approach for RTFC is to decrease the back-emf during operation by reducing the number of turns per coil involved in the energy conversion.

Changing the number of turns per coil can be done by (1) physically changing the number of active turns, (2) changing the turn-to-flux link factor, or (3) changing the number of poles. We have already seen how the memory motor can change the number of poles by demagnetizing the magnets. Changing the number of turns may be accomplished by using winding taps with two rectifiers and two switches [8].

For illustration, the speed dependence of the maximum power output for a typical IPM motor with a hypothetical capability to change the number of turns at will is shown in the figures below. Figure 7(a) shows how the base speed, peak power, power, current, and speed ranges grow as the number of turns is reduced from 9 to 5. Figure 7(b) shows the limit power curves for a turn-switching scheme focused on maximum power generation.

We now discuss the methodology for maximizing power delivery with respect to the number of turns per coil. It is representative of the approach that will be used for optimization with respect to other motor parameters.

A reduction in the effective number of turns per coil, N_s, decreases the electrical inductance, $L_s=N_s^2 L_1$, and ohmic resistance, $R = N_s R_1$, where L_1 and R_1 are the inductance and resistance, respectively, of a coil comprising one single turn. This approach will result in higher currents for the same voltage levels and in enhanced efficiencies. The following discussion explains how the equation may be derived for the number of turns per coil that will deliver maximum power as a function of angular frequency.

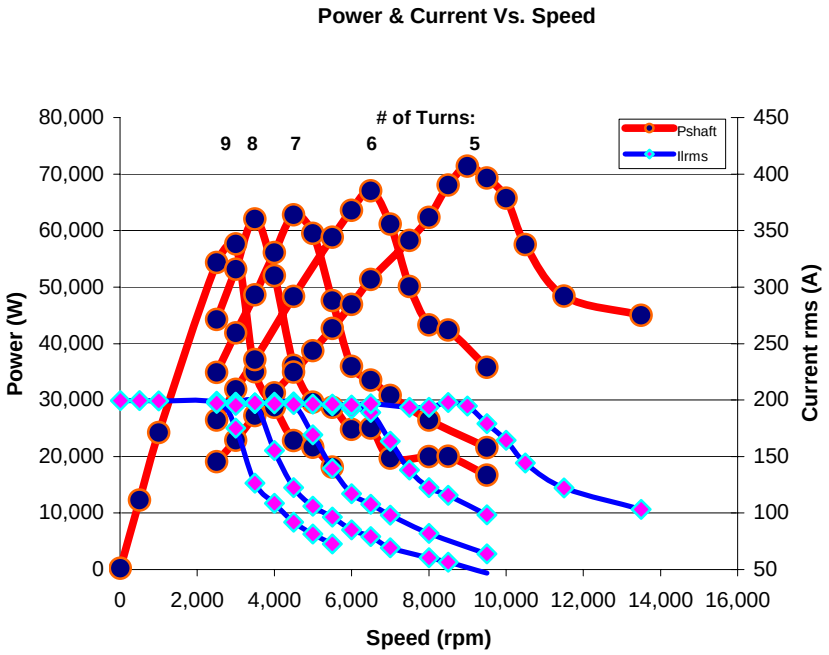

(a) Performance curve dependency on number of turns.

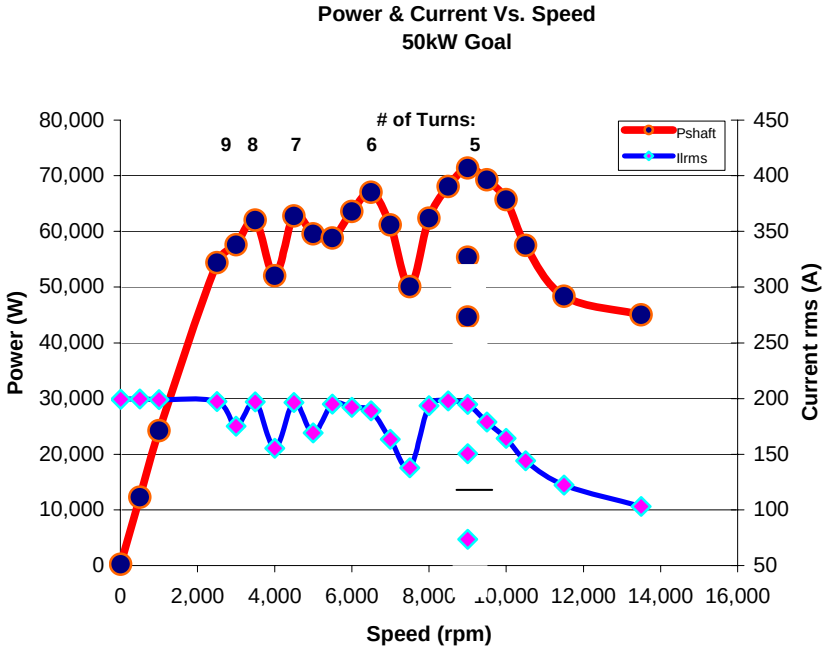

(b) Extending CPSR by reducing the number of turns.

Figure 7. Using the number of turns per slot to control CPSR.

As shown in Figure 7(a), the number of turns per coil that produces maximum power changes inversely with speed. Analytical determination of the number of turns that delivers maximum power as a function of frequency begins with

$$P = P(\alpha, N_s, \omega, L_d, L_q, \phi, R, V) \ ,$$

where

- α is the advance angle (the angle between the voltage and the current)
- N_s is the number of turns per coil
- ω is the rotational frequency, radians/s
- L_d is the d-axis inductance, H
- L_{d1} is the d-axis inductance of a single turn, H
- L_q is the q-axis inductance, H
- L_{q1} is the q-axis inductance of a single turn, H
- φ is the flux, V-s
- R is the resistance, ohms
- V is the supply voltage

The equation, $\partial P / \partial \alpha = 0$, is solved for the advance angle that delivers maximum power. The result is

$$\alpha = arctan\left(\frac{R - L_q \omega}{L_d \omega} \right) . \quad (1)$$

The advance angle is a function of N_s because $R = N_s R_1$, $L_q = N_s^2 L_{q1}$, and $L_d = N_s^2 L_{d1}$; consequently, α as a function of N_s is substituted into Eq. (1) and the equation,

$$\partial P(\alpha\{N_s\}, N_s, \omega, L_d, L_q, \phi, R, V) / \partial N_s = 0 \ , \quad (2)$$

is solved for N_s. As part of its modeling effort, ORNL has numerically obtained the solution for the number of turns that will achieve maximum power delivery.

Air-gap variation

A seventh approach to weaken the magnetic field is to mechanically increase the air gap. This technique increases the reluctance, which weakens the field by reducing the magnet's flux. The concept demands precise control and requires energy to move the rotor while it is spinning. Axial-gap motors with one stator are better suited for this type of control than radial-gap motors, because it is easier to control the distance between two flat parallel planes than to control the distance between two low-angle cones. For example, a 0.005-in. gap increase of an axial-gap motor requires the rotor to be moved along the axis of rotation by 0.005 in., while a radial-gap motor with a 1° cone requires the rotor to be moved along the axis of rotation by 0.286 in. For example, a 2° cone requires a 0.143-in. axial movement to achieve a gap increase of 0.005 in. Oh and Emadi have applied this method at the Illinois Institute of Technology to improve the efficiency and operating range of wheel motors [9].

In summary, seven methods of RTFC to increase the speed range while maintaining the efficiency of a PMSM are discussed. Conventional vector control maintains a torque producing quadrature current, i_q, and a magnet field-weakening d-axis current, i_d. The component of the dc d-axis current must be maintained during operation at high speed and results in increased stator current resistance losses with the accompanying loss in efficiency. Vector control is well established and allows speed range extension by flux weakening. It does require an expensive absolute encoder and fast control algorithms. In general,

efficiency considerations make those methods of flux control that require temporary intervention or pulses preferable to those requiring continuous action during operation. The most attractive method of RTFC is the pole number change. This has the potential to enhance vector control because it would perform the same current decomposition to form a d-axis current pulse that would demagnetize magnet(s) as operation at high speed begins and re-magnetize magnet(s) as high speed operation ceases. As the speed of a PM motor increases, the number of turns per coil must be reduced to achieve peak power delivery. Reducing the number of turns per coil is also a method of reducing the back-emf to accomplish RTFC. Its benefits are additional power as well as higher-speed operation. Another attractive but complicated method of RTFC is the coil number change, which would have to be used in conjunction with the pole number change because the ratio of coils to poles must remain constant. A number of papers have discussed changing the coil number for an induction motor, which automatically induces fewer poles when the number of coils is reduced. For a PM motor, the number of magnet poles may only be reduced by demagnetization. Mechanical RTFC, such as variable-gap control, can work for an axial-gap PM motor, but it is much more difficult for a radial-gap motor because of the requirement that the gap be precisely controlled by axial motion of a conical rotor. The usual problem remains of energy expended as the gap is opened and closed to accomplish field weakening.

To date, most of the efforts have focused on changing magnetic-flux-flow paths. We feel that the alternatives, which change the magnet properties or number of turns, should be examined for applicability to FreedomCAR machine targets.

3. Inductance Control

High-power density and efficiency resulting from elimination of rotor windings and reduced magnetic-flux losses have made the rare earth PM motor a leading candidate for DOE's Office of FreedomCAR and Vehicle Technologies traction drive motor. These traction drives are generally powered by radial-gap motors, having the magnets on or embedded in a rotating cylinder separated from the inside surface of a slotted cylindrical stator by an annular gap. The two main types of radial-gap PM rotors are those with magnets mounted on the surface of a supporting back iron, called SPM motors, and those with magnets mounted in slots in the rotor, called IPM motors.

Most early PM motor research was on the SPM motor, which was thought to have an inherently low stator inductance. A low stator inductance can lead to currents dangerously exceeding rated current as the back-emf across the inductance increases with speed; consequently, part of the attempted solution has been to increase the stator inductance to reduce the rate of current rise. Although analysis suggested that there should be no problem designing sufficiently high stator inductance into SPMs, attempts to do so were often not successful; and a motor design was sought that would have a higher intrinsic inductance.

Commercial research at Toyota has focused on IPM motors because they possess a high saliency ratio, which helps them operate over a high CPSR; but they are more difficult to fabricate. ORNL's position has been to continue research on brushless direct current motors because of ease of fabrication and increased power output.

Recently there has been a revival of interest in a fractional-slot PMSMs [12] made with concentrated windings because they possess three important features. First, they can increase the motor's inductance sufficiently to reduce the characteristic current to the value of the rated current, which will enable them to operate at high CPSR. This feature also limits short-circuit fault currents. Second, their segmented structure simplifies assembly problems and is expected to reduce assembly costs. Third, the back-emf waveform is nearly sinusoidal with low cogging.

In the 1980s, Sneyers, Novotny, and Lipo [25] first investigated the viability of IPM motors as traction devices and were followed in 1987 by Jahns [10]. Then Schiferl and Lipo [26] in 1990 developed the criterion for optimal field-weakening, which is expressed by the equation, $I_{ch} = \frac{\psi_m}{L_d}$, where I_{ch} is the characteristic current, ψ_m is the magnet's flux linkages, and L_d is the inductance. The importance of I_{ch} is summarized by the statement, "If a lossless motor is designed such that its rated current is equal to the

characteristic current, it will have an infinite CPSR." The seminal paper was that of Soong and Miller [27]. In this paper they normalized the parameters of the motor and introduced the concept of the IPM parameter plane. For the SPM motor, they chose as a design parameter the normalized flux linkage, ψ_{mn}. For optimal performance defined to allow infinite CPSR, this value must be $\psi_{mn}=1/\sqrt{2}$. Furthermore, they state that present-day (1980s) SPM motors have values of ψ_m between 0.83 and 0.96. Adnanes and Undeland [28] perform a similar normalization but choose X_s, the normalized d-axis reactance, as their parameter. For the SPM motor, the optimal value is again $X_s=1/\sqrt{2}$. They further state that X_s is typically in the range of 0.3–0.35. Both papers concentrate on IPM motors and present-day research efforts have followed this trend. While neither paper states that an optimum SPM value cannot be obtained, the general thinking has been that, (1) since the magnet is the only source of air-gap flux density, ψ_m must be large; and (2) since the magnet acts like an additional air gap, the d-axis inductance must be low. However, the SPM motor is much easier to manufacture than the IPM motor, and research efforts at ORNL have continued with the emphasis on techniques for increasing L_d of SPMs.

To examine this design in depth, ORNL entered into a collaborative agreement with UWM to build and test a 6-kW laboratory demonstration unit. Design, fabrication, and testing of the unit to 4000 rpm were completed during FY 2005. The motor will be sent to ORNL to explore ways to control its inverter to achieve higher efficiency during FY 2006.

To review coil parameters, recall that each coil, which has two sides and two ends, is rectangular, with opposite sides referred to as side 1 and side 2 lying in two slots whose angular separation is the coil pitch, τ_p. This angular separation may be defined in mechanical radians, ω_m, or more usefully in electrical radians, ω_e, where $\omega_e = \omega_m$ p and p is the number of pole pairs. The angular separation of the two sides determines if the winding is integer-slot or fractional-slot. Angular separation of opposite sides of the coil is referenced to the angular width of one magnet pole so that the word "fractional" in the term "fractional-slot" means the fraction of a magnet covered by the coil.

An important parameter is the number of slots per pole per phase, N_{spp}. If there are 24 slots, 4 poles and 3 phases $N_{spp}=2$ and, since this parameter is an integer, we refer to the winding as an integral-slot winding. Typically, these motors have double-layer windings, meaning that each slot will contain coil sides from two different coils; consequently, there are as many coils as slots. This motor could be wound as a single-layer winding with only 12 coils each wound in slots 180° apart, but there are advantages to the double layer.

PMSMs have sinusoidal back-emfs and thus must have sinusoidal distributed windings. The two choices are (1) full pitch, or (2) fractional pitch, often termed "short chorded" because the chord connecting coil side 1 and coil side 2 is shorter than one required to cross a complete magnet pole. A fractional-pitch winding is determined by the ratio of the coil span to the magnet span. If this ratio is unity, the winding is full pitch; and if the ratio is less than unity, the winding is fractional pitch (short chorded). If this ratio is less than unity, the back-emf will be decreased.

It is well known that a fractional-slot winding has the advantage of behaving as a winding with many slots per pole per phase [29], thus reducing the distribution factors of the harmonics. Liwschitz [30] has developed the distribution and pitch factors of the harmonics of fractional-slot windings. However, these windings were developed for standard ac machines.

With the emergence of the PMSM with IPMs, the sinusoidal-distributed winding became the winding of choice. However, it was recognized that there were disadvantages [11] that increased the costs in the manufacturing process. The stator became a prime target for cost reduction efforts and concentrated coils [11], where each coil is wound around one tooth, became a viable candidate by allowing segmented stator poles and a high slot fill factor (70% compared with 50%). Figure 8 shows the different winding configurations.

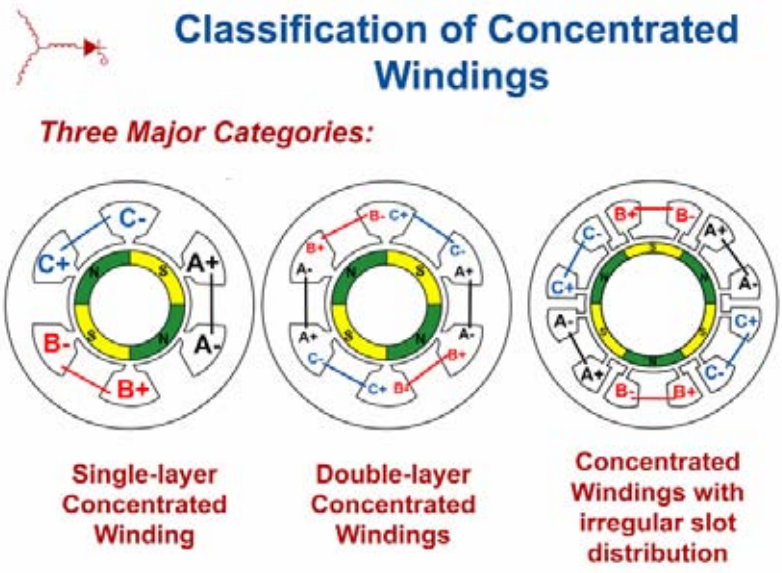

Figure 8. Concentrated winding configurations.

During this time frame, the electromagnetic design and performance characteristics of PMSMs with surface-mounted magnets and concentrated windings were presented in two papers [31, 32]. Two important observations are evident:

(1) There are combinations of slots and poles that allow a fractional-slot concentrated winding to have a high-winding factor and a balanced three-phase output (Table 1 of [31]).
(2) A characteristic of concentrated windings [32] is that they generate both odd and even mmf waves, which leads to increased leakage inductance. This would also increase the d-axis inductance, L_d, and hence the CPSR of the motor.

The major conclusion of this paper was that SPM machines could be designed to achieve optimal flux-weakening conditions by introducing concentrated fractional-slot stator windings. By optimal conditions, it is meant that the d-axis inductance, L_d, for infinite CPSR can be achieved.

As of this time frame, there were no previous publications that describe specific design techniques for applying such windings to achieve optimal flux-weakening conditions in SPM machines. This need was then met by El-Refaie and Jahns [12] of the University of Wisconsin when they developed a design technique and applied it to the design of a 36-slot, 42-pole PMSM with fractional-slot concentrated winding and surface-mounted magnets. The results showed promise as a candidate for the FCVT program, and ORNL entered into collaboration with the University of Wisconsin to build and test a 6-kW, 36-slot/30-pole PMSM with SPMs and concentrated fractional-slot windings. ORNL modeled the motor using SPEED software in order to verify its performance against the UWM test data.

The 6-kW, 36-slot/30-pole concentrated winding fraction-slot motor has now completed its verification testing cycles, and both the results and the analytical techniques used in the design are published [12]. The basic repeating unit of the SPM machine is shown in Figure 9.

The design data and calculated parameters are summarized in Tables 1–5. The analytical and experiment results of the verification tests are shown in Table 6.

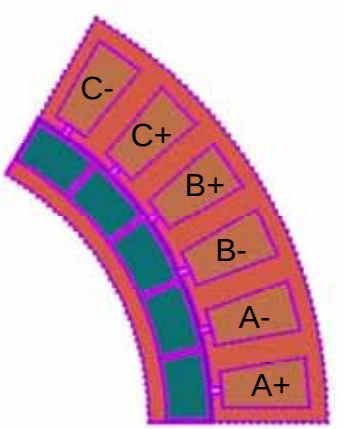

Figure 9. Basic repeating unit of the 6-kW SPM motor with fractional-slot concentrated windings [12].

Table 1. Stator dimensions and winding data for the 36-slot/ 30-pole SPM machine [12]

Number of slots	36	Number of poles	30
Number of phases	3	Slots/pole/phase	2/5
Series turns	108	Number of turns/coil	18
Number of coils	6	Number of parallel paths	1
Outer diameter	280 [mm]	Active length	60 [mm]
Total length	72 [mm]	Slot fill factor	35%
Slot opening width	2 [mm]	Slot bottom width	10[mm]
Slot top width	14.6[mm]	Slot opening height	3 [mm]
Slot height	25.4 [mm]	Back iron depth	9 [mm]
Tooth width	11.4 [mm]	Phase resistance	63[mΩ]

Table 2. Rotor dimensions for the 36-slot/30-pole SPM machine [12]

Rotor outer radius	88.6 [mm]	Magnet outer radius	101.6 [mm]
Inner radius	63.6 [mm]	Air gap thickness	1 [mm]
Magnet depth	13 [mm]	Magnet span	11.4^{o} [mech]

Table 3. Calculated inductances for the 36-slot/30-pole SPM machine [12]

Self inductance (including harmonic leakage)	225[μH]	Mutual inductance (including harmonic leakage)	~0
Self slot leakage inductance	805[μH]	Mutual slot leakage inductance	~0
Total self inductance	1.03[mH]	Net mutual inductance	~0

Table 4. Calculated current and magnet parameters for the 36-slot/30-pole SPM machine [12]

Magnet remanent flux density, B_r	0.55 [Tesla] @ 100°C	Magnet relative permeability, μ_r	1.22
RMS PM flux linkage, Ψ_m	34.8 [mWb_{rms}]	RMS characteristic current, $I_{ch}= \Psi_m/L_d$	33.8 [A_{rms}]
RMS rated current, I_R	43 [Arms]	Flux=weakening index FWI $=I_{ch}/ I_R$	0.79
Copper current density	7 [A_{rms}/mm^2]	Air-gap shear stress	3.1 [psi] = 21 [kPa]

Table 5. Breakdown of material mass for the 36-slot/30-pole SPM machine [12]

Copper mass	2.8 [kg]	Iron mass	12.6 [kg]
Magnet mass	3.6 [kg]	Total mass	19 [kg]

Table 6. Verification test results [12]

		100% load								P_{out}/P_{in}
rpm	mech rad/s	I_q	I_d	I	V_{phase}	$P_{in} = 3IV_{phase}$	T_{out}	P_{out}	Eff	
		Amps	Amps	Amps	Volts	Volt-amps	N-m	Watts	%	
800	83.78	43.0	0.0	43	85.0	10965	60	4901	86.0	44.7
2000	209.44	21.6	–26.7	34.3	87.7	9035.675	30.5	6392	91.0	70.74
3000	314.16	14.4	–26.5	30.2	87.7	7935.028	20.4	6415	92.0	80.84
4000	418.88	10.8	–26.4	28.5	87.7	7504.579	15.3	6404	91.9	85.33
Experimental										
800	83.78	43.0	0.0	43	81.0	10449	64	5400	84.0	51.68
2000	209.44	24.8	–26.9	36.6	89.0	9768.88	29	6075	90.3	62.19
3000	314.16	18.4	–14.6	23.5	91.0	6412.421	19.4	6099	90.0	95.11
4000	418.88	16.6	–14.9	22.3	91.0	6089.614	14.7	6146	91.7	100.9

It is noteworthy that bonded neodymium-iron-boron magnets were used to minimize eddy-current losses in the magnets. Because of its relatively low B_r (0.55T) and relative permeability μ_r (1.22), its length of 13 mm is large compared with that of an induction motor (IM). Also unlike IMs, the slot-leakage inductance was almost a factor of four higher than the self inductance.

The important result is shown in Table 4 which shows the flux-weakening index, FWI = I_{ch}/I_r =0.79. This means the d-axis inductance, L_d, is higher than the optimal value so that the rated current is smaller than the characteristic current; however, as seen in Table 7 and in [13], the motor met its design goal of CPSR = 6.

We now compare the results with the results of the ORNL calculations, which employ the SPEED software. The motor as represented in the SPEED program is shown in Figure 10. Each of the 18 coils is wrapped around a separate tooth, and each slot has only one coil side inserted. Figure 11 is the winding diagram for one phase.

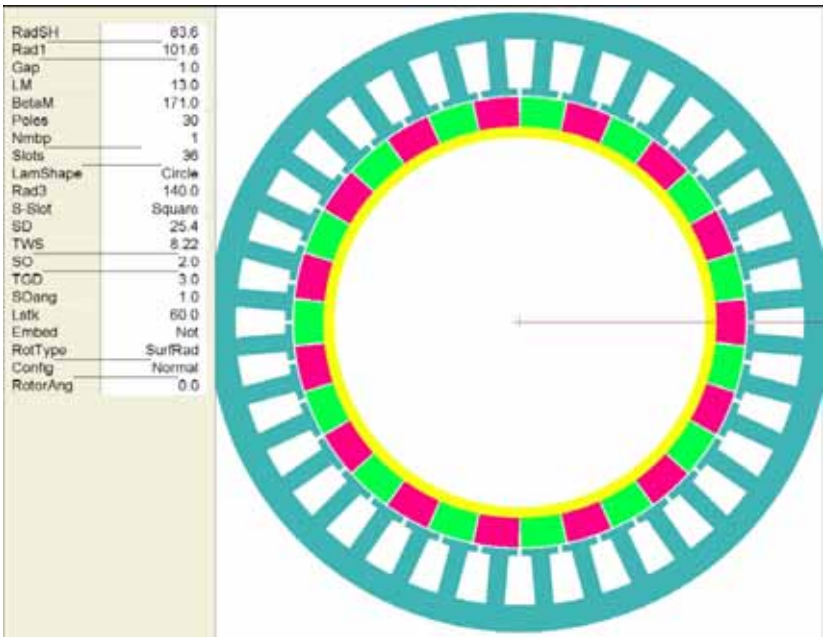

Figure 10. Configuration of the ORNL model of a 6 kW fractional-slot PMSM motor made with concentrated windings.

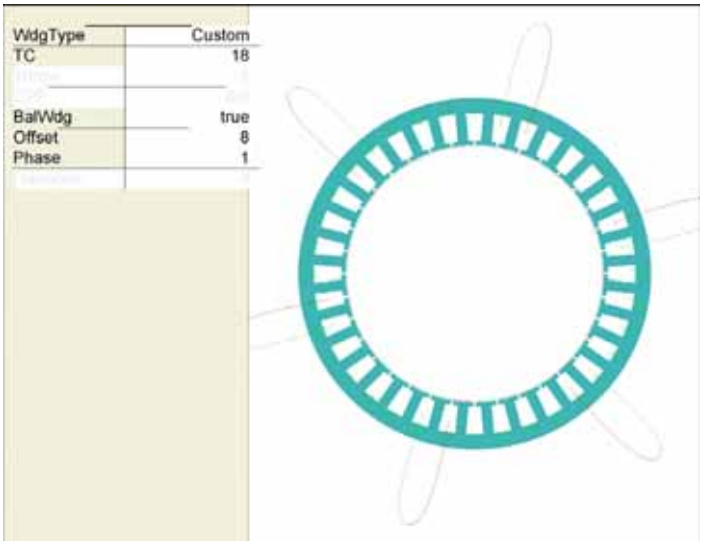

Figure 11. One phase of the coil winding configuration for the ORNL model of a 6 kW fractional-slot PMSM motor with concentrated windings.

Calculations by UWM and ORNL for the 6-kW fractional-slot motor with concentrated windings are compared in Table 7.

Table 7. Comparison of 6 kW fractional-slot motor analyses

Parameters per phase	Wisconsin	ORNL (SPEED software)
Gap inductance	0.225 mH	0.293 mH
Slot inductance	0.805 mH	0.767 mH
End-turn inductance	–	0.04 mH
Total stator inductance	1.03 mh	1.1 mh
Resistance	0.063 mΩ	0.047 mΩ
Back-emf	41.87 rms volts	55.75 rms volts

The most significant deviation is the 33% difference in the back-emf. In discussions with UWM, it was determined that SPEED uses a one-dimensional analysis to model the air-gap flux density, whereas UWM uses the technique of Zhu [33], which is based on a two-dimensional solution of LaPlace's equation. Using this technique, the back-emf of Figure 12 was generated.

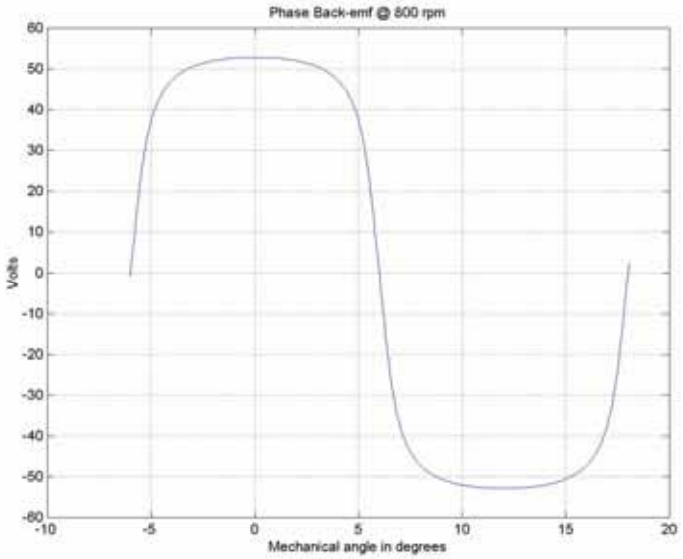

Figure 12. Peak back-emf per phase of 6 kW motor at 800 rpm.

From its harmonic content, shown in Figure 13, the fundamental rms back-emf per phase at 800 rpm becomes, $E = 64/\sqrt{2} = 45V_{phase}^{rms}$, which agrees well with the UWM value of 41.9 V_{rms}.

In general, there is good correlation between the ORNL and UWM analyses and the actual motor response. The 6-kW motor, as analyzed in the SPEED program, can be approximately modeled by the circuit of Figure 14. The winding resistances differ, but they do not dramatically affect the results.

Slotting influences the magnetic field in two ways. First, it reduces the total flux per pole and increases the effective air gap. This effect is accounted for by the Carter Coefficient, k_c. It also affects the distributions of the flux in both the air gap and the magnets. To account for the second effect, the Fourier permeance function, $\lambda(\theta)$, is introduced in Figure 15. The back-emf is then multiplied by this function to obtain the corrected back-emf.

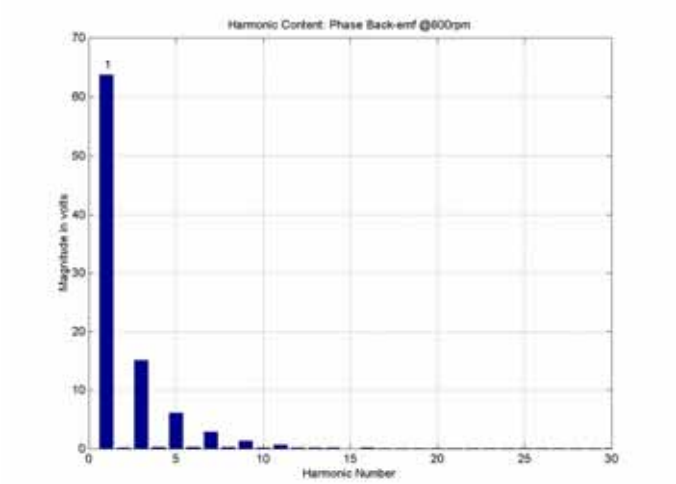

Figure 13. Harmonic content in back-emf of 6 kW motor at 800 rpm.

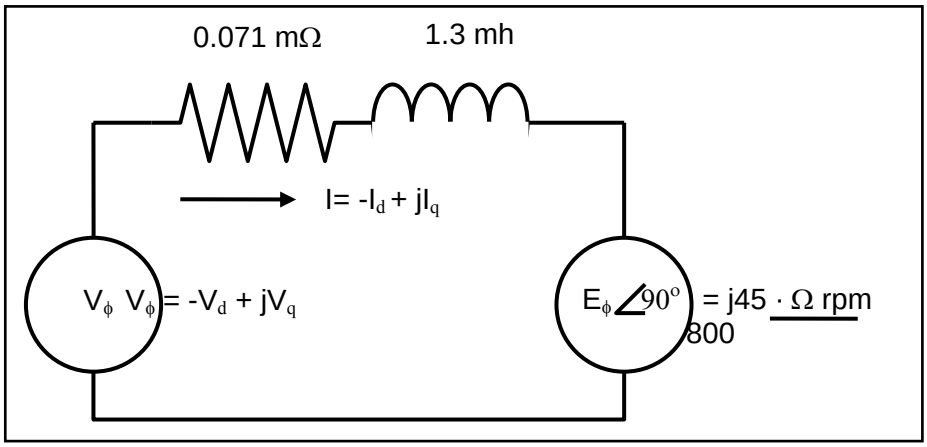

Figure 14. Per-phase equivalent circuit of 6 kW motor.

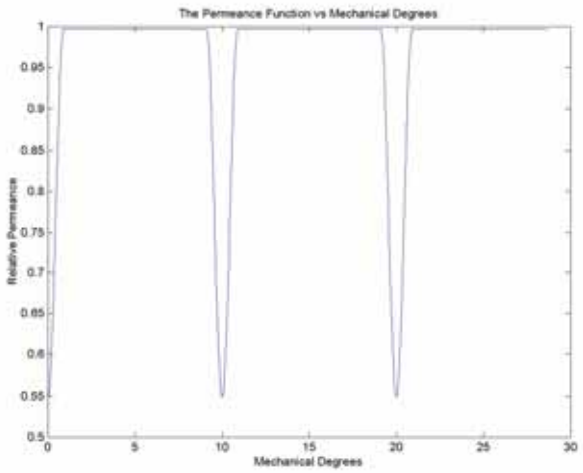

Figure 15. Relative permeance.

4. Inverter Control

It is well known that the ability of the PMSM to operate over a wide CPSR is dependent upon the machine inductance [15, 16, 28, 29, 34]. Early approaches for extending CPSR operation included adding supplementary inductance in series with the motor [15] and the use of anti-parallel thyrsistor pairs in series with the motor phase windings [16]. The increased inductance method is compatible with a VSI controlled by PWM, which is called CPA. The thyristor method has been called DMIC. Neither of these techniques has met with wide acceptance since they both add cost to the drive system and have not been shown to have an attractive cost/benefit ratio. Recently, a method has been developed to use fractional-slot concentrated windings to significantly increase the machine inductance [12]. This latest approach has the potential to make the PMSM compatible with CPA without supplemental external inductance. If the performance of such a drive is acceptable, then the method may make the PMSM an attractive option for traction applications requiring a wide CPSR.

A 30-pole, 6-kW, 6000-maximum-rpm prototype of the fractional slot PMSM design has been developed [35]. This machine has significantly more inductance than is typical of regular PMSMs. The prototype is to be delivered in late 2005 to ORNL for testing and development of a suitable controller. In advance of the test/control development effort, ORNL has used the PMSM models developed over a number of previous studies to evaluate the steady state performance of high-inductance PMSM machines with a view toward control issues. The detailed steady state model developed includes all motor and inverter loss mechanisms and will be useful in assessing the performance of the dynamic controller to be developed in future work.

The main problem found with high-inductance machines driven by CPA is that the motor current at high speed depends solely on machine parameters and is virtually independent of load level and the dc supply voltage. Thus the motor current is virtually the same at no load as at full load, resulting in poor efficiency at less than full-load conditions. DMIC is shown to produce a motor current at high speed that is proportional to load and has the potential to maintain high efficiency at full- and partial-load conditions [14]. However, an important concern with DMIC is found to be the reverse recovery losses of the thyristors at high speed. Because the turn-off of the thyristors in DMIC is naturally soft, it is possible that economical converter-grade components can be used, provided the fundamental switching frequency is about 1 kHz or less. The high pole count (30 poles) of the prototype motor results in a fundamental rate of 1.5 kHz at a top speed of 6,000 rpm and results in substantial recovery losses in the thyristors. The reverse recovery losses can be reduced by using inverter-grade components, which are available but cost more. The cost and additional losses associated with the thyristors used in DMIC may be offset by efficiency enhancements.

Another significant issue regarding high-inductance PMSMs uncovered in this study involves the amount of inductance required to meet CPSR requirements. It is generally believed that there is an "optimal value" for field weakening given by

$$L_{\infty} = \frac{E_b}{\Omega_b I_R} \tag{3}$$

where E_b is the rms magnitude of the line-to-neutral back-emf at base speed, Ω_b is the base speed in electrical radians per second, and I_R is the rms current rating of the motor windings. The prototype machine that is to be delivered to ORNL has about 1.7 times more inductance than was calculated using the original design equations. The inventors of the fractional slot concentrated winding method, and developers of the prototype machine, remarked that they were "too successful" in incorporating inductance into their machine and that steps would be taken to modify the design methodology to reduce the inductance to the optimum value. This study will show a significant advantage of having the higher inductance rather than the "optimal" value. Specifically, it is shown that the higher inductance enables the motor to develop the required power at lower current, thereby reducing motor and inverter losses and

improving efficiency. While an inductance higher than the value cited above is warranted, it still does not make the motor current proportional to load. Consequently, the problem of low efficiency at high speed and less than full load is not resolved.

A final point uncovered in this study concerns the dc supply voltage that provides the underlying source for the traction drive. A common definition of "base speed" is the speed at which the voltage applied to the motor armature is equal to the magnitude of the back-emf. The results in this study indicate that the dc supply voltage should be adequate to drive rated current into the motor winding at the specified base speed. At a minimum, this requires sufficient voltage to overcome not only the back-emf but also the voltage drop across the internal impedance of the machine. For a high-inductance PMSM, the internal impedance at base speed can be considerable, and substantial additional voltage is required to overcome the internal voltage drop. It is further shown that even more voltage than the minimum required for injecting rated current at base speed can be beneficial. In particular, this allows the required power to be developed at lower current, thereby reducing losses in the motor and in the inverter components. Further, it is shown that the current is minimized at a unique speed that varies with voltage. Consequently, there may be room for optimization. For example, if the drive spends a substantial amount of its operating life in the vicinity of one-half of maximum speed, then it can be desirable to choose a dc supply voltage that causes the motor current to achieve its minimum value at half full speed.

The findings of this study are demonstrated on two example motors whose parameters are given in Table 8. Motor 2 is patterned after the high-inductance prototype that is to be delivered to ORNL. Motor 1 has the characteristic inductance value as indicated by the formula above. The parameters of the two cases are identical except for the winding inductance. The parameters in Table 8 were taken from ref. [13].

The detailed technical assessment of Motor 1 and Motor 2 includes the evaluation of losses, not only in the motor but also in the inverter. The motor losses are in the copper resistance and the speed-sensitive rotational losses. The transistors in the inverter are typically controlled by sinusoidal PWM. A detailed PSPICE simulator is available to analyze the performance of the PMSM controlled by PWM when operating at constant speed. A simplified per-phase fundamental frequency model validated and used for this study is shown in Figure 16. It is a phasor model of the motor drive at a selectable but constant speed.

In the per phase model of Figure 16, the phasor $\overline{\mathrm{V}}$ represents the fundamental frequency line-to-neutral voltage applied to the motor by the inverter. V is the rms magnitude and δ is the inverter lead angle. Phasor $\overline{\mathrm{E}}$ represents the phase-to-neutral motor back-emf and is chosen as the reference phasor, such that the angle of $\overline{\mathrm{E}}$ is zero.

Neglecting the armature resistance, the phasor current of the motor is

$$\begin{aligned} \bar{I} &= \frac{V_{\max}}{nX_b}\sin\delta + j\left[\frac{E_b}{X_b} - \frac{V_{\max}}{nX_b}\cos\delta\right], \\ &= I_r + j\, I_x \end{aligned} \tag{4}$$

where I_r is the torque producing component of current in phase with the back-emf. This component is like the q-axis current in the d-q model. I_x is the component of current that is orthogonal to the back-emf and results in no net torque production. This is the field weakening component of current and is like the d-axis current in the d-q model. The total motor current has an rms magnitude of

$$I = \sqrt{I_r^2 + I_x^2} = \frac{\sqrt{V_{\max}^2 - n2V_{\max}E_b\cos\delta + n^2E_b^2}}{nX_b} \quad (5)$$

Table 8. Parameters of Motor 1 and Motor 2

Parameter	Motor 1	Motor 2
Number of poles	30	30
Base speed	900 rpm	900 rpm
Top speed	6000 rpm	6000 rpm
CPSR requirement	6.667:1	6.667:1
Back-emf magnitude at base speed, E_b (root-mean-square (rms) volts per phase)	46.5 @ 900 rpm	46.5 @ 900 rpm
Voltage constant, K_v (rms volts per elec. rad/sec)	0.03289	0.03289
Rated power	6 kW	6 kW
Rated torque	63.66 Nm	63.66 Nm
Rated rms current	43.0 A	43.0 A
Resistance per phase	71 mΩ	71 mΩ
Inductance per phase	765 μH	1300 μH
Rotational losses $P_{rot}(n)$ @ n = rpm/900		
1000 rpm (n = 1.11)	8.3 W	8.3 W
2000 rpm (n = 2.22)	33.3 W	33.3 W
3000 rpm (n = 3.33)	75 W	75 W
4000 rpm (n = 4.44)	133.3 W	133.3 W
5000 rpm (n = 5.56)	208.3 W	208.3 W
6000 rpm (n = 6.67)	300 W	300 W

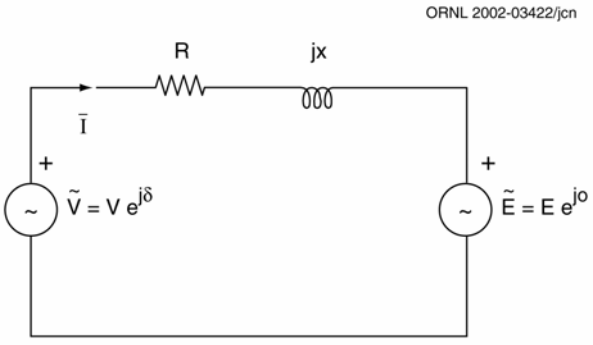

Figure 16. Fundamental frequency model of per-phase of a PMSM.

The total power injected into the motor by the inverter is

$$P_{in} = 3\,\mathrm{Re}(\bar{V}\,\bar{I}^{*}) = \frac{3V_{\max}E_b}{X_b}\sin\delta\,, \tag{6}$$

while the total power converted by the motor is

$$\begin{aligned} P_m &= 3\,\mathrm{Re}(\bar{E}\bar{I}^{*}) = \frac{3V_{\max}E_b}{X_b}\sin\delta \\ &= P_{\max}\sin\delta \end{aligned}\,, \tag{7}$$

where

$$P_{\max} = 3\frac{V_{\max}E_b}{X_b} \tag{8}$$

is the maximum power that can possibly be converted, which corresponds to the lead angle being 90° . Since we have neglected the winding resistance, P_{in} equals P_m and the common value is

$$\begin{aligned} P_m = P_{in} &= \frac{3V_{\max}E_b}{X_b}\sin\delta \\ &= P_{\max}\sin\delta \end{aligned}\,. \tag{9}$$

This expression shows that it is easy to control the motor to deliver rated power above base speed. All that is necessary is that the inverter lead angle, δ, be held fixed at that value that causes P_m to be equal to the rated value, P_R, so that

$$\begin{aligned} \delta &= \sin^{-1}\left(\frac{X_b P_R}{3V_{\max}E_b}\right) \\ &= \cos^{-1}\left(\frac{E_b}{V_{\max}}\right) \end{aligned}\,. \tag{10}$$

Observe that, as the speed becomes unbounded, the motor current magnitude approaches a limiting value given by

$$\begin{aligned} \lim_{n\to\infty} I_r &= \lim_{n\to\infty}\frac{V_{\max}}{nX_b}\sin\delta = 0 \\ \lim_{n\to\infty} I_x &= \lim_{n\to\infty}\left(\frac{E_b}{X_b} - \frac{V_{\max}}{nX_b}\cos\delta\right) = \frac{E_b}{X_b} = \frac{E_b}{\Omega_b L} \\ \lim_{n\to\infty} I &= \lim_{n\to\infty}\frac{\sqrt{V_{\max}^2 + n(n-2)E_b^2}}{nX_b} = \frac{E_b}{X_b} = \frac{E_b}{\Omega_b L} = I_{CH} \end{aligned}\,. \tag{11}$$

The limiting rms current magnitude is called the "characteristic current" [12] denoted as I_{CH} .

The following information is for DMIC operation of a PMSM. A recent paper [14] used a fundamental frequency model to analyze the performance of the sinusoidal back-emf PMSM driven in constant power mode by DMIC. The inverter includes a common three-phase voltage source inverter supplemented with an alternating current (ac) voltage controller between the inverter output and the motor. The ac voltage controller consists of three pairs of anti-parallel SCRs as shown in Figure 17. Each SCR pair is a full ac switch. In steady state, the fundamental frequency components of the voltage across and current through the switch are 90° out of phase, reflecting the lossless behavior of the switch and giving rise to an "equivalent reactance" interpretation of the SCRs. On a per-phase basis, a fundamental frequency phasor model has the form shown in Figure 18 with winding resistance and rotational losses neglected. In the figure, the parameter X_{thy} is the equivalent reactance of an SCR pair.

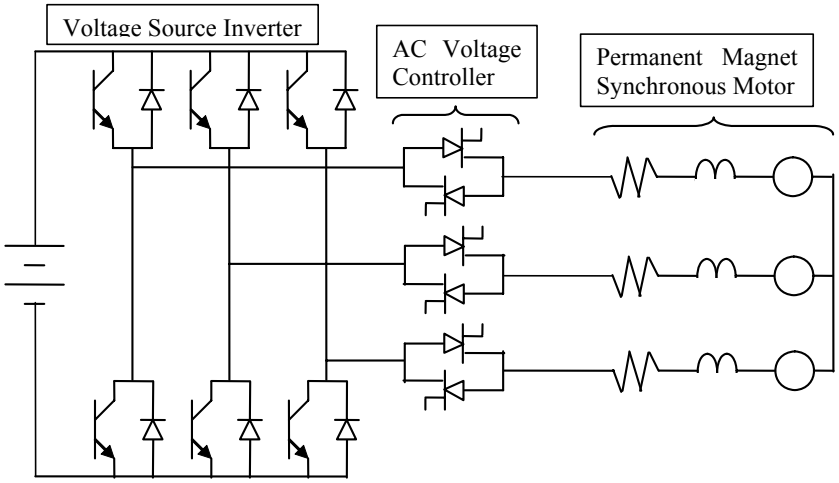

Figure 17. DMIC inverter topology.

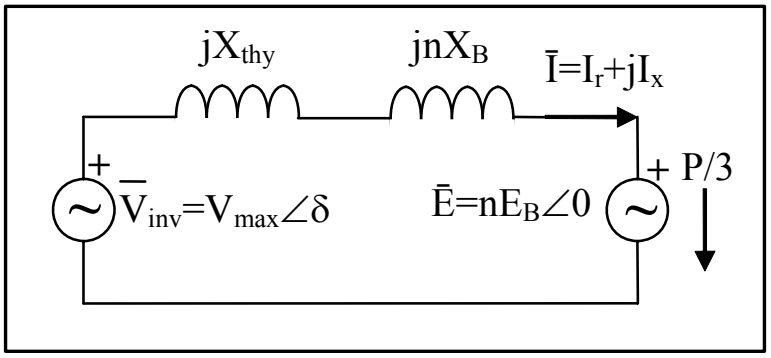

Figure 18. Per-phase fundamental frequency phasor model for constant power mode.

As noted in [14], the equivalent reactance of the ac switch is not constant but varies with the firing angle of the SCRs. The firing angle of the SCRs also controls the developed power of the motor. Since the equivalent reactance of the switch varies with the developed power, one cannot infer that the equivalent reactance interpretation can be extended to a fixed equivalent inductance that is in series with the motor winding. The total reactance presented to the inverter is the sum of the thyristor reactance and

the motor reactance, $X_{thy} + nX_b$. Thus no matter how small the machine reactance may happen to be, the thyristor reactance can be adjusted, through firing angle control, to make the motor behave as though it were a high-reactance machine. This is why the DMIC achieves an infinite CPSR even when the motor inductance is less, even substantially less, than the minimum required to be driven by CPA.

The inverter lead angle depends on the dc supply voltage and the developed power and is found to be

$$\delta = \sin^{-1}\left(\frac{X_b P}{3V_{\max} E_b}\right), \tag{12}$$

and the resulting rms motor current at speed, n, is

$$I = \frac{\sqrt{V_{max}^2 - 2nV_{max}E_b \cos\delta + n^2 E_b^2}}{nX_b}. \tag{13}$$

Note that at any finite speed the rms current depends, at least to some degree, on dc supply voltage through the dependence on $V_{\max}$, on the developed power through the dependence on δ, and on motor parameters, E_b and X_b. However, at high speed, the rms current approaches the "characteristic current" given by

$$\lim_{n\to\infty} I = \frac{E_b}{X_b} = \frac{E_b}{\Omega_b L}. \tag{14}$$

The characteristic current for DMIC operation depends only on motor parameters.

It may be shown that the phase quadrature component of motor current is

$$I_x = \frac{nE_b - V_{\max}\sqrt{1 - \left(\frac{XP}{3nE_bV_{\max}}\right)^2}}{X}. \tag{15}$$

Differentiating I_x with respect to X, setting the derivative equal to zero, and solving for the current minimizing reactance, X^*, yields

$$X^*_{thy} = \frac{3V_{\max}\sqrt{n^2E_b^2 - V_{\max}^2}}{P} - nX_b$$

$$= n\left(\frac{3V_{\max}\sqrt{E_b^2 - \frac{V_{\max}^2}{n^2}}}{P} - X_b\right)$$

with,

$$I_x^* = \frac{P}{3V_{\max}}\sqrt{1-\left(\frac{V_{\max}}{nE_b}\right)^2}$$

$$I_r^* = \frac{P}{3nE_b} \quad . \qquad (16)$$

This equation for X^*_{thy} clearly shows that no fixed inductance can provide the same effect as the thyristors in the DMIC inverter.

The model was applied to the two motors. Figure 19 shows that providing additional dc supply voltage beyond the minimum needed to support base speed condition is beneficial in reducing motor current and therefore reducing motor copper losses. In the inverter, there may be some increase in switching and reverse recovery losses as a result of the additional supply voltage; but there will be reductions in conduction losses that are at least proportional to the reduction in current if not more. Since the conduction losses are typically the main inverter loss mechanism, the inverter losses will also decline with higher supply voltage.

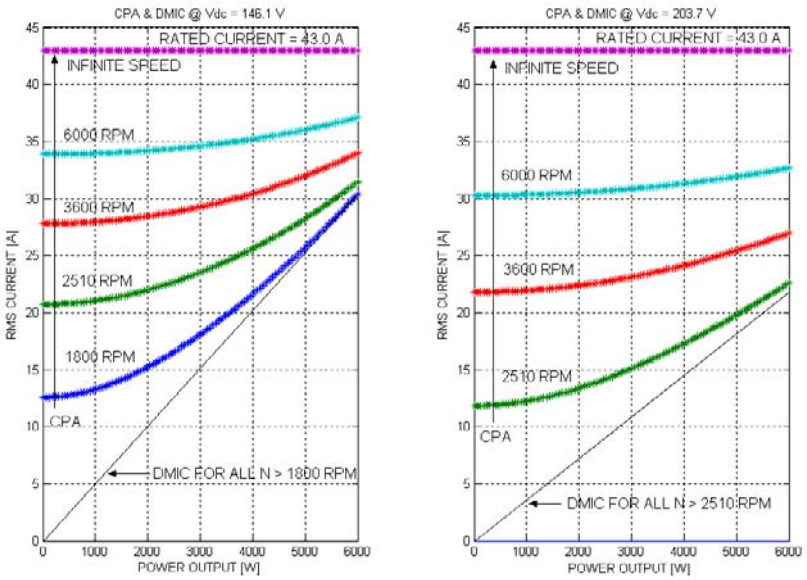

Figure 19. RMS motor current vs. power output during high-speed operation of Motor 1 with 146.1-V and 203.7-V dc supply voltages, when driven by CPA or by DMIC.

Figure 20 shows the high-speed current magnitude control capability of CPA and DMIC for Motor 1 and Motor 2 when both machines operate from a 203.8-V dc supply. Figure 20, however, shows the added benefit of having an inductance that is greater than the "optimal" value of L_∞. Recall that the inductance of Motor 1 is exactly L_∞, 765 μH, while Motor 2 has significantly more inductance (1300 μH). Comparing the two figures, it can be observed that when the motor is driven by CPA, the higher inductance results in a lower current magnitude at any given speed and power level, thereby improving efficiency. Also note that for the high-inductance machine, the curves for the various speeds shown—1800, 3600, and 6000 rpm—are much closer to the performance of the DMIC-driven motor, which has a single curve describing all operating speeds greater than 1800 rpm. While the performance with CPA is closer to DMIC for a high-inductance machine, the current with the DMIC drive is always at least as low as with the CPA; therefore, DMIC should have an efficiency advantage, especially at high speed and less than full load. Although not shown here, a further increase in dc supply voltage, for example from 203.7 to 250 V, would further reduce the motor current with DMIC but would have very modest impact on the CPA drive. Figure 20 clearly indicates that it may be very advantageous to have an inductance greater than L_∞. Thus it is difficult to accept L_∞ as an "optimum" design target for traction drives.

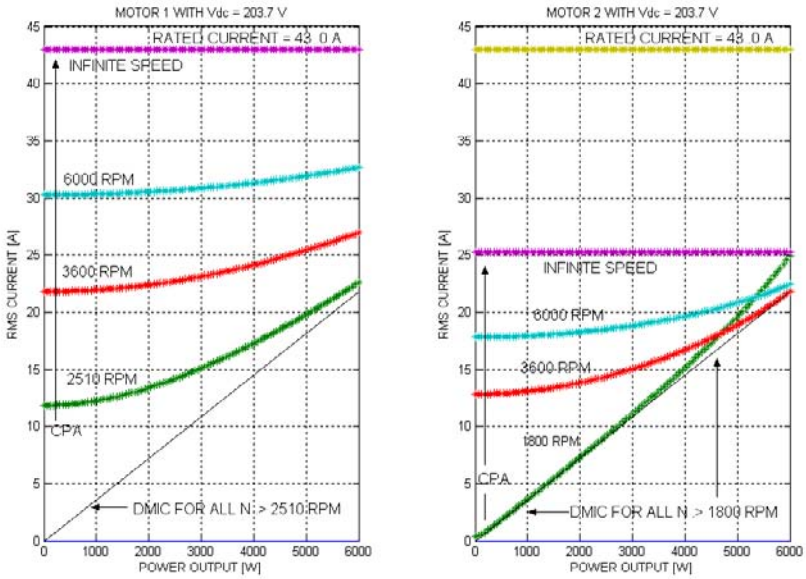

Figure 20. RMS motor current vs. power output during high-speed operation of Motor 1 and Motor 2 with 203.7 V dc supply.

The results in this section highlight the key difference between CPA and DMIC with respect to motor current magnitude control during high-speed operation. At high speed, the rms motor currents for the two different PMSM motor control methods approach

$$I_{CPA} = \frac{E_b}{X_b} = \frac{E_b}{\Omega_b L}$$
$$I_{DMIC} = \frac{P}{3V_{\max}} = \frac{\pi P}{3\sqrt{2}V_{dc}} \quad . \tag{17}$$

The motor current at high speed with CPA is the characteristic current that depends **only** on motor parameters. If the motor inductance is sufficiently large, then the characteristic current is less than the rated current, thereby enabling operation across a wide CPSR. On the other hand, the characteristic current is independent of load, meaning that the efficiency can be poor under light-load and variable-load conditions at high speed. Since the characteristic current is independent of dc supply voltage, providing a dc supply voltage beyond that necessary to support rated torque at base speed cannot reduce the motor current at high speed.

The motor current at high speed with DMIC is proportional to load power so that good efficiency can be maintained under light-load and variable-load conditions. Also, the high-speed current is independent of machine inductance. Whether the inductance is large or small, the high-speed current will be the same. The difference in behavior between a large or small motor inductance will lie in the firing of the thyristors, which will always adjust the total inductance to minimize the rms amps per developed watt. Finally, with DMIC, the high-speed current is inversely proportional to supply voltage. Therefore, significant reduction in motor current magnitude and attendant reductions in motor and inverter losses can be achieved by providing supply voltage in excess of that required to support the specified base speed conditions.

Approximate values of the device average and rms currents can be obtained using the per-phase fundamental frequency model shown in Figure 21. The model applies for both CPA and DMIC, but X_{thy} is zero for all operating conditions when using CPA.

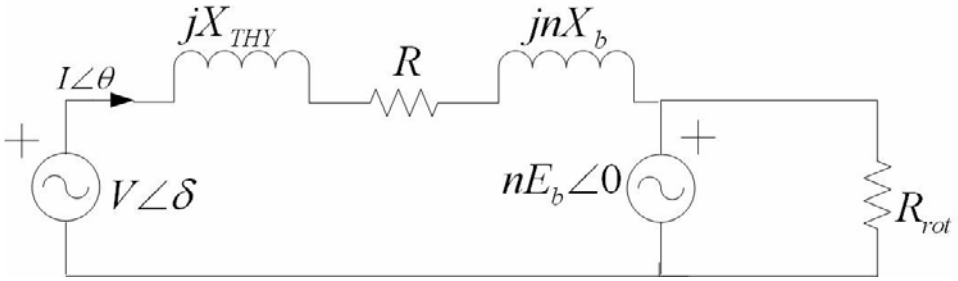

Figure 21. Per-phase model used to calculate average and rms device currents.

The model of Figure 21 explicitly represents motor copper and rotational losses since

$$P_{cu} = 3I^2R$$
$$P_{rot} = 3\frac{\left(nE_b\right)^2}{R_{rot}} \quad . \tag{18}$$

In this study, the winding resistance is fixed for both the example motor designs. No correction is attempted for temperature or skin effect.

Finally, we use the two motor examples to explore the benefits of having inductance higher than the optimal value, the potential benefit of providing extra dc supply voltage, the potential benefit of DMIC versus CPA, and the impact of thyristor reverse recovery losses on the performance of DMIC drives.

First we look at the benefits of inductance higher than optimal. Motor inductance is a critical factor in determining the CPSR of a PMSM when driven by CPA. For the two motors being evaluated in this study, the first has the "optimal" inductance of 765 μH while the second has a much larger value, 1300 μH. The performance of these two motors was compared over the entire torque speed range using the fundamental frequency model. Each motor is supplied by a dc voltage sufficient to achieve rated torque, 63.7 Nm, at the specified base speed. For the low-inductance motor, the supply voltage is 151 V;

the higher inductance requires a 208-V supply. Performance was simulated for values of rpm from 20 to 6000 rpm in steps of 20 rpm and for about the same number of equally spaced load levels at each value of rpm. Since the speed increment was 20/6000 of full speed, the load increment was chosen to be 25/6000 of full load. Results of the simulations are shown in Figures 22 through 25. The plots are 3-dimensional renderings with shading. The colors used in the shading denote magnitude. The highest value is red, the lowest value is dark blue. The transition from high value to low value is red to yellow to green to aqua to blue. The x-axis of each plot is rpm from 0 to 6000, while the y-axis is torque from 0 to 63.7 Nm. The z-axis variable displayed is the efficiency difference, because it lucidly exposes regions where one system performs better than another one.

Based on the comparisons in Figure 22. it is seen that the optimal characteristic inductance for field weakening does not lead to performance superior to that of Motor 2, which has 1.7 times as much inductance, when both motors are driven by CPA. The characteristic current of Motor 2 is lower than for Motor 1. Since the machine current approaches the characteristic current at high speed, there is a definite advantage to being able to operate at low current. So long as each machine is given sufficient dc supply voltage to support rated torque at base speed, the higher-inductance machine will have greater efficiency at high speed.

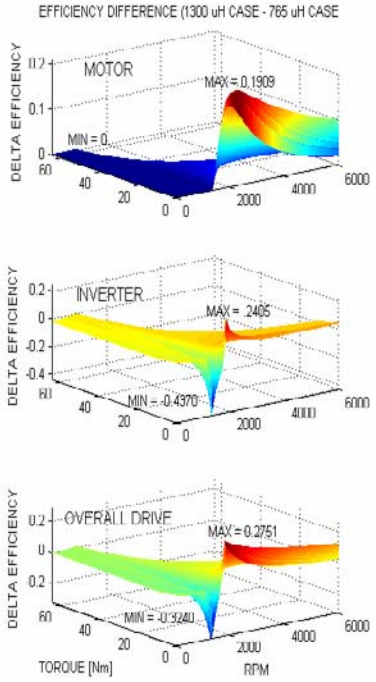

Figure 22. Efficiency difference comparison of Motor 2 (with 208 V dc supply voltage) minus Motor 1 (with 151 V dc supply voltage) when driven by CPA over the full torque speed envelope.

Next we consider the impact of having a dc supply voltage larger than the minimum required to support rated torque at base speed, which can be considered a form of "cheating" to achieve CPSR objectives. Any motor having an inductance higher than the "optimal" value of L_∞ has an infinite CPSR. Therefore, any increase in supply voltage above the minimum would not provide improved CPSR but might impact motor current and efficiency. In Figure 22, the performance of Motor 1 and Motor 2 were compared, with both machines having the minimum dc supply voltage—151 V for Motor 1 and 208 V for Motor 2—to support rated torque at base speed. Since the only difference in these two machines is the

inductance, it is reasonable to infer that Motor 1 might benefit from the higher voltage that would inherently be required by the parameter of Motor 2. The performance of Motor 1 was simulated over the entire torque-speed envelope for these two supply conditions, and the results are shown in Figure 23.

Figure 23 shows the efficiency of the lower-voltage case subtracted from the higher-voltage case at each torque–speed operating condition. This is done for the motor, inverter, and overall drive efficiency. The figure shows that there is a substantial benefit to the motor efficiency when operating at high speed. The benefit is the result of the fact that the minimum rms motor current is reduced by the additional supply voltage whether winding resistance is included or neglected. The motor efficiency at high speed is increased by as much as 0.1909 during high-speed operating conditions. There is a small region in the vicinity of base speed with low load where the lower voltage results in greater efficiency. But for high-speed operation, the additional dc supply voltage improves efficiency.

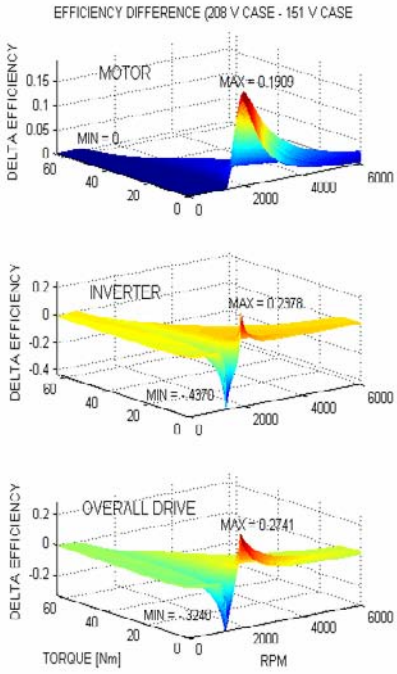

Figure 23. Comparison of efficiency difference when Motor 1 dc supply voltage is raised from 151 to 208 V.

Figure 24 contains simulation results over the entire torque–speed envelope for Motor 1 when driven by CPA and by DMIC. In both cases, the dc supply voltage is 151 V, which is the minimum necessary to support rated torque at base speed. The field weakening component of current in the DMIC drive is proportional to the load, as is the rms current. In the CPA drive, the rms current approaches the characteristic current. Since the torque-producing current decreases with speed and is identical for both the CPA and DMIC cases, the field-weakening current tends to the characteristic current at high speed. Because the rms current in the DMIC drive is proportional to the load, this drive can maintain high motor efficiency at high speed. At high speed, and especially at light load, the motor, inverter, and total losses are lower with DMIC. At low speed, the conduction losses of the DMIC thyristors result in greater inverter and overall losses. At high speed, the inverter losses of the DMIC, including the thyristors, are lower because of the high speed current minimization of DMIC. These effects are also seen in Figure 24, in which the motor, inverter, and overall efficiency of the CPA case are subtracted from the corresponding DMIC case over all torque–speed conditions. The motor is the main beneficiary of DMIC; because of the lower current at high speed, the motor efficiency is higher by as much as 0.2420. The

inverter efficiency is lower at and below base speed because of the added thyristor conduction losses, but the inverter efficiency is higher during high-speed operation by as much as 0.1375. Regarding overall efficiency, the DMIC may be as much as 0.0549 lower than the CPA during low-speed operation and as much as 0.2685 higher while operating in the constant power mode. If the drive spends most of its operating time at or above base speed, then the efficiency of the DMIC may be significantly better than CPA when inverter-grade thyristors are used in the DMIC drive.

Finally, we investigate the impact of converter- versus inverter-grade thyristors in the DMIC drive. Converter-grade thyristors are cheaper but have higher reverse recovery losses. Inverter-grade thyristors cost more but have lower losses and higher switching speed. For Motor 1 with 151-V dc supply, the difference in inverter efficiency and total efficiency is shown in Figure 25. Below base speed, the two cases are nearly identical. Above base speed, the reverse recovery losses of the converter-grade thyristor are larger than those of the inverter-grade. Figure 25 shows that the inverter-grade thyristor may have an

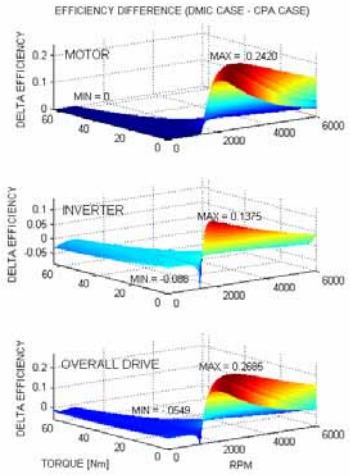

Figure 24. Comparison of efficiency difference when Motor 1 is driven by DMIC and by CPA using inverter-grade thyristors from a 151-V dc supply voltage.

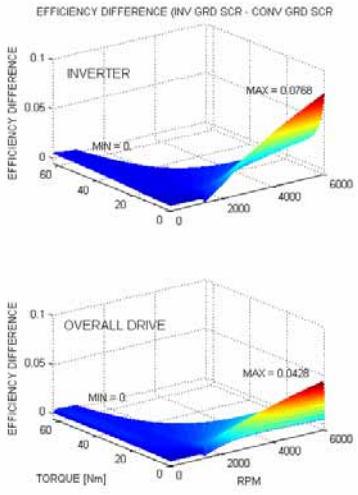

Figure 25. Efficiency difference between inverter- and converter-grade SCRs for Motor 1 driven by DMIC from a 151-V dc supply voltage.

efficiency that is at most 0.0768 larger than for the converter-grade. The figure also shows that the total efficiency with inverter-grade thyristors is as much as 0.0428 larger than for converter-grade. These differences occur at 6000 rpm, where the fundamental frequency is 1.5 kHz. Although the thyristor commutation in the DMIC occurs at natural current zero crossings, it is not clear whether converter-grade thyristors are even capable of such a switching rate. The authors have done testing with converter-grade thyristors in a DMIC drive operating at 300 Hz, and performance was satisfactory. The motors under investigation have 30 poles, which is the cause of their high fundamental rate. At this point, it is not known whether converter-grade thrysistors, which are cheaper, have switching frequencies sufficiently high to drive high-pole-count PMSMs.

5. Reluctance Control

International technology has focused research on the IPM motor to produce an HEV that will capture a large share of the world market. One of the beneficial features of this technology is the additional torque produced by reluctance. The objective of this task is to analytically describe the role that reluctance plays in PM motors, to explore ways to increase reluctance torque without sacrificing the torque produced by the PMs, and to compare three IPM configurations with respect to torque, power, amount of magnet material required (cost), and percentage of reluctance torque. Results of this comparison will be used to determine the research direction to obtain maximum torque and power while using a minimum amount of magnet material.

Since locomotion applications tend to prefer motors with wide ranges of speed to eliminate the need for or reduce the complexity of gear-boxes, it is important to find ways to increase the speed range of PM motors. One obvious possibility is to use a multilevel voltage source where available voltage would increase with rotor speed. Inverter drive costs, which are already the major component of a PM drive system, may limit this approach to two voltage stages, with the higher stage enabled at the higher speeds. Presently, improvements in stator and rotor topologies, together with control approaches, have enabled better overall performance/cost potential.

Once a PM machine is built, the strength and number of magnets in the rotor, and the number of poles and turns in the coils of the stator, traditionally remain constant; thus the amount of PM-generated magnetic flux linked by the coils of the stator remains fixed. As a result, the back-emf voltage induced by the PMs increases linearly with the speed of the rotor.

Rotor speed increases the back-emf voltage and thus causes a rapid reduction in the available supply voltage, which is normally constant. When there is no longer any supply voltage available to drive current into the stator, the maximum speed has been reached.

Reluctance is a property used in magnetic circuits that accounts for the ratio of geometric length to area and the magnetic properties of a medium, such as permeability, μ, in which a magnetic flux flows. The expression for reluctance is $\mathcal{R} = l/(\mu A)$, where l is the length of the flux path and A is the area normal to the flux [36]. Reluctance relates magnetic flux to mmf in a manner similar to the way that resistance and inductance relate current to voltage in an electric circuit. Since the externally controllable and measurement parameters of a motor are electric, it is customary to study the performance of motors in terms of electric rather than magnetic quantities. The relationship between magnetic reluctance and electric inductance is complex except for the simplest of cases, like that of a coil wrapped with N_t turns of wire around a magnetic path of reluctance, $\mathcal{R}$. This simple relationship is $L = N_t^2/\mathcal{R}$, which shows that electric inductance is proportional to the inverse of magnetic reactance. Consequently, high inductance corresponds to low reluctance.

Next is an analysis showing the relative benefit of flux weakening and saliency. In PM motors, optimal torque production occurs when the back-emf voltage and the stator current are in phase. When they are not, the current component normal to the back-emf produces a magnetic field that opposes or reinforces that of the PM, depending on its direction. The time-dependent linked flux then includes stator reaction components in both the d- and the q-axes, such that

$$\lambda_d = \lambda_{pm} + \lambda_{rd} = \lambda_{pm} + L_d\, i_d \qquad (19)$$
$$\lambda_q = \lambda_{rq} = L_q\, i_q,$$

where

i_q is the current component in-phase with the PM's back-emf (q-axis direction), which is the primary torque-producing component of current,

i_d is the current component normal to the back-emf (d-axis direction), which is the flux-producing component of current,

$\lambda_{rd} = L_d\, i_d$ represents the flux linkages created by the stator current's i_d component,

$\lambda_{rq} = L_d\, i_d$ represents the flux linkages created by the stator current's i_q component,

L_d and L_q are the inductances when the rotor is in the d-axis and q-axis positions.

Equation (15) shows that when i_d is negative, the reaction field has a d-axis component opposing that of the PM, thereby weakening the flux. This in turn causes a reduction in the q-axis back-emf voltage; consequently, higher I_q currents at the same or higher speeds for the same total current are possible, thus extending the motor's operating speed range. This extension is achieved at the cost of additional ohmic losses in the stator, but it reduces the angle, α, between the stator's voltage, V, and current, I, thus improving the power factor.

Figure 26 shows the RMS phasor diagram describing the operation of a generic PM motor driven sinusoidally with flux-weakening, since the current is in the negative d-axis direction.

As discussed in the caption of Figure 26, in addition to flux weakening, extra mechanical power is produced when the saliency ratio, defined as

$$\xi = L_q/L_d\ , \qquad (20)$$

is larger than unity. In surface-mounted PM motors characterized by $\xi = 1$, the stator reaction back-emf, E_r, is perpendicular to the stator current, I, and thus their vector product is zero. Hence, in surface-mounted PMs, I_d has no effect in power production, although it increases the ohmic losses and improves the power factor.

A discussion of characteristic current follows. The magnitude of the d-axis current needed to completely cancel the PM magnetic flux is often referred to as the motor's "characteristic current." In the open literature, the characteristic current is also identified as I_x [12]. By setting $\lambda_d = 0$, in Eq. (19) we obtain

$$i_{ch} = |\, -\, i_d\, | = \lambda_{pm}\, /L_d\ . \qquad (21)$$

Surface-mounted PMs, for which $L_q = L_d$, when operated with an amount I_{ch} of d-axis current in the negative direction would have no speed limit, since the back-emf induced by the PM would be zero. Unfortunately, the inductance, L_d, is small in PM motors; consequently, the magnitude of the characteristic current is large, showing that large currents cause only small amounts of flux weakening.

The power output for a PM with an I_d equal to the characteristic current, I_{ch}, in Eq. (21) injected in the negative direction would be

$$Pout_{ch} = I_q\, (E_{pm} + (\lambda_{pm}\, /L_d)(L_q - L_d)\, \omega) = I_q\, E_{pm}\, L_q/L_d = I_q\, E_{pm}\, \xi\ . \qquad (22)$$

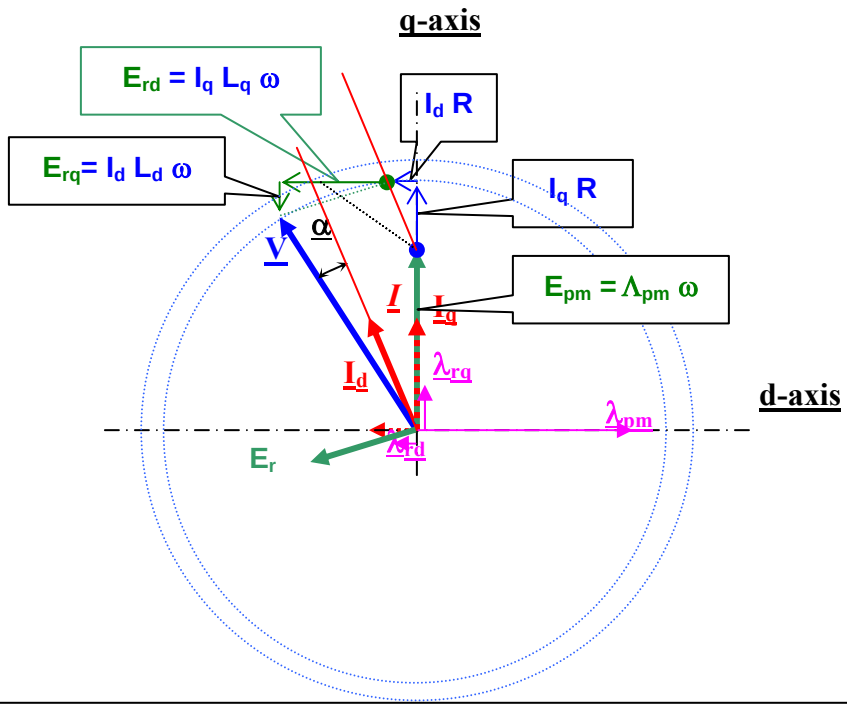

The power input is: $P_{in} = I\ V \cos(\alpha)$
$= I_q (E_{pm} + I_q R - I_d L_d \omega) + I_d (I_d R + I_q L_q \omega)$
$= I_q E_{pm} + (I_q^2 + I_d^2) R + I_d I_q (L_q - L_d) \omega$
The power output is: $P_{out} = I_q (E_{pm} - L_d I_d \omega) + I_d (L_q I_q \omega)$
$= I_q (E_{pm} + I_d (L_q - L_d) \omega) = I_q (E_{pm} + I_d L_d (\xi - 1) \omega)$
For surface mounted PMs, where $L_q = L_d$, I_d in the negative direction weakens the magnet so that the motor may be driven at higher speeds. However, there is no increase in output power, while the input power must increase to supply the additional resistance heat loss.

Figure 26. Standard RMS phasor diagram of a PM motor with flux weakening.

IPM motors differ in that they have the PMs inserted in the body of the rotor. This not only provides mechanical support for the magnets and protects them from the environment and from demagnetization, but also makes the inductance of the rotor position dependent, so that $L_d < L_q$. Consequently, when an I_d current is inserted in the negative direction shown in Figure 26 to weaken the flux, extra mechanical power is generated in the motor. IPMs are thus considered as hybrids of PM and reluctance technologies. In addition, in IPMs, the boundary between the rotor poles and the air-gap is high-permeability silicon steel. It allows phase-advance to give the PM flux a tangential component within the rotor pole, thus skewing the air-gap flux distribution to such a degree that stator teeth are saturated. This allows for an externally controlled variation in reluctance that is not possible in SPM motors.

As shown in the caption of Figure 26, the power output for any PM is

$$P_{out} = I_q (E_{pm} + I_d (L_q - L_d) \omega) = I_q (E_{pm} + I_d L_d \omega (\xi - 1)). \quad (23)$$

Thus the torque expression,

$$T = P_{out}/\omega = I_q E_{pm}/\omega + I_d I_q (L_q - L_d) = Torque_{PM} + Torque_{Reluctance}, \quad (24)$$

has two components. In IPMs, the reluctance term is not zero and contributes to the motor's output.

Equation (24) shows that the total torque output can be maintained while reducing the PM torque by compensating with an increase in the reluctance torque. When the strength of the PM flux is reduced, λ_{pm} and the magnitude of the characteristic current are also reduced. This makes flux-weakening by insertion of negative current in the d-axis less costly and more practical.

Solving Eq. (24) for E_{pm}, substituting $E_{pm} = \Lambda_{pm}\,\omega$, and taking the partial derivative of Λ_{pm} with respect to ξ for fixed P_{out}, ω, I_d, I_q, and L_d, we obtain the relationship between the change of PM strength needed and a change in the degree of saliency,

$$\delta\lambda_{pm} = - I_d L_d \delta\xi \,. \tag{25}$$

That is, an increase of saliency would result in a decrease in magnet strength required proportional to the product of $I_d \bullet L_d$, the values of the d-axis inductance and d-axis current component.

In terms of the characteristic current, Eq. (25) becomes

$$\delta\lambda_{pm}/\lambda_{pm} = - I_d/I_{ch}\delta\xi \,, \tag{26}$$

and integration yields

$$\lambda_{pm} = k\, e^{\,- Id/Ich\xi} \,, \tag{27}$$

where k is an integration constant. This is an important relationship since it shows that the magnet strength needed diminishes exponentially with the degree of saliency and with the amount of d-axis current injected relative to the value of the characteristic current. Therefore, decreasing the value of the characteristic current and increasing the saliency are clear goals for improving PM motor performance.

Equations (19) through (27) provide the following insights.

(a) Equation (21) shows that to reduce the magnitude of a motor's characteristic current, one may reduce the magnitude of the PM flux linked, and/or increase the value of the d-axis inductance.

(b) Equation (23) shows that IPM motors are superior to surface-mounted motors for flux weakening, since under flux-weakening conditions they provide extra mechanical power output because their saliency is larger than unity.

(c) Equation (25) shows the desirability of increasing the saliency and the d-axis inductance in order to reduce the amount of PM flux linkage needed by a motor. This would further enhance the motor's flux-weakening capabilities and reduce the cost of PMs while maintaining the motor's power level.

(d) Equation (27) shows that for equal motor power output, the magnet strength needed diminishes exponentially with the degree of saliency and with the amount of d-axis current injected relative to the value of the characteristic current. **Therefore, decreasing the value of the characteristic current and increasing the saliency should be clear goals for improving PM motor performance.**

(e) Equation (20) shows that to increase the saliency ratio, ξ, one should increase the quadrature inductance, L_q. One could decrease the d-axis inductance, L_d, but it would be counterproductive because of (a) and (c), which call for an increase in L_d.

If L_d is increased as recommended by (a) and (c) above, then a proportional or larger increase should be sought for L_q in order to maintain or augment the saliency ratio as recommended by (d).

We have investigated three PM motors that exhibit varying amounts of reluctance. The inset PM was assessed for the impact of trading PM for iron; the V-shaped single-layer IPM was assessed for the impact of embedding the PMs in the iron and of trading PM for iron; and the U-shaped multilayered IPM was assessed for the effect of changing the amount of PM material in an embedded PM design. For each design, the performance vs amount of PM material was studied to determine the optimal configuration. Parametric computations of performance were performed using the SPEED Consortium's brushless dc

computer simulator for each design. The topologies, methodologies, and results obtained are presented and discussed in the next section.

Three IPM motor configurations, which exhibit different reluctance properties, have been parametrically characterized for comparison of torque, power, and amount of magnet material. Figures 27 through 29 show two variations of their structures with two different distributions of PM and iron.

Figures 27(a) and 27(b) correspond to the inset type motor, whose magnets are flush with the rotor surface. In the parametric calculations for this motor, the angular pitch, β_M, of the PM is varied from a low value of 5° to a high value of 175° in 10°increments. The degrees are with respect to one complete electrical cycle, which includes a north and a south pole. In Figure 27(a), one quadrant represents a 360° electrical cycle, which includes 12 stator teeth. The angular pitch, β_M, is the angle in electrical degrees subtended by the magnet. In Figure 27(a), this includes four teeth, which leads to 360° × 4/12 = 120°. Note that as the pitch of the magnets decreases, the width of the iron web between the magnets increases. Also note that for the highest pitch, the expected behavior is that of an SPM motor.

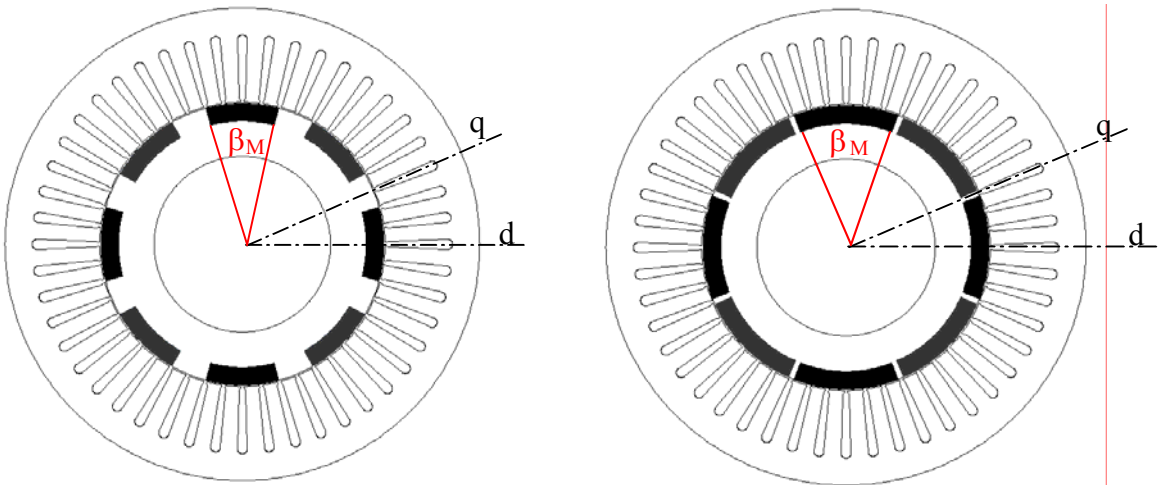

(a). Low magnet fraction, $\beta_M = 120^o$. **(b). High magnet fraction, $\beta_M = 175^o$.**

Figure 27. Inset surface-mounted PM motors.

Figures 28(a) and 28(b) correspond to the V-shaped IPM motor. In the parametric calculations for this motor, the lower radial position of the PMs is kept constant while the angular pitch of the PM at the rotor's surface is varied from a low value of 50° to a high value of 175° in 10° increments. Note that as the pitch of the magnets decreases, the width of the iron web between the magnets increases. In this design, we have reluctance variations due to the iron web, as in the inset type motor; but in addition we have the soft-PM effect of iron pole-caps that allow control of the shape of the distribution of flux crossing the air-gap.

Figures 29(a) and 29(b) correspond to the dual-layer U-shaped IPM motor. In the parametric calculations for this motor, the angular pitch of the PM at the rotor's surface and the lower radial position of the PMs are kept constant, while the length of the lower magnets in the two layers of U-shaped PMs is varied proportionally. The length of the innermost layer's magnet, yI_1, is varied from a low value of 2.4 mm to a high value of 17 mm in 0.73-mm increments. Note that the width of the iron web at the air-gap boundary remains constant, while the amount of magnetic material increases with the value of yI_1.

Each motor topology was explored using the brushless dc motor simulation software, a product of the SPEED Consortium. All of the motors have the same stator and overall rotor dimensions. The same operating conditions, such as max current and voltage, were used for all to provide the basis for comparative analysis.

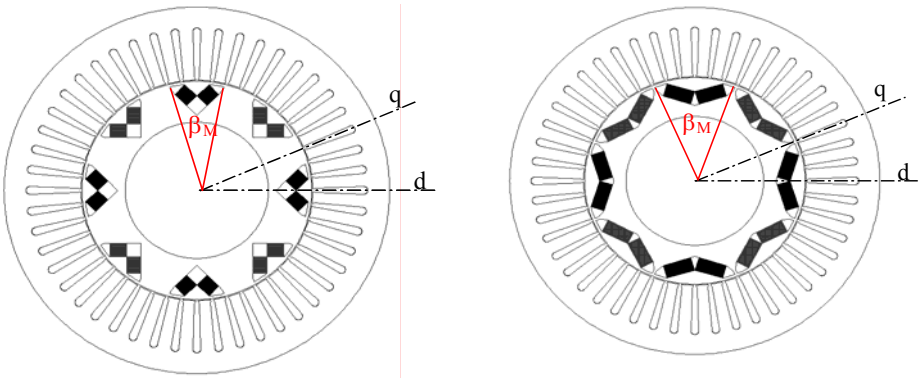

(a). Low magnet fraction, $\beta_M = 50^o$. (b). High magnet fraction, $\beta_M = 160^o$.

Figure 28. V-shaped interior PM motors (type 4).

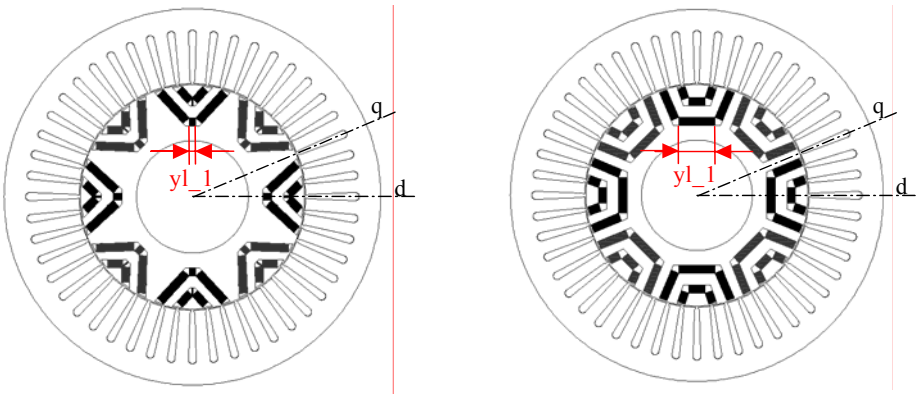

(a). Lowest magnet fraction, yI_1=2.4 mm. **(b). Highest magnet fraction, yI_1=17 mm.**

Figure 29. U-shaped interior PM motors (type 6).

The simulation software computed the PM and reluctance torques, power output, current peak and RMS, back-emf, and so on, characterizing the performance of the motors. The analysis excluded thermal flux and mechanical stress analysis, although these would be of interest for further study.

For each of the three topologies, parametric studies were performed that bracketed a range of advance angles within a range of speeds for each magnet configuration. The magnet-to-iron ratio was varied by means of the PM angular pitch parameters, β_M or yI_1, as appropriate.

Figure 30 shows how the amount of PM material varies with the varying parameter, β_M or yI_1, in each motor type. Note that Beta M = β_M in the figure. There is a large difference between the three topologies. At each speed, there is an optimal phase advance, which determines the flux-weakening current component, for maximum torque production. This phase advance is not necessarily the same for optimum motor efficiency. The results presented here correspond to the phase advance that resulted in the highest torque.

Figure 31 for the inset PM motor is of interest because it shows that there is a magnet fraction of about 115/180=0.64 for which about 75% of the torque is reluctance torque over the whole speed range. This is a 36% reduction in magnet area, which could amount to a cost savings if the thickness of the magnet does not have to be increased to maintain required PM performance.

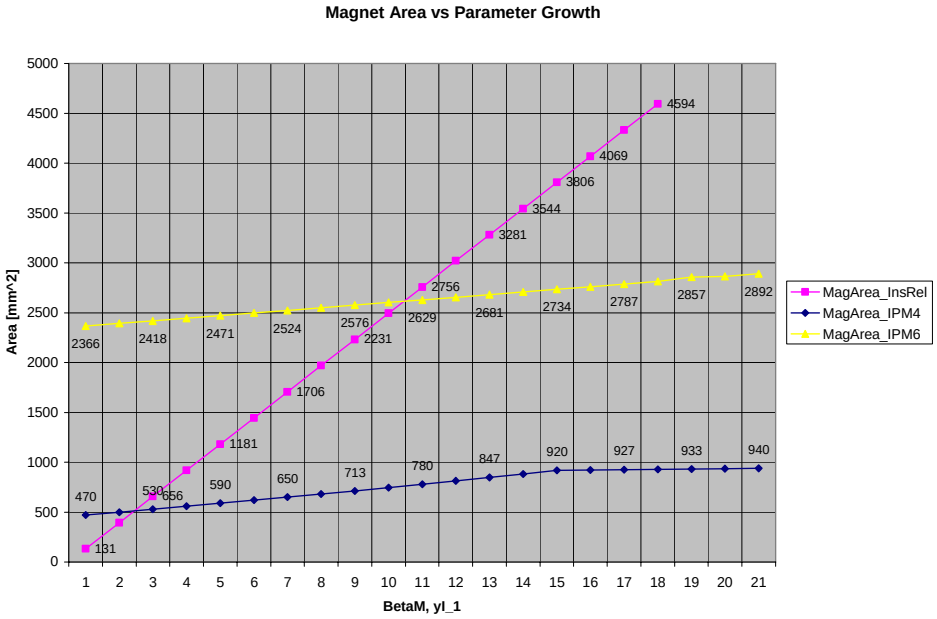

Figure 30. Amount of PM material in terms of cross-sectional surface area as a function of β_M or yl_1 for each of the three rotor configurations.

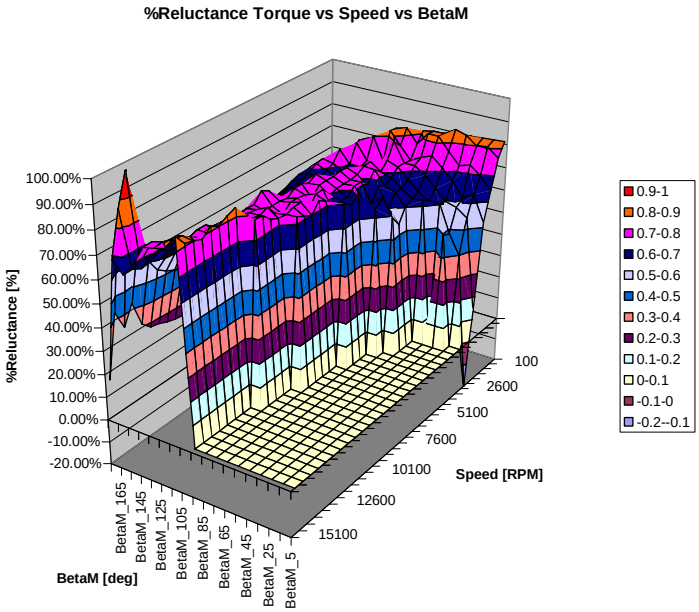

Figure 31. Relationship between magnet pitch, β_M, speed, and percentage of reluctance torque for the inset PM motor.

The reluctance torque has its strongest contribution in the current limited region below the base speed where maximum torque is required. Thanks to the reluctance contribution, higher peak torques can be achieved at low speeds for the same current limit. This suggests that to improve the performance of a PM motor, one could reduce the magnitude of the PM energy in the rotor, a radical thought, by reducing the PM mass or its magnetic strength and increasing the rotor's saliency to compensate the loss in PM torque with increased reluctance torque. In turn, the reduction in PM energy results in a reduced rate of change in

the back-emf and magnetic losses as the speed increases. This increases the speed range, improves the efficiency, and reduces the motor's heat removal load. The impact on power output and efficiency from changing the amount of magnetic material and its magnetic strength in a PM motor depends also on the control strategy used. ORNL has investigated the impact of trading PM material for iron in an inset PM controlled with the optimal displacement angles for each speed and PM material geometric and magnetic characteristics.

This task was initiated because of Figure 32. The reluctance torque is represented by the distance between the total torque and the PM torque produced by a four-pole motor as the magnet fraction is varied from 0 to 180 electrical degrees. Figure 32 shows that the total torque passes through a maximum at a magnet fraction of about ¾, suggesting that there is a magnet fraction at which the torque is optimum. Furthermore, at that point there is a significant increase in the torque above that produced by the magnets alone. At the onset of this task it was thought that the primary benefit of a reluctance-assisted PM motor was that it could achieve a required torque with less magnet material, which would allow it to operate at a higher CPSR. Alternately, it can achieve a higher torque than an SPM motor.

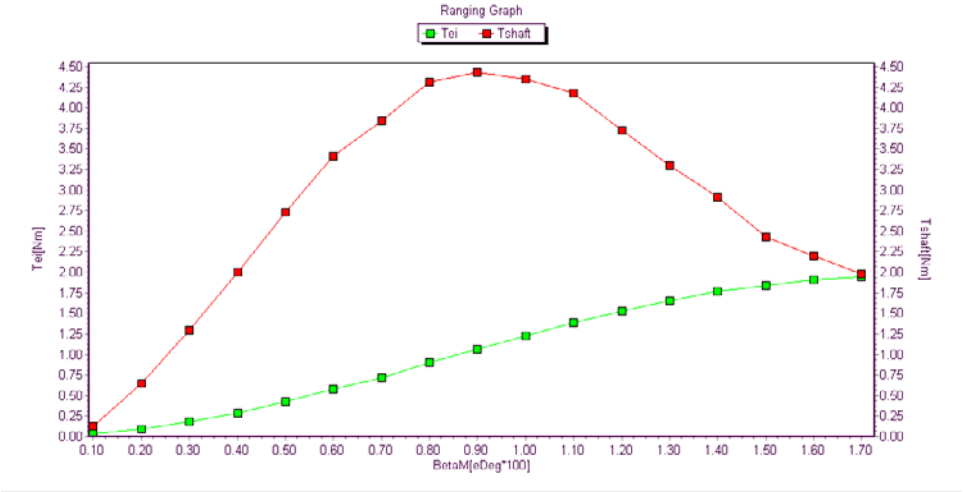

Figure 32. Magnet torque and total shaft torque of a four-pole inset reluctance-assisted PM motor for a range of magnet fractions.

The rest of this effort was to examine the equations used to design IPMs and to determine the optimal magnet fraction.

The use of lumped-parameter equations for modeling is appealing because it facilitates understanding, but it requires the determination of inductances, resistance, and flux linkages with the degree of detail appropriate for the simulation goals. Most challenging is the characterization of magnetic saturation since, especially in the case of IPM motors, the magnetic flux paths vary significantly with the rotor's relative position to the stator-generated rotating field and with the magnitude of the stators' currents.

It is best to have measured values of the lumped parameters, and second best is to obtain them by means of finite element computations. Most often, though, they are obtained by means of calculations based on geometry, equivalent circuits, and adjustment factors.

The focus of performance can be on power output or efficiency and may flip from one to the other depending on the situation. For automotive applications, it seems appropriate to focus on efficiency; but then one needs to consider the speed–torque cycle for each particular application. We consider that, in addition to the standard efficiency/torque maps, the overall efficiency for a set of standard driving cycles could be a criterion to determine optimal configurations, which, in our case, is for the optimal reluctance-assisted PM configuration.

Conclusions

Voltage Control

- The Z-source inverter is an excellent FCV technology.
- **Its present configuration** does not migrate naturally into conventional ICE-powered HEV configurations. The problem is that the Z-source inverter's front end diode, which is important in its operating cycle, is either an obstacle to regeneration or an unnecessary voltage drop in ICE configurations.
- Although there is some objection to the Z-source inverter's diode, even in an FCV, for applications that require inverter efficiencies above 98% [37], a recent report [22] has shown that the Z-source inverter is 1% better than a traditional PWM inverter, thereby meeting the 97% FreedomCAR efficiency specification. Further advantages include 20% lower semiconductor ratings and a CPSR greater by a factor of 1.68 than traditional PWM inverters. An inherent benefit is higher reliability because it is not subject to damage from shoot-through.
- The report [22] also explains an additional self-boost mode discovered during testing, which comes into play when the traction motor is operating at low speed, low power, and low power factor. This mode is necessary to successfully start a cold fuel cell and is controllable when there is a battery, required by all FCVs, in the inverter system; however, it could be a problem for other applications.

Flux Control

- Conventional *vector control* maintains a torque-producing quadrature current, i_q, and a magnet field-weakening d-axis current, i_d. The component of the d-axis current must be maintained during operation at high speed and results in increased stator current resistance losses with an accompanying loss in efficiency. Vector control technology is well established and allows CPSR extension by flux weakening. It does require an expensive absolute encoder and fast control algorithms.
- In general, efficiency considerations make those methods of flux control that require temporary intervention or pulses preferable to those requiring continuous action during operation.
- The most attractive method of real time flux control (RTFC) is the *pole number change*. This has potential to enhance vector control because it would perform the same current decomposition to form a d-axis current pulse that would demagnetize magnet(s) as operation at high speed begins and re-magnetize magnet(s) as high-speed operation ceases.
- Preliminary studies have shown that as the speed of a PM motor increases, the number of *turns per coil* must be reduced to optimize power delivery. Reducing the number of turns per coil is also a method of reducing the back-emf to accomplish RTFC. Benefits include additional power as well as increased CPSR.
- Another attractive method of RTFC is changing the *number of coils*, which would have to be used in conjunction with the pole number change because the ratio of coils to poles must remain constant. A number of papers have discussed changing the coil number for an induction motor, which automatically induces fewer poles when the number of coils is reduced. For a PM motor, changing the number of coils is further complicated by having to change the number of magnet poles, which may only be reduced by demagnetization.
- Mechanical RTFC, such as variable-gap control, can work for an axial-gap PM motor but is much more difficult for a radial-gap motor because of the requirement that the gap be precisely controlled by axial motion of a conical rotor. The usual problem remains of energy expended as the gap is opened and closed to accomplish field weakening.

Inductance Control

- The biggest contributor to the phase inductance in a fractional-slot motor is the slot inductance, which places a premium on the design of the slot-opening configuration. The slots are long and

slender and are not necessarily the optimal design. This could pose problems in forming the laminations.
- The results of the losses in the magnet seem low.
- The higher fill factor of the concentrated winding allows a more compact motor, which leads to higher power density and higher specific power.
- For the 6-kW motor with soft magnetic material and a lower remanence requiring larger thicker magnets, values from the 2-dimensional Zhu method of calculating back-emf compare more favorably with experimental data than do values from the 1-dimensional method.
- The 6-kW motor analyzed with SPEED software was concurrently modeled with a per-phase equivalent circuit. The two analyses compared well with the experimental UWM results.
- The effect of stator slotting on permeance of the 6-kW motor has been calculated and compares well with UWM calculations.
- FreedomCAR specifies that the electric motor must be able to deliver 55 kW for 18 seconds. An additional desirable industrial requirement added to requests for proposals to motor vendors in FY 2005 was that the motor should deliver this intermittent power from 20 to 100% of maximum speed, which points out that an advanced cooling technique is a major requirement for this motor. To produce this amount of power, the required rms current is approximately 460 A and the rms bus voltage is approximately 224 V, both of which exceed maximum specifications, which are 400 A and 200 V. This design problem will be addressed in the next phase of this study.
- FreedomCAR specifies that the electric motor's efficiency should be greater than 93% from 10% to 100% of maximum speed. An additional desirable industrial requirement added to requests for proposals in FY 2005 is that this efficiency should be reached at 20% of rated torque. This will be difficult to attain and will demand accurate core loss calculations and place a premium on the type and thickness of the laminations.

Inverter Control
- Study regarding control of PMSMs
  - More inductance and more voltage are better.
  - Even with the benefit of both characteristic inductance and high voltage, CPA suffers from low efficiency.
  - DMIC solves this problem by ensuring that the current used is proportional to load.
  - Automobiles spend most of their time at half speed and partial load.
  - As gas prices soar and efficiency becomes more important to the consumer, DMIC has the potential to provide the highest efficiency possible.
- Study regarding validation of methodology
  - Expressions for the modulation index, m_a, and inverter lead angle, δ, which were derived based on an algebraic fundamental frequency model, have been found to be very accurate when used in a detailed time domain simulation that includes PWM switching.
  - Expressions for average and rms currents in diodes, transistors, and thyristors were compared with detailed time domain simulations above and below base speed.
    - Below base speed, where simulations for CPA and DMIC control are the same, simulated losses at carrier frequencies of 8505 and 2025 Hz, agreed with theoretical model losses within 1%.
    - Above base speed, where separate simulations were necessary for CPA and DMIC, simulated losses for CPA control were within 2.5% of the theoretical model for transistor average and rms current and diode average currents. Simulated loss of the diode rms current, which was not quite as good, was within 8% of the theoretical model.
    - Simulated losses for DMIC control were within 1% of the theoretical model for the average transistor, by-pass diode, and thyristor currents. Simulated loss of the transistor and thyristor rms currents, which were not quite as good, were within 9% of the theoretical model.

- Since diode losses are generally 1/2 transistor losses, and conduction losses of the diodes are weighted more by forward voltage drop and average current than by diode resistance (rms current losses), the simplified theoretical model is sufficiently accurate for this study.

— Study regarding operation of PMSMs under CPA control
- Characteristic motor current, which permits operation at high CPSR, depends solely on machine parameters, E_b, Ω_b, and L, and is independent of motor load and dc supply voltage. This lowers its efficiency at partial-load conditions. Providing voltage higher than necessary to support rated torque at base speed cannot reduce the current at high speed.
- It is advantageous to have the inductance higher than "optimal" because it enables the motor to develop the required power with lower current and attendant efficiency increase.
- Even more voltage than the minimum required for injecting rated current at base speed can be beneficial because of lower current and attendant efficiency increase.
- The speed at which minimum current, n_{min}, occurs depends linearly on developed power and inversely on the maximum fundamental inverter voltage. n_{min}, is a unique speed, which varies with voltage, leaving room for optimization. If a motor spends a substantial amount of time at half speed, it could be desirable to choose a dc supply voltage that causes the minimum current at half speed. This would involve using a dc supply larger than the minimum and using control to restrain the torque envelope.
- Control of the voltage lead angle at high speeds allows a PMSM to operate at constant power, but it does not ensure operation within rated current. Inductance is the critical factor that ensures operation within rated current.
- The limiting current at high speed is mostly for field-weakening and therefore produces little torque.
- At full load, the motor with characteristic inductance behaves as well with CPA control as with DMIC control.

— Study regarding operation of PMSMs under DMIC control
- Higher inductance results in reduced current at only one speed and power level under CPA control, whereas DMIC control minimizes current at all power levels and speeds, n>2.
- DMIC motor current is proportional to load at high speed, which leads to decreased current and attendant increased efficiency at partial load.
- Although originally for motors with low inductance, DMIC has potential for significant loss reduction for PMSMs with large inductances.
- DMIC control maintains an inverter power factor of 1 for all speeds greater than n_{min}, the speed at which minimum current occurs. Under CPA control n_{min} is a single speed at which a PMSM operates at an inverter power factor of 1. At all speeds above n_{min} the CPA power factor leads.
- With DMIC, high-speed current is inversely proportional to supply voltage so that extra supply voltage can lead to improved efficiency.
- Depending on the application, particularly the speed/loss profile, loss reduction may more than compensate for the losses introduced by the addition of the SCRs required by DMIC.
- At half speed and quarter load, Motor 1 under DMIC delivers 7.5% (percentage points) more power at 3000 rpm and 8.6 % more power at 6000 rpm than Motor 1 under CPA control.

— Study regarding the grade of SCR that may be used
- Increasing reverse recovery losses of thyristors, which increase with speed, is a problem that can be reduced with inverter-grade components at increased cost; however, cost and losses may be offset by efficiency enhancement.
- The question about converter-grade SCRs being able to sustain operation in the FreedomCAR application at a fundamental switching rate of 1.5 kHz at top speed of 6000 rpm must be answered in the laboratory by experimentation.

Reluctance Control

- Preliminary analyses confirmed that
  - To reduce the magnitude of the characteristic current, which is the current required to completely cancel the PM magnetic flux, $I_{ch} = \frac{\lambda_{pm}}{L_d}$, one may reduce the magnitude of the PM flux linked or increase the value of the d-axis inductance.
  - Since the saliency ratio is L_q/L_d, the equation for power delivered (using the convention that increasing d-axis current increases power delivery) may be expressed as $P_{del} = I_q\left[E_{pm} + I_d L_d \omega_{el}\left(\xi - 1\right)\right]$, which shows that IPM motors with non-zero saliency are superior to surface-mounted motors for flux weakening because, under flux weakening conditions, they provide extra mechanical power output.
  - The equation $\delta\lambda_{pm} = -I_d L_d \delta\xi$ shows that increasing the saliency and d-axis inductance will reduce the PM flux linkage needed by a motor. This would enhance the motor's flux weakening and reduce the cost of PMs while maintaining the motor's power level.
  - The equation $\lambda_{pm} = ke^{-\frac{I_d \xi}{I_{ch}}}$ shows that for equal motor power output, the magnet strength needed diminishes exponentially with the saliency and with the amount of d-axis current relative to the characteristic current.
  - If one increases L_d as recommended by the first and third bulleted items above, then one should increase L_q at least proportionally to maintain saliency. Likewise, an increase in saliency ratio should be accomplished only by an increase in L_q.
  - The role of reluctance in PM motors may be rephrased in terms of the work inductance together with the inverse of its preceding verb; i.e. "increase the inductance, L_d" would be replaced by "decrease the reluctance, R_d."
- Preliminary studies of the three types of IPM motors showed
  - Torque at low speeds was significantly higher than for similar SPM motors, as expected based on earlier work.
  - The drop in power delivery with increasing speed is lower for all of the IPMs studied, as expected, because they have weaker magnet strength, which increases their maximum operating speed.
  - For the PM motor with inset magnets, the optimal magnet fraction, which delivers 40 kW at a CPSR of 10, is 0.69.
- The use of lumped-parameter equations for modeling is appealing since it facilitates understanding; but it requires the determination of inductances, resistance, and flux linkages with the degree of detail appropriate for the simulation goals.
- Characterization of magnetic saturation is challenging since, especially in the case of IPM motors, magnetic flux paths vary significantly, not only with the rotor's position relative to the stator-generated rotating field but also with the magnitude of the stator's currents. It is best to have measured values of the lumped parameters. Next best is to obtain them by means of finite element computations. Most often, though, they are obtained by means of calculations based on geometry, equivalent circuits and adjustment factors.
- The focus of performance can be on power output or efficiency and may flip from one to the other depending on the application.
- It is necessary, in addition to the standard efficiency/torque maps, to determine the overall efficiency for a set of standard driving cycles. These results should be the criterion to define optimal configurations.

Future Direction

- **Voltage Control**
  - — Use of the Z-source inverter with ICE-hybrid vehicles will require development of a bi-directional version to make use of regeneration.
- **Flux Control**
  - — To date, most of the efforts have focused on changing magnetic-flux-flow paths. We feel that the alternatives, which change the magnet properties or number of turns, should also be examined for applicability to FreedomCAR HEVs.
- **Inductance Control**
  - — Since slot inductance contributes most of the phase inductance, the design of the slot-opening configuration and its impact on forming laminations will be explored further in FY 2006.
  - — Calculation of core loss and magnet losses will be studied further, and a way to check their validity for fractional-slot PMSMs will be sought.
  - — Delivering 55 kW at 2000 rpm with an integral slot PMSM requires an rms current of about 460 A and an rms bus voltage of about 224 V, both of which exceed maximum specifications, which are 400 A and 200 V. Similar difficulties are encountered for the fractional-slot PMSM. Designing around this problem will be addressed in the next phase of this study.
  - — Collaboration will continue with UWM to prepare a design package for fabrication of a 30/55-kW fractional-slot motor with concentrated windings.
- **Inverter Control**
  - — Laboratory experimentation will be necessary to determine if cheaper converter-grade SCRs are able to sustain operation in the FreedomCAR application at a fundamental switching rate of 1.5 kHz at a top speed of 6000 rpm.
  - — Provide two control schemes for driving the 6-kW PMSM motor with fraction-slot concentrated windings.
  - — Scheme 1 will minimize current at high speeds to reduce operating costs at partial loads.
  - — Scheme 2 will be the least expensive.
  - — Rapid prototype the scheme or schemes with promise.
  - — Interface with a dynamometer and test to determine the partial load regions where operating costs may be reduced.
- **Reluctance Control**
  - — Technology developed in this task will be used to explore extending the CPSR of reluctance traction drive motors.

Publications

J. W. McKeever, S. C. Nelson, and G. J. Su, *Boost Converters for Gas Electric and Fuel Cell Hybrid Electric Vehicles*, ORNL/TM-2005/531, Oak Ridge National Laboratory, May 2005.

P. J. Otaduy and W. C. Johnson, *The Role of Reluctance in PM Motors*, ORNL/TM-2005/86, Oak Ridge National Laboratory, April 2005.

P. J. Otaduy and J. W. McKeever, *Real Time Flux Control in PM Motors*, ORNL/TM-2005/175, Oak Ridge National Laboratory, Sept. 2005.

J. M. Bailey and J. W. McKeever, *Fractional-Slot Surface Mounted PM Motors with Concentrated Windings for HEV Traction Drives*, ORNL/TM-2005/183, Oak Ridge National Laboratory, Sept., 2005.

J. S. Lawler and J. W. Mckeever, *Control of Surface Mounted Permanent Magnet Motors with Special Application to Fractional-slot Motors with Concentrated Windings*, ORNL/TM-2005/184, Oak Ridge National Laboratory, Sept. 2005.

P. J. Otaduy and J. W. McKeever, *Modeling Reluctance Assisted PM Moators*, ORNL/TM-1005/185, Oak Ridge National Laboratory, Oct. 2005.

J. S. Lawler, J. M. Bailey, and J. W. McKeever, "Minimum Current Magnitude Control of Surface PM Synchronous Machines during Constant Power Operation," *IEEE Power Electronics Letters*, **3**(2), June 2005.

J. S. Lawler, J. M. Bailey, J. W. McKeever, and P. J. Otaduy, "Impact of Continuous Conduction on the Constant Power Speed Range of the Switched Reluctance Motor," *Int. Electric Machines and Drives Conf*., San Antonio, TX, May 15–18, 2005.

References

1. M. Okamura, E. Sato, and S. Sasake, "Development of Hybrid Electric Drive System Using a Boost Converter," EVS-20, Session 5, The 20th International Electric Vehicle Symposium and Exposition, Long Beach, CA, Nov. 15–19, 2003.
2. F. Z. Peng, "Z-source Inverter," *Proc. Of IEEE, IAS 2002*, pp. 775–781.
3. O. I. Elgerd, *Electrical Energy Systems Theory: Introduction*, McGraw-Hill Book Company, chapter 4, 1971.
4. J. S. Hsu, "Direct Control of Air Gap Flux in Permanent Magnet Machines," Paper No. TR7-001 in *IEEE Transactions on Energy Conversions*, 2000.
5. J. S. Hsu, "High Strength Undiffused Brushless Electric Motors and Generators," Patent 6,057,622, June 3, 2003.
6. V. Ostovic, "Pole-Changing Permanent Magnet Machines," *IEEE Trans. Ind. App.* **38**(6), November/December 2002.
7. R. J. Parker, *Advances in Permanent Magnetism*, a Wiley-Interscience publication, John Wiley and Sons, 1990.
8. G. Liang, J. Miller, and X. Xu, "A Vehicle Electric Power Generation System with Improved Output Power and Efficiency," *IEEE Trans. Ind. App.*, **35**(6), November/December, 1999.
9. S. C. Oh and A. Emadi, "Test and Simulation of Axial Flux Motor Characteristics for Hybrid Electric Vehicles," *IEEE Trans. On Vehicular Technology*, **53**(3) May, 2004.
10. T. M. Jahns, G. B. Klieman, and T. W. Newmann, "Interior Permanent Magnet Synchronous Motors for Adjustable-Speed Drives," *IEEE Trans. Ind. App*., **IA-22**(4), 738–747, July/August, 1986.
11. T. M. Jahns, *Interim Report:Cost Reduction Opportunities for Permanent Magnet Synchronous Machines,* Oak Ridge National Laboratory, May 24, 2004.
12. A. M. El-Refaie and T. M. Jahns, "Optimal Flux Weakening in Surface PM Machines using Concentrated Windings," *2004 IEEE Ind. App. Soc. Annual Meetings*, Seattle, WA, October 2004 (scheduled for publication in the *IEEE Trans. Ind. App*., May/June 2005).
13. A. M. El-Refaie, T.M. Jahns, P.J. McCleer, and J. W. McKeever, "Experimental Verification of Optimal Flux Weakening in Surface PM Machines Using Concentrated Windings," *Conf. Rec. IEEE Ind. App. Soc. Annual Meeting*, Hong Kong, China, October 2–6, 2005.
14. J. S. Lawler, J. M. Bailey, and J. W. McKeever, "Minimum Current Magnitude Control of Surface PM Synchronous Machines During Constant Power Operation," *IEEE Power Electronics Letters,* **1**(2), June 2005.
15. T. Sebastian and G. R. Slemons, "Operating Limit of Inverter-Driven Permanent Magnet Motor Drives," *Trans. Ind. App.*, **IA-23(**2), 327–333, March 1987.
16. J. S. Lawler, J. M. Bailey, and J. W. McKeever, *Extended Constant Power Speed Range of the Brushless Dc Motor through Dual Mode Inverter Control,* ORNL/TM-2000/130, Oak Ridge National Laboratory, 2000.
17. N. Mohan, T. Undeland, and W. Robbins, *Power Electronics: Converters, Applications, and Design*, Chapter 5, John Wiley and Sons, 1989.
18. F. Z. Peng, "Z-Source Inverter," *IEEE Transactions of Industry Applications*, **39**(2), March/April 2003.
19. F. Z. Peng et al., "Z-Source Inverter for Adjustable Speed Drives," *IEEE Power Electronics Letters*, **1**(2), 33–35June 2003.

20. M. Okamura, E. Sato, and S. Sasaki, "Development of Hybrid Electric Drive System Using a Boost Converter," EVS-20, Session 5, The 20th International Electric Vehicle Symposium and Exposition, Long Beach, California, November 15–19, 2003.
21. B. Ozpineci et al., "Optimum Fuel Cell Utilization with Multilevel DC-DC Converters," pp. 1572–1576 in *Conference Proceedings of the 19th Annual IEEE Applied Power Electronics Conference and Exposition*, **3**, 2004.
22. Michigan State University, "Z-Source Inverter for Fuel Cell Vehicles," submitted to Oak Ridge National Laboratory's Engineering Science and Technology Division at the Power Electronics and Electric Machines Research Center, Oak Ridge TN, August 31, 2005.
23. Fang Z. Peng, slide 13 of presentation "Z-Source Inverter for Hybrid Electric and Fuel Cell Powered Vehicles," DOE FreedomCAR and Vehicle Technologies Program Annual Review of Advanced Power Electronics and Electrical Machines, June 7–9, 2004.
24. D. W. Novotny and T. A. Lippo, *Vector Control and Dynamics of AC Drives*, Clarendon Press, Oxford, 1996 (republished 2000).
25. B. Sneyers, D. W. Novotny, and T. A. Lipo, "Field-Weakening in Buried Permanent Magnet AC Motors Drives," *IEEE Transactions*, **IA-21**, 398–407, 1985.
26. R. F. Schiferl and T. A. Lipo, "Power Capability of Salient Pole Permanent Magnet Synchronous Motor in Variable Speed Drive Applications," *IEE Transactions*, **IA-26**, 115–123, 1990.
27. W. L. Soong and T. E. J. Miller, "Field Weakening Performance of Brushless Synchronous AC Motor Drives," pp. 331–340 in *IEE Proceedings of the Electronics Power Appl.*, **141**(6), November 1994.
28. A. K. Adnanes and T. M. Undeland, "Optimum Torque Performance in PMSM Drives Above Rated Speed," pp. 169–175 in *Proceedings of IEEE Industry Applications Society Annual Meeting*, October 1991.
29. Liwschitz, Garik, and Whipple, *Electric Machinery Vol II AC Machines*, D. Von Nostrand Company, New York, 1946.
30. M. M. Liwschitz, "Distribution Factors and Pitch Factors of the Harmonics of Fractional-Slot Windings," *AIEE Transactions* **62**, 664–666, October 1943.
31. J. Cros and P. Viarouge, "Synthesis of High Performance PM Motors with Concentrated Windings," *IEEE Transactions on Energy Conversion*, **17**(2), June 2002.
32. F. Magnussen and C. Sadarangani, "Winding Factors and Joule Losses of Permanent Magnet Machines with Concentrated Windings," pp. 333–339 in *Proceedings of 2003 IEEE International Electric Machines & Drives Conference (IEMDC)*, **1**, Madison, Wisconsin, June 2003.
33. Z. Q. Zhu, "Instantaneous Magnetic Field Distribution in Brushless Permanent Magnet dc Motors, Part I: Open-Circuit Field," *IEEE Transactions on Magnetics*, **29**(1), January 1993.
34. A. K. Adnanes, "Torque Analysis of Permanent Magnet Synchronous Motors," pp. 695–701 in *23rd Annual IEEE Power Electronics Specialists Conference Record*, June 29–July 3, 1992.
35. A. M. El-Refaie and T. M. Jahns, "Optimal Flux Weakening in Surface PM Machines using Fractional-Slot Concentrated Windings," *IEEE Trans. Industry Applications,* **41**(3), 790–800, May–June, 2005.
36. A. E. Fitzgerald, C. Kingsley, Jr., and S. D. Umans, *Electric Machinery*, McGraw-Hill, 1990.
37. J. S. Lai, "Fuel Cell Power Conversion Technologies," Presentation to ORNL Power Electronics and Electric Machines Research Center, September 2, 2005.

3.2 Electric Motor Research and Development

Principal Investigator: John S. Hsu
Team Members: Curtis Ayers, Steven Campbell, Chester Coomer, Michael Jenkins, Kirk Lowe, Randy Wiles
Oak Ridge National Laboratory
National Transportation Research Center
2360 Cherahala Boulevard
Knoxville, TN 37932
Voice: 865-946-1325; Fax: 865-946-1262; E-mail: hsujs@ornl.gov

DOE Technology Development Manager: Susan A. Rogers
Voice: 202-586-8997; Fax: 202-586-1600; E-mail: Susan.Rogers@ee.doe.gov

ORNL Program Manager: Mitch Olszewski
Voice: 865-946-1350; Fax: 865-946-1262; E-mail: olszewskim@ornl.gov

---

Objectives

The drive motor is an extremely important component in both fuel-cell-powered and hybrid electric vehicles (HEVs). It provides all or part of the torque for moving the vehicle. All other components in the drive train are dependent upon the traction motor for providing the torque in the most efficient manner that meets system cost, size, weight, and reliability targets. Investigations of a reluctance interior permanent magnet (RIPM) with brushless field excitation (RIPM-BFE) machine, of a hybrid secondary uncluttered PM (HSUPM) machine, and of corona starting voltages with a conventional insulation system were all part of the motor development work conducted in FY 2005.

The objective of the FY 2005 research and development effort was to build an RIPM-BFE machine having a core length 30% shorter than that of the Toyota Prius motor (with the same diameter and same speed). In FY 2005, a HSUPM machine was conceptually designed. It reduces costs by combining the generator and the motor into one machine so that only one set of PMs and one frame are required. Torque production can be increased as a result of the rotating armature.

The objective of the corona/voltage study was to see how much the voltage could be increased in a motor before corona occurs in order to assess the motor's insulation capability. This gives valuable background data for considering high-voltage drive systems.

Approach

The project scope includes the design, simulation, drawings, fabrication, and testing of the RIPM-BFE machine, as well as the conceptual design of an HSUPM machine, in an effort to reduce motor size. Corona/motor voltage investigations were also performed to ascertain the voltage limitations and penalties associated with the higher-voltage operation of motors.

Major Accomplishments

The detailed results of the development of the RIPM-BFE motor are presented in the reports *Interior Permanent Magnet Reluctance Machine with Brushless Field Excitation*, ORNL/TM-2005/222, September 2005, and *Finite-Element Analyses of An IPM Reluctance Motor with Rotor Side-Poles*, ORNL/TM-2005/209, September 2005. Overviews of these reports will be provided later. In short, the concept of the RIPM-BFE machine was proved viable. The BFE coils were proved to be able to enhance and weaken the air-gap flux. This research led to a new concept for a machine with side PMs without

excitation coils. Engineering designs will be needed to optimize the design of this machine in FY 2006. The simulation software also needs to be improved to reflect the detail of the engineering drawings.

Preliminary conceptual rotor drawings of the HSUPM machine were generated in FY 2005. The proof of concept work will continue with the fabrication, design, and testing in FY 2006.

There is a strong desire on the part of the auto industry to push the motor voltage higher to reduce both the inverter size and the starting battery current. The corona tests performed in FY 2005 provide information for permissible starting voltages for the insulation systems of 480-V class motors. The detailed results are given in *Corona and Motor Voltage Interim Report*, ORNL/TM-2005/60, April 2005. The results from this report show that motor insulation requirements dictate the voltage limits for a high-voltage system.

Technical Discussion

RIPM-BFE Motor

In a conventional PM machine, the air-gap flux produced by the PM is fixed. It is difficult to enhance the air-gap flux density because of limitations of the PMs in a series-magnetic circuit. However, the air-gap flux density can be weakened by using power electronic field weakening to the limit of demagnetization of the PMs. This report presents the test results of controlling the PM air-gap flux density through the use of a stationary brushless excitation coil in an RIPM-BFE motor. Through the use of this technology, the air-gap flux density can be either enhanced or weakened. There is no concern with demagnetizing the PMs during field weakening. The leakage flux of the excitation coil through the PMs is blocked. The prototype motor built on this principle confirms the concept of flux enhancement and weakening through the use of excitation coils.

The RIPM-BFE was invented at Oak Ridge National Laboratory (ORNL). It offers a high torque per ampere by using a brushless excitation coil to enhance the flux. The motor eliminates the system need for a dc/dc boost converter at medium and high speeds. The core loss of the motor is low because the flux can be weakened through the excitation coil.

The design of the sample RIPM-BFE prototype machine is shown in Figure 1.

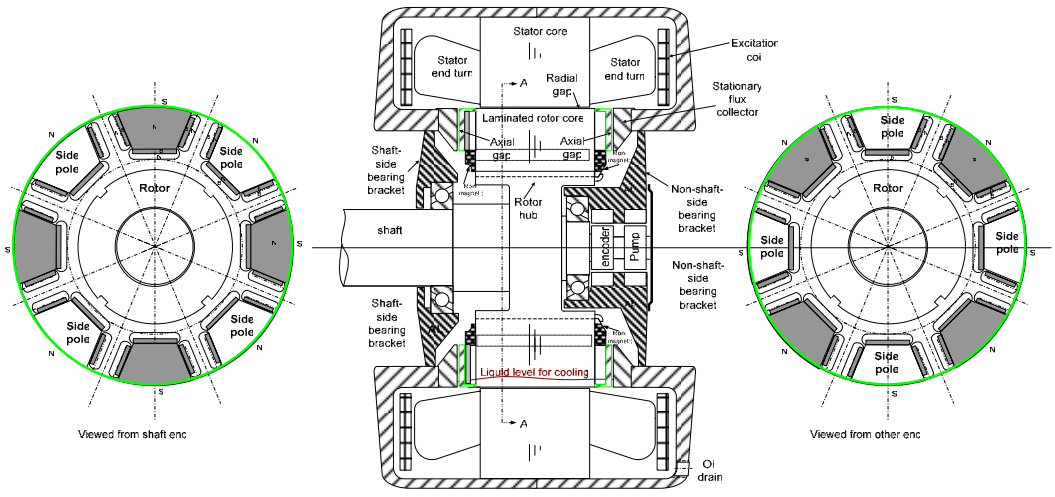

Figure 1. A sample RIPM-BFE prototype machine.

The electro-mechanical simulation was completed on the RIPM-BFE machine. It showed positive results for the overall design characteristics as well as the ability to weaken/enhance the magnetic flux of the machine. The simulations were performed, with a magnet thickness of 0.240 in. Engineering drawings

were completed and sent to both ORNL and outside fabrication facilities for building the prototype machine.

Magnets for the RIPM-BFE rotor were fabricated by vendors outside of ORNL. The rotor laminations were designed to closely match the electro-mechanical simulated lamination design as seen in Figure 2. These laminations were fabricated from 0.014-in.-thick coated silicon steel (29 Ga. M19 C5 non-oriented fully processed). For comparison purposes, the laminations were fabricated with a diameter identical to that of the 2005 Toyota Prius hybrid system (THS II) drive system motor. The rotor inner diameter was modified from that of the Prius in order to incorporate the magnets.

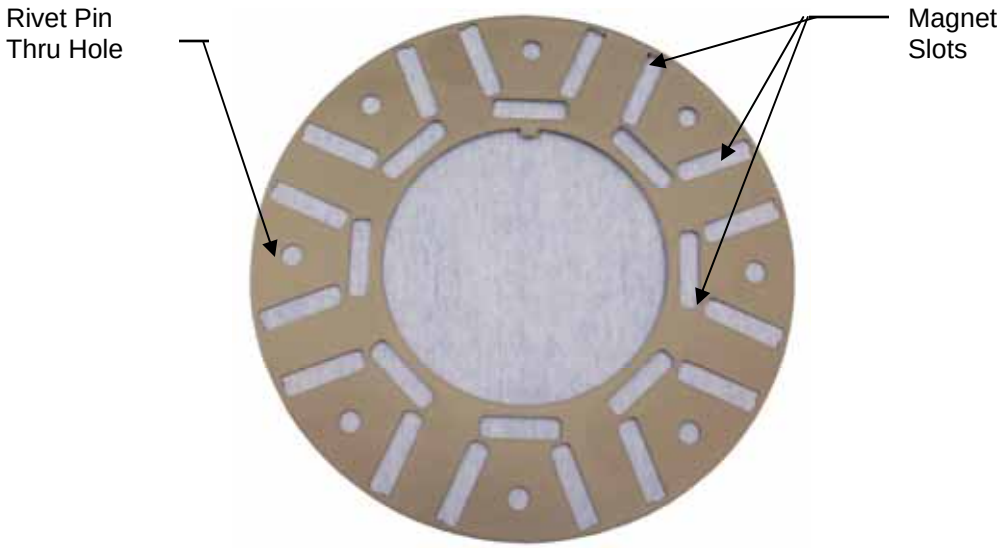

Figure 2. RIPM-BFE rotor lamination.

The stator used in the RIPM-BFE machine is a thinner version of the THS II traction drive motor (see Figure 3). The stator lamination stack was reduced to a final thickness of 2.5 in. The stator was re-wound and inductance and resistance measurements were recorded between each phase of the windings to ensure an electrically balanced stator.

Figure 3. RIPM-BFE stator.

The excitation coils were fabricated at ORNL. Each of the two coils was fabricated from 20-gauge class "H" magnet wire and each contained 880 turns. To check the electrical balance of each coil, a resistive measurement was taken. The coils had a resistance of 19.30 and 19.37 ohms, respectively. Figure 4 shows the finished excitation coils.

Figure 4. RIPM-BFE motor excitation coil.

The rotor laminations were placed over the rotor hub and mechanically fastened to the hub using the aluminum "spider" shown in Figure 5. Non-permanent magnetic pole pieces were placed around each face of the rotor in the spider slots, as shown in Figure 5. Additionally, the laminations were pulled together using the non-permanent magnet pole piece and a rivet-pin that passes through the laminations and is fastened into position with screws and the non-permanent magnetic pole piece. The 0.100-in. pole magnets were placed at the locations shown in Figure 5 and then held in position with the magnet retaining ring (see Figure 6).

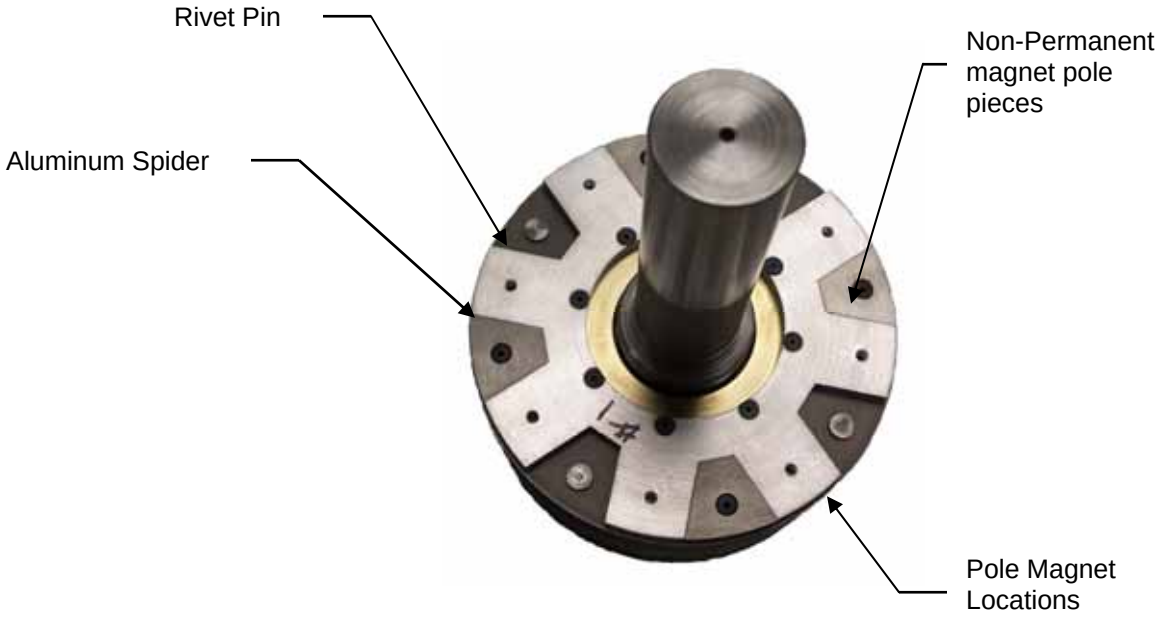

Figure 5. RIPM-BFE rotor.

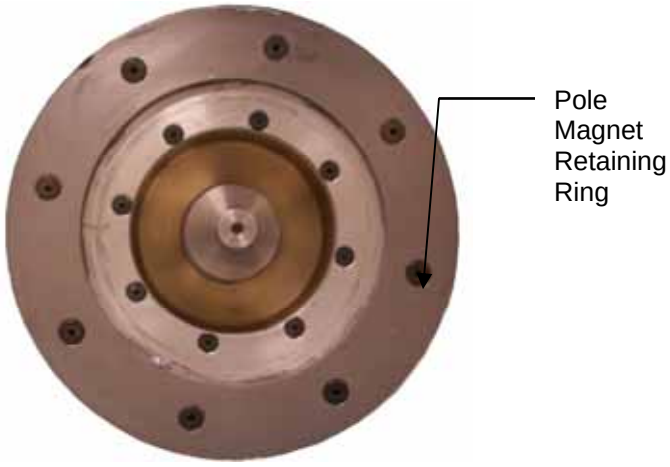

Figure 6. Assembled RIPM-BFE rotor.

The 0.100-in. magnets were placed axially in the lamination slots, and all side pole and axial lamination magnets were fixed in place with Master Bond Supreme 10HT epoxy. The epoxy was baked at 100°C for a minimum of 4 hours to facilitate the curing process, but not at a high enough temperature to permanently de-magnetize the PMs. Once the rotor was assembled, it was returned to the fabrication shop and each face of the rotor was trued. Non-magnetic material was machined and used as a fastening ring and heat-shrunk around the circumference of each of the rotor faces. This ring was used to prevent the pole magnets from being slung out in the event that the epoxy failed during operation. Mechanical measurements were made at each of the eight mechanical fastening positions and recorded. The mean thickness of the assembled rotor was 3.515 in.

The motor housings were assembled with spray rings mounted along the inside diameter at the top edge of both the excitation coil and the stator windings (see Figure 7). These spray rings will enable cooling oil to be pumped through the motor and sprayed directly onto both the excitation coil and the stator windings. The cooling oil will then be gravity-fed to the bottom of the motor and pumped through a heat exchanger.

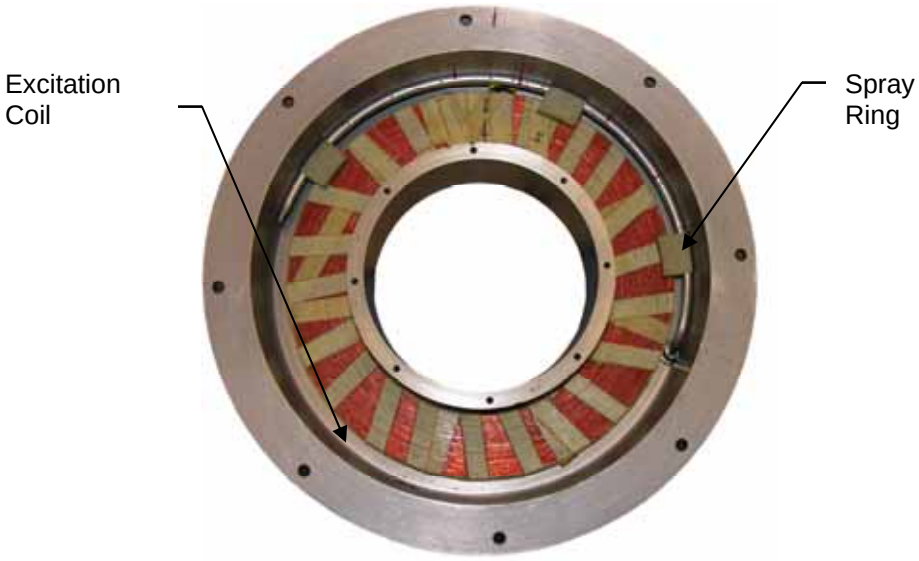

Figure 7. RIPM-BFE motor housing with excitation coil and spray ring.

After the stator and rotor were inserted into the motor housing, the radial gap between the two was measured. A total of 0.028 in. of radial gap was present. Gauss measurements were taken to record the radial air-gap magnetic flux at each stator tooth. These measurements revealed that the rotor magnetism was uniform and all magnets were in their proper orientation. The axial air-gap was measured between the magnetic retaining ring on the rotor face and the motor housing. Each side of the rotor had an air gap of 0.067 in.

The following figures show the comparison of the air-gap flux densities between the ORNL 0.240-in. thick magnet motor without field excitation and the THS II motor. The maximum air-gap flux density of the ORNL motor is 1.27 Tesla, which is 1.63 times the 0.78-Tesla flux density of the THS II. Figures 8 and 9 represent the air-gap flux density of the ORNL RIPM-BFE motor and of the THS II motor, respectively.

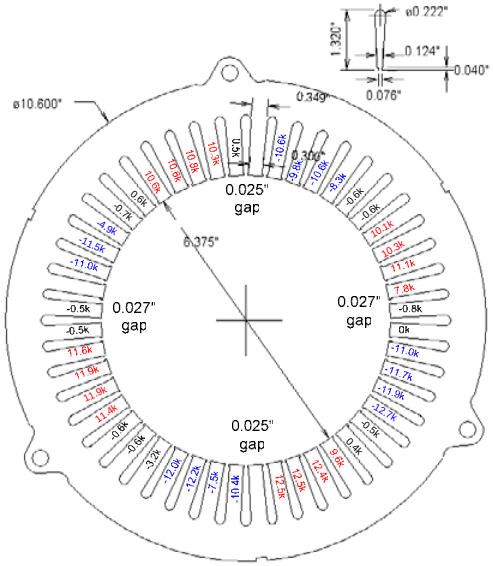

Figure 8. Air-gap flux density distribution of RIPM-BFE 2.5-in. core-length motor.

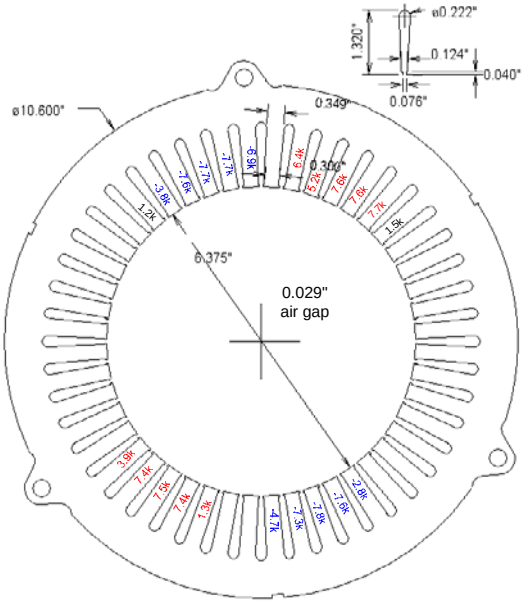

Figure 9. Air-gap flux density distribution of THS II 3.3-in. core-length motor.

As an alternative approach, the motor can be simplified to employ side PMs to produce a strong fixed PM machine without the use of field excitation.

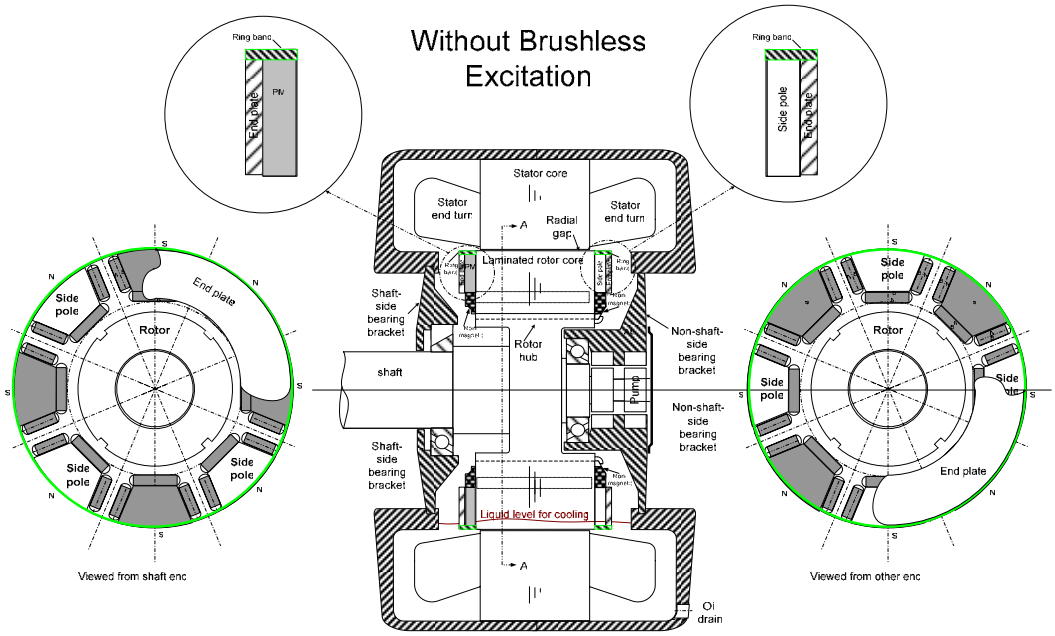

Figure 10. Machine design with side PMs to produce a strong fixed PM machine without field excitation.

Figures 11 and 12 show the locked-rotor torque versus rotor angular position at various field excitations. The tests were conducted at 50, 100, 150, 200, and 250 A.

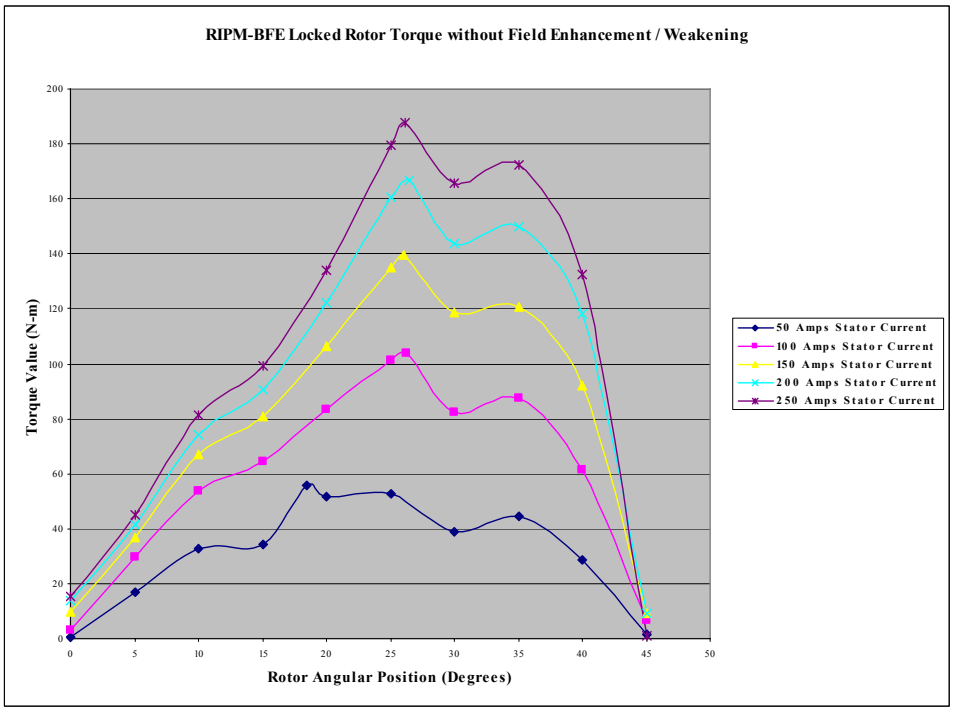

Figure 11. RIPM-BFE locked-rotor torque vs rotor angular position without field enhancement/weakening.

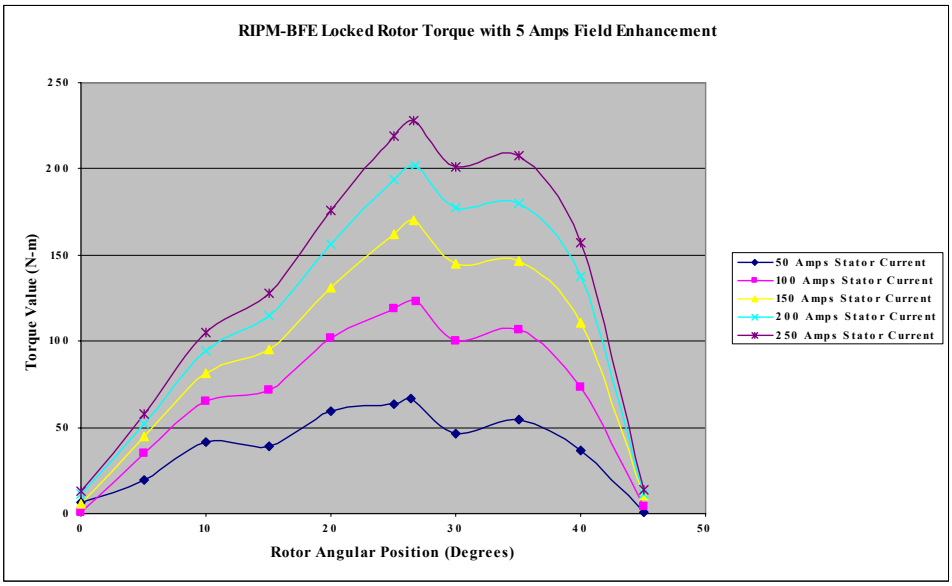

Figure 12. RIPM-BFE locked-rotor torque vs rotor angular position with 5 A of field enhancement.

Figure 13 shows locked-rotor torque comparisons between the 3.3-in.core length Prius motor and the 2.5-in. RIPM-BFE motor obtained through testing. The RIPM-BFE motor produces a stronger PM torque even with a shorter core length, but it has a weaker reluctance torque component, especially at higher currents. This indicates that magnetic saturation may be occurring. Further engineering work can solve this problem through optimization of the design.

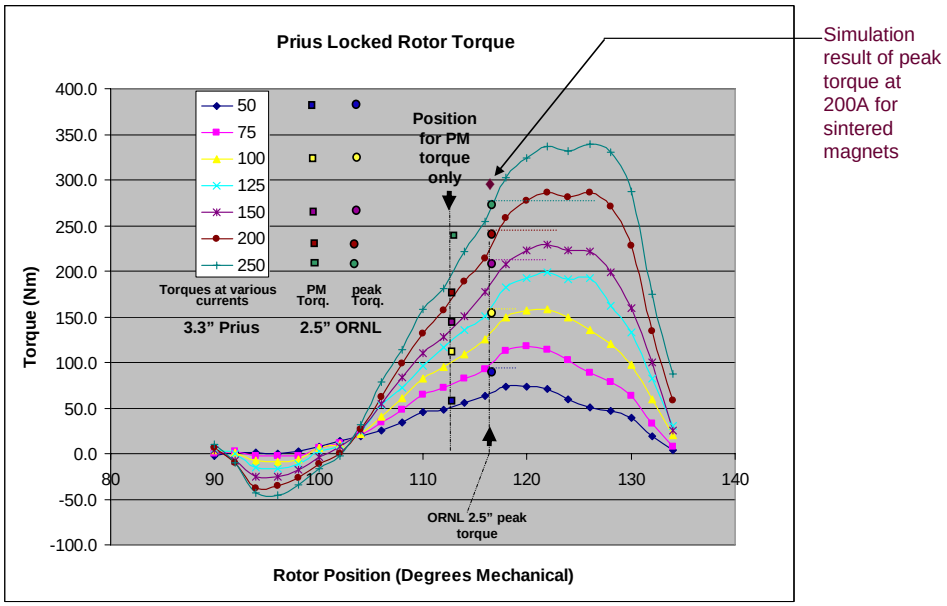

Figure 13. Comparison of PM torque components and peak-torque components between a 2.5-in. ORNL machine and a 3.3-in. THSII machine.

Corona Initiating Voltage for 480-V (rms) Insulation System

Electric power is equal to the product of voltage and current. For a given power, if a higher voltage and lower current are used, the size of the cable and the inverter switching components necessary to carry the current can be reduced. The use of higher voltage also requires higher-quality and thicker electrical insulation that reduces the available slot area for motor windings. One mechanism of insulation breakdown is corona that gradually erodes the insulation and shortens the life expectancy of motors.

Figure 14 shows the corona test setup. A neon transformer with 120–15,000 V per side with the center tap to ground was used to produce high voltages. Smooth sinusoidal utility power was supplied to the primary winding of the neon transformer through a 120-V isolation transformer. An inductor coil wound on a ferrite core was used to sense the corona discharging current. The two terminals of the inductor coil were connected to ground and to the center tap of the high-voltage winding of the neon transformer. The oscilloscope input probes were connected across the inductor to pick up the corona discharging current signals. A current limiter was connected in series with the high-voltage output to protect the high-voltage winding from over-current from the neon transformer. Silicone gel, silicone oil, or high-voltage putty was used to cover all exposed conductors at the non-grounded, high-voltage side to prevent corona produced by the instrumentation setup. After the power to the setup was switched off, an insulated grounding pole was used to discharge any energy stored in the setup before its reconnection. High-voltage gloves and insulation pads were used for protection during the tests.

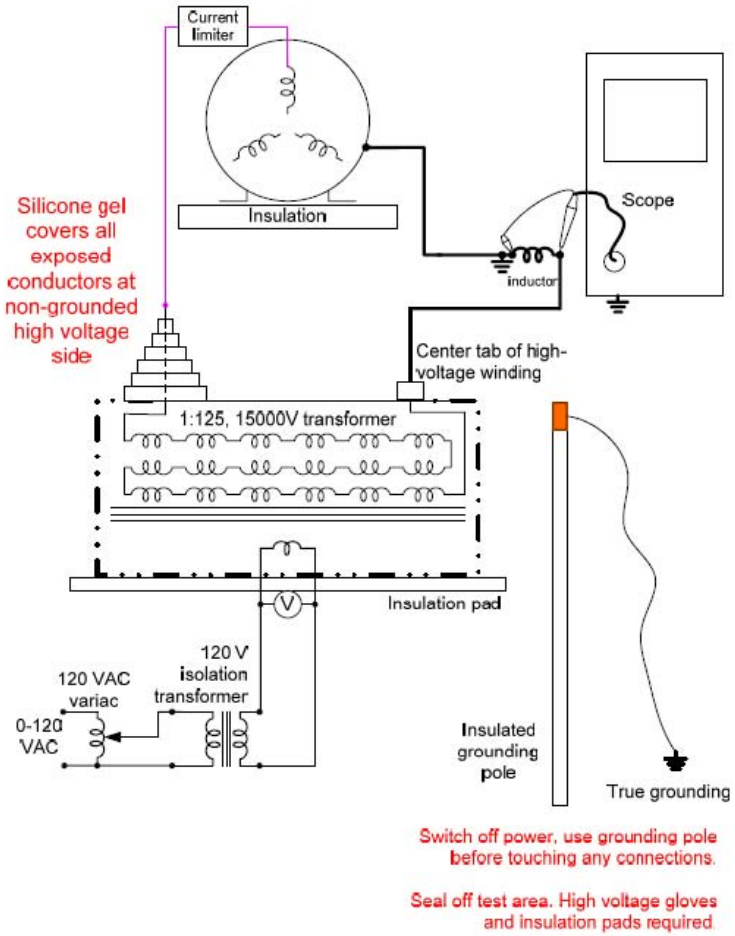

Figure 14. Corona initiating voltage test setup.

To verify that the test setup did not produce a false corona signal before the high-voltage lead was connected to the motor, the high-voltage lead end was covered with high-voltage putty. A clean trace (Figure 15) was observed while the high voltage was adjusted through the range of 0 to 9000 Vrms.

For motors used in electric vehicles and HEVs, the back-emf at high speeds can be higher than the inverter output voltage, causing corona. High-voltage spikes due to inverter switching can also be a source of corona. To determine how high the voltage can be raised for electric vehicle and HEV applications, this investigation establishes the voltage where corona initiates in a National Electrical Manufacturers Association mush-wound stator and an HEV bobbin-wound stator. Table 1 summarizes the test results at 60 Hz. The phase-to-phase corona initiates at only 1638 Vrms for a mush-wound stator (Figure 16). The phase-to-ground (or frame) corona initiates higher at 2650 Vrms. The bobbin-wound

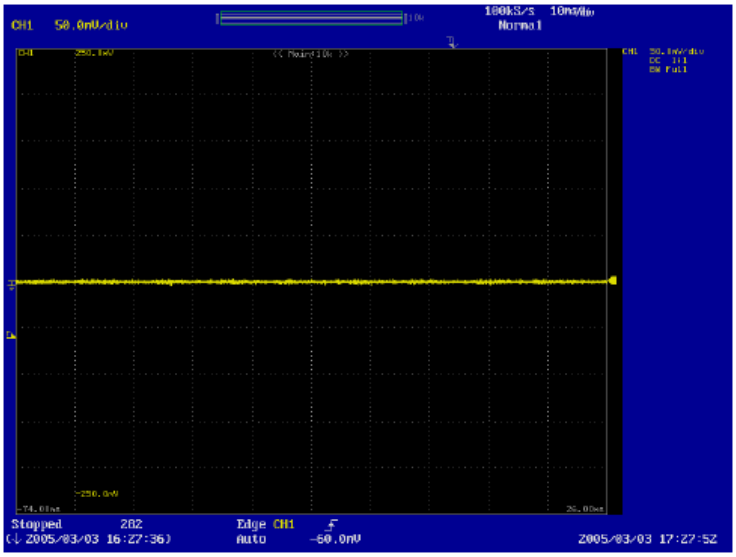

Figure 15. Clean trace without corona from 0 to 9000 Vrms with silicone-sealed lead end.

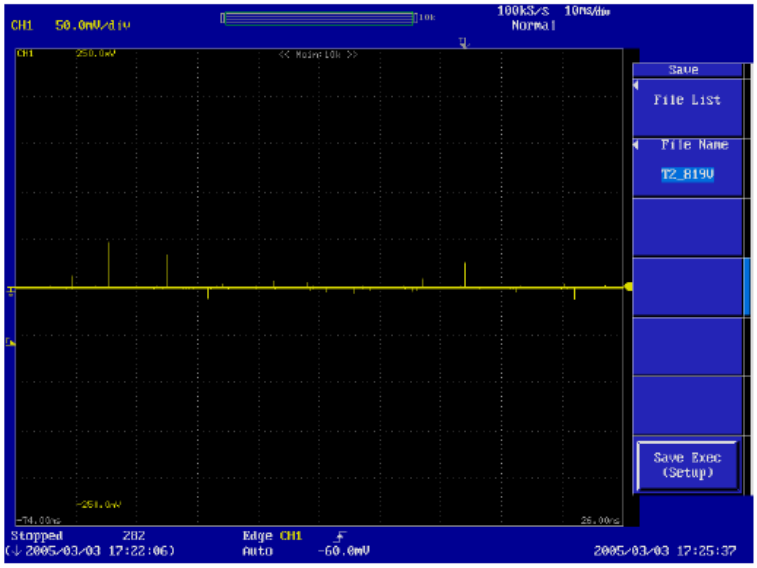

Figure 16. Corona initiating at 1638 Vrms for phase-to-phase and phase-to-ground test.

Table 1. Summary of test results of corona

Winding type		Corona initiating voltage (Vrms)
Mush-wound stator	Phase-to-frame	2650
	Phase-to-phase	1638
Bobbin-wound stator	Phase-to-frame	3176

stator shows slightly better performance than the mush-wound stator with a higher corona-initiating voltage of 3176 Vrms.

It should be pointed out that this corona-initiating voltage is for clean sinusoidal waveforms only. For inverter-fed motors, there are additional voltage spikes due to phase width modulation switching, The voltage where corona initiates would need to be reduced, depending on the magnitude of the spikes. The insulation system of mush-wound winding motors must be carefully examined because its phase-to-phase corona- initiating voltage is low.

Conclusion

The RIPM-BFE motor concept has been proved. Engineering modification of the design is required to optimize the motor performance. The RIPM-BFE motor was simulated and built with a stator core length of 2.5 in., 0.8 in shorter than the 3.3 in. of the THS II stator core. Its back-emf is higher than that of the THS II motor, which is indicative of the enhancement of the air-gap flux density in the ORNL motor. The ORNL PM torque component is slightly higher than that of the THS II motor at all stator current levels. The reluctance torque component of the RIPM-BFE motor is about the same at a low stator current of 50 A. When the stator current increases to 250 A, there is a significant difference between the ORNL motor and the THS II motor reluctance torque components. The RIPM-BFE motor requires further design modification to deal with this saturation issue to achieve a higher-reluctance torque component at high-phase currents.

The RIPM-BFE motor is particularly suitable for short-core-length motors with weak PMs because the axial dc flux produced by the brushless stationary field winding can enter one end of the rotor axially and then distribute in the radial air gap for entry into the stator core. If the core length is long, the radial air gap area per pole can be much greater than the axial area per pole where the axial dc flux enters the rotor. For a given axial flux, the greater the radial area, the lower the radial flux density; hence there will be a weaker influence of the excitation current on the radial air-gap flux density.

The RIPM motor without external field excitation coils demonstrated a technology for increasing the air-gap PM flux density when side PMs are used. The air-gap flux density reached 1.2 Tesla, slightly exceeding the Br of the PMs used in the rotor. This may open a door for further improvement in motor development with RIPM and RIPM-BFE motors.

Test results for corona-initiating voltages for mush-wound and bobbin-wound windings were experimentally obtained. On the basis of the corona tests, for high-voltage motor designs, the insulation system, especially for mush-wound windings, needs to be closely examined because of low phase-to-phase corona-initiating voltages.

Future Direction

The drive motor is an extremely important component in either a fuel-cell vehicle or an HEV. From a systems perspective, motor research must take all the components of the drive system into consideration. The RIPM-BFE motor was developed to simplify the boost requirement and to offer the possibility of using weaker and cheaper PMs. Other system issues still need to be examined; for instance, batteries

supplied by foreign manufacturers for HEVs cannot meet the demands of U.S. car makers. Motor designs that lower the demand on the batteries could be an important research area.

Further engineering optimization of the RIPM-BFE motor design is necessary to overcome magnetic saturation issues. This motor is particularly suitable for a short-core-length machine that can significantly transfer the axial-direction flux produced by the brushless field excitation coil to the radial air-gap flux. Designs using this motor technology have the potential to use weaker, less costly PMs. Future designs that assess the feasibility of using injected, bonded magnets in this machine and higher-speed motors may very well yield less costly motors with higher performance capabilities.

A new concept for a motor design with side magnets can provide a machine with a stronger fixed PM air-gap flux density. This technology can be used in either the RIPM-BFE or the RIPM motor and can result in a higher PM air-gap flux density for both strong and the low-cost weak magnets.

Patents

The available ORNL patents and patents pending on the RIPM-BFE machine and the HSUPM machines are as follows:

- "High Strength Undiffused Brushless Electric Motors and Generators," U.S. Patent 6,573,634, June 3, 2003.
- "Hybrid-Secondary Uncluttered Induction Machine," U.S. Patent No. 6,310,417, October 30, 2001.
- "Simplified Hybrid-Secondary Uncluttered Induction (HSU-I) Machine," U.S. Patent 6,891,301, May 10, 2005.
- "Hybrid-Secondary Uncluttered Permanent-Magnet (HSU-PM) Machine," patent pending no. 10/706,577.
- "Improvements on High Strength Undiffused Machine," patents pending nos. 60/675,419, and 11/162753.
- "HSUB Reluctance Machine," patent pending no. 11/019,075.
- "Compact HSUB Electric Motor/Generator," patent pending no. 10/848,450.
- "High Slot Utilization Systems for Electric Machines," patent pending no. 0813-01-100305.
- "Motor with Low Battery Requirement," patent pending No. 1636-01-100405.

3.3 Advanced Traction Motor Development (RFP)

Principal Investigator: Sam Nelson
Oak Ridge National Laboratory
National Transportation Research Center
2360 Cherahala Boulevard
Knoxville, TN 37932
Voice: 865-946-1327; Fax: 865-946-1262; E-mail:neslonsscjr@ornl.gov

DOE Technology Development Manager: Susan A. Rogers
Voice: 202-586-8997; Fax: 202-586-1600; E-mail: Susan.Rogers@ee.doe.gov

ORNL Program Manager: Mitch Olszewski
Voice: 865-946-1350; Fax: 865-946-1262; E-mail: olszewskim@ornl.gov

---

Objectives

The objective of this task is to develop advanced traction drive motors that would not readily be pursued by industry alone because of high risks and uncertain or long-term outcomes. The overall objective is to design, develop, fabricate, deliver, and test advanced traction drive motors that will meet the 2010 FreedomCAR goals and traction motor technical targets. The goal of this task is to develop an advanced traction drive motor with improved motor torque capability as well as improved efficiency and power density and reduced cost.

Approach

A solicitation was developed with qualification requirements for the potential offerors, including goals and specifications (i.e., efficiency, power density, torque, minimal speed requirements) for development of an advanced traction drive motor. A survey was made of potential traction drive motor developers, and a request for proposals (RFP) was sent to potential bidders. The proposals received from traction drive motor bidders were studied and evaluated based on (1) technical approach, (2) corporate experience, (3) personnel qualifications, and (4) project management. The proposal with the greatest value and with the lowest risk for the development of advanced traction drive motors was selected by the evaluation team.

Phase 1 of the task is to perform the research and development (R&D) required, resulting in a design for an advanced traction drive motor. Phase 2 of the task is to fabricate and deliver for test and evaluation an advanced traction drive motor in accordance with the specifications presented in the solicitation.

Major Accomplishments

A solicitation was issued to traction drive motor suppliers to determine their interest in developing advanced traction drive motors that will meet 2010 FreedomCAR goals and specifications. The RFP was issued on February 18, 2005, with an initial closing date of March 30, 2005. The RFP resulted in the receipt of four proposals, none of which met all of the qualification criteria. The RFP was amended on June 7, 2005, to modify the qualification criteria with a June 14, 2005, closing date. The amendment did not result in any additional proposals, but three of the proposals met the revised qualification criteria. Site visits were made to each offeror to gain additional information about the proposals and the offeror's capabilities. An evaluation team report was prepared documenting the assessment of each proposal. A Phase 1 contract was awarded in August 2005 to UQM Technologies, Inc., to design an advanced traction drive motor.

Technical Discussion

Oak Ridge National Laboratory (ORNL) motor scientists are being used during the procurement and performance period of this task to enhance and complement the supplier's technical capabilities. This task included the development of a solicitation with specifications and goals for the advanced traction drive motor. The advanced traction drive motor is to have a 30-kW continuous and 55-kW peak power capability. The motor is to have a constant power speed ratio (CPSR) of 5 with a minimum top speed of 10,000 rpm and an efficiency of 93% from 10 to 100% of rated speed at 20% of rated torque. An RFP was issued, and a variety of traction drive motor design technologies were proposed by the offerors. The designs were evaluated, and the design that was considered by the evaluation team to have the greatest value and lowest risk for advanced traction drive development was selected.

Phase 1 design activity was initiated in August by UQM Technologies of Golden, Colorado. To date, the design process has focused on creating parametric models of the Prius motor geometry and verifying the results with ORNL test data for the Prius. The Prius dimensions and material properties parameters have been entered into the models, auto-generated, and solved for back–electromotive force (EMF) waveform shapes and amplitude. Inductance models for the Prius have also been created and solved. The custom element mesh for the parametric Prius-style model is shown in Figure 1, along with the no-load flux distribution.

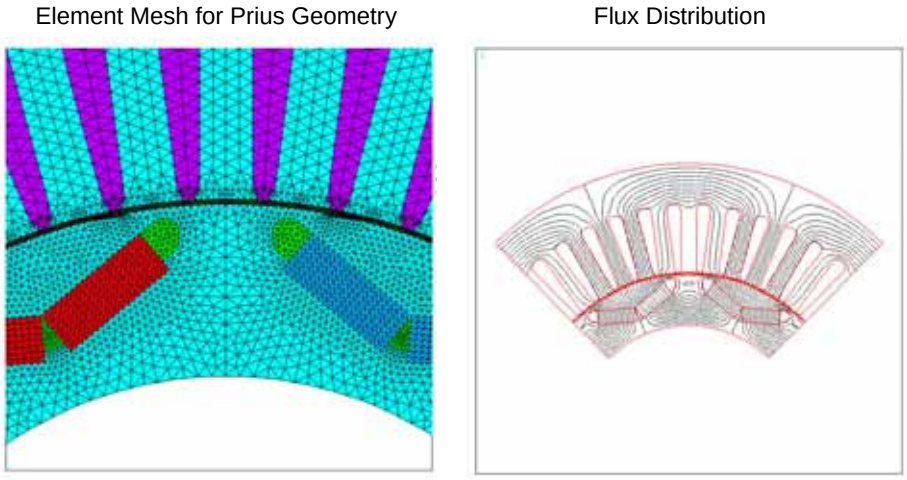

Figure 1. Element mesh for Prius geometry and flux distribution.

The back-EMF waveform and magnitude can be calculated accurately by solving for the flux distribution at several different rotor angles. The back-EMF waveform predicted by finite element analysis for the Prius motor is illustrated in Figure 2. The predicted back-EMF constant for the Prius motor was 140.5 V_{LL}/krpm, which correlated closely with the measured results from ORNL, 141.7 V_{LL}/krpm.

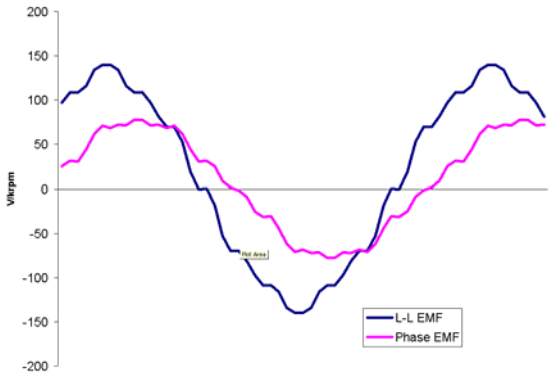

Figure 2. Predicted back-EMF waveform of the Toyota Prius traction drive motor.

Conclusion

ORNL motor scientists will work closely with UQM Technologies during the R&D tasks associated with the design of the traction drive motor. Phase 1 will involve detailed analysis and design, a cost study, and the analysis of potential processes, materials, configurations, and manufacturing methods that will meet the requirements for an advanced traction drive system that will meet the solicitation specifications and the 2010 FreedomCAR goals.

Future Direction

During FY 2006, this task will result in the development of an advanced traction drive motor design. The progress and merits of the Phase 1 design activity will determine if a Phase 2 task is funded. A Phase 2 task would require the fabrication and delivery of a prototype traction drive motor system for test and evaluation.

3.4 Development of Improved Powder for Bonded Permanent Magnets

Principal Investigator: Iver E. Anderson
Metallurgy and Ceramics Program
Ames Laboratory, Iowa State University
Ames, IA 50011
Voice: 515- 294-9791; Fax: (515) 294-8727; E-mail: andersoni@ameslab.gov

DOE Technology Development Manager: Susan Rogers
Voice: (202) 586-8997; Fax: (202) 586-1600; E-mail: susan.rogers@ee.doe.gov

ORNL Program Manager: Mitch Olszewski
Voice: 865-946-1350; Fax: 865-946-1262; E-mail: olszewskim@ornl.gov

---

Contractor: Ames Laboratory, Iowa State University, Ames, Iowa
Prime Contract No.: W-7405-Eng-82

Objectives

- Increase the maximum operating temperature from 120 to 200˚C while maintaining desirable magnetic properties of permanent magnet (PM) materials to enable electric drive motors with improved operating characteristics.
- With goal of cost reduction for the new high temperature PM materials in electric drive motors, develop improved processing for bonded isotropic magnets produced by net-shape molding technologies for high-volume manufacturing.

Approach

- Develop innovative permanent magnet alloy design and processing technology for production of improved PM alloy powders for bonded isotropic magnets with a tolerance for high temperatures.
- Investigate PM alloy design improvements through melt-spinning methods, with the specific goal of developing an improved spherical magnet alloy powder through gas atomization processing.
- Develop an enhanced gas atomization process and a gas-phase powder surface reaction capability for simplified production and environmental protection of fine spherical powder for isotropic bonded magnets.
- Conduct experimental isotropic permanent magnet molding trials on as-atomized and annealed magnet powders to characterize isotropic bonded magnet properties and microstructures in collaboration with industrial partners, e.g., Arnold Magnetic Technologies (AMT) and Unique Mobility (UQM) and research partners, e.g., ORNL.

Major Accomplishments

- Developed a new TiC addition to MRE-Fe,Co-B to enhance glass forming ability and temperature stability in an improved PM alloy (WT-096) with elevated remanence and energy product at ambient temperature.
- Achieved a cross-over temperature of 125C (well below the expected operating temperature maximum of 180-200C) for superior maximum energy product, comparing the latest alloy design (WT-096) in melt spun ribbon to the best commercial ribbon (MQP-14-12).

- Completed industrial validation of the enhanced Ames magnet alloy (WT-096) in melt spun ribbon/flake particulate form by commercial production (by Magnequench International) of 100kg of annealed particulate, which achieved 96% of the maximum energy product of the laboratory ribbon magnetic properties, 11.6MGOe.
- Developed a combined Zr and TiC formulation for the MRE-Fe,Co-B magnet alloy (WT-102) by melt spinning that has desirable phase nucleation and temperature stability properties at low wheel speeds in the on-going effort to translate these new PM alloys to gas atomization processing of fine spherical powders to gain additional advantages for net-shape bonded magnet molding.
- Completed the first successful gas atomization trial of the Zr + TiC modified MRE-Fe,Co-B magnet alloy (WT-102) in the research scale atomization system after several stages of process method development, but post-process chemical analysis indicated that the intended levels of Zr and B were not reached, which compromised the resulting magnetic properties.
- Utilized an expanded industrial partnership with Arnold Magnetic Technologies (AMT), a major commercial manufacturer of bonded isotropic magnets, to confirm the improved environmental stability of compression molded (PPS bonded at Ames Lab) magnets made from improved Ames flake particulate (WT-076) after fluorination, compared to similarly bonded magnets made from commercial PM particulate.
- Provided the first of two sets of net-shape isotropic bonded magnet samples to ORNL for testing in their experimental electric motor system and in other magnetic characterization devices.

Technical Discussion

Introduction

To meet the cost and performance objectives of advanced electric drive motors for automotive applications, it is essential to improve the alloy design and processing of permanent magnet powders. This work is critical to enable the widespread introduction of electric drive automobiles, generally referred to as hybrids or fuel cell vehicles, a key technology goal of the President of the US and the US Department of Energy. Two primary objectives to be pursued for PM materials are: (1) to increase the useful operating temperature for magnets to 200˚C and (2) to reduce the finished magnet cost to a practical level, considering motor design improvements. Currently, high performance anisotropic sintered magnet material can operate with high torque in an electric motor at temperatures ranging up to about 120˚C, and the finished cost of anisotropic sintered magnetic material is approximately $90/kg. Difficult motor assembly procedures and the need for corrosion protection (by surface coatings) also add to the cost for PM motors made from sintered anisotropic permanent magnets. As an alternative PM material form, polymer-bonded isotropic particulate magnets offer the benefit of greatly simplified manufacturing and improved (polymer encapsulation) corrosion protection, but at a more moderate level (about 15-25% of anisotropic sintered magnets) of stored magnetic energy, that are compatible with advanced alternative PM motor designs. However, to exploit the potential of bonded isotropic PM materials for such motors, it is necessary to develop a particulate magnet material with high-temperature properties that can be loaded to a high volume fraction in an advanced polymer binder. Improving materials and processing to allow for increased operating temperature and simplified production of net-shape bonded isotropic magnets by gas atomization and injection molding will be a significant advance toward mass production of advanced electric drive motors at reduced cost.

Approach

Melt spinning methods will continue to be used for efficient screening of magnet alloy design modifications, using parameters that simulate the quenching rates accessible during gas atomization, the desired spherical powder processing method. A major aspect of the project is the refinement of our design strategy for a family of novel MRE-Fe-B magnetic alloys (MRE = mixed rare earth, e.g., Y, Dy,

Nd) to increase the remanence and energy product at ambient temperatures for isotropic PM material while maintaining superior temperature coefficient values to 200˚C, with commercial isotropic flake particulate properties as benchmarks. The coupling of this melt spinning work with an increased number of gas atomization trials will accelerate the pace of specific alloy design for the rapid solidification of fine spherical powders. It was this stronger coupling of melt spinning and gas atomizing experiments that guided the alloy design model from MRE-Fe-Co-B-Zr to MRE-Fe-Co-B-TiC (WT-096) and, most recently, to the MRE-Fe-Co-B-TiC-Zr (WT-102) composition that was established for use in the current gas atomization experiments. Our recent composition refinements also included major enhancement of the ratio of Y and Dy to promote increased remanence. Additional adjustments of the B level and the substitution of alternative refractory metal elements for Zr and the carbide phase, currently TiC, are all in the latest plans to fine-tune the balance between quenchability and nucleation of 2-14-1 phase for maximum impact on as-solidified magnetic properties in spherical powders. Of course, the importance of magnet alloy development for PM drive motors that can see high temperatures drives continued emphasis on retention of sufficient magnetic properties in fine spherical powders at temperatures up to 200˚C.

Comprehensive characterization of closely-related gas atomized and melt spun samples of a variety of promising MRE-Fe-B compositions will be continue as a strong emphasis in both as-solidified and annealed states. The initial magnetic characterization at both ambient and elevated temperatures will be followed by x-ray diffraction and calorimetric characterization on all new samples. In addition, the bulk property measurements will be enhanced by additional microstructural observation with SEM, TEM, and 3-D atom probe (at HTML) to gain critical understanding about the product phase morphologies and spatial distributions that give rise to differences in as-solidified properties and in annealing response. After achieving enhanced understanding of the microstructural basis for the improved temperature stability of the magnetic properties of MRE-Fe-B-TiC alloys, we will now be exploring the means (by alloying) to enhance nucleation of the 2-14-1 phase in the interior of atomized particles. Our overall goal is to explore the generality of MRE-Fe-B alloy rapid solidification behavior during gas atomization that minimizes glass formation and allows annealing to be avoided, because of the potential processing simplification advantage that can lead to reduced costs for bonded magnet production.

Recent receipt of the large (100kg) batch of annealed, flake particulate made from our improved MRE-Fe-Co-B-TiC alloy (WT-096) opened the door to greatly expanded bonded magnet testing at this stage in the program, particularly focused on environmental effects at elevated temperature and on extensive development of a protective coating for this type of particulate. Thus, many more samples can be made for sharing with our industry and research collaborators, as well as for testing in our own magnetometer systems. To this end, the compression molding process will be streamlined to permit generation of increased numbers of bonded magnet samples with conventional (about 60%) loading from a PPS binder blended with experimental and commercial PM powders to facilitate increased comparisons with benchmark magnetic properties. This work requires production of multiple heated die sets. This up-scaling work will also address the batch size of the current fluidized bed coating processes, specifically intended to process the flake particulate that is now available. In these studies, the fluidized bed fluorination process will be refined for the available flake particulate to optimize the coating barrier properties for protection of PM powders during the magnet molding process and bonded magnet use. This oxidation and corrosion protection is needed both during the injection molding process and for sustained magnetic properties during bonded magnet use. Thus, it is necessary to improve the reaction parameters to develop an optimum surface film thickness to enable the full passivation potential to be achieved for the new bonded magnets. As previously demonstrated, the powder surface film will be characterized by air oxidation tests coupled to Auger electron spectroscopy and microstructural analysis. Bonded isotropic magnet samples from commercial and experimental atomized powders will be provided to our industrial partner to compare the effect on reversible and irreversible magnetic loses on experimental powders with an improved coating to losses in commercial powder, using ambient and elevated temperature exposures. Since the flake particulate is already in a fully annealed state from the vendor, the immediate up scaling

of the powder annealing capability is not needed. Also, significant portions (multiple kg's) of the as-received flake particulate of WT-096 will be shared with AMT, our industrial partner who is highly skilled at conventional fabrication of bonded magnets that will be tested in experimental PM motor systems both at our research partner, ORNL, and at a new industrial partner, Unique Mobility (UQM). Some time will need to be committed to coordinating this partnership to help advance the development of motors that are specifically intended to exploit the beneficial properties of bonded magnets. AMT may also modify of the particulate conditioning, compounding and molding parameters with our particulate to enhance volumetric loading and to explore the parameter space for PPS molding. These results on generic motor part molding should be useful for eventual application in specific motor fabrication projects with USCAR partners.

Enhancement of the process scale of gas atomization is highly desirable to produce prototype fine spherical powder batches for injection molding process development in collaboration with an industrial partner. As described in the first section of the Approach, a reasonably optimized alloy may be available, but another factor still must be developed and verified to enable production of these modified MRE-Fe-B alloys as fine powder in our 5X scale gas atomization system. This factor is adaptation of the fluorination process or another type of surface reaction/passivation approach for in situ treatment during the high-pressure gas atomization process to reduce the hazard and oxidation losses that are typical for powders with high surface area of this type of RE alloy. Our passivation process development will build on the results of our post-atomization fluidized bed coating experiments and will be extended to provide in-situ coating capability during the gas atomization process, using the atomization spray chamber of our research gas atomizer as a reaction vessel and the dispersed, high temperature state of the as-atomized powder spray as a natural fluidized (turbulent) state. The ability to modify the surface film and enhance the protective characteristics of the surface modified powder will be explored initially using the downstream addition of an NF^3-Ar gas mixture. The proper downstream location was determined by analysis of multiple process temperatures within the research atomizer chamber and by consideration of the spray chamber flow patterns and dynamic thermal conditions. As previously demonstrated, the powder surface film will be measured by powder oxidation tests coupled to Auger electron spectroscopy and microstructural analysis. In addition, flammability and explosivity testing will also be conducted on the passivated powder samples by an outside vendor. Bonded isotropic magnet samples from these in situ passivated atomized spherical powders will be provided to our industrial collaborator, AMT, to compare the reversible and irreversible magnetic loses of these experimental powders to losses in commercial spherical powder (if available), using ambient and elevated temperature exposures. If sufficient hazard reduction (to a "moderate" explosivity rating) can be achieved, the larger scale atomization system will be employed to produce prototype spherical powder batches that can be used for experimental injection molding trials at AMT.

Results

After some experimentation, the prototype alloy for MRE-Fe-B alloys, where MRE = Y + Dy in equal atomic ratio, was produced as a spherical gas atomized powder batch (BT-4-204). The microstructure of this spherical powder has recently been re-examined in detail because of the desirable magnetic properties that were developed (and previously reported). It was anticipated that the type of solidification pattern that resulted from rapid solidification of this simplified mixed rare earth alloy in gas atomized droplets could serve as a model for comparison with the current more complex alloys that have greater remanence, energy product, and temperature stability in ribbon form, but not as spherical powders. To this end, the two micrographs in Fig. 1 show the cross-sections of similar sized powder particles from BT-4-204 in a polished/etched condition in the SEM (Fig. 1a) and in a thin foil in the TEM (Fig. 1b). Both micrographs display a "rim and core" structure that is typical of this fine/moderate size of spherical powder. This structure is indicative of the rapid solidification pathway followed by these alloy droplets where the rim solidifies first and severely restricts the convective cooling rate of the remaining liquid in

the core. In this case, the lack of complex alloy additions allows the core region to nucleate a fairly coarse grained structure of the 2-14-1 phase, with a resulting decrease in the magnetic properties, below the optimum.

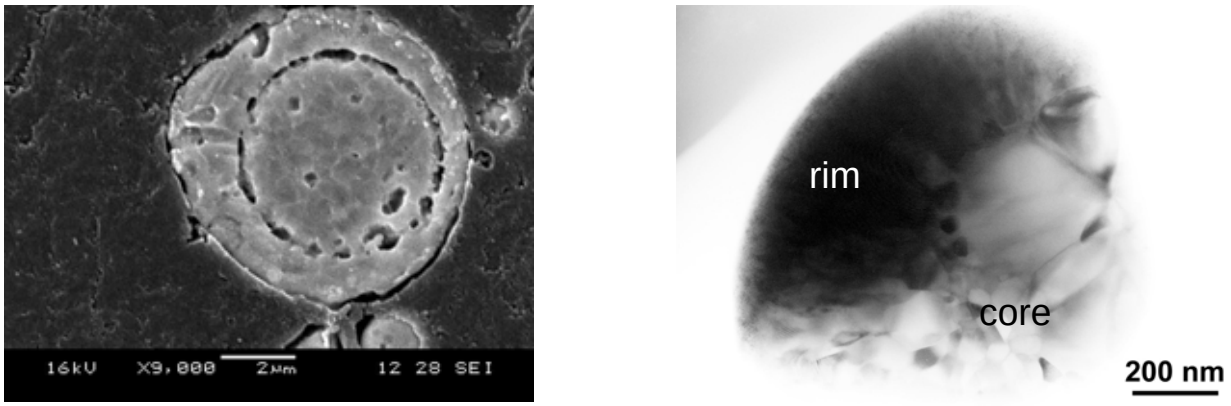

a) b)

Figure 1. Typical microstructures from the BT-4-204 powder batch showing a) an SEM micrograph of a 25-38µm particle in cross-section, and b) a TEM micrograph of a 10-20µm particle from a thin foil specimen.

Using a melt spinning approach and starting from the equi-atomic level of Y and Dy in the prototype $YDyFe_{14}B$ magnetic phase composition, results have shown that a significant substitution of Nd (x = 0.45-0.50) can enhance the remanence and energy product at ambient temperatures, as reported previously. Building from these result, the minor increase in temperature sensitivity (when the MRE contains Nd) was suppressed by elevation of the Curie temperature with minor Co substitutions for Fe of less than 12 at.%. Since these PM alloys in the as-solidified form required annealing to develop optimum magnetic properties, the alloys needed a slight enrichment in the MRE level above stoichiometry to develop a small amount of secondary phase to help stabilize the microstructure during annealing. Thus, the $(Y\text{-}Dy\text{-}Nd)_{2.2}(Fe\text{-}Co)_{14}B$ alloy design that resulted from the experimentation last year was the starting point for further modification for improved quenchability and high temperature stability during this year by the addition of TiC. The outcome of the TiC experiments resulted in an enhanced alloy considered to have reached a reasonable stage of development for comparison (as melt-spun/annealed/chopped flake particulate) to the best commercially available microcrystalline, isotropic PM alloys that are intended for high temperature service. Figure 2 compares the temperature dependence of the WT-096 ribbon to the available data from two similar commercial magnet alloy ribbons (the data overlaps), where all samples were annealed to an optimum

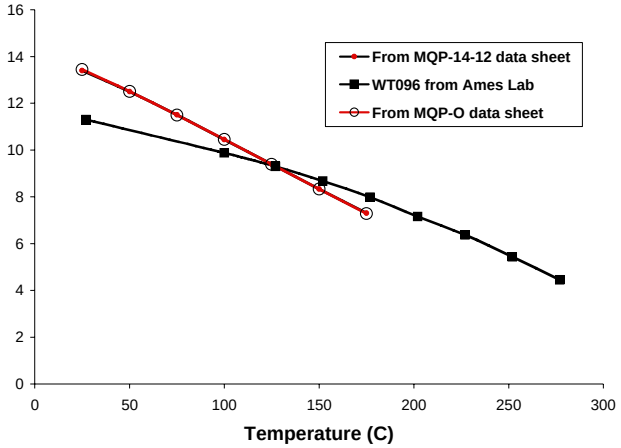

Figure 2. Comparison of temperature dependence of maximum energy product for an alloy design from this project and two commercial alloys that are intended for high temperature use.

condition. It can be seen from Fig. 2 that we have achieved a cross-over temperature of 125C (well below the expected operating temperature maximum of 180-200C) for superior maximum energy product, comparing the latest alloy design (WT-096) in melt spun ribbon to the best commercial ribbon (MQP-14-12).

As a logical step in the march toward implementation of our magnet alloy design for use in high temperature applications, e.g., drive motors in hybrid vehicles, it was decided to have a prototype quantity, 100kg of flake particulate made by the worldwide leader in this technology, Magnequench International. At the end of this fiscal year, the industrial validation of the enhanced Ames magnet alloy (WT-096) in melt spun ribbon/flake particulate was completed following shipment (by Magnequench International) of 100kg of annealed particulate (MQP-11HTP). Figure 3 shows that this commercially produced product achieved 96% of the maximum energy product of the laboratory ribbon magnetic

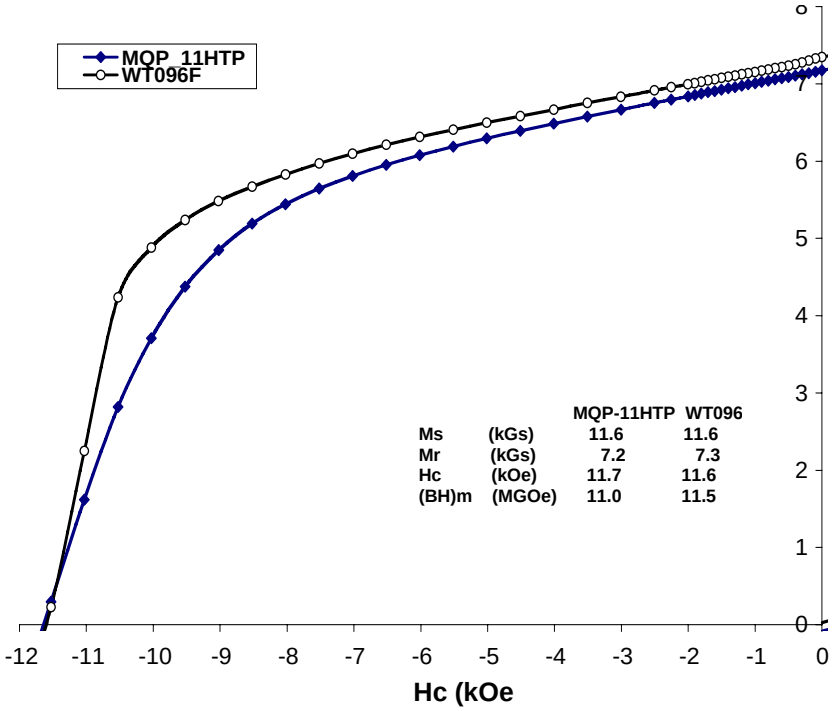

properties, 11.5MGOe.

Figure 3. Second quadrant SQUID magnetization curves from the laboratory produced (WT-096) and commercially produced (MQP-11HTP) ribbon flake of the MRE-Fe-Co-TiC alloy that resulted from this project.

Although very useful for a full series of very important experiments, including several industrial interactions that were mentioned in the Approach section, the final objective of this project includes the translation of the alloy from processing by melt spinning to processing by gas atomization, to exploit the advantages for bonded magnet molding that follow from a fine spherical powder morphology. To make this translation possible it was decided to utilize the potent nucleation effect of Zr for the 2-14-1 phase (reported last year) along with the advantages for quenchability and high temperature stability of TiC. Thus, we developed a combined Zr and TiC formulation for the MRE-Fe,Co-B magnet alloy (WT-102) by melt spinning experiments. As intended, Fig. 4 reveals that this alloy has desirable phase nucleation and temperature stability properties at low wheel speeds (simulating gas atomization processing) and a very minor amount of glass formation in the as-spun condition, detected as the sudden but small dip in magnetization in the second quadrant of this magnetization loop..

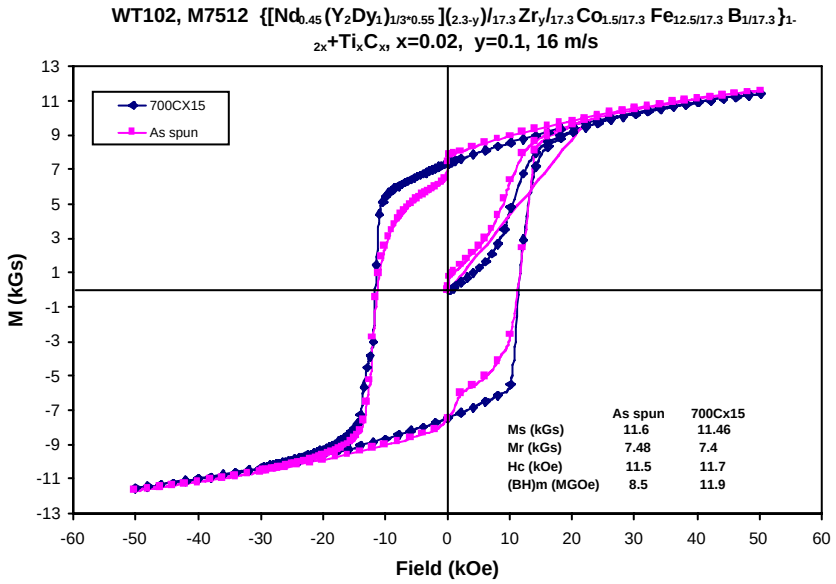

Figure 4. SQUID magnetization/demagnetization loop for the WT-102 alloy ribbon.

After encountering several problems during experimental gas atomization trials, we redesigned the method and materials and were able to complete the first successful gas atomization trial of the Zr + TiC modified MRE-Fe,Co-B magnet alloy (WT-102) in the research scale atomization system toward the end of the current fiscal year. While an operational success at producing a high yield of fine spherical powders, SQUID magnetometer measurements of size classified powders from the batch revealed disappointing magnetic properties. The most likely reason for the lack of correspondence to the previous melt spun ribbon results was revealed by post-process chemical analysis (see Table 1.) that indicated lower than intended levels of Zr and B, which compromised the resulting magnetic properties.

Table 1. Summary of compositional analysis (labeled "NSL") of recent powder batch

	GA1-52, -20 um		
	Starting	**NSL Analysis**	**Target**
Y	6.68	5.84	6.47
Dy	6.11	6.4	5.92
Nd	13.3	13.71	12.88
Co	7.91	8	7.98
Fe	62.18	62.2	63
Zr	0.82	0.53	0.82
Ti	1.55	1.59	1.56
C	0.39	0.39	0.39
Si	0.05		
B	1.044	0.89	0.98

Utilizing an expanded industrial partnership with Arnold Magnetic Technologies (AMT), a major commercial manufacturer of bonded isotropic magnets, experiments were performed to test the degradation of total magnetic flux due to exposure to elevated temperatures. The tests, called STILT at AMT, were conducted at each increment of temperature elevation in a sequence that proceeded to 200C to detect the total reversible and irreversible flux loss due to exposure to an ambient environment. The last step in the test is to re-magnetize each bonded magnet to observe the residual loss or total irreversible loss. As Fig. 5 shows, the PPS bonded magnet sample made from fluorinated flake particulate of a previous Ames MRE-Fe-Co-B-Zr alloy (WT-076) was tested against an unfluorinated version of the same PPS bonded alloy (only to 150C), a commercial PPS bonded particulate and two other epoxy bonded samples. Polyphenyl-sulfide (PPS) was selected previously as the most suitable polymer for the high operating temperatures and stress levels that are anticipated in eventual vehicle applications. The results confirm that the improved environmental stability of compression molded (PPS bonded at Ames Lab) magnets made from improved Ames flake particulate (WT-076) after fluorination, compared to similarly bonded magnets made from unfluorinated experimental alloy particulate and commercial PM particulate. However, it should be noted that the commercial sample (Nd-Fe-Nb-B) bonded in PPS had a very similar irreversible loss (about 0.5%) after re-magnetization, indicating some reasonable resistance to oxidation and corrosion.

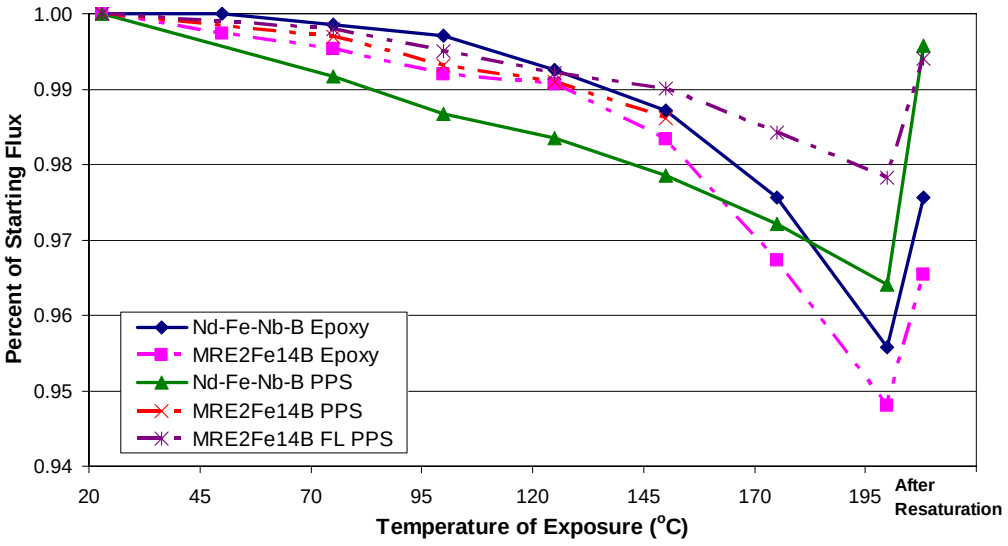

Figure 6. STILT test results performed on several types of bonded magnet samples at AMT.

As mentioned in the Approach section, one advantage of obtaining a large batch of flake particulate made from our most advanced melt spinning composition, MRE-Fe-Co-B-TiC (WT-096), is that much of it can be used to perform independent application testing. One of the most important types of application testing involves the special bonded magnet shapes in experimental electric motors, as an method to test new motor concepts with a magnet type that is suitable for large-scale manufacturing. To meet this objective, a procedure was devised in consultation with AMT to permit flake particulate to be compounded with PPS, injection molded into rectangular blocks, and machined by AMT into magnet segments for ORNL. ORNL will fasten the PPS bonded magnets into an experimental motor, modified for high temperature operation, and test the motor operating characteristics over a wide temperature range. The first set of PPS bonded magnets, molded by AMT from Nd-Nb-Fe-B (MQI) particulate, is under test as a baseline at ORNL, with an example illustrated in Fig. 7. The second set of magnets currently is being molded by AMT from Ames Lab alloy (WT-096) particulate, produced by MQI. It is likely also that a new collaboration with UQM will involve the provision of new PPS bonded magnet samples to meet their own experimental electric motor requirements.

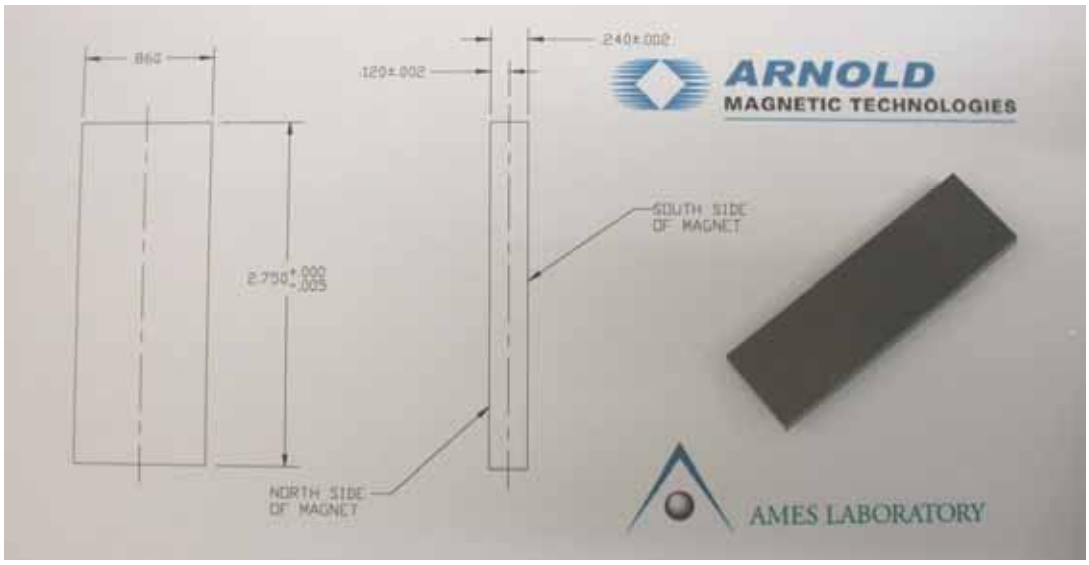

Figure 7. Illustration of one type of PPS bonded magnet sample that was produced by AMT and provided to ORNL for testing in an experimental electric motor.

Conclusions

Considerable progress on a novel alloy design approach for a PM compound with high-temperature magnetic stability has produced a US Patent application and a new MRE-Fe-B family of 2-14-1 compounds with increased remanence and energy product, approaching the best commercial isotropic flake particulate. In fact, the significantly reduced temperature coefficients for remanence and coercivity of the new alloy permit the maximum energy product to surpass the commercial material properties for all temperatures above 125C. With these characteristics, an important intermediate goal has been met by the

successful industrial trial production of a large batch, 100kg, of this enhanced alloy in melt spun flake particulate. Much progress in application testing should be possible as a result of this new resource, including collaborations with several groups that are testing advanced electric motor designs. Recent success in gas atomization trials of MRE-Fe-Co-B-Zr-TiC suggest that the processing conditions are well in hand, but that the initial alloying method needs some further modification to provide an unambiguous test of this new alloy design. A full translation of the alloy design from melt spinning to gas atomization processing remains as one of the major remaining challenges to be met. It also must be realized that a robust passivation process that works efficiently with the gas atomization process must be developed to permit full scale industrial production of spherical ultrafine gas atomized powder, providing motivation for our on-going efforts related to in situ fluorination. Test results by an industrial partner already indicated the advantages for bonded magnet service life. The results of this year's work clearly demonstrate our progress on the path toward an improved PM particulate material and magnet fabrication process that will enable high performance traction motors to be manufactured at a considerably reduced cost.

Future Directions

- Further refine the design strategy for the novel MRE-Fe-B magnetic alloys (MRE = mixed rare earth, e.g., Y, Dy, Nd) to increase the remanence and energy product at ambient temperature for isotropic PM material while maintaining superior temperature coefficient values to 200˚C, with commercial isotropic particulate properties as benchmarks.
- Collaborate with industrial partners, e.g., Arnold Magnetic Technologies (AMT), on independent testing program to study bonded isotropic magnet samples produced by industrial and laboratory molding processes using prototype batch of flake particulate made with Ames MRE-Fe-B alloy composition (optimized for melt spun flake) to permit direct comparisons with current best (flake) materials, measuring progress against APEEM goals.
- Collaborate with research partners, e.g., ORNL, and industrial partners, e.g., Unique Mobility, to test bonded isotropic net shape magnets produced by industrial molding and fabrication processes using prototype batch of flake particulate made with Ames MRE-Fe-B alloy composition in experimental motor designs to characterize performance and temperature tolerance, measuring progress against APEEM goals.
- Perform comprehensive characterization of closely-related spherical powder and flake particulate samples of promising MRE-Fe-B compositions in both as-solidified and annealed states using magnetic, calorimetric, and structural methods, including TEM and 3-D atom probe observations (in collaboration with ORNL) to gain critical understanding (microstructure/magnetic property relationships) of the differences in rapid solidification between gas atomization and melt spinning processes, respectively. This will enable successful translation of improved alloy designs from flake to spherical powders, which are superior for injection molding to net shape.
- Extend the compression molding process to generate bonded magnet samples with increased (> 60 vol.%) loading and sample size from a PPS binder blended with experimental and commercial PM powders to facilitate direct comparisons with benchmark magnetic properties, in collaboration with industrial partner, e.g., AMT.
- Improve the fluidized bed fluorination process for MRE-Fe-B alloy powder to optimize the coating barrier properties for protection of PM powders during the magnet molding process and bonded magnet use, including trials of melt spun flake particulate (in magnetic fluidized bed) and gas atomized spherical powders, which will enable the full potential for high temperature use to be achieved for the new bonded magnets.
- Develop the fluorination process or another type of surface reaction approach to develop minimal flammability and explosivity during the high-pressure gas atomization process, building on the results of fluidized bed coating experiments. This will enable successful formation of an industrial partnership with a commercial powder producer.
- Enhance the process scale of the gas atomization work, assuming improved composition and minimal hazard has been achieved, to produce prototype quantities of fine spherical powder for injection or compression

molding process development in collaboration with an industrial partner, e.g., AMT. The up-scaling work will also address the batch size of the current powder annealing and fluidized bed coating processes, if needed.

FY 2005 Publications and Presentations

Invited Talks

I.E. Anderson, "Novel High Temperature Permanent Magnetic Alloys that Depart from Neodymium-Iron-Boron (2-14-1) Compounds", Advanced Particulate Materials Association, Winter Business Meeting, April 6–8, 2005 Ames, Iowa.

R.W. McCallum, "Development of Improved Powder for Bonded Permanent Magnets in Vehicle Drive Motor Applications" Properties and Applications of Magnetic Materials Conference May 9 – 11, 2005, IIT, Chicago, Illinois.

Conference Presentations

W. Tang, K.W. Dennis, Y. Q. Wu, M. J. Kramer, I. E. Anderson And R. W. McCallum, "New YDy-based R2(Fe,Co)14B Melt-spun Magnets (R=Y+Dy+Nd)", Presented at The 5th Pacific Rim International Conference on Advanced Materials and Processing, Beijing, China, November 2-5, 2004.

W. Tang, K.W. Dennis, Y. Q. Wu, M. J. Kramer, I. E. Anderson And R. W. McCallum, "Effect of Zr substitution on microstructure and magnetic properties of new YDy-based R2Fe14B magnets (R=Y+Dy+Nd)", Presented in the 49th Annual Conference on Magnetism and Magnetic Materials, Jacksonville, Florida, November, 7-11, 2004.

N.L. Buelow, I.E. Anderson, R.W. McCallum, M.J. Kramer, W. Tang, and K. Dennis, "Microstructural Investigation of Mixed Rare Earth Iron Borides Processed Via Melt Spinning and Gas Atomization," presented at the 2005 TMS Annual Meeting, San Francisco, CA, February 13-17, 2005.

N.L. Buelow, I.E. Anderson, R.W. McCallum, M.J. Kramer, W. Tang, and K. Dennis, "Microstructure and Magnetic Properties of Gas Atomized Powders of Mixed Rare Earth Iron Boron," presented at the PM2-TEC 2005 Meeting, Montreal, Quebec, CAN, June 19-23, 2005.

N.L. Buelow, I.E. Anderson, R.W. McCallum, M.J. Kramer, W. Tang, K. Dennis, and S. Constantinides, "Properties of Polymer Bonded Permanent Magnets Made with Melt-Spun Mixed Rare Earth Iron Boron," presented at the PM2-TEC 2005 Meeting, Montreal, Quebec, CAN, June 19-23, 2005.

Publications

N. L. Buelow, I. E. Anderson, R. W. McCallum, M. J. Kramer, W. Tang, and K. W. Dennis, "Comparison of mixed rare earth iron boride gas atomized powders to melt spun ribbon for bonded isotropic permanent magnets," in *Advances in Powder Metallurgy & Particulate Materials - 2004*, compiled by Russell A. Chernenkoff and W. Brian James, Metal Powder Industries Federation, Princeton, NJ, 2004, part 10, pp 230 to 243.

W. Tang, K.W. Dennis, Y. Q. Wu, M. J. Kramer, I. E. Anderson And R. W. McCallum, "Studies of new YDy-based R2Fe14B magnets for high temperature performance (R=Y+Dy+Nd)," *IEEE Trans. Magn.,* 40(2004)2907.

I. E. Anderson, W. Tang, And R. W. McCallum, "Particulate processing and properties of high-

performance permanent magnets*," International J. of Powder Metallurgy*, 40(2004)37.

W. Tang, K.W. Dennis, M. J. Kramer, I. E. Anderson And R. W. McCallum, "New YDy-based R2Fe14B melt-spinning magnets (R=Y+Dy+Nd)," *Materials Science Forum*, 475(2005)2155.

W. Tang, K.W. Dennis, Y. Q. Wu, M. J. Kramer, I. E. Anderson And R. W. McCallum "Effect of Zr substitution on microstructure and magnetic properties of new YDy-based R2Fe14B magnets (R = Y+Dy+Nd)," *J. Appl. Phys*., 97(2005)10H106,

N.L. Buelow, "Microstructural Investigation of Mixed Rare Earth-Iron-Boron Permanent Magnet Alloys Processed Via Melt-Spinning and High-Pressure Gas-Atomization," M.S. Thesis, Iowa State University, August 2005.

N.L. Buelow, I.E. Anderson, R.W. McCallum, M.J. Kramer, W. Tang, and K. Dennis, "Microstructure and Magnetic Properties of Gas Atomized Powders of Mixed Rare Earth Iron Boron," in *Advances in Powder Metallurgy & Particulate Materials-2005*, compiled by C. Ruas and T.A. Tomlin, Metal Powder Industries Federation, Princeton, NJ, part 9 (2005) pp. 74-88.

N.L. Buelow, I.E. Anderson, R.W. McCallum, M.J. Kramer, W. Tang, K. Dennis, and S. Constantinides, "Properties of Polymer Bonded Permanent Magnets Made with Melt-Spun Mixed Rare Earth Iron Boron," in *Advances in Powder Metallurgy & Particulate Materials-2005*, compiled by C. Ruas and T.A. Tomlin, Metal Powder Industries Federation, Princeton, NJ, part 10 (2005) pp. 308-319.

Patents

None.

References

R. W. McCallum, K. W. Dennis, B. K. Lograsso, and I. E. Anderson, "Method of Making Bonded or Sintered Permanent Magnets," U.S. Patent 5,240,513, August 31, 1993.

I. E. Anderson, B. K. Lograsso, and R. L. Terpstra, "Environmentally Stable Reactive Alloy Powders and Method of Making Same," U.S. Patent 5,372,629, December 13, 1994.

R. W. McCallum, K. W. Dennis, B. K. Lograsso, and I. E. Anderson, "Method of Making Bonded or Sintered Permanent Magnets (continuation)," U.S. Patent 5,470,401, November 28, 1995.

I. E. Anderson and R. L. Terpstra, "Apparatus for Making Environmentally Stable Reactive Alloy Powders," U.S. Patent 5,589,199, December 31, 1996.

I. E. Anderson, B. K. Lograsso, and R. L. Terpstra, "Environmentally Stable Reactive Alloy Powders and Method of Making Same," U.S. Patent 5,811,187, September 22, 1998.

R. W. McCallum and D. J. Branagan, "Carbide/Nitride Grain Refined Rare Earth-Iron-Boron Permanent Magnet and Method of Making," U.S. Patent 5,803,992, September 8, 1998.

R. W. McCallum and D. J. Branagan, "Carbide/Nitride Grain Refined Rare Earth-Iron-Boron Permanent Magnet and Method of Making," U.S. Patent 5,486,240, January 23, 1996.

D. J. Branagan and R. W. McCallum, "The Effects of Ti, C, and TiC on the Crystallization of Amorphous $Nd_2Fe_{14}B$," *J. Alloys and Compds.*, **245** (1996).

D. J. Branagan, T. A. Hyde, C. H. Sellers, and R. W. McCallum, "Developing Rare Earth Permanent Magnet Alloys for Gas Atomization," *J. Phys. D: Appl. Phys.*, **29**, p. 2376 (1996).

M. J. Kramer, C. P. Li, K. W. Dennis, R. W. McCallum, C. H. Sellers, D. J. Branagan, L. H. Lewis, and J. Y. Wang, "Effect of TiC Additions to the Microstructure and Magnetic Properties of $Nd_{9.5}Fe_{84.5}B_6$ Melt-spun Ribbons," *J. Appl. Phys.*, **83**(11), pt. 2, p. 6631 (1998).

D. J. Branagan and R. W. McCallum, "Changes in Glass Formation and Glass Forming Ability of $Nd_2Fe_{14}B$ by the Addition of TiC," *J. Alloys and Compds.*, **244** (1–2), p. 40 (1996).

4. Power Electronics Research and Technology Development

4.1 Wide-Bandgap Semiconductors

Principal Investigator: Burak Ozpineci
Oak Ridge National Laboratory
National Transportation Research Center
2360 Cherahala Boulevard
Knoxville, TN 37932
Voice: 865-946-1329; Fax: 865-946-1262; E-mail: ozpinecib@ornl.gov

DOE Technology Development Manager: Susan A. Rogers
Voice: 202-586-8997; Fax: 202-586-1600; E-mail: Susan.Rogers@ee.doe.gov

ORNL Program Manager: Mitch Olszewski
Voice: 865-946-1350; Fax: 865-946-1262; E-mail: olszewskim@ornl.gov

---

Objectives

- Assess the impact of replacing silicon (Si) power devices in transportation applications with devices based on wide-bandgap (WBG) semiconductors, especially silicon carbide (SiC)-based ones.
- Develop device models for system-level simulation studies and analyze the impact of SiC devices on the system performance.
- Build and test SiC-based power converters for hybrid electric vehicles (HEVs) to validate the predictions.
- Test the reliability of the SiC devices.

Approach

- Maintain an awareness of the state of the art in WBG semiconductors.
- Develop models of WBG semiconductor devices, especially SiC diodes, junction field-effect transistors (JFETs), and metal oxide semiconductor field-effect transistors (MOSFETs).
- Simulate the performance of an HEV traction drive and a dc-dc converter using these device models.
- Test, characterize, and model a 55-kW Si-SiC hybrid [Si-insulated gate bipolar transistor (IGBT), SiC Schottky diodes] inverter and compare it with a similar all-Si inverter.
- Test, characterize, and model a 7.5-kW all-SiC inverter to compare with an all-Si inverter and validate the system models and demonstrate the system-level benefits.
- Build dc-dc converters to test the reliability of the SiC and Si devices.

Major Accomplishments

- Acquired several SiC Schottky diodes, JFETs, and MOSFETs.
- Tested, characterized, and modeled SiC Schottky diodes, JFETs, and MOSFETs. Physics-based models for JFET and SiC Schottky diodes were also developed in Saber.
- Tested, a 55-kW Si-SiC hybrid traction inverter built in collaboration with Cree and Semikron and compared its performance with a 55-kW all-Si inverter. Both were modeled in Saber using the device models developed from the device characterization data.
- Tested a 7.5-kW all-SiC inverter (SiC JFETs and SiC Schottky diodes) that was built in collaboration with Rockwell Scientific and compared its performance with a commercially available all-Si inverter

(Si IGBTs and Si pn diodes). The all-SiC inverter was modeled in Saber using the JFET models and SiC Schottky diode models.

- Tested the reliability of SiC and Si devices by using them in buck converters and operating the buck converters for long periods of time.

Technical Discussion

With the increase in demand for more efficient, higher-power electronics with higher-temperature capabilities, design engineers face new challenges [1, 2]. Silicon (Si) power devices have reached their theoretical limits in terms of higher-temperature and higher-power operation by virtue of the material's physical properties. To overcome these limitations, research has focused on wide-bandgap materials such as silicon carbide (SiC), gallium nitride (GaN), and diamond because of their superior material advantages such as large-bandgap, high-thermal conductivity, and high-critical breakdown field strength.

SiC Field-Effect Transistor Devices

FET devices are majority-carrier devices and are preferred over minority-carrier devices in power applications; however, Si FET devices, like Si Schottky diodes, can be used only in low-voltage (< 300 V) applications because of their high on-state resistance. Even the first experimental SiC FET devices have blocking voltages over 1000 V with reasonable on-state resistances. It is expected that in the near future SiC FET devices will dominate Si minority-carrier devices in medium-voltage (< 3000 V) applications.

SiC MOSFET

Static characteristics

A MOSFET is a unipolar device that is normally off. The forward characteristics of the same SiC MOSFET for a temperature range of −50°C to 175°C are shown in Figure 1. The on-state resistances of the device are calculated from the slopes of the curves and are plotted with respect to temperature in Figure 2. It is interesting to note that this device has a negative temperature co-efficient up to 50°C and a positive temperature coefficient above that. MOSFETs are majority-carrier devices and are expected to have positive temperature coefficients. The reason for this is that at lower temperatures, the contribution of the channel resistance to the total on-state resistance is dominant [3,4]. The channel mobility increases with temperature because the interface traps are closer to the conduction band [4,5]; thus, the channel resistance decreases with temperature. Consequently, at low temperatures the MOSFET on-resistance decreases. Above a certain temperature value, the channel resistance is not dominant, and because of the other dominant on-resistance components, the MOSFET overall on-resistance increases.

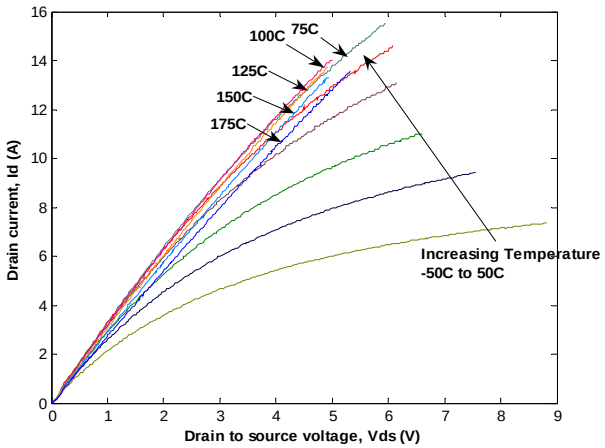

Figure 1. Forward characteristics of SiC MOSFET at different temperatures.

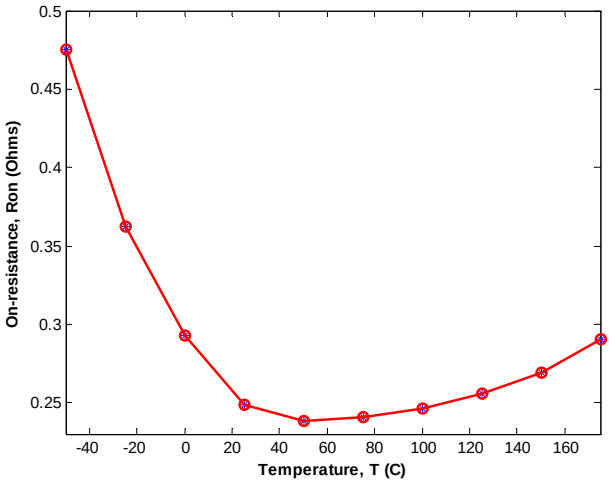

Figure 2. On-resistance of SiC MOSFET at different temperatures.

Dynamic characteristics

The gate-drive circuit developed at ORNL in FY 04 for SiC JFET was modified and used to determine the dynamic characteristics of the SiC MOSFET. The gate-drive voltage for the MOSFET was selected to be 20 V as determined from the forward characteristics to obtain the optimum performance. Operation at 250 kHz was achieved with a series-gate resistance of 7.2 Ω and a peak-gate current of 0.6 A. The gate and switching waveforms for a SiC MOSFET are shown in Figure 3. The device has a turn-off delay td of 40 ns, fall time tf of 100 ns, turn-on delay td of 20 ns, and rise time tr of 100 ns.

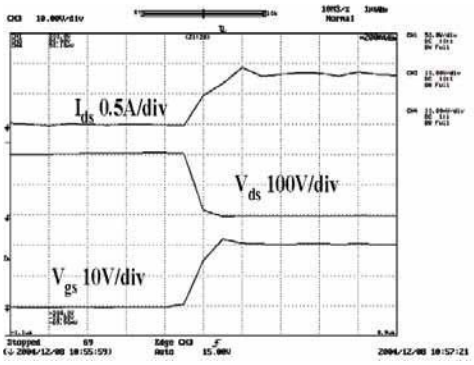

(a)

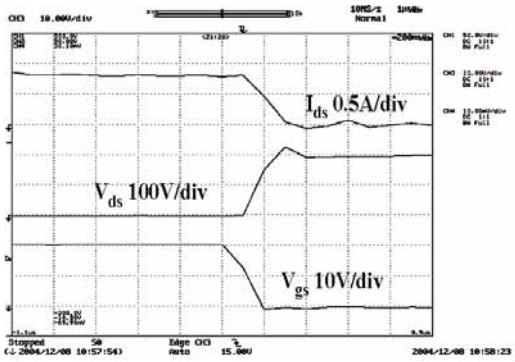

(b)

Figure 3. The gate and switching waveforms of the SiC MOSFET.

MOSFETs have fast dynamic responses, which are required for high-frequency switching. The turn-on and turn-off energy losses for the SiC MOSFET were calculated by integrating the instantaneous power over the turn-on (ton) and turn-off times (toff). The energy losses calculated for the SiC MOSFET at different temperatures for operation at 5 kHz, 50% duty cycle, 100 V, and 0.8 A are shown in Figure 4. It is evident from the plot that the total switching losses do not vary much with temperature.

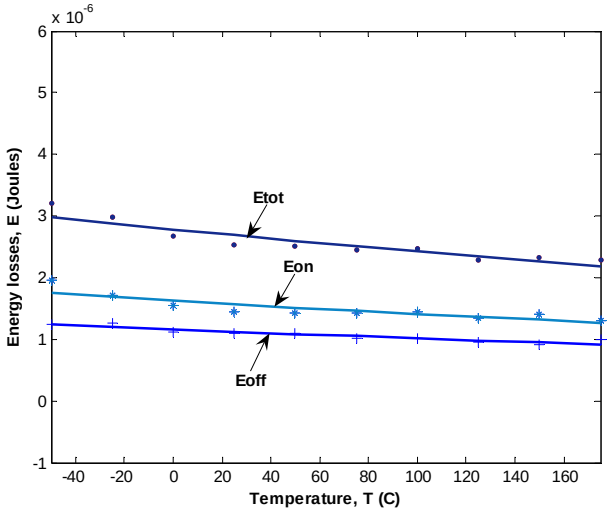

Figure 4. Energy loss plot of SiC MOSFET.

55-kW Si-SiC Hybrid Inverter

SiC Schottky diodes have been proven to have better performance characteristics than those of similar Si pn diodes [6], especially with respect to their switching characteristics because they have negligible reverse-recovery losses. Their superior switching performance impacts the main power switches by reducing the stress on them and thus improving system performance. SiC Schottky diodes are already commercially available at low-current ratings. These diodes are being used in niche applications such as power factor correction circuits. It is expected that the first impact of SiC devices on inverters will be as a result of SiC Schottky diodes replacing the Si pn diodes.

Oak Ridge National Laboratory (ORNL) collaborated with Cree and Semikron to build a hybrid 55-kW (Si IGBT–SiC Schottky diode) inverter by replacing the Si pn diodes in Semikron's automotive inverter with Cree's SiC Schottky diodes.

The inverter module SKAI (Semikron Advanced Integration) from Semikron was developed for hybrid electric vehicle (HEV) traction drives. It is a three-phase 55-kW inverter unit (Figure 5) built using 600-V, 600-A IGBTs and 600-V, 450-A pn diode modules. Cree has developed 75-A, 600-V, 4 × 6.65 mm SiC Schottky diodes as shown in Figure 6. The yield was about 46.7%, with 67 good devices from the wafer. For this project, Semikron replaced each Si pn diode (9 × 9mm) in their automotive integrated power module (AIPM) with two 75-A SiC Schottky diodes.

Figure 5. Semikron inverter unit.

Figure 6. 75-A Schottky diodes developed by Cree.

SiC diode modeling

The SiC Schottky diode model used in this project was developed at the University of Arkansas. It is a robust model that can accurately model forward and reverse recovery and track accurately over temperature. Moreover, many details pertaining to the fabrication of the diode need not be known by the user, making parameter extraction flexible. The diode model parameters were extracted from the on-state characteristics, and from the reverse-recovery waveforms.

The on-state validation of the model with the SiC 75-A diode from Cree is seen in Figure 7. The percentage error is approximately 0.3–0.4% in the 100^{o}C and 150^{o}C curves and approximately 2–3 % in the 25^{o}C curve.

Figure 8 shows the reverse recovery of the SiC diode and the corresponding behavior of the model (in dotted lines). As seen in the figure, the model accurately tracks the test data.

Simulation of Si IGBT—SiC Schottky diode hybrid inverter

After the modeling and parameter extraction of the devices, the device models were used to construct a three-phase voltage-source inverter in Saber. The IGBT that was used for constructing the Semikron inverter was not available in the Saber library. Therefore, another IGBT with similar ratings was used as the transistor switch. The load consisted of a 1.24 Ω resistor and a 1.5 mH inductor and the input dc bus voltage was set at 325 V. An all-Si inverter with Si IGBTs and diodes was also simulated. The simulation results showed that the Si IGBT- SiC Schottky diode hybrid had much better efficiencies than the all-Si inverter.

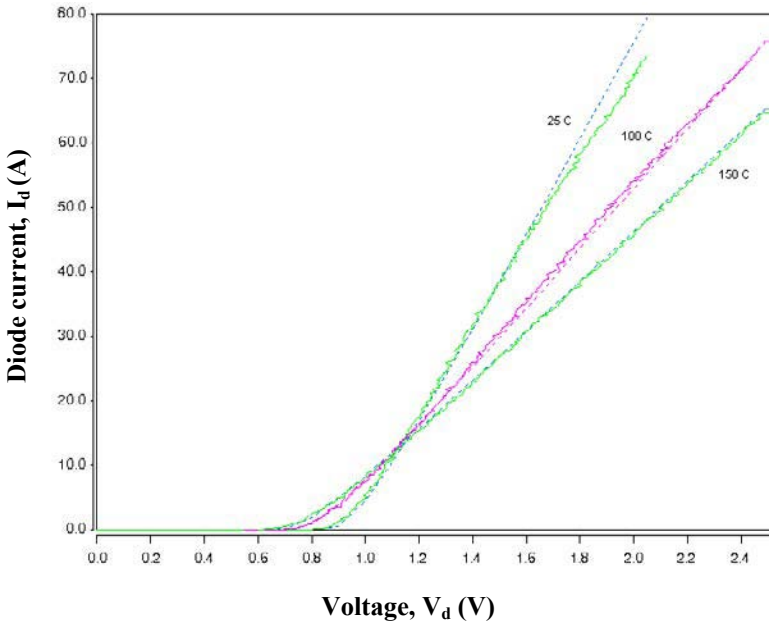

Figure 7. Measure (solid line) and simulated (dotted line) on-state waveforms of SiC Schottky diode at different temperatures.

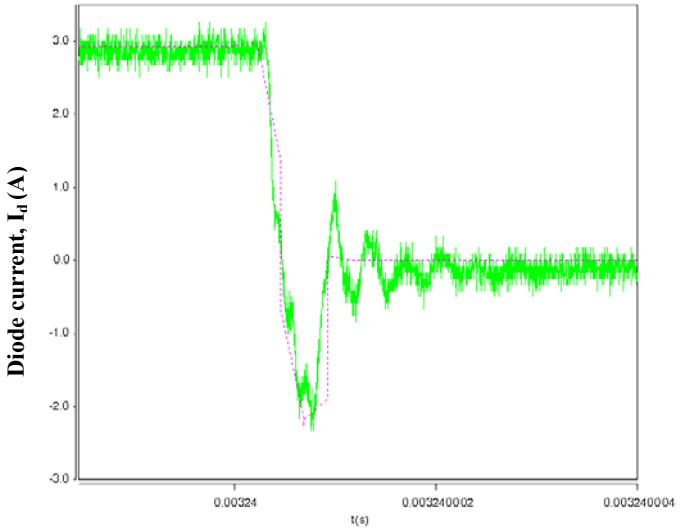

Figure 8. Measured (solid) and simulated (dotted) reverse-recovery waveforms of the SiC Schottky diode from Cree.

The difference in efficiencies between the simulated inverters is clearly visible in Figure 9. When the Si diode in the all-Si inverter was replaced with the SiC Schottky diode, a 1.5–2% increase in the operational efficiency was observed.

Two major tests were performed, R-L load tests to investigate the inverters power handling capability and dynamometer tests to determine the inverters dynamic performance. Both the hybrid inverter and the all-Si inverter were tested using the same test procedure.

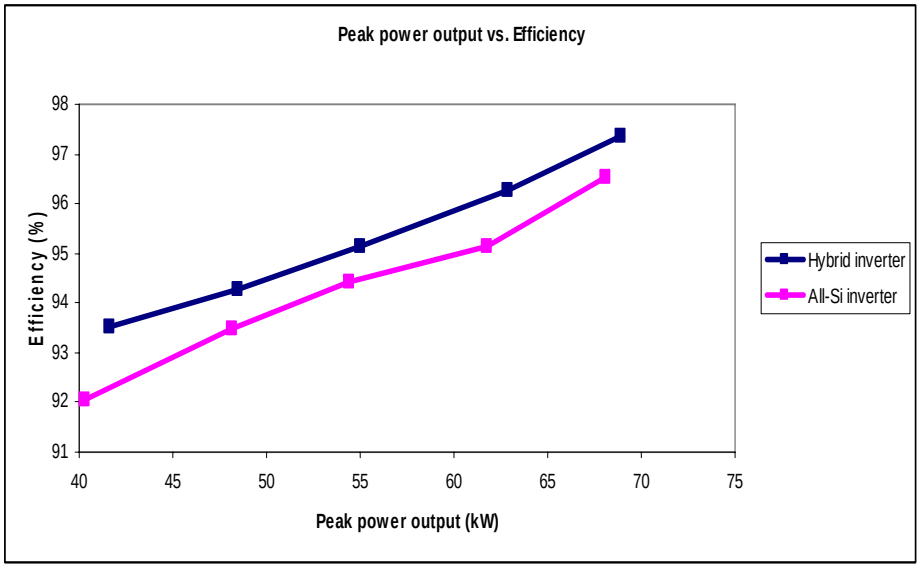

Figure 9. Comparison of peak-power output vs efficiencies for hybrid and all-Si inverter testing.

R-L load test

Operation. For this test, the dc-link voltage was varied from the minimum operating voltage (200 V) to the maximum bus voltage (450 V). The bus voltage trip fault occurs for voltages beyond 450 V. The load resistance was set to the minimum value and the current was controlled using the current controller. The coolant was set at 20ºC at a flow rate of 2.5 gpm. The open-loop frequency of operation and the pulse-width modulation (PWM) frequency were fixed, and the current command was varied for a particular dc-link voltage. The command current was increased in steps of 10 A without exceeding the power rating of the inverter or the power rating of the load. The procedure was repeated by increasing the open-loop frequency in steps of 25 Hz. The coolant temperature was changed to 70ºC, and the data was recorded for a wide range of current and open-loop frequencies.

Results. The data obtained for both the inverters were analyzed and the corresponding efficiencies were calculated. The efficiency versus output-power plot for one of several operating conditions comparing the inverters is shown in Figure 10. The hybrid inverter efficiencies are higher than the all-Si inverter for all operating conditions. The results show up to 33.6% reduction in the losses when everything is kept the same and SiC Schottky diodes are used instead of Si pn diodes. The percentage loss reduction was calculated comparing the power losses between the hybrid inverter and the all-Si inverter as follows:

$$\text{Percentage loss reduction} = \left(d_{ploss\,(Si)} - d_{ploss\,(SiC)}\right) \Big/ \left(d_{ploss\,(Si)}\right) \times 100$$

Dynamometer tests

Motoring mode. The dc-voltage input to the inverter was set at the nominal battery operating voltage (325 V dc). The direction of rotation was set to forward and the motor speed was increased from 750 rpm to the rated base speed for a specific continuous load torque. Data was obtained for a wide range of speed and torque values by varying the load torque (from 100, 150, 200 Nm) using the dynamometer controller.

The efficiency plots for various speeds and a load torque of 200 Nm are shown in Figure 11. The average loss reduction in motoring mode was up to 10.7%. Note that one of the reasons the average loss reduction is less in the motoring compared to the R-L load test is that the power levels achieved are much less in motoring.

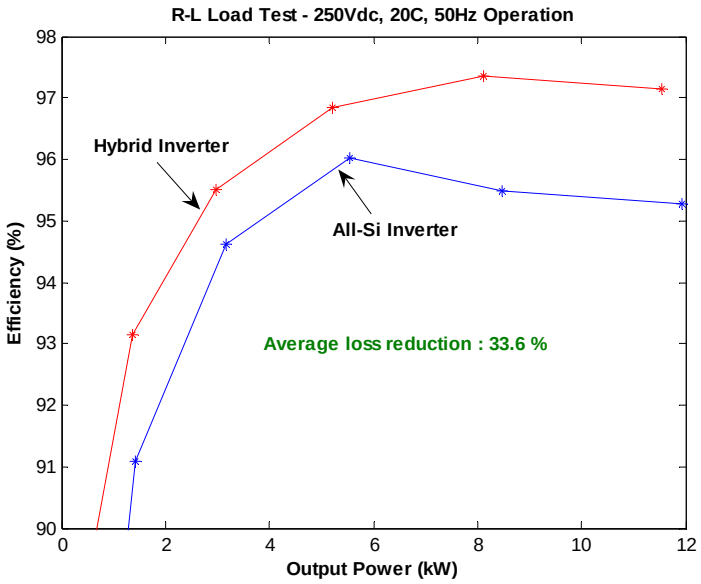

Figure 10. R-L load-test efficiency curves for one of the load conditions.

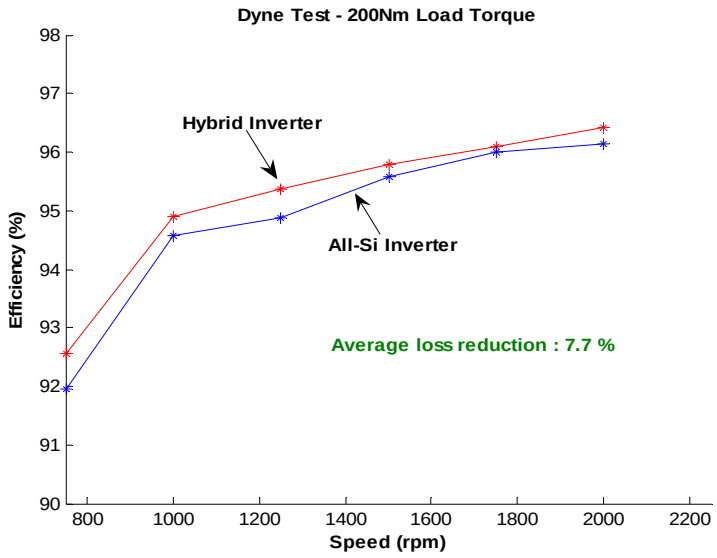

Figure 11. Dynamometer test—motoring mode efficiency plots at 70ºC.

Regeneration mode. The dc-voltage input to the inverter was set at the nominal battery-operating voltage. The direction of rotation was set to be forward. The dynamometer controller was adjusted to control the speed. The motor speed was increased from 750 rpm to the rated speed for a specific operating current of the inverter to achieve a specific load torque. The current was varied from zero to the values corresponding to different torque values and then decreased to zero. The procedure was repeated to obtain the data for a wide range of speed and torque values. The curves comparing the efficiency of the inverters at 70ºC with a 200 Nm load are shown in Figure 12. The results show up to 12.71 % reduction in average losses similar to the results obtained in the motoring mode.

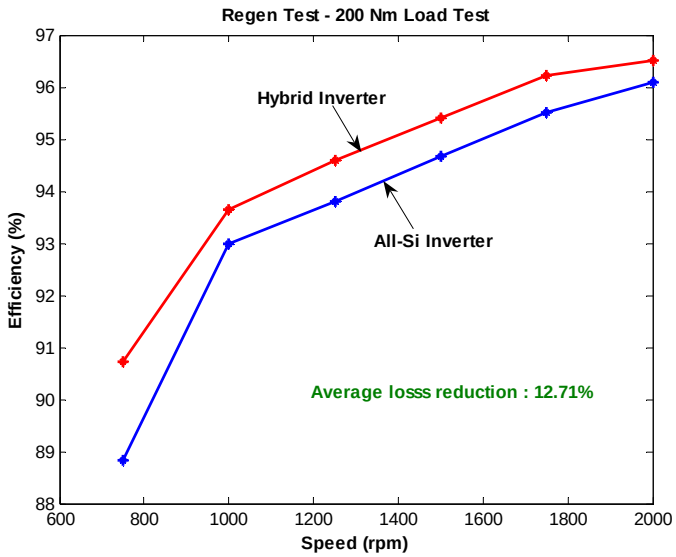

Figure 12. Dynamometer test—regeneration mode efficiency plots at 70ºC.

The IGBTs used in the actual inverter and in the simulation are not the same. Therefore, a direct comparison of the efficiencies of the simulation and the testing would not be accurate. But it is seen that the efficiencies of the simulation and the testing do have the same trend.

7.5-kW All-SiC Inverter

A 7.5-kW all-SiC inverter was built in collaboration with Rockwell Scientific to study the impact of replacing the Si devices with SiC devices in the inverters. The SiC inverter module was built using 1200-V, 7.5-A JFETs and 1200-V, 15-A SiC Schottky diodes. The main switches in each phase leg consisted of two JFETs with 7.5-A ratings in parallel.

A Si inverter module with similar ratings was selected to compare its performance with the all-SiC unit. The picture of the SiC inverter module is shown in Figure 13.

Figure 13. All-SiC module.

SiC JFET modeling

The device physics-based analytical SiC JFET model used for this project was developed by the University of Arkansas [7]. The on-state validation was done for only the unipolar operation because the JFET is mainly used in that area as shown in Figure 14. The simulated values agree with the measured values with an error of approximately 2–3%. The switching characteristics are shown in Figures 15 and 16. The model tracks the actual waveforms as expected. As observed in the transient modeling results, the switching time is on the order of 0.1 µs for a 25 Ω gate resistance, and the various depletion capacitances

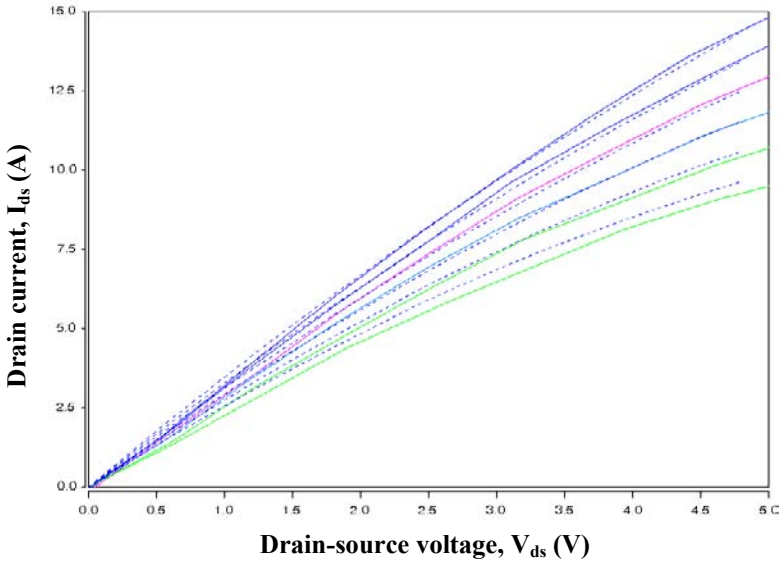

Figure 14. Rockwell SiC JFET measured (solid) and simulated (dotted) on-state waveforms at 25°C for different gate voltages (V_{gs} ranging from 0V to -2.5V).

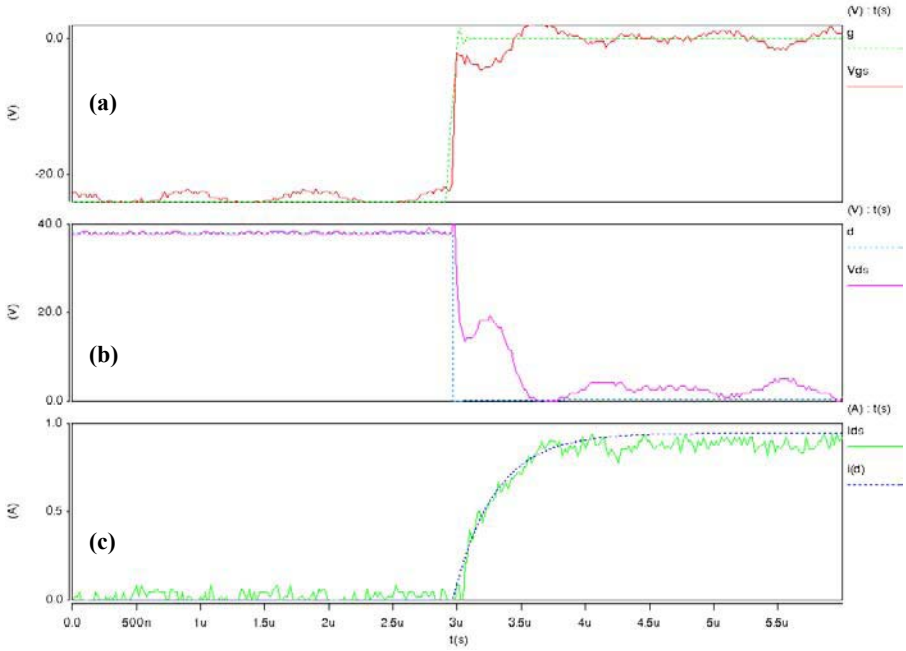

Figure 15. SiC JFET simulated (dashed) and measured (solid) turn-on waveforms at 25oC: (a) gate voltage, (b) drain voltage, and (c) drain current.

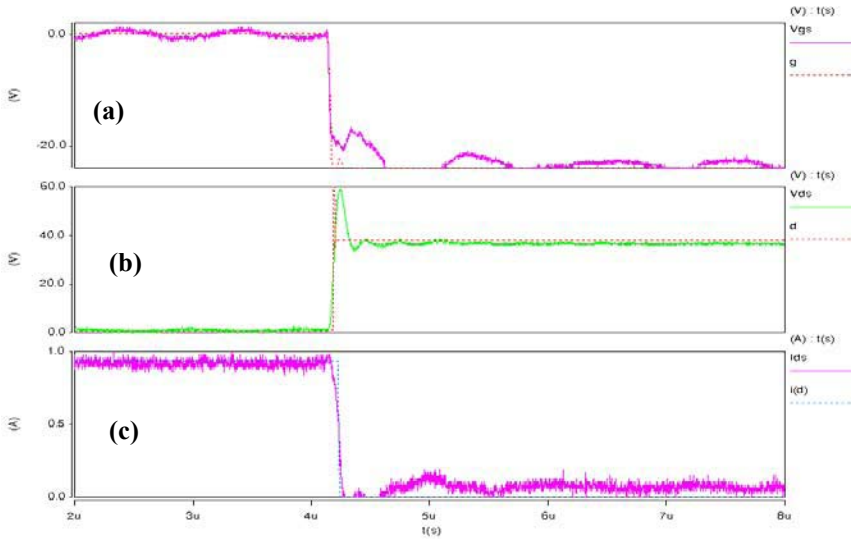

Figure 16. SiC JFET simulated (dashed) and measured (solid) turn-off waveforms at 25°C: (a) gate voltage, (b) drain voltage, and (c) drain current.

described in the model can accurately predict the switching characteristics of the SiC JFET. The turn-off waveforms are seen to be much faster compared to the turn-on times because the discharging of the junction and package capacitances happens over a shorter interval of time.

Simulation of all-SiC inverter

The SiC JFET and diode models were used to construct an all-SiC inverter. This is a technology demonstrator that shows a full power electronic system in SiC being successfully simulated. The validated models were used to construct the inverter system. The all-SiC inverter from Rockwell was first tested to ascertain the performance and collect test data for the inverter model validation.

A balanced three-phase 15 Ω resistive load was used to simulate the operating conditions. The switching frequency was set to 10 kHz, and the output frequency was set to 50 Hz. The inverter was simulated for different values of dc voltages and modulation indices. As explained before, the SiC JFETs used in the inverter were modeled and all the parameters were extracted. The 1200-V, 15-A SiC diode in the inverter was also modeled by the procedure explained previously. The results of the diode fitting are seen in Figures 17 and 18.

The efficiency of the all-SiC inverter was seen to range from 83.2 to 87.8 %.

Inverter testing

Inductive load tests

Operation. The gate signals to the inverter modules were checked with no load on the inverter. The inverters were connected to a three-phase R-L load. The operating current was controlled by varying the load resistance. The dc-link voltage was varied from 0 to a maximum bus voltage of 400 V. The frequency of operation was fixed and the load was varied for a particular dc-link voltage. The load was increased in steps without exceeding the power rating of the inverter and also not exceeding the power rating of the load. The procedure was repeated by increasing the output frequency command in steps of 10 Hz.

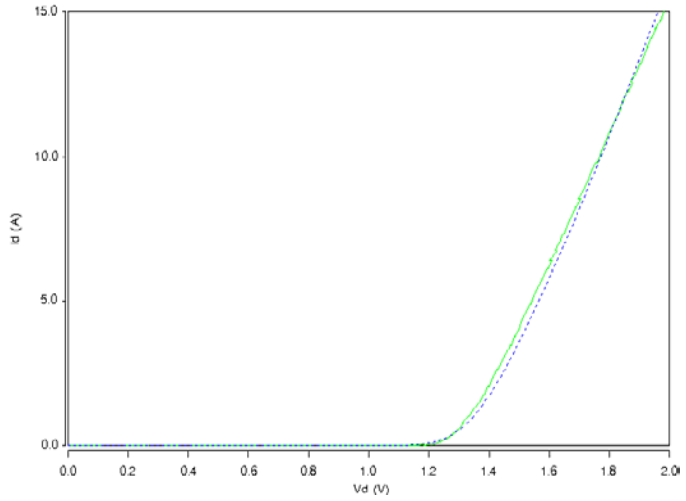

Figure 17. On-state validation of SiC diode at 25°C – measured (solid) and simulated (dashed).

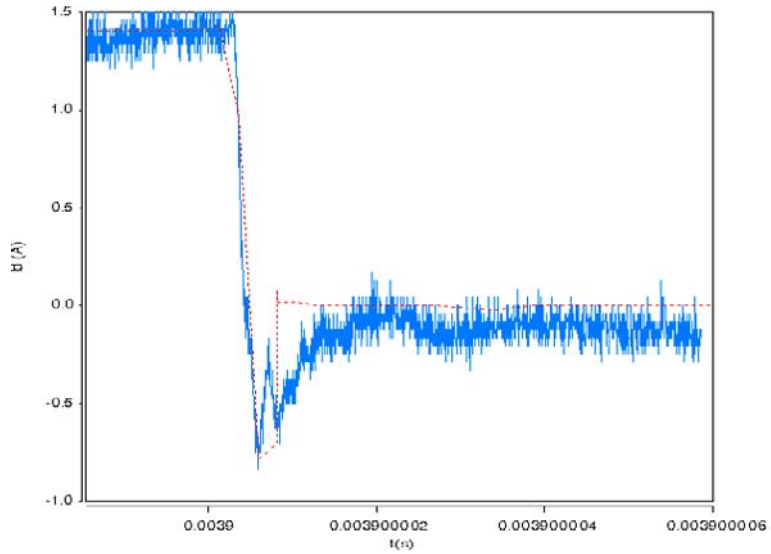

Figure 18. Reverse-recovery validation of SiC diode at 25°C – measured (solid) and simulated (dashed).

Results. The operating waveforms for the SiC inverter for a particular load setting are shown in Figure 19. The plot of efficiency curves for one of the different operating conditions is shown in Figure 20. It can be seen from the plot that the efficiencies of the Si inverter module are much higher than those of the SiC module.

To better understand why the all-SiC inverter efficiencies are worse than the all-Si inverter, the static characteristics of the IGBT, SiC JFET, and the diodes in the inverter modules were compared as shown in Figures 21 and 22 respectively.

The on-state voltage drop of the Si IGBT is much less compared to the SiC JFET at higher-current levels because of the higher on-resistance of the SiC JFET. At lower currents, however, the SiC JFET has a lower on-state voltage drop. The Si pn and SiC Schottky diodes, on the other hand, have similar static characteristics. Because of the higher on-state resistance of the SiC JFETs, the all-SiC inverter has higher conduction losses.

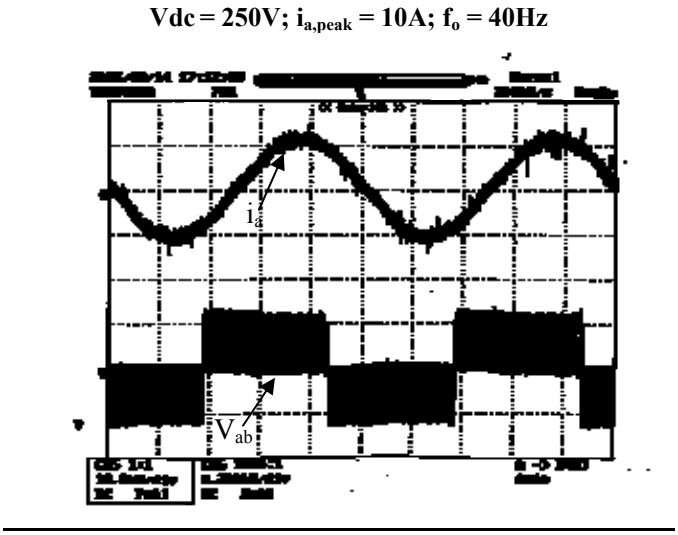

Figure 19. Operating waveforms of SiC module for R-L load test.

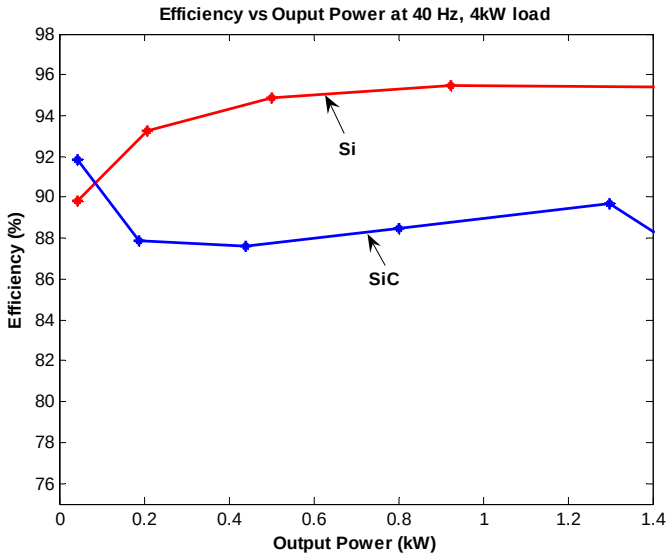

Figure 20. Efficiencies comparison plot at 40-Hz operation for R-L load test.

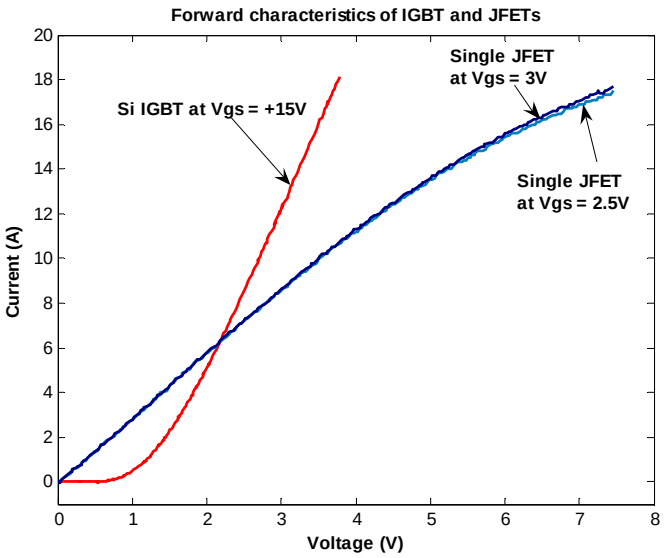

Figure 21. Forward characteristics of IGBT and JFET in the Si and SiC modules.

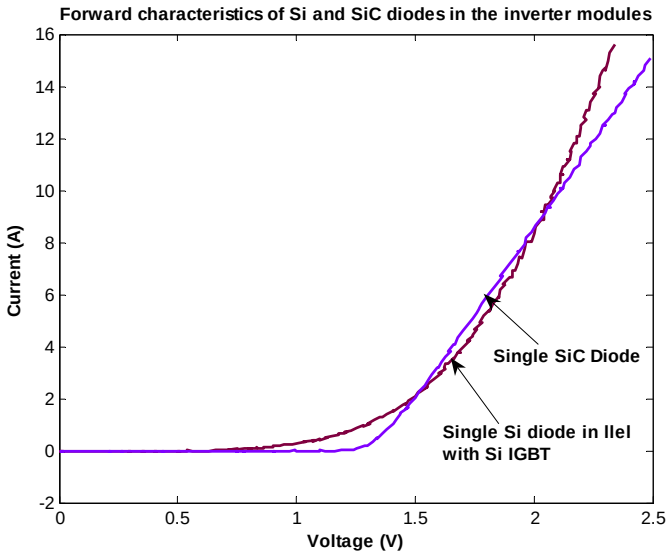

Figure 22. Forward characteristics of diodes in the Si and SiC modules.

Duration tests

Underhood, reliable operation of power modules in hybrid electric vehicles is an important transportation requirement. Most common failures in power modules are due to power cycling over high-operating temperatures. To test the reliable operation of the SiC power devices, four different buck converters were developed with Si IGBTs, Si pn diodes, SiC JFETs, and SiC Schottky diodes. The devices in the converters were operated at different voltage and current levels and at different frequencies in order to subject them to thermal stress and study their behavior. The analysis of test data and results will be presented in the following sections.

Operation. The buck converters were fed from a single dc supply source, and the load current was varied by changing the input voltage. The operating current for each buck converter was limited to a maximum of 2 A because of the current ratings of the SiC JFETs. These JFETs were obtained through SiCED, a Siemens-based company. They were operated continuously for 7.5 hours every day for six months. During this time, their operation was closely observed and their case temperatures recorded. The temperature profiles have been filtered to get rid of the noise picked up by the thermocouples.

After experimenting with several test conditions, the operating voltage was fixed at 200 V for safe operation without device failure, and the duration tests were continued. The converters were operated at 10 kHz, 50% duty cycle, and 200 V. The temperature profiles recorded for each device for 7.5 hours are shown in Figure 23a. These profiles show that for the same main switch, the SiC diodes are operating at higher temperatures compared to the Si diodes. A previous ORNL simulation study [2] has shown that the conduction losses of SiC Schottky diodes dominate at lower switching frequencies and they are much higher than those of the Si pn diodes. The thermal profiles in Figure 23a confirm the results of that simulation study.

Figure 23b shows that SiC JFETs, without heat sinks, operate at much lower temperatures compared to Si IGBTs, which implies that the SiC devices have lower losses compared to the Si IGBTs. The comparison of static characteristics of SiC JFET and Si IGBT is shown in Figure 24 in which it can be seen that in the current range, the JFET has lower conduction losses.

It is also interesting to observe in Figure 23b that the Si IGBT and the SiC JFET with the SiC diodes operate at lower temperatures compared to the ones that operate with the Si pn diodes. This is again attributed to the better reverse recovery characteristics of the SiC Schottky diodes.

Figures 25 and 26 show all the profiles obtained for different switching frequencies plotted together. It can be observed from these figures that the operating temperatures of the SiC diodes do not change much with increases in switching frequency. This is because the switching losses of SiC Schottky diodes are significantly lower than those of the Si pn diodes. However, the Si diodes have higher-switching losses and hence their operating temperatures rise as the frequency increases.

Since Si IGBTs are limited in their switching frequency, the buck converters with Si IGBTs were tested separately at lower-switching frequencies. The temperature profiles of the switches and diodes for a 200-V, 50% duty cycle and in a frequency range of 15–25 kHz are shown in Figure 27. This figure shows that the temperature profiles of the Si IGBTs with SiC Schottky diodes do not change much with switching frequency. However, the temperatures of Si IGBTs with Si diodes increase with switching frequency. This also shows that the SiC diodes have less effect on the main power switch because of the negligible reverse-recovery losses. Even though the temperatures of the Si IGBT in the all-Si converter increase as the switching frequency increases, the Si pn diode compared to the SiC Schottky diode still operates at a slightly lower temperature.

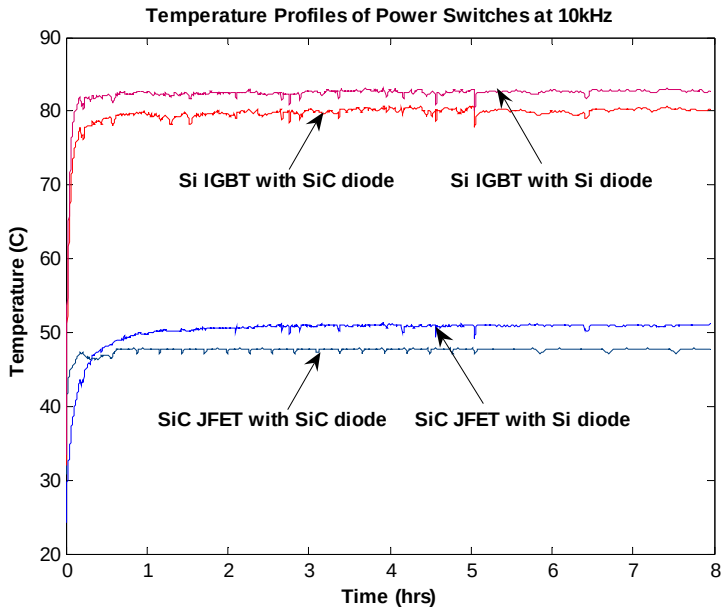

(a) Switches

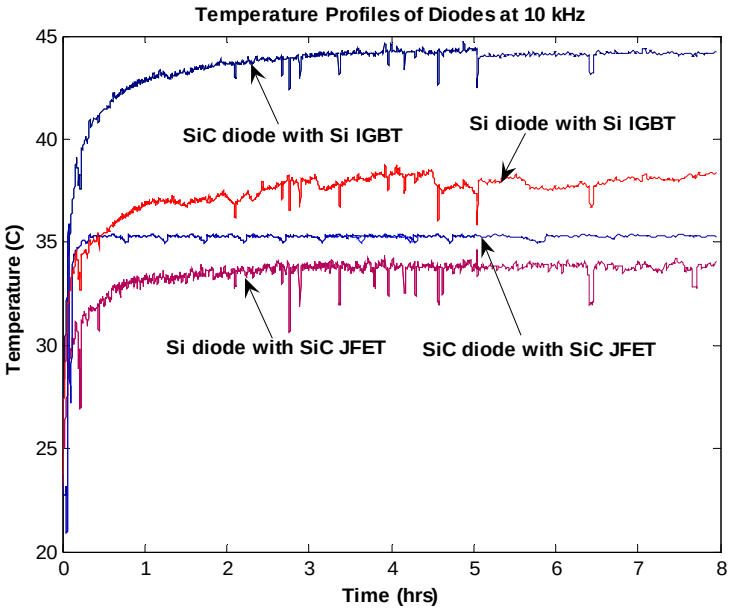

(b) Diodes

Figure 23. Temperature profile for 10-kHz operation.

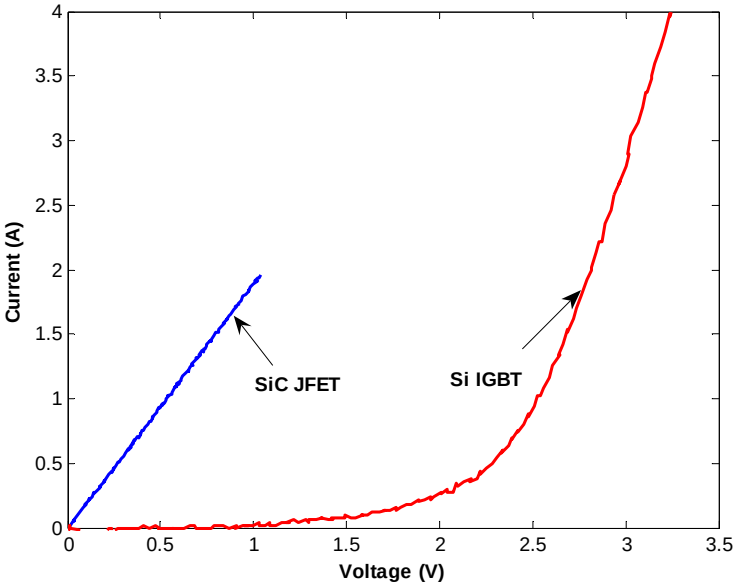

Figure 24. Comparison of static characteristics for Si IGBT and SiC JFET.

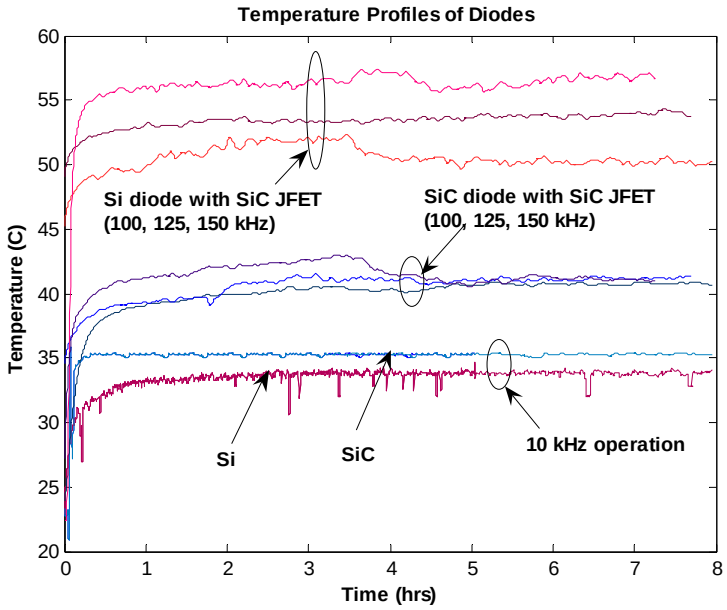

Figure 25. Temperature profile for diodes at different operating frequencies.

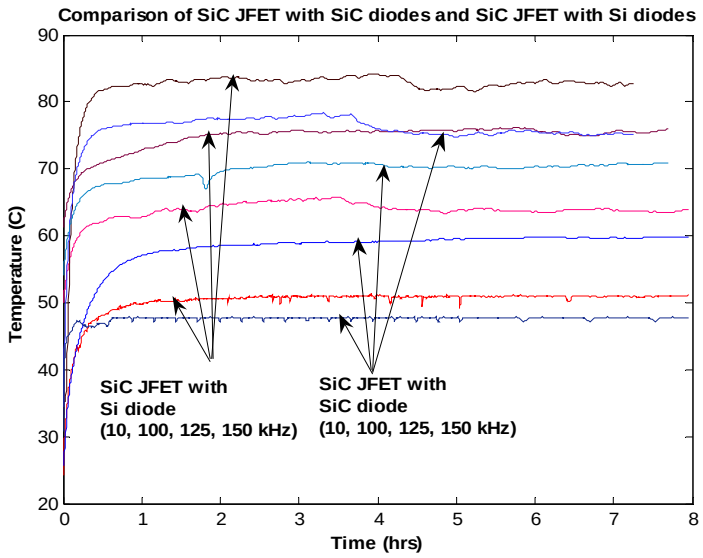

Figure 26. Temperature profile for switches at different operating frequencies.

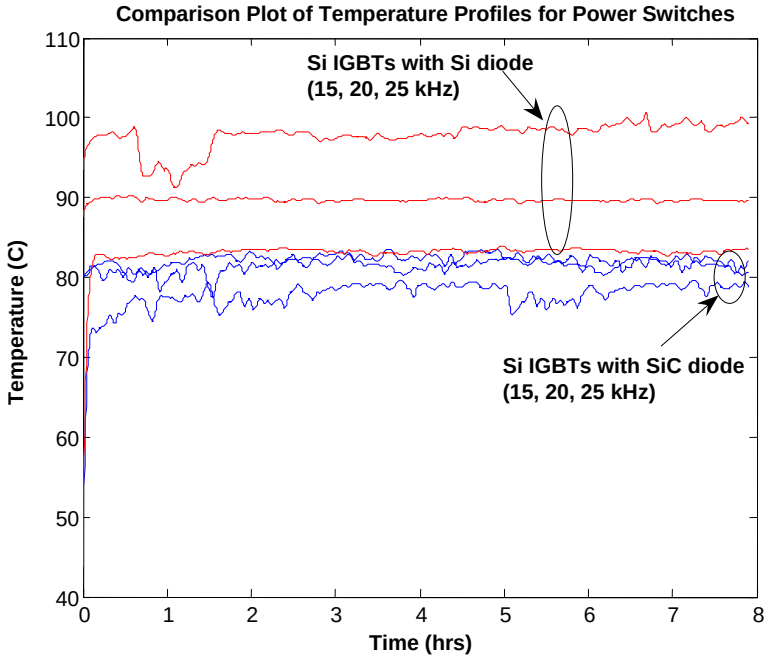

Figure 27. Plot of temperature profile for power switches at different frequencies

During the tests, several power switches failed at different operating conditions. The diodes never failed over several months of operation. Si IGBTs failed at certain operating conditions because of the thermal limits of the devices. Only case temperatures were measured; the junction temperatures would be much higher. Also, the devices were operated without any snubber circuit, thus the power switches were stressed even more than under normal operation.

SiC JFETs operated without any failures even at higher voltage levels and without heat sinks. However, the JFETs failed repeatedly after several days of operation. After investigating the devices that

failed, it was found that gate-to-source of some devices were shorted while some had open drain-to-source failures. This shows that these experimental samples need more reliability improvement.

Conclusion

With the present SiC Schottky diode technology, when SiC Schottky diodes are used in traction drive inverters instead of Si pn diodes, the average losses of the inverter can be reduced by up to 33.6%. The cost issue still remains to be a problem.

The 7.5-kW all-SiC inverter and buck converter tests showed that more research is required on SiC JFETs to improve their characteristics and reliability. Even though the reliability of SiC power switches is of concern, their performance is still promising. It is important to follow the present developments in SiC power-device technology closely because the pace of improvement has increased considerably. Better, less expensive, and more reliable SiC power devices are not too far away.

Future Direction

FY 2006–2007: Conduct research in high-temperature packaging for SiC power devices, as present device packaging cannot handle the temperatures at which SiC devices are capable of operating. External collaboration will be required. Conduct a feasibility study to build a 55-kW all-SiC inverter by using the device and system-level simulation models developed based on the results from the inverter tests performed in FY05.

FY 2007–2008: Provided that the feasibility study shows that the SiC technology is ready for a 55-kW all-SiC inverter, build this inverter and compare it to an all-Si inverter at full scale.

FY 2006–2008: Continue acquiring, testing, characterizing, and modeling new SiC devices.

Publications

M. Chinthavali, L. M. Tolbert, B. Ozpineci, "4H-SiC GTO Thyristor Loss Model for HVDC Converter," pp. 1238–1243 in *IEEE Industry Applications Society Annual Meeting,* October 3–7, 2004, Seattle, Washington.

M. Chinthavali, B. Ozpineci, L. M. Tolbert, "High Temperature Characterization of SiC Power Electronic Devices," pp. 43–47 in *IEEE Workshop on Power Electronics in Transportation,* October 21–22, 2004, Dearborn, Michigan.

M. Chinthavali, B. Ozpineci, L. M. Tolbert, "Enhancing Power Electronic Devices with Wide Bandgap Semiconductors," *International Journal of High Speed Electronics*, in press.

M. Chinthavali, B. Ozpineci, L. M. Tolbert, "High Temperature and High Frequency Performance Evaluation of 4H-SiC VJFET and Schottky Diodes," *IEEE Applied Power Electronics Conference,* March 6–10, 2005, Austin, Texas.

B. Ozpineci, M. Chinthavali, L. M. Tolbert, "A 55 kW Three-Phase Automotive Traction Inverter with SiC Schottky Diodes," *IEEE Vehicle Power and Propulsion (VPP) Conference*, September 7–9, 2005, Illinois Institute of Technology, Chicago, IL.

M. Chinthavali, B. Ozpineci, L. M. Tolbert, A. S. Kashyap, *Wide Bandgap Electronics,* ORNL TM report, October 2005.

References

1. B. Ozpineci, L. M. Tolbert, S. K. Islam, and F. Z. Peng, "Testing, Characterization, and Modeling of SiC Diodes for Transportation Applications," pp. 1673–1678 in *IEEE Power Electronics Specialists Conference*, Cairns, Australia, June 23–27, 2002.
2. L. M. Tolbert, B. Ozpineci, S. K. Islam, and F. Z. Peng, "Impact of SiC Power Electronic Devices for Hybrid Electric Vehicles," pp. 765–771 in *SAE 2002 Transactions Journal of Passenger Cars–Electronic and Electrical Systems*, ISBN 0-7680-1291-0, 2003.

3. M. Ruff, H. Mitlehner, and R. Helbig, "SiC Devices: Physics and Numerical Simulation," pp. 1040–1054 in *IEEE Transactions on Electron Devices*, June 1994.
4. D. Peters, H. Mitlehner, R. Elpelt, R. Schorner, and D. Stephani, "State of the Art Technological Challenges of SiC Power MOSFETs Designed for High Blocking Voltages," *European Conference on Power Electronics and Applications*, Toulouse, France, September 2–4, 2003.
5. S. H. Ryu, A. Agarwal, J. Richmond, J. Palmour, N. Saks, and J. Williams, "10 A, 2.4 kV Power DIMOSFETs in 4H-SiC," pp. 321–323 in *IEEE Electron Device Letters*, June 2002.
6. M. Chinthavali, B. Ozpineci, and L. M. Tolbert, "Enhancing Power Electronic Devices with Wide Bandgap Semiconductors," Advanced Workshop on 'Frontiers of Electronics' (WOFE'04), Aruba, December 17–22, 2004.
7. A. S. Kashyap, "Compact Modeling of Silicon Carbide Junction Field Effect Devices," M.S. Thesis, Department of Electrical Engineering, University of Arkansas, Fayetteville, Arkansas, 2005.

4.2 Integrated dc/dc Converter for Multi-Voltage Bus Systems

Principal Investigator: Gui-Jia Su
Oak Ridge National Laboratory
National Transportation Research Center
2360 Cherahala Boulevard
Knoxville, TN 37932
Voice: 865-946-1330; Fax: 865-946-1400; E-mail: sugj@ornl.gov

DOE Technology Development Manager: Susan A. Rogers
Voice: 202-586-8997; Fax: 202-586-1600; E-mail: Susan.Rogers@ee.doe.gov

ORNL Program Manager: Mitch Olszewski
Voice: 865-946-1350; Fax: 865-946-1262; E-mail: olszewskim@ornl.gov

---

Objectives

- Develop integrated dc/dc converters for triple-voltage busses (14-V/42-V/high-voltage) to reduce component count, size, and cost.
- Produce converter prototypes and testing data that can demonstrate the converter's capability for bidirectional power flow control among the three busses and can be useful in setting FreedomCAR technical targets for dc/dc converters.

Approach

The following approaches are taken to reduce the cost and size, and to increase the efficiency and power density, of dc/dc converters for multi-bus systems in hybrid electric vehicles (HEVs) and fuel cell–powered vehicles (FCVs).

- Minimize the number of switches and thus the associated gate drivers to reduce the components count and cost.
- Employ soft switching and synchronous rectification to increase efficiency and power density.
- Employ soft switching to lower electromagnetic interference (EMI) noise.
- Refine the topology to further reduce the components count.
- Use flexible topology—same circuit applicable to both dual- and triple-voltage systems.

Major Accomplishments

- A half-bridge–based dc/dc converter was developed that can interconnect the three voltage busses and can reduce component count by 50% compared with conventional technologies. A novel control scheme was also devised that can control the power flow among the three busses.
- For hardware demonstration and to produce test data for cost and performance evaluation, a 2-kW converter prototype was designed and built.
- Testing of the converter was successfully completed and a conversion efficiency of 92 % was achieved over a wide load range.
- To further reduce the component count, a reduced-parts converter was designed and fabricated. Initial testing data have proved the concept and indicated it is a promising alternative topology. Further testing will be conducted to gather performance data.

Technical Discussion

Introduction

The 14-V electrical system in current automobiles has reached its capability limits and cannot meet the demands of future electrical loads. As HEVs and FCVs emerge, there is an increasing desire to replace more engine-driven mechanical and hydraulic systems with electrical systems to increase efficiency. Presently, 42-V systems are being proposed to cope with the increasing electrical loads. During the transition to the 42-V system, most automobiles are expected to employ a 14-V/42-V dual-level voltage system, in which a bi-directional dc/dc converter is required to connect the two voltage networks. Additionally, most battery-powered HEVs employ a high-voltage (200 ~ 500-V) bus for the traction motor drive. In HEVs with a 42-V alternator, a dc/dc converter supplied from the 42-V bus may be used to charge the high-voltage battery, as shown in Figure 1(a). On the other hand, for HEVs having a generator directly connected on the high-voltage bus, a dc/dc converter is typically required to charge the 14-V and/or 42-V batteries.

Furthermore, FCVs will require a bi-directional dc/dc converter to interconnect the fuel cell–powered high-voltage bus and the low-voltage busses for vehicle auxiliary loads. For the reasons mentioned earlier, both the 14-V and 42-V busses may be employed to power vehicle accessory loads, as shown in Figure 1(b). An energy storage device is also required for fuel cell start-up and for storing the energy captured by regenerative braking, because the fuel cells lack energy storage capability. One way to accomplish this is to use the vehicle 14-V or 42-V battery with the bi-directional dc/dc converter. During vehicle starting, the high-voltage bus is boosted up to around 300 V by the dc-dc converter drawing

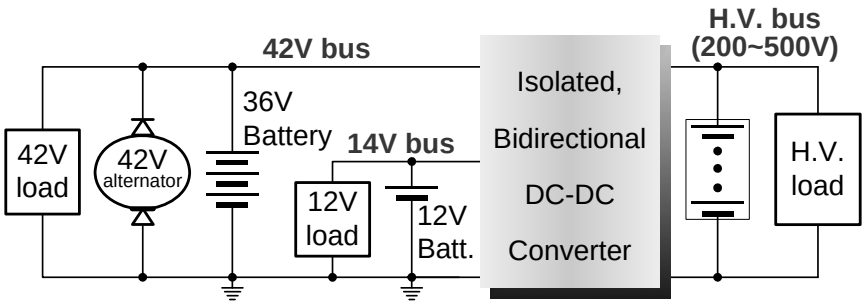

(a) Hybrid electric vehicles

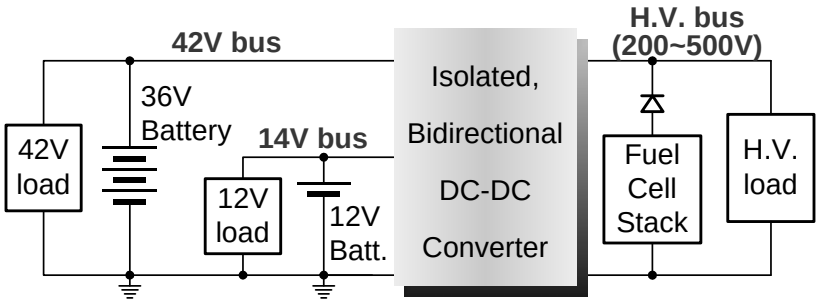

(b) Fuel cell–powered vehicles

Figure 1. A dc/dc converter interconnecting 14-V/42-V/high-voltage bus nets in HEVs and FCVs.

power from the 14-V or 42-V battery. This high-voltage bus then supplies power for the fuel cell compressor motor expanding unit controller and brings up the fuel cell voltage, which in turn feeds back to the high-voltage bus to release the loading from the battery.

In summary, a triple-voltage bus system (14-V/42-V/high-voltage) will likely be employed in HEVs and FCVs, as shown in Figure 1, before all vehicle auxiliary electrical components are moved to the 42-V bus. While dc/dc converters are available to interconnect any two of the busses, to reduce component count, size, cost, and volume, it is desirable to employ an integrated dc/dc converter to interconnect the three voltage busses instead of using two separate converters. Aside from bi-directional power control capability, the converter needs to provide galvanic isolation between the low- and high-voltage busses to meet safety requirements. Further, soft switching is preferred over hard switching because it offers a reduced level of EMI and switching losses.

In this project, a low-cost, soft-switched, isolated bi-directional dc/dc converter is being developed for interconnecting the three bus nets. The converter is based on a dual half-bridge topology and uses snubber capacitors and the transformer leakage inductance to achieve zero-voltage switching (ZVS). Therefore, no extra resonant components are required for ZVS, further reducing the component count. The inherent soft-switching capability and the low component count of the converter allow high powerdensity, efficient power conversion, and compact packaging. A novel power flow control scheme based on a combined duty ratio and phase shift angle control was also devised. A 2-kW prototype was designed, built, and tested to produce hardware demonstration and testing data that will be useful in setting FreedomCAR technical targets for dc/dc converters.

dc/dc Converter for Triple Voltage Busses

Description of the dc/dc converter

Figure 2 shows a schematic of the dc/dc converter, which consists mainly of dual half-bridge inverters/converters and a high-frequency transformer, *Tr*. The high-frequency transformer provides the required galvanic isolation and voltage level matching between the 14-V and 42-V busses and the high-voltage bus, while the 14-V and 42-V busses share a common ground. The leakage inductance of the transformer is used as the intermediate energy storing and transferring element between the two low-voltage busses and the high-voltage net. The snubber capacitors, C_{r1}~C_{r4}, resonate with the transformer leakage inductance to provide ZVS.

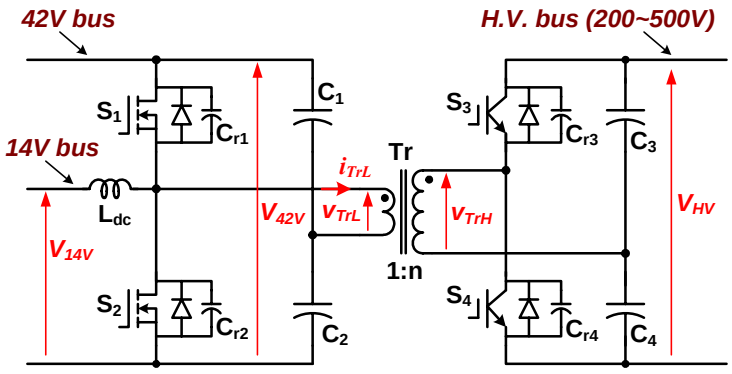

Figure 2. Schematic of the soft-switched bi-directional dc/dc converter.

Duty ratio control is used for power flow control between the 14-V and 42-V busses, making the two bus voltages, V_{14V} and V_{42V}, track to each other by $V_{14V}=d \cdot V_{42V}$, where d is the duty ratio of the switches S_1 and S_3. For 14-V/42-V systems, the duty ration is fixed at d=1/3 for normal operation and can be changed

to adjust the state of charge of the low-voltage batteries if necessary. In addition, a phase shift angle, ϕ, between the transformer primary and secondary voltages is employed for power flow control between the 42-V and high-voltage busses as shown in Figure 3, where d=1/3. The power transferred through the transformer can be expressed by

$$P = \frac{V_{42v} V_{HV}}{n} \cdot \frac{\phi}{2\pi f_{sw} L_s} \cdot [\frac{2}{9} - \frac{\phi}{4\pi}] \ , \qquad (1)$$

where n is transformer turns ratio, Ls is transformer leakage inductance, and fsw is switching frequency.

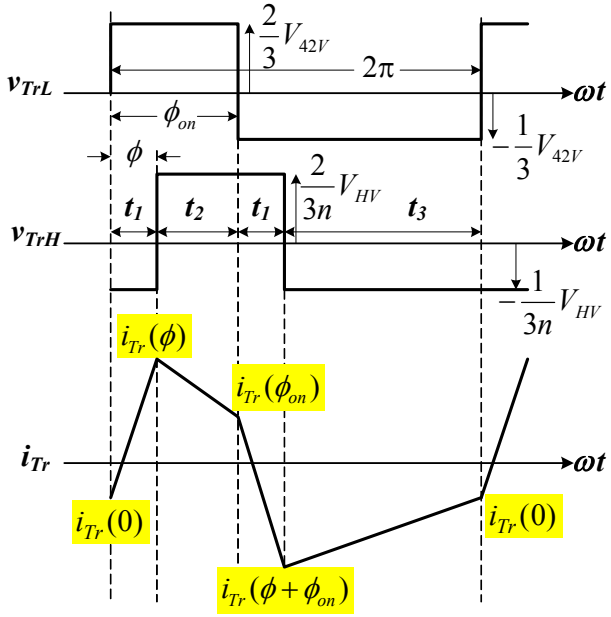

Figure 3. Ideal transformer voltage and current waveforms illustrating power flow control between the 42-V and high-voltage busses at d=1/3.

For a given design, the maximum power is determined by

$$P_{\max} = \frac{V_{42v} V_{HV}}{n} \cdot \frac{2}{81 f_{sw} L_s} \text{ at } \phi_{P_{\max}} = \frac{4\pi}{9} . \qquad (2)$$

Figure 4 plots the power versus the phase shift angle at different voltage levels of V_{HV} with n=8, Ls=0.16µH, fsw=40 kHz, and V_{42v}=42V for a prototype design.

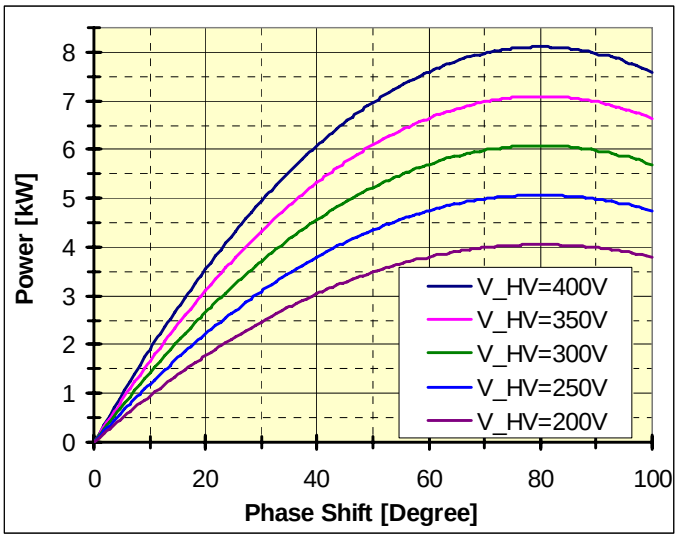

Figure 4. Power v.s. phase shift angle at various levels of V_{HV} (n=8, Ls=0.16µH, fsw=40 kHz, V_{42v}=42V).

Simulation and Experimental Results

A 2-kW prototype was designed, built, and tested to verify the power flow control scheme and to evaluate its performance. Specifications of the prototype are listed below.

- Rating: 2 kW continous/5 kW maximum
- Efficiency: >92% over a wide load range

A detailed circuit simulation was first performed to verify the design goal, which is to guarantee at least 2 kW of power can be transferred through the transformer at a voltage range of 200~400V for the high-voltage bus. Figure 5 shows simulation results where power is transferred from the low-voltage busses to the high-voltage net, in (a) at V_{HV}=200V, 2.1 kW is provided to the high-voltage bus, while in (b) at V_{HV}=400V, power is increased to 5.1 kW. Figure 6 shows simulated waveforms when the power flow is reversed. The simulation results confirm the design goal of the power ratings.

A 2-kW prototype was then designed and built based on the analytical, simulation, and preliminary proof-of-concept testing results. Figure 7 shows a photo of the prototype, which is laid on a 0.375-in. liquid-cooled heat sink with a footprint 7.5 in. wide by 13.5 in. long. It was intentionally laid loosely to provide spaces for easy probing access.

The high-voltage switches are implemented with two CoolMOS metal oxide semiconductor field-effect transistors (MOSFETs made by IXYS, which are rated at 600V/50A with an on-resistance of 35 mΩ. High-speed insulated-gate bipolar transistors (IGBTs) will also be tested. The low-voltage switches are MOSFETs made by International Rectifier, rated at 75V/90A with an on-resistance of 4.5 mΩ.

The inductor was fabricated using a Metglas^{TM} amorphous,C-core (AMCC-32) with the following specifications:

- Winding: 16-mil-thick copper foil
- Inductance: 10 µH
- Current rating: 100 A

The high-frequency transformer was fabricated using Ferroxcube E-cores, E65/32/27. Two different grades of soft ferrite, 3F3 and 3C94, will be tested for the transformer core. The primary winding uses a 10-mil-thick copper foil and has two turns, while the secondary winding uses 3 litz wires of 16 AWG in parallel and has 16 turns. The two windings are interleaved to minimize the leakage inductance.

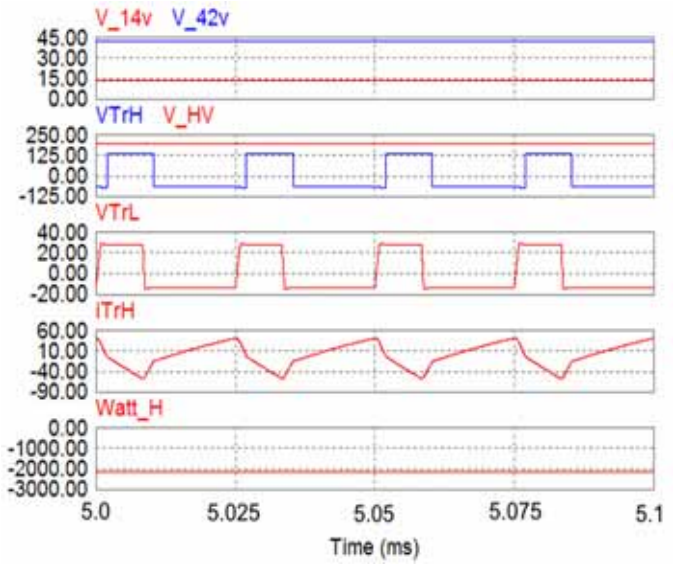

(a) V_{HV}=200V, power transferred to the high-voltage bus: 2.1 kW

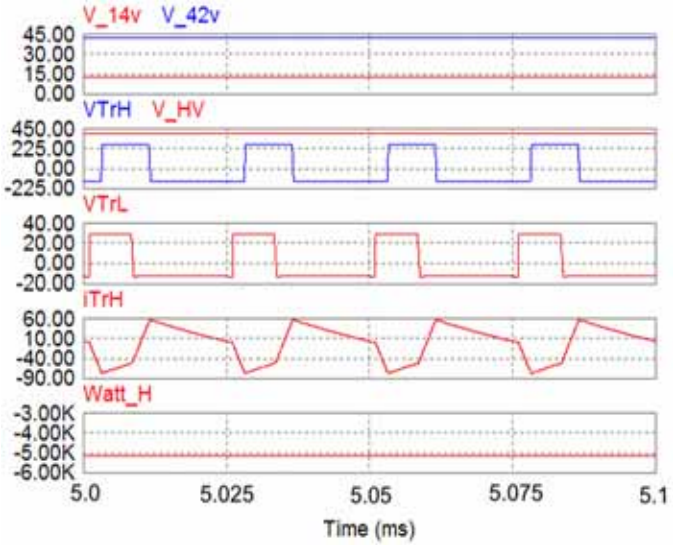

(b) V_{HV}=400V, power transferred to the high-voltage bus: 5.1 kW

Figure 5. Simulation results showing power is transferred from the low-voltage busses to the high-voltage net.

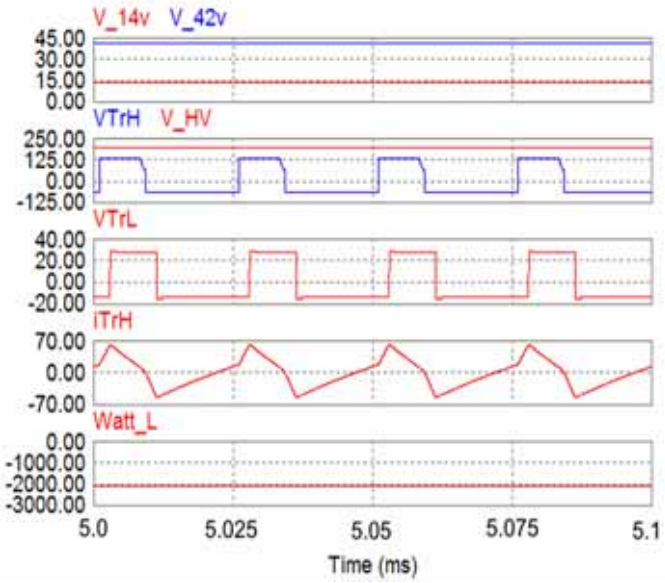

(a) V_{HV}=200V, power transferred to the low-voltage busses: 2.0 kW

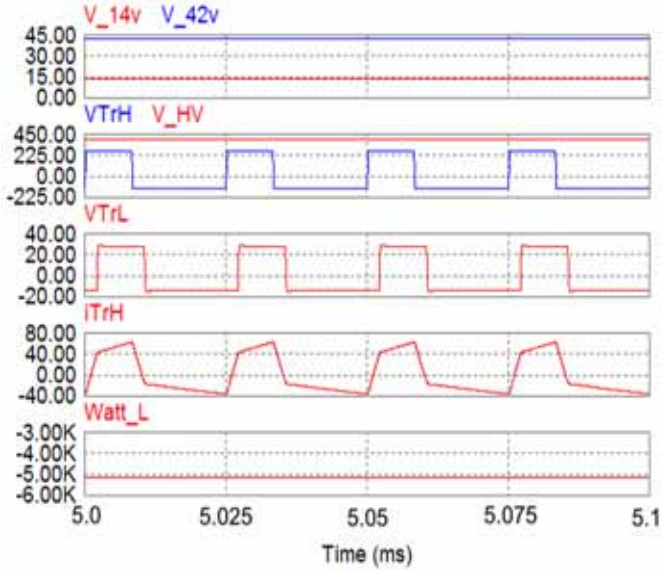

(b) V_{HV}=400V, power transferred to the low voltage busses: 5.1 kW

Figure 6. Simulation results illustrating power is transferred from the high-voltage net to the low-voltage busses.

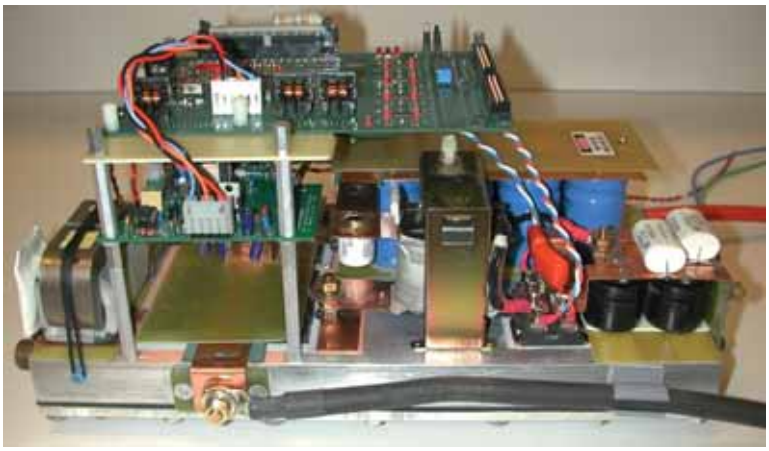

Figure 7. Photo of the prototype.

Figures 8, 9, and 10 show typical testing waveforms when power was transferred from the 42-V bus to the 14-V and high-voltage busses, from the high-voltage bus to the 14-V and 42-V busses, and from the14-V bus to the high-voltage and 42-V busses, respectively. Figure 11 plots power conversion efficiency against the output power, indicating efficiencies of 92 % were achieved over a wide load range.

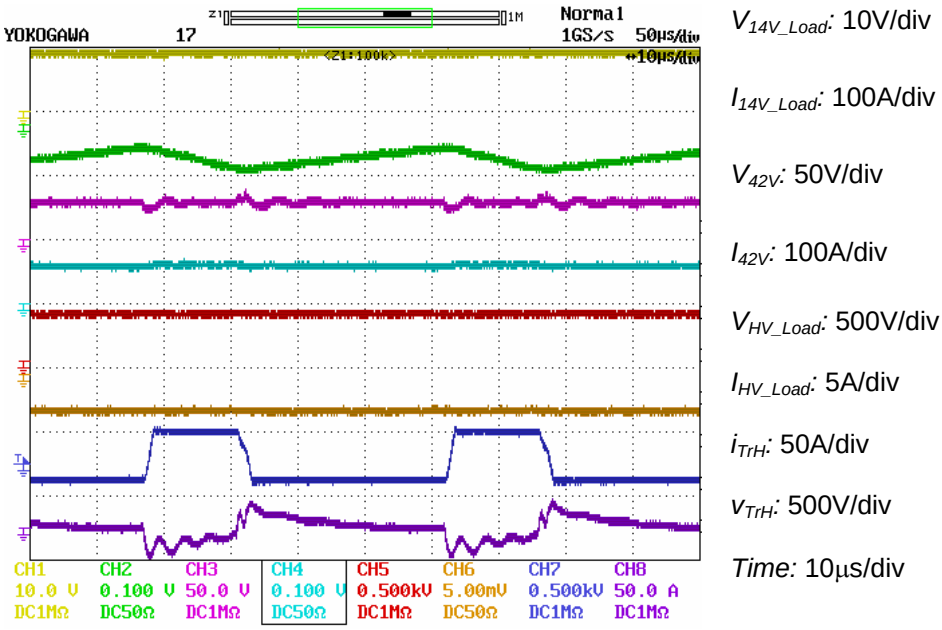

Figure 8. Typical testing waveforms for 42-V to 14-V and high-voltage power transfer.

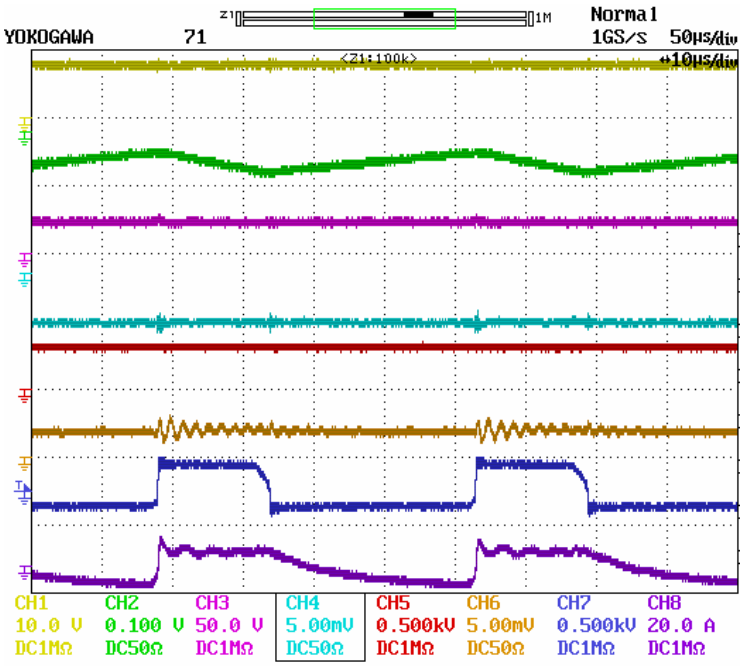

V_{14V_Load}: 10V/div

I_{14V_Load}: 100A/div

V_{42V_Load}: 50V/div

I_{42V_Load}: 5A/div

V_{HV}: 500V/div

I_{HV_Load}: 5A/div

i_{TrH}: 50A/div

v_{TrH}: 500V/div

Time: 10µs/div

Figure 9. Typical testing waveforms for high-voltage to 14-V and 42-V power transfer.

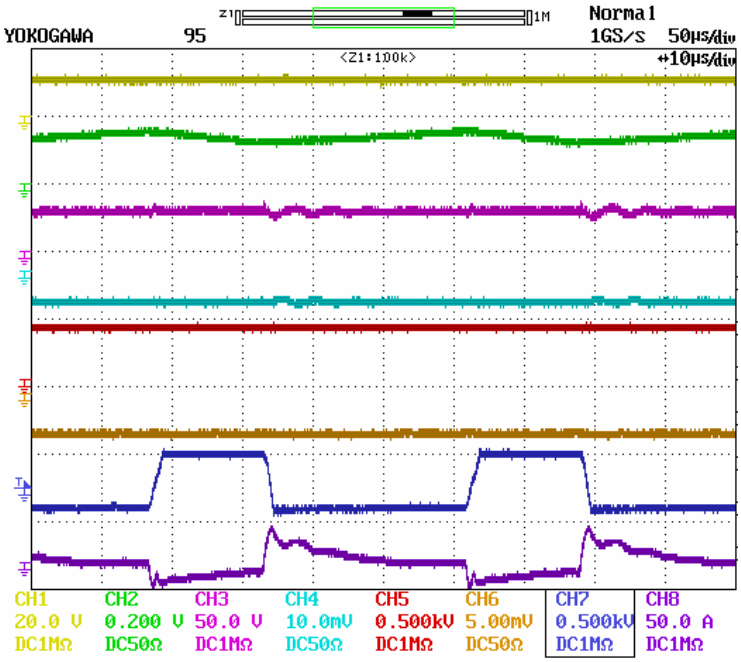

V_{14V}: 20V/div

I_{14V}: 200A/div

V_{42V_Load}: 50V/div

I_{42V_Load}: 10A/div

V_{HV_Load}: 500V/div

I_{HV_Load}: 5A/div

i_{TrH}: 50A/div

v_{TrH}: 500V/div

Time: 10µs/div

Figure 10. Typical testing waveforms for 14-V to 42-V and high-voltage power transfer.

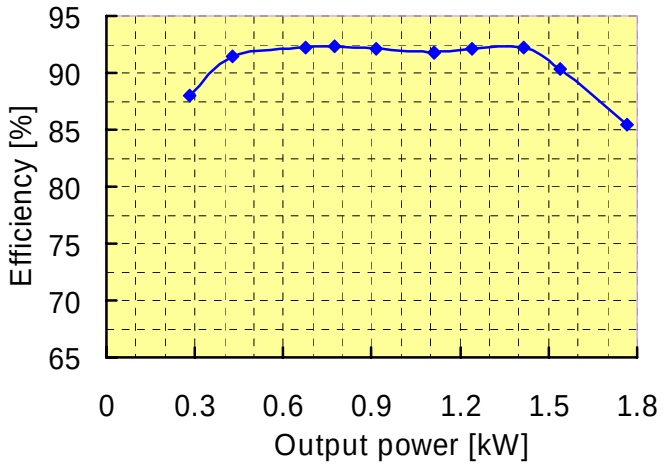

Figure 11. Efficiency chart.

Reduced-Part-Count dc/dc Converter for Triple Voltage Busses

To further reduce the component count, weight, and size of the converter, the inductor, L_{dc} in Figure 2, which is the heaviest part except for the aluminum heat sink, has been eliminated. A 2-kW prototype was designed and fabricated. Figure 12 shows a photo of the reduced-part-count prototype. Initial testing was conducted for power transfer between the 42-V and high-voltage busses. Figures 13 and 14 show testing waveforms when power was transferred from the 42-V bus to the 14-V and high-voltage busses at 1.1 kW and 1.4 kW, respectively. Figure 15 illustrates waveforms when power was transferred from the high-voltage bus to the 14-V and 42-V busses at 0.54 kW. The initial testing results clearly verified the bi-directional power flow control capability of the reduced part count version. Further testing will be conducted to collect data for cost and performance evaluations.

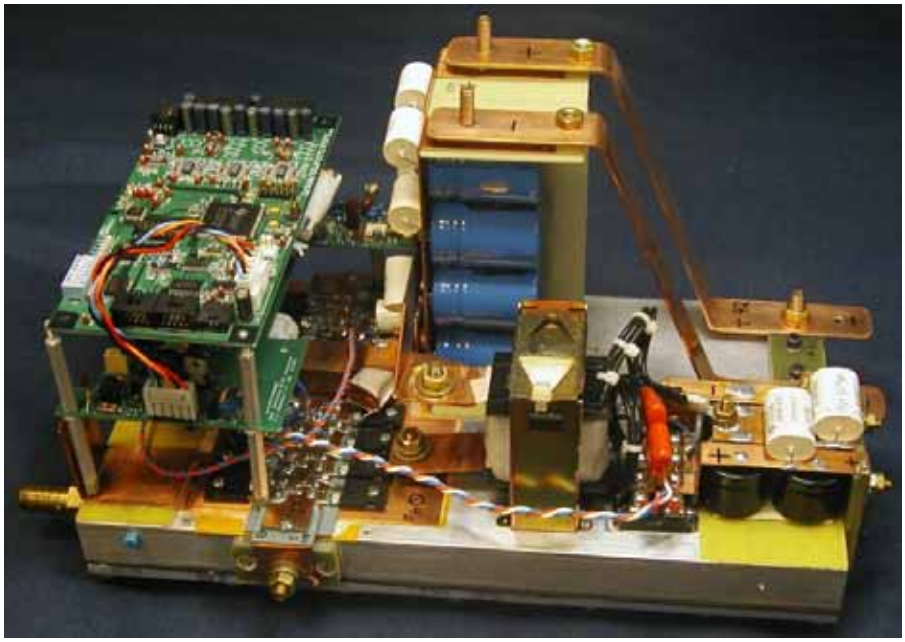

Figure 12. Photo of the reduced-part count prototype.

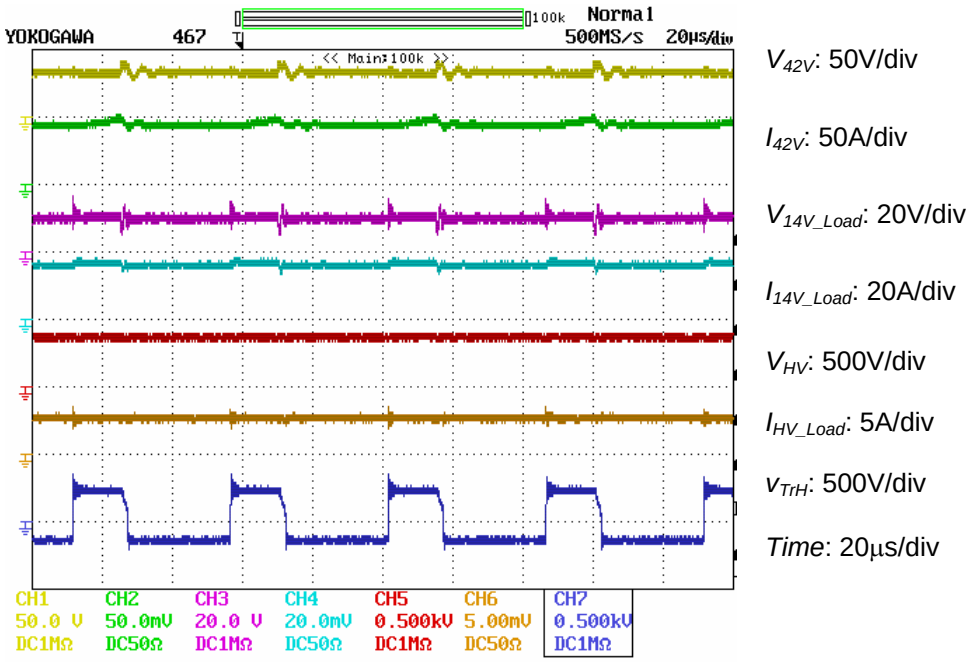

Figure 13. Testing waveforms for 42-V to 14-V and high-voltage power transfer at 1.1 kW.

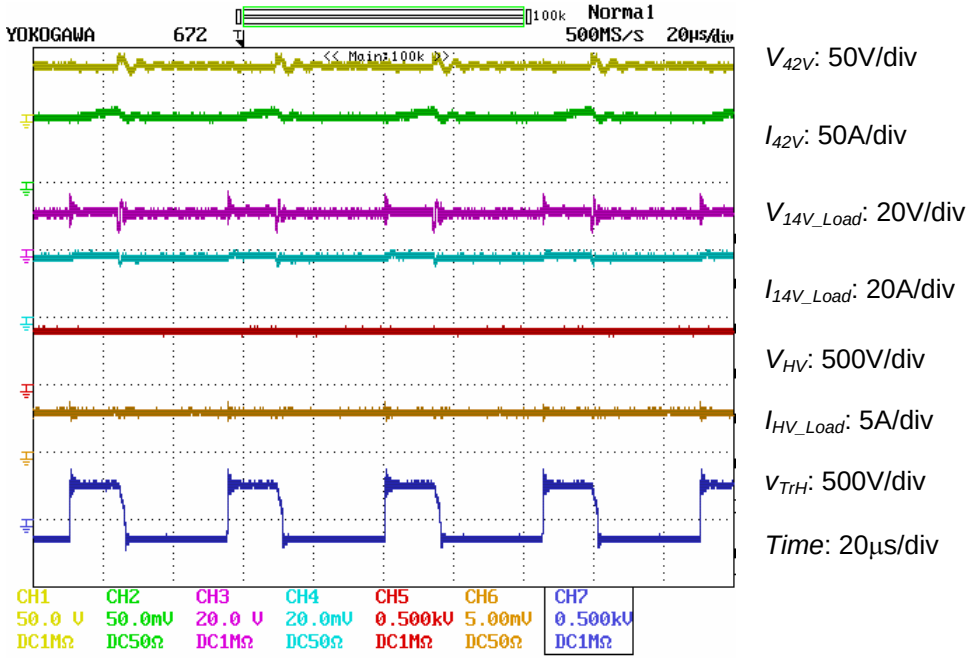

Figure 14. Testing waveforms for 42-V to 14-V and high-voltage power transfer at 1.4 kW.

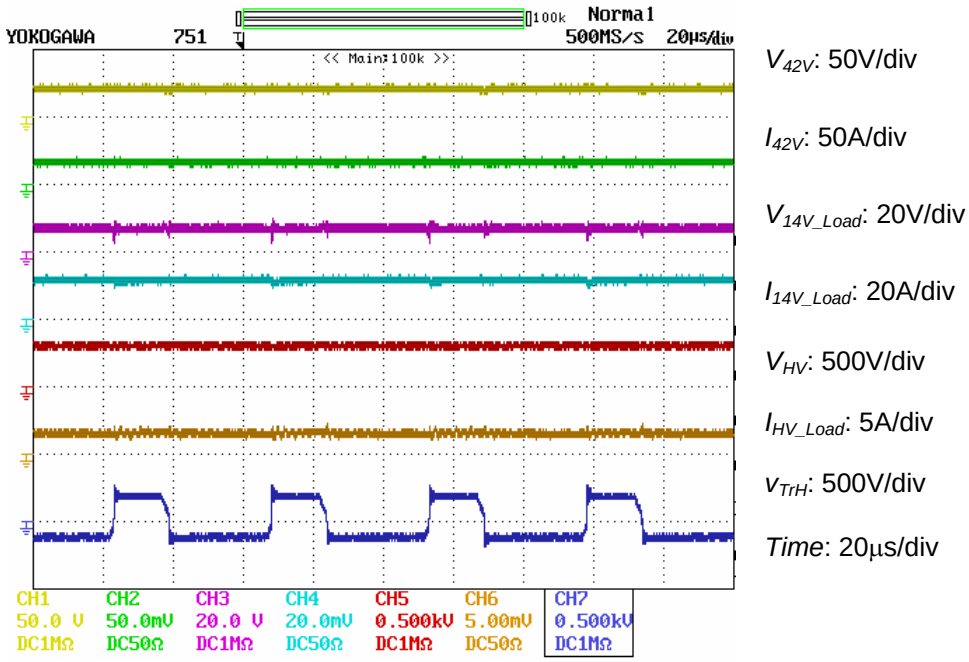

Figure 15. Testing waveforms for high-voltage to 42-V and 14-V power transfer at 0.54 kW.

Conclusions

The developed integrated dc/dc converters for triple-voltage-bus (14-V/42-V/high-voltage) systems for HEV and FCV applications has the following features:

- Uses only four switching devices, leading to significant cost savings and higher power density.
- Employs soft switching and synchronous rectification, contributing to high efficiency and low EMI.
- Requires no auxiliary circuits or complex control dedicated for soft switching.
- Uses flexible power flow management as a result of the capability to transfer power among all three voltage busses by employing a combined duty ratio and phase shift angle control scheme.

Simulation and testing results on a 2-kW prototype have confirmed the operating principles, demonstrated efficiencies of up to 92 %, and shown that the number of components can be reduced by 50 % over conventional technologies. The initial testing data on the reduced-part version proved the concept and indicated that it is a promising alternative to the first version. Future testing will provide data for detailed performance and cost analysis.

Future Direction

To increase power levels, a modular approach using the 2-kW converter as a building block for higher power units will be explored.

Publications

"A Low Cost, Triple-Voltage Bus DC/DC Converter for Automotive Applications," pp. 1015–21 in *IEEE Applied Power Electronics Conference and Exposition* (APEC), vol. 2, March 6–10, 2005, Austin, Texas.

"A Small Signal Analysis of A Dual Half Bridge Isolated ZVS Bi-directional dc-dc Converter for Electrical Vehicle Applications," pp. 2777–82 in *Proceedings of IEEE PESC'05*, June 12–16, 2005, Recife, Brazil.

"A Low Cost, Triple-Voltage Bus DC/DC Converter for Automotive Applications," submitted to *IEEE Transactions on Industry Applications*.

4.3 Integrated Inverter for HEVs and Fuel Cell Powered Vehicles

Principal Investigator: Gui-Jia Su
Oak Ridge National Laboratory
National Transportation Research Center
2360 Cherahala Boulevard
Knoxville, TN 37932
Voice: 865-946-1330; Fax:865-946-1400; E-mail:sugj@ornl.gov

DOE Technology Development Manager: Susan A. Rogers
Voice:202-586-8997;Fax: 202-586-1600; E-mail:Susan.Rogers@ee.doe.gov

ORNL Program Manager: Mitch Olszewski
Voice: 865-946-1350; Fax:865-946-1262; E-mail: olszewskim@ornl.gov

---

Objectives

- Develop integrated power conversion topologies to reduce the component count, size, and cost of power electronics systems for traction drives and compressor motor drives in hybrid electric vehicles (HEVs) and fuel cell–powered vehicles (FCVs) by reducing the cost and size of the compressor drive by 30%.
- Produce a 75-kW/5-kW dual inverter prototype and demonstrate its capability to independently control three-phase main and two-phase auxiliary permanent magnet (PM) motors.

Approach

- In order to reduce the cost of a compressor drive in HEVs and FCVs, a two-phase motor and inverter was employed to reduce the manufacturing cost of the motor as a result of eliminating one stator phase winding. While a stand-alone two-phase inverter may require three or four phase legs, the number of phase legs was reduced to two by integrating the inverter into the three-phase inverter of the traction motor drive, yielding a 1/3 reduction in the number of switches and associated gate driver components compared with a three-phase inverter. The integration further enables sharing of the dc bus filter capacitors, gate drive power supplies, and control circuitry between the two inverters. In short, a 30% reduction in compressor drive cost and size can be achieved through the use of this concept.

Major Accomplishments

- To demonstrate the size reduction of the compressor drive and to experimentally verify the capability of independently controlling two motors, a 75-kW/5-kW dual inverter prototype was designed and built using the latest trench-gate insulated gate bipolar transistor (IGBT) power modules. A new digital signal processing (DSP) control board based on a Texas Instruments chip has also been designed and fabricated for controlling the IGBTs in the dual inverter. Testing of the inverter controlling two PM motors was completed successfully. A 30% reduction in the compressor drive's component cost and size was achieved compared with a three-phase alternative approach.

Technical Discussion

1. Background

Traditionally, in vehicles powered by internal combustion engines, the engine drives the compressor for heating, ventilating, and air-conditioning (HVAC). The efficiency of the air-conditioning system is not optimized, as the compressor is operated in repetitive run-and-stop modes according to the thermostat settings, and must follow engine speeds. Switching to a motor-driven compressor allows the use of continuously adjustable speed control to reduce air-conditioner energy consumption and enhance HVAC performance by changing the compressor speed according to the cooling/heating requirements. Because of their superior performance compared with their conventional engine-belt–driven counterparts, electric-motor–driven compressors are being deployed in automobiles with a 42-V power net and in HEVs where a high-voltage bus is readily available. Other advantages of electrically driven HVAC compressors are that

- The operating speed can be increased to a much higher level to substantially reduce the size of the motor and compressor.
- The packaging is more flexible, as the location is not restricted to the accessory drive side of the engine.
- Refrigerant leakage into the atmosphere is reduced because rotating seals are eliminated.
- Tailpipe emissions are reduced and fuel economy is improved because the electric compressor enables HEVs to shut off the engine during vehicle stops or at low vehicle speeds when engine power is not required.

Moreover, FCVs require an electrically-driven HVAC compressor.

Figure 1 shows an existing configuration in HEVs that employ two separate three-phase inverter drives for traction and compressor motors. To reduce the cost of the automotive accessory drives such as compressor motors, two-phase inverter-fed induction motor drives have been used to replace wound-field or PM dc motors for heating, ventilating, demisting, engine cooling, and water-pumping applications in the automotive industry. A two-phase motor can be controlled by either a four-leg inverter or a lower-cost two-leg inverter plus a split-capacitor leg, as illustrated in Figure 2. A three-phase motor fed by a three-phase inverter typically requires a three-leg inverter employing six switches. Unlike a semiconductor switch leg, the split-capacitor leg does not need additional gate drive or control circuits. Capacitors, however, have their own drawbacks, such as lower reliability and a short service lifespan. These drawbacks become aggravated by the harsh environments expected in HEV/FCV applications. It is therefore desirable to eliminate the split-capacitor leg.

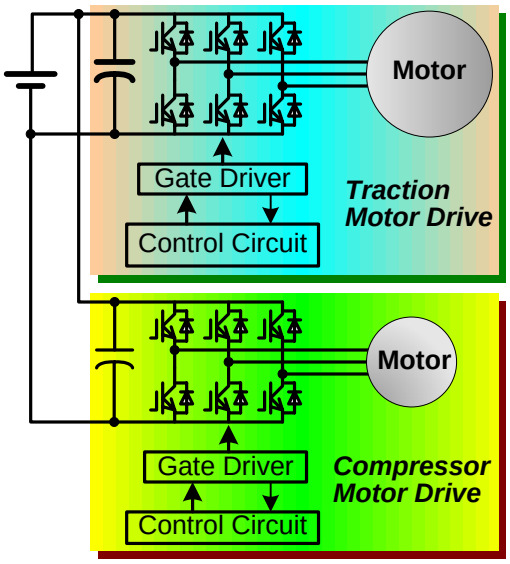

Figure 1. Existing configuration employing two separate three-phase inverter drives for traction and compressor motors in HEVs.

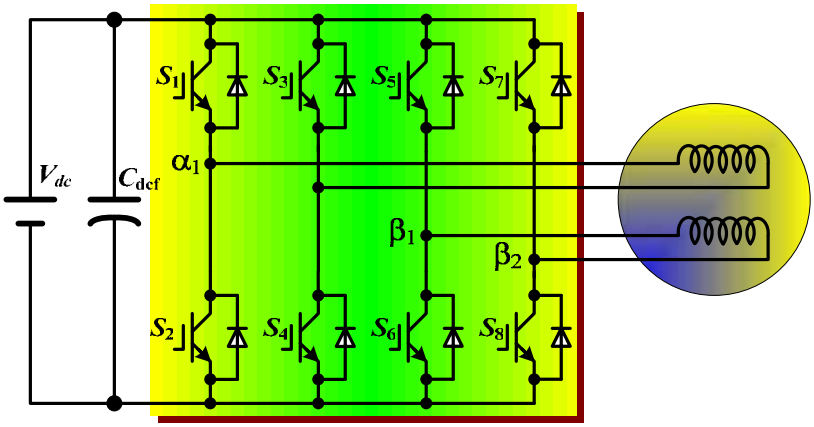

(a) Four-leg two-phase inverter

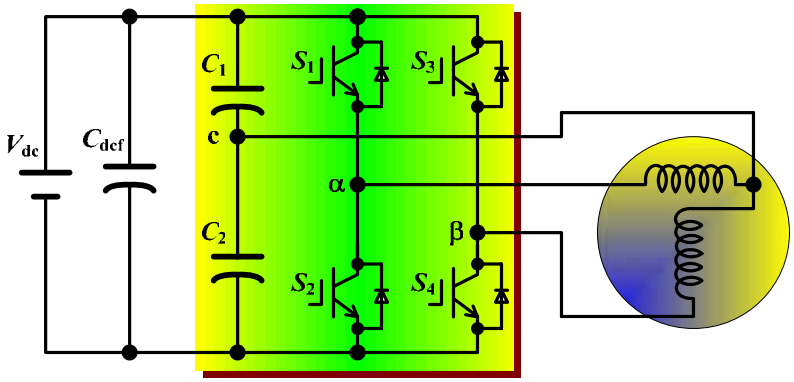

(b) Three-leg two-phase inverter

Figure 2. Possible two-phase motor drive configurations.

In this project, an integrated dual inverter with five legs has been developed for speed control of a three-phase traction motor and a two-phase compressor motor to further reduce the compressor drive cost. The two-phase inverter is first integrated into the three-phase inverter for the traction motor, so the dc bus filter capacitors, gate drive power supplies, and control circuit can be shared. Furthermore, the split-capacitor leg is eliminated by tying the common terminal of the two-phase motor to the neutral point of the three-phase traction motor. Integrating the compressor drive into the traction motor drive in this fashion results in a lower-cost, smaller-volume drive system. Both simulation studies and prototype testing with induction motors conducted in the previous year have verified the independent speed control of the two motors. While induction motors cost less, PM motors provide higher efficiency and power density. They also have different control requirements. This report concentrates on the design, fabrication, and testing of a new 75-kW/5-kW dual inverter controlling two PM motors.

2. Integrated Dual Inverter Topology

Description of the intergrated dual inverter

Figure 3 shows the proposed five-leg integrated inverter for driving a three-phase traction motor and a two-phase compressor motor. The inverter consists of a dc source, V_{dc}; a filter capacitor, C_{dcf}; and five phase legs, U, V, and W for feeding the traction motor, and a and b for the compressor motor. The two-phase motor has two windings, phase-a and phase-b; and the two phase windings are connected at one end to form a common terminal, T_{com}, with the other ends remaining separated to form two independent phase terminals, T_a and T_b.

The first three legs of the inverter—U, V, and W, consisting of the switches S1~S6—form the three-phase main inverter, which through pulse-width modulation (PWM) provides three sinusoidal currents to the three-phase motor. The remaining two legs, a and b, are connected to the independent phase terminals of the two-phase motor, T_a and T_b, respectively, forming an auxiliary two-phase inverter. In addition, the common terminal, T_{com}, is connected to the neutral point, N, of the three-phase motor to eliminate the split-capacitor phase leg. The two phase legs, a and b, use PWM to provide two sinusoidal currents with a phase shift of 90 electrical degrees from the two-phase motor. The sum of the two-phase currents, i_a and i_b, will split evenly into three parts; each part flows through one of the phase windings of the three-phase motor and the associated phase leg of the three-phase inverter as the return path.

Figure 4(a) shows an equivalent circuit of the integrated drive system, in which the inverter is represented by five voltage sources—v_u, v_v, v_w, v_a and v_b—corresponding to the five phase legs, U, V, W, a, and b, respectively. All the voltage sources are referred to the midpoint of the dc source, V_{dc}. By connecting the common terminal, T_{com} to the neutral point, N, of the three-phase motor, the sum of the two-phase currents, i_N (= i_a + i_b), will split evenly into three parts. Each part will flow through one of the phase windings of the three-phase motor and the associated phase leg of the three-phase inverter as the return path, assuming a symmetrical three-phase motor and inverter. The two-phase motor currents are therefore zero-sequence components flowing in the three-phase stator and will have no effect on the operation of the three-phase motor because the zero-sequence currents will not produce torque, as shown in Figure 4(b). In other words, the torque-producing currents of the two motors can be controlled independently.

In Figure 4(b), the zero-sequence circuit (ZSC) of the three-phase stator is separated from the positive and negative sequence circuits, where R_{ms} and l_{m0s} represent the resistance and inductance of the ZSC, and v_0 is the zero-sequence component of the three-phase voltage sources, v_u, v_v, and v_w, which may or may not exist depending on the PWM scheme. The zero-sequence voltage, v_0, can be calculated by

$$v_0 = \frac{v_u + v_v + v_w}{3} \tag{1}$$

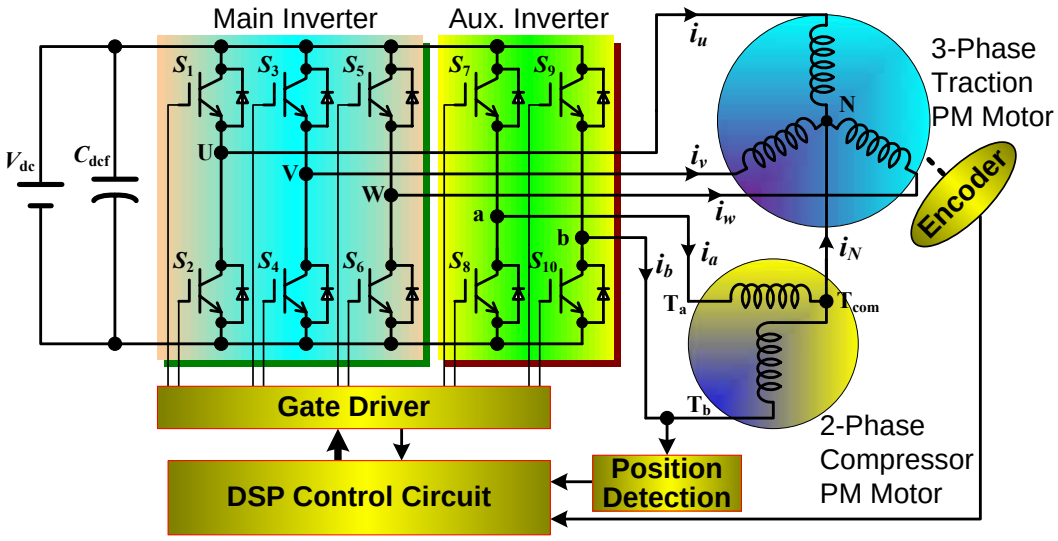

Figure 3. Proposed integrated inverter for driving a three-phase traction motor and a two-phase compressor motor.

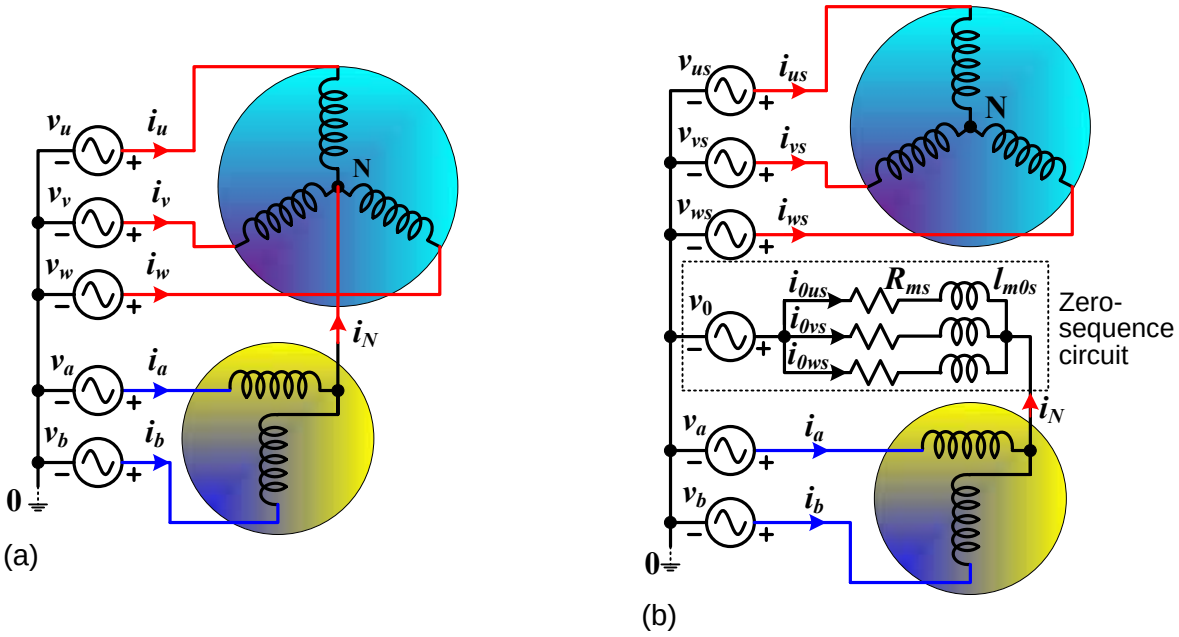

Figure 4. Equivalent circuits showing (a) inverter phase legs as voltage sources and (b) the zero-sequence circuit of the main motor as the current return path of the two-phase motor.

The terms v_{us}, v_{vs}, and v_{ws} are the phase voltages referenced to the zero-sequence voltage of the three phases U, V, and W, respectively, and are expressed by

$$\begin{cases} v_{us} = v_u - v_0 \\ v_{vs} = v_v - v_0 \\ v_{ws} = v_w - v_0 \end{cases}. \quad (2)$$

The zero-sequence voltage component, v_0, which could be generated by certain PWM strategies such as space vector modulation schemes, can be cancelled by injecting the same component into the modulation signals for the two-phase inverter so that v_0 will not produce current in the circuit, as will be shown in the simulation and experimental results.

Effects on the current rating of the main motor

Because the stator windings of the three-phase motor are used as the current return paths of the two-phase motor, the stator current rating may need be increased to accommodate the two-phase motor currents. However, the increase of the main motor current is negligible if the two-phase motor current is sufficiently small compared with that of the main motor, which is typical in the intended automotive applications, as shown below.

The phase-U current of the main motor i_u can be expressed by

$$i_u = i_{us} - \frac{i_a + i_b}{3}, \quad (3)$$

where i_{us} is the required current if the three-phase motor is operated alone without connection to the two-phase motor. Because the two motor currents will usually have different frequencies, the r_{ms} value of the main motor phase current, i_u, can therefore be calculated by

$$I_{u,rms} = \sqrt{I_{us,rms}^2 + \frac{2I_{a,rms}^2}{9}}, \quad (4)$$

where $I_{a,rms}$ is the required rms current of the two-phase motor. For instance, given a 350-A_{rms} traction motor and a 25-A_{rms} compressor motor, i.e., $I_{us,rms}$=350A and $I_{a,rms}$=25A, the resulting traction motor current is

$$I_{u,rms} = \sqrt{350^2 + \frac{2 \times 25^2}{9}} = 350.2\text{Arms}, \quad (5)$$

giving a negligible increase of 0.2 A, less than 0.06%.

Component count reduction

Compared with the conventional system consisting of two separate three-phase inverters, one phase-leg including two switches and their associated gate drivers can be eliminated. Moreover, it is apparent that by integrating the two-phase auxiliary inverter into the main three-phase inverter, the dc bus filter capacitor and gate drive power supplies can be shared between the two inverters. Furthermore, a single control circuit typically based on a microprocessor or digital signal processor (DSP) with built-in motor control hardware—such as a/a converters, PWM counters, and encoder interface circuitry—can be used to

execute control algorithms for the two motors. With a proper control algorithm, the motors can be run in either motoring mode. i.e., providing power to the motor shaft, or generating mode, in which power is transferred from the motor shaft to the inverter dc source. In short, for the compressor drive, the inverter components including semiconductor switches and gate drive circuits can be reduced by more than one-third.

3. Inverter Design, Test Setup and Experimental Results

Inverter design and test setup

A prototype inverter rated at 75 kW for the traction drive and 5 kW for the compressor drive was designed and fabricated. The design uses the latest trench-gate 600-V/600- six-pack IGBT intelligent module from POWEREX and two 600-V/75-A dual-pack IGBTs, which are mounted on a water-cooled heat sink with a footprint of 12×7 in., as shown in Figure 5. Four film capacitors rated at 600 V/260 µF are employed in the dc bus filter. A new DSP control board based on a TI chip, TMS320F2812, has been designed and fabricated for controlling the IGBTs. The DSP chip has two sets of PWM hardware and thus can control two motors simultaneously. Figure 6 shows a photo of the complete inverter assembly with the DSP control board, a main gate driver board underneath the DSP board, an auxiliary gate driver board for the dual-pack IGBTs, and a control power supply. The assembly has a footprint of 12 in. width × 11 in. depth and a volume of 385 $in._3$, of which over one-third, 149 $in._3$, is occupied by the capacitors.

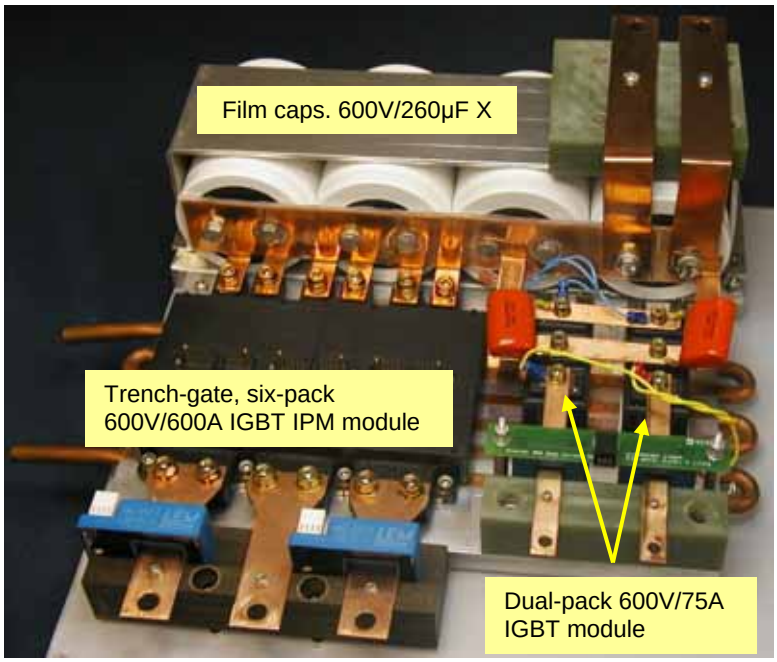

Figure 5. Dual inverter prototype without the gate driver and control boards.

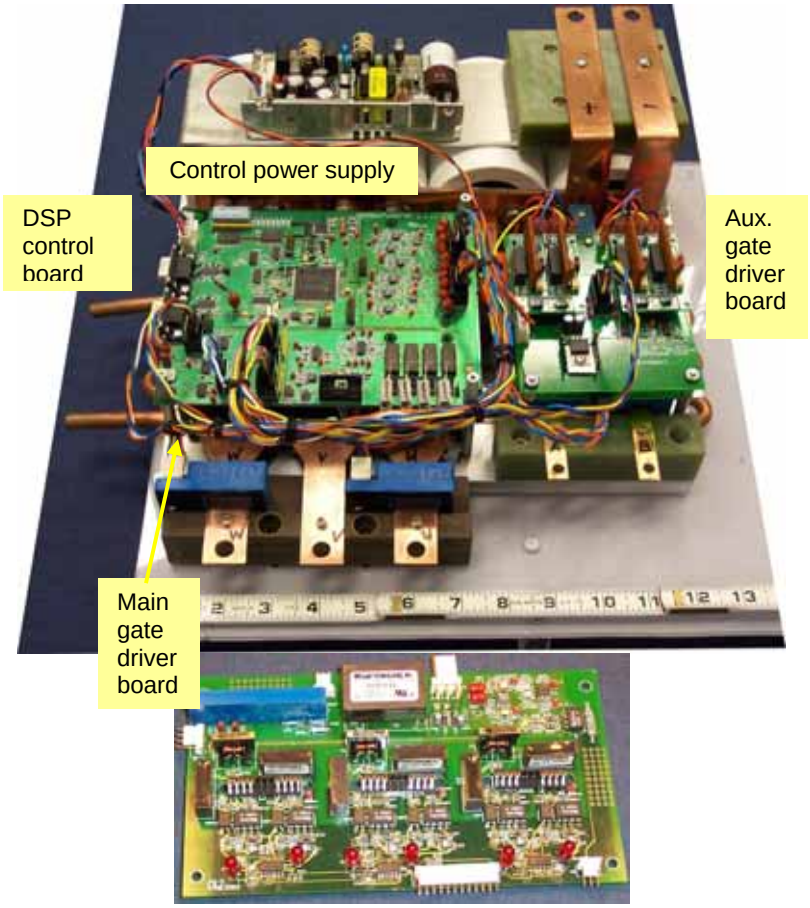

Figure 6. Dual inverter prototype—complete assembly.

Figures 7–9 show the test setup of the inverter and motors. For testing, a three-phase PM motor with eight poles, rated at 8.2 kW and 2000 rpm, was used as the traction motor because a PM motor with a power and speed range that meets FreedomCAR motor requirements was not readily available when the design and testing were conducted. For the compressor motor, a three-phase, eight-pole PM motor rated at 5.5 kW and 4000 rpm was modified to form a two-phase motor, as shown in Figure 10(a), in which phase-b and phase-c windings are connected in series. This connection results in an equivalent asymmetrical two-phase PM motor with two orthogonal windings with a turns ratio of $\sqrt{3}:1$, as can be seen from the magnetomotive force vectors shown in Figure 10(b).

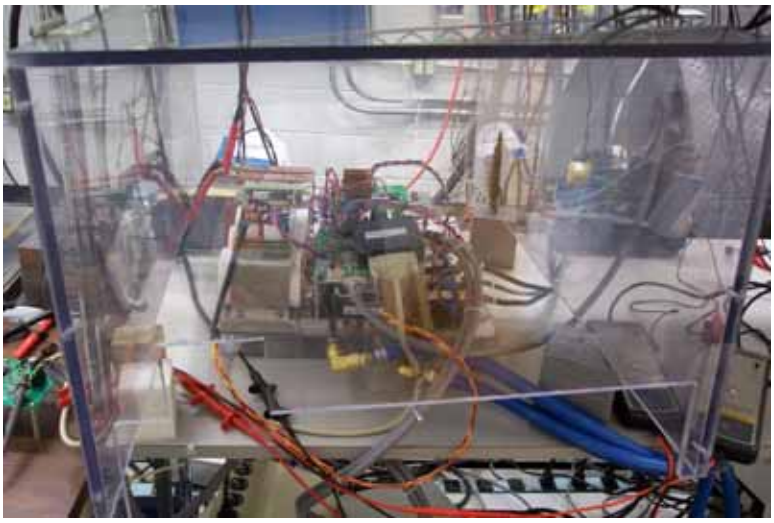

Figure 7. Dual inverter prototype connected for testing.

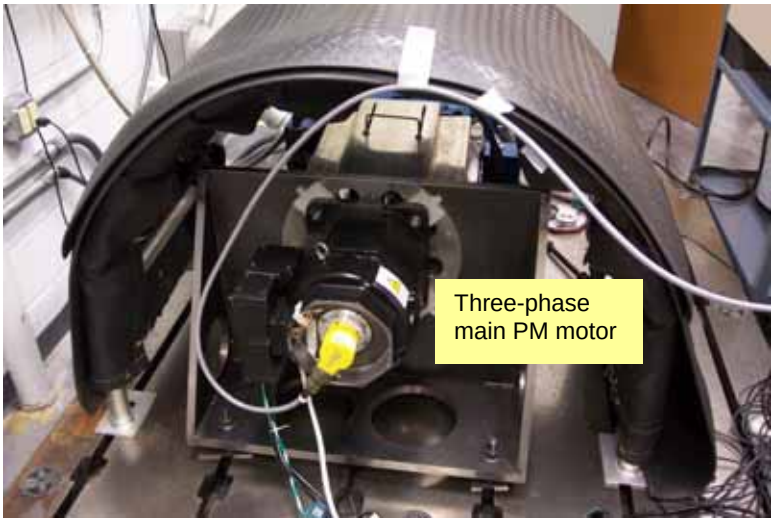

Figure 8. Three-phase main PM motor mounted on the motor test bed with a 100-HP dyne.

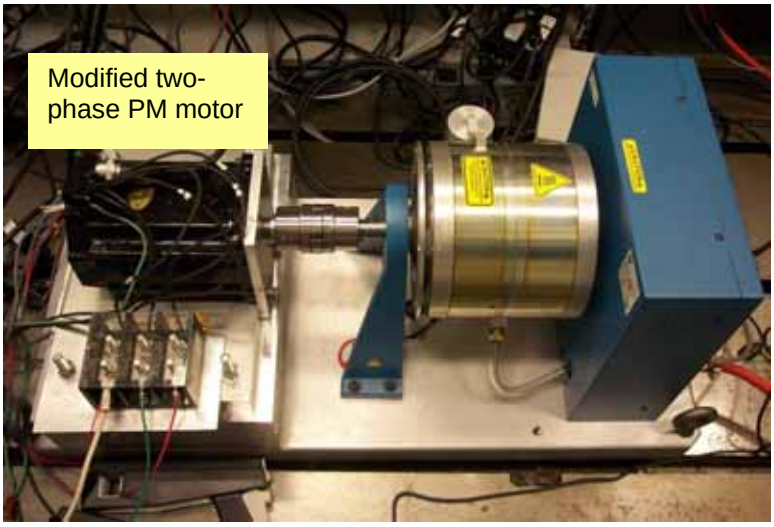

Figure 9. Two-phase PM motor mounted on a portable 5-HP eddy current dyne motor test bed.

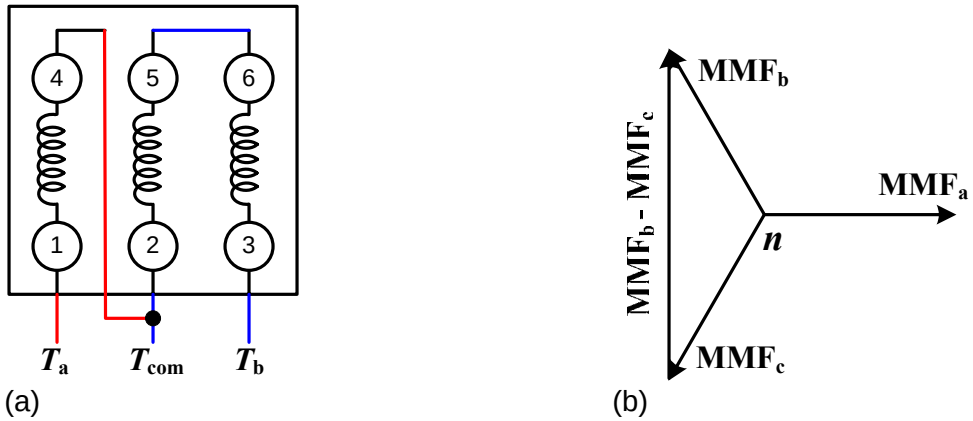

Figure 10. Modification of the three-phase motor into a two-phase one.

Experimental results

Extensive testing was conducted to verify the integrated drive operations. Figures 11–16 give testing waveforms at various load conditions, which clearly show that the speed of the two motors can be controlled independently. In Figures 11 and 12, the main motor was not running while the two-phase motor was loaded with 10 N·m at 505 rpm and 7.5 N·m at 1000 rpm, respectively. In Figures 13 and 14, the two-phase motor was stopped while the main motor was loaded with the rated torque of 40 N·m at 500 rpm. In Figure 13, the speed was increased to1852 rpm and the load torque to 43 N·m. Figure 14 shows the unit delivering the rated power of 8.2 kW. In Figure 15, the main motor was loaded with 40 N·m at 750 rpm, while the two-phase motor was loaded with 12 N·m at 505 rpm. In Figure 16, the main motor was loaded with 40 N·m at 1000 rpm, while the two-phase motor was loaded with 12 N·m at 800 rpm. It should be noted that because of their asymmetrical windings, the two-phase motor currents, i_a and i_b, are not equal.

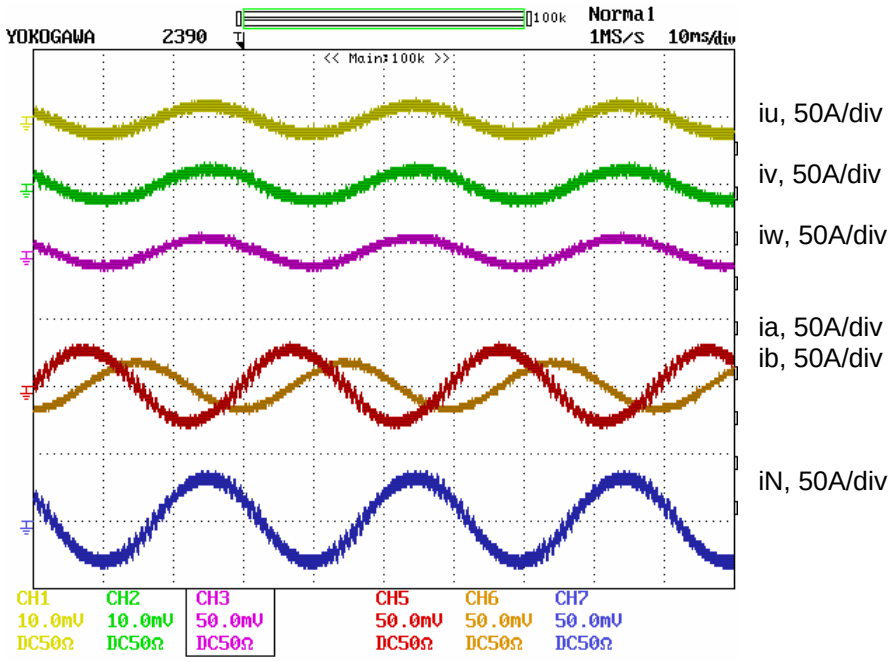

Figure 11. The main motor is not running while two-phase motor loaded with 10 N·m at 505 rpm. 10ms/div.

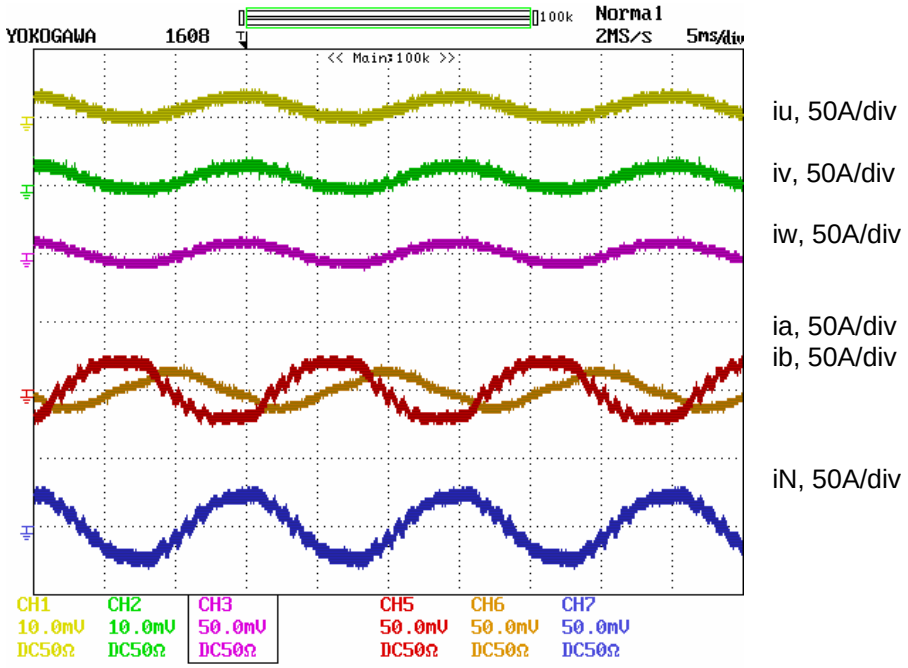

Figure 12. The main motor is not running while two-phase motor loaded with 7.5 N·m at 1000 rpm. 5ms/div.

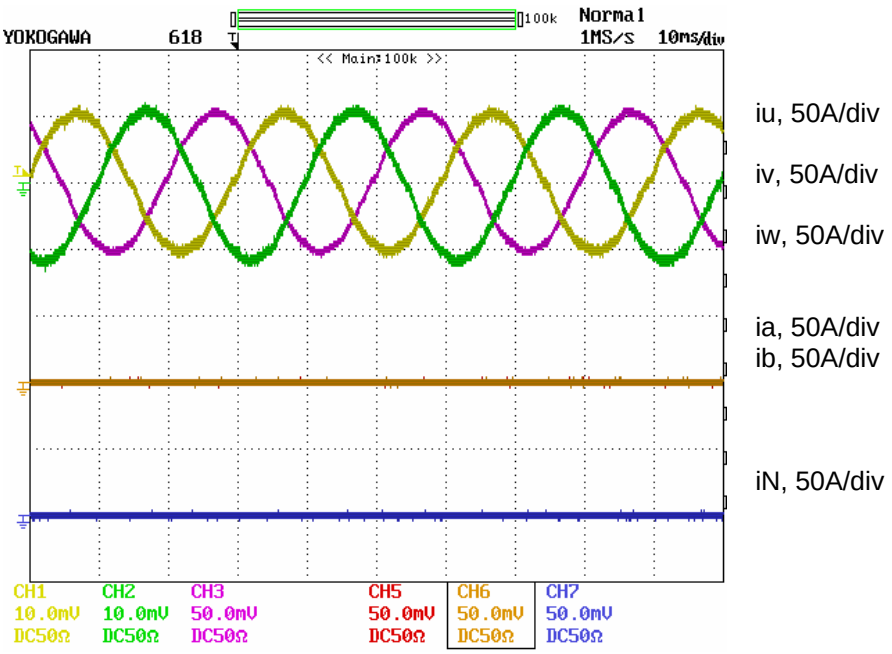

Figure 13. The two-phase motor is not running while the main motor is loaded with 40 N·m at 500 rpm. 10ms/div.

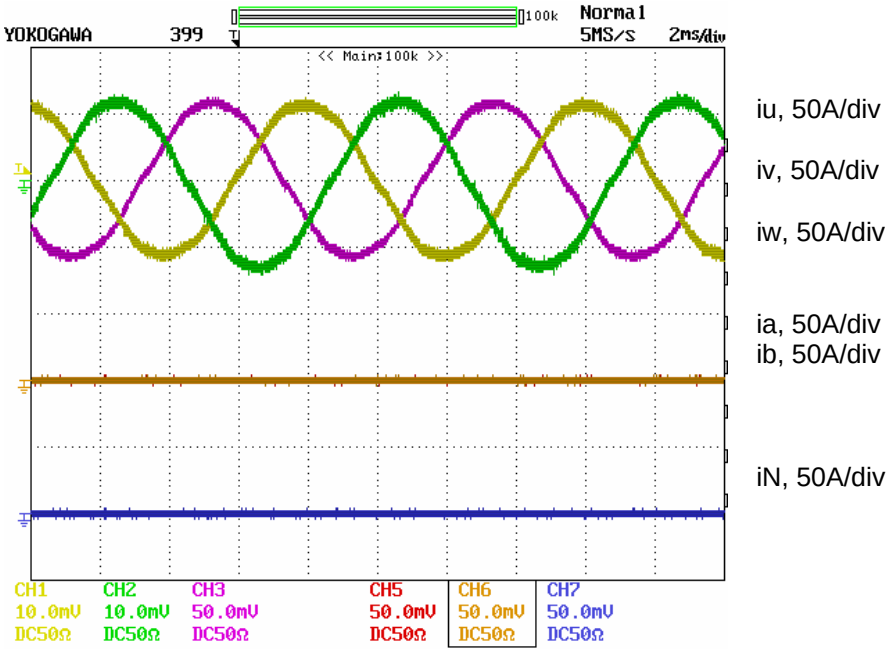

Figure 14. The two-phase motor is not running while the main motor loaded with 43 N·m at 1852 rpm. 2ms/div.

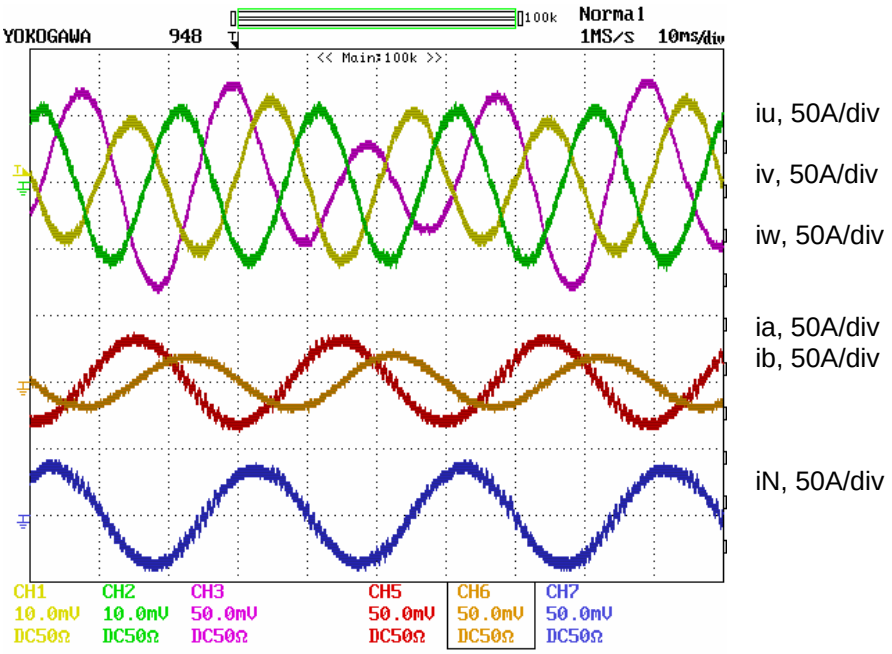

Figure 15. The main motor is loaded with 40 N·m at 750 rpm, and the two-phase motor is loaded with 12 N·m at 505 rpm. 10ms/div.

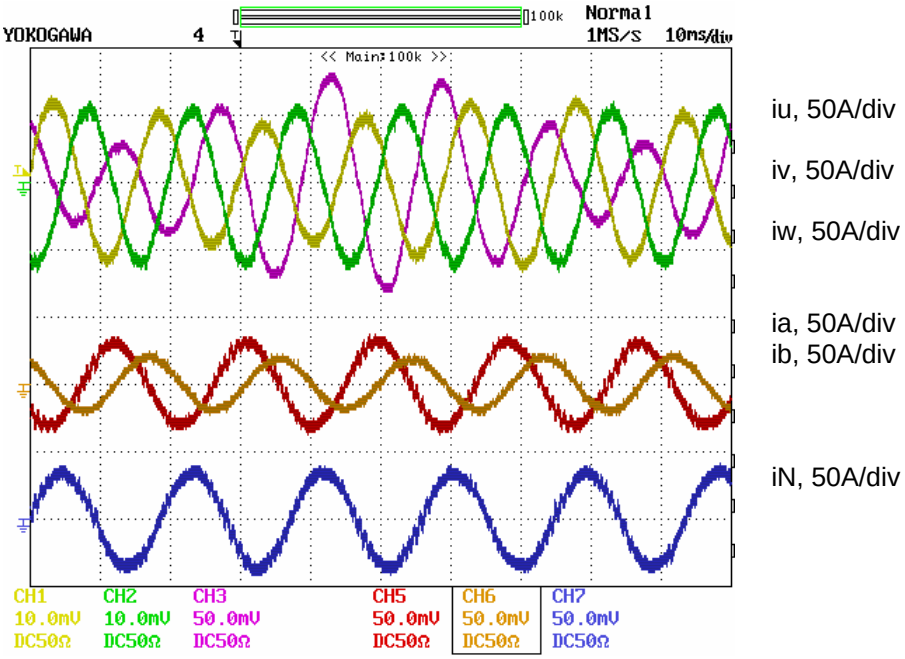

Figure 16. The main motor is loaded with 40 N·m at 1000 rpm, and the two-phase motor is loaded with 12 N·m at 800 rpm. 10ms/div.

Conclusions

The proposed integrated traction and compressor motor drive employing a five-leg inverter can significantly reduce the cost of the compressor motor drive in HEV/FCV applications. For the compressor drive, the inverter components, including semiconductor switches and gate drive circuits, can be reduced by more than one-third. An additional cost savings is due to the fact that the compressor drive does not require a separate control circuit; it is incorporated into the traction motor controller through software. Finally, the two-phase motor is ultimately cheaper to manufacture because one stator phase winding is eliminated.

The testing results show that

- The split-dc bus capacitors for a two-phase compressor motor drive can be eliminated by using the traction motor stator windings as the current return paths.
- Increase in the current rating of the main inverter switches and the traction motor due to the two-phase motor current is negligible.
- The speed of the traction and compressor motors can be controlled independently. The test results on the independent control characteristics of the two motors and on the voltage waveforms agree fully with the analytical predictions.
- The fundamental components of the two motors have no influence on each other.
- The proposed dual inverter is applicable to induction motors, ac synchronous PM machines, and brushless dc motors.

Future Direction

Secure a PM motor that has power and speed ratings comparable to the FreedomCAR requirements and test the inverter up to its full power capability.

Publications

"A Five-Leg Inverter for Driving a Traction Motor and a Compressor Motor," pp. 117–123 in *Proceedings of the 8th IEEE Workshop on Power Electronics in Transportation* (WPET2004), Novi, Michigan, Oct. 21–22, 2004.

"An Integrated Traction and Compressor Drive System for EV/HEV Applications," pp. 719–725 in *Proceedings of the IEEE Applied Power Electronics Conference and Exposition* (APEC), vol. 2, Austin, Texas, March 6–10, 2005.

Patents

"Integrated Inverter for Driving Multiple Motors/Generators," Oak Ridge National Laboratory Invention Disclosure ID 1316, S-101905.

4.4 Z-Source Power Converter for Fuel Cell–Powered Vehicles

Donald J. Adams
Oak Ridge National Laboratory
National Transportation Research Center
2360 Cherahala Boulevard
Knoxville, Tennessee 37932
Voice: (865) 946-1321; Fax: (865) 946-1262; adamsdj@ornl.gov

DOE Technology Development Manager: Susan A. Rogers
Voice: 202-586-8997; Fax: 202-586-1600; E-mail: Susan.Rogers@ee.doe.gov

ORNL Program Manager: Mitch Olszewski
Voice: 865-946-1350; Fax: 865-946-1262; E-mail: olszewskim@ornl.gov

---

Objective

- To develop and demonstrate a low-cost, high-efficiency, and reliable inverter for traction drives of fuel cell–powered vehicles.

Approach

- Investigate the current inverter systems for traction drives and propose a new Z-source inverter traction drive system.
- Perform a comprehensive comparison, model development, and computer simulation of the existing topologies versus the new Z-source inverter.
- Design and prototype a 55-kW Z-source inverter for IM traction drive to prove the concept.
- Perform testing and performance study of the Z-source inverter prototype.

Major Accomplishments

- In FY 2004, detailed specifications were developed for a Z-source inverter prototype for fuel cell vehicle traction-drive applications. A comprehensive cost comparison, model development, and computer simulation were performed, and a report was issued.
- During FY 2005, a 55-kW prototype was developed and built. Subsequent tests and evaluations at both Michigan State University (MSU) and Oak Ridge National Laboratory (ORNL) proved the viability of the technology to achieve improved efficiencies at reduced cost. Several papers were issued and are listed in the publications section of this report.

Technical Discussion

Today's power conversion technology is based on the two traditional converter topologies: voltage-source (V-source) and current-source (I-source) converters (or inverters depending on power flow directions). Both the V-source converter and I-source converter have conceptual and theoretical limitations and barriers that prevent economical and efficient solutions to many applications.

A new converter topology and theory called the Z-source power converter was recently invented at MSU. It can overcome some of the problems of the traditional V-source and I-source converters. The Z-source converter is comprised of an impedance network to couple the main converter circuit to the power source or load. The unique feature offered by the Z-source network is that, unlike the traditional V-source or I-source, it can be open and short circuited, which provides a mechanism for the main converter circuit to step up or step down voltage as desired. The Z-source network provides great flexibility for the source,

main circuit, and load. Because of the wide voltage range of the fuel cell, the traditional inverter and the motor need to be oversized to accommodate the required large constant power speed range. The Z-source inverter could be a cheap and reliable solution for this application.

Great interest was shown by DOE, the national laboratories, and the FreedomCAR Technical Team in further development of the Z-source converter technology. In FY 2004, ORNL entered into an arrangement with MSU to collaborate and fund this development for automotive traction applications.

Currently, two types of inverters are used in fuel cell (FCV) and hybrid electric vehicle (HEV) traction drives: the traditional pulse width modulation (PWM) inverter and the dc/dc–boosted PWM inverter. For FCVs, the fuel cell voltage to the inverter decreases with an increase in power drawn from the fuel cell. Because of the wide voltage change and the limited voltage level of the battery and/or fuel cell stack, the conventional PWM inverter topology imposes high stresses on the switching devices and motor and limits the motor's constant power speed range (CPSR). The dc/dc–boosted PWM inverter topology can alleviate the stresses and limitations; however, it has other problems, such as the high cost and complexity associated with the two-stage power conversion. To demonstrate the superiority of the Z-source inverter for FCVs, a comprehensive analytical comparison of the Z-source inverter versus the two existing inverter topologies, performed using a 50-kW (max) fuel cell stack as the prime energy source and a 34-kW Solectria AC55 induction motor as the traction drive motor, showed that the Z-source inverter can increase conversion efficiency by 1% over a wide load range, extend CPSR by 1.55 times, and minimize the switching device power rating (SDPR), a cost indicator, by 15%. The three system configurations are shown in Figures 1–3.

In an inverter system, each switching device has to be selected according to the maximum voltage impressed and the peak and average current going through it. To quantify the voltage and current stress (or requirement) of an inverter system, SDPR is used. The SDPR of a switching device/cell is expressed as the product of voltage stress and current stress. The total SDPR of an inverter system is defined as the aggregate of the SDPRs of all the switching devices used in the circuit. Total SDPR is a measure of the total semiconductor device requirement and is thus an important cost indicator for an inverter system.

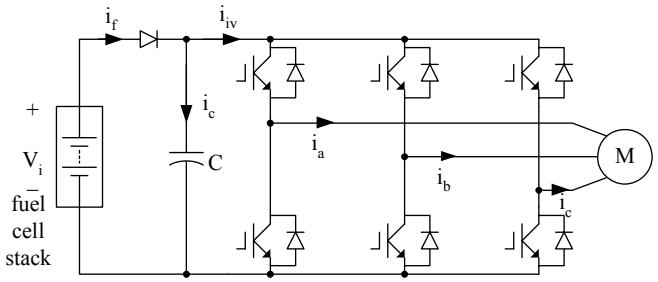

Figure 1. System configuration using conventional PWM inverter.

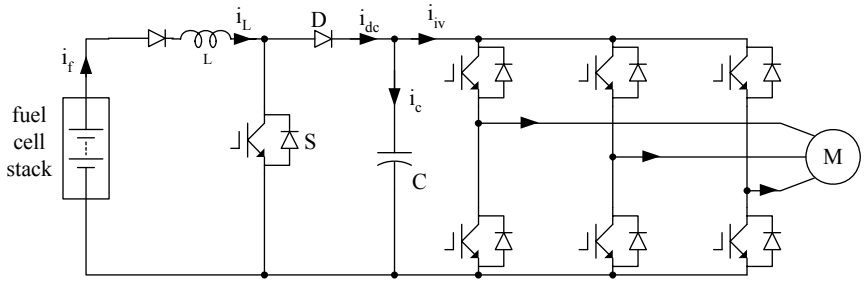

Figure 2. System configuration using dc/dc boost + PWM inverter.

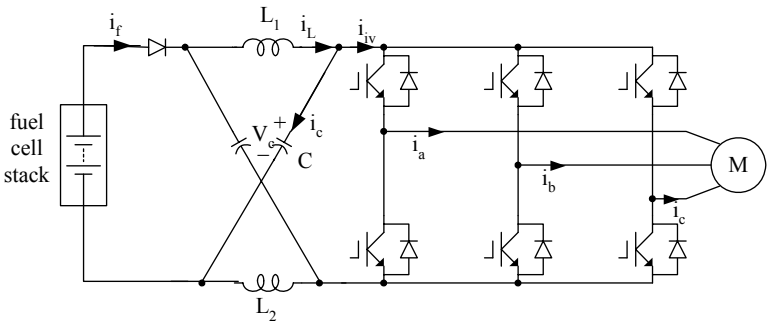

Figure 3. System configuration using the Z source inverter.

The specifications used in the design, analysis, and prototype development were as follows:

- Continuous power: 30 kW
- Peak power: 55 kW for 18 seconds
- Inverter efficiency: >97% at 30 kW
- Input fuel cell voltage: 0–420 V dc
-

As seen in Table 1, the Z-source inverter's average SDPR is the lowest of the three, and the conventional PWM inverter's SDPRs are the highest in both average and peak values. The average SDPR also indicates thermal requirements and conversion efficiency.

Table 1. Switching device power comparison

Inverter systems	Total average SDPR (kVA)	Total peak SDPR (kVA)
PWM inverter	238	747
PWM plus boost dc/dc	225	528
Z-source inverter	199	605

The SDPR numbers are the theoretical ratings of semiconductors required by the three inverter topologies. However, commercially available integrated power modules (IPMs) [or insulated gate bipolar transistors (IGBTs)] are limited in terms of voltage and current ratings. Assuming that the voltage rating is limited to 600 V, and the current rating is chosen to be two times the average current stress of each inverter topology, the selected devices and price quotes from a distributor are listed in Table 2. Again, the Z-source has the lowest price among the three inverters. In addition, because it has fewer components, a higher mean time between failures can be expected, which leads to better reliability. Table 3 shows the comparisons of passives required in the inverter systems to provide a further indication of size and cost.

Efficiency is an important criterion for any power converter. High efficiency can reduce thermal requirements and cost. An efficiency comparison was conducted based on the following conditions: the conventional inverter is always operating at a modulation index of 1, the dc/dc boost plus PWM inverter boosts the dc voltage to 420 V, and the Z-source inverter outputs the maximum obtainable voltage while keeping the switch voltage under 420 V. The same motor model is used to calculate the motor loss.

Table 2. Actual price comparison

Inverter systems	Selected devices (Number of pieces)	Total price
PWM inverter	PM400DSA060, 600V/400A dual pack (3)	$269.60*3 = **$808.80**
PWM plus boost dc/dc	PM400DSA060, 600V/400A dual pack (1) plus PM200CL060, 600V/200A 6 pack (1)	$240+$269.60 = **$509.60**
Z-source inverter	PM300CL060, 600V/300A 6 pack (1)	**$308.88**

Table 3. Required passive components

Inverter systems	Number of inductors	Inductance (μH)	Average inductor current (A)	Number of capacitors	Capacitance (μF)	Capacitor rms ripple current (A)
Conventional PWM inverter	0	N/A	N/A	1	667	106
dc/dc boost + PWM	1	510	200	1	556	124
Z-source inverter	2(1)	384	200	2	420	115

Switching devices were selected for each inverter topology to calculate their losses. The switches for the main inverters were FUJI IPM 6MBP300RA060; the switch for the dc/dc boost converter was FUJI 2MBI 300N-060. The operating conditions are listed in Table 4. The calculated efficiencies of inverters, as well as of the inverter plus the motor, are shown in Figures 4 and 5, respectively. Based on this simulated comparison, the Z-source inverter provides the highest efficiency.

Table 4. Operating conditions at different power levels

Power rating		50 kW 56 kVA	40kW 47kVA	30 kW 38 kVA	20 kW 27 kVA	10 kW 14 kVA
Fuel cell voltage (V)		250	280	305	325	340
Motor current (A)	Conventional PWM inverter	209.4	158.5	115.9	77.3	39.7
	dc/dc boost +PWM inverter	124.7	105.6	84.2	59.9	32.1
	Z-source inverter	129.5	105.3	81.1	56.2	29.6

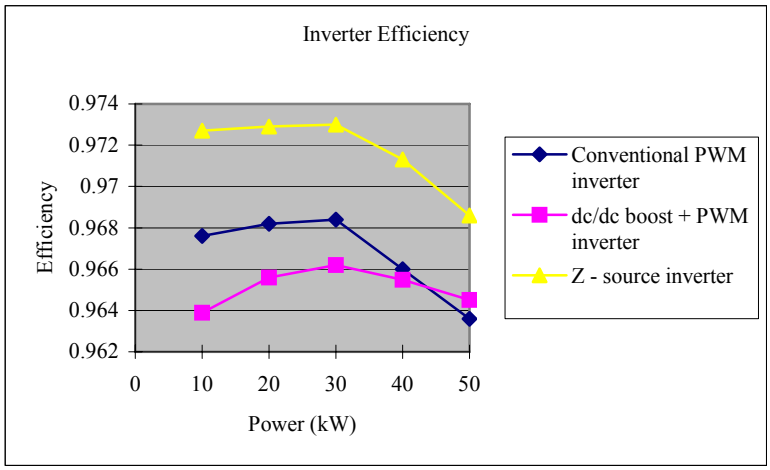

Figure 4. Calculated efficiency of inverters.

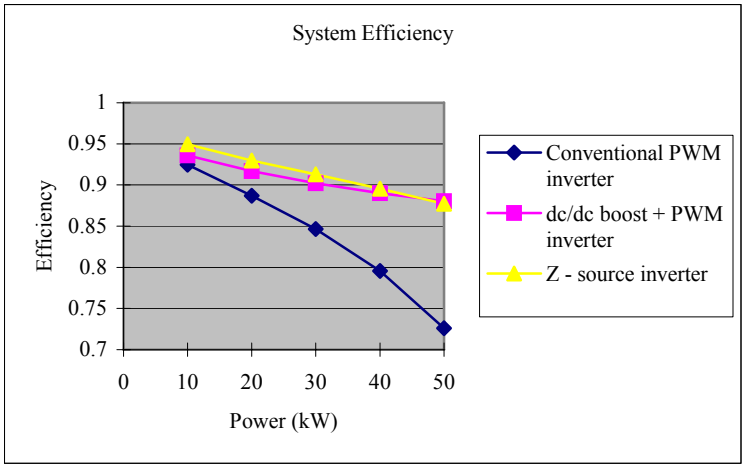

Figure 5. Calculated efficiency of inverters plus motor.

The comprehensive comparison results show that the Z-source inverter can increase inverter conversion efficiency by 1% over the two existing systems and inverter-motor system efficiency by 2 to 15% over the conventional PWM inverter. The Z-source also reduces the SDPR by 15%, which leads to cost reduction. Moreover, the CPSR is greatly extended (1.55 times) compared with the system driven by the conventional PWM inverter. Thus the Z-source inverter system can minimize stresses and motor size and increase output power greatly. Along with these promising results, the Z-source inverter offers a simplified single-stage power conversion topology and higher reliability because shoot-through can no longer destroy the inverter. The existing two inverter systems suffer the shoot-through reliability problem. In summary, the Z-source inverter is very promising for this application.

A prototype was developed at MSU and was shipped to ORNL after initial evaluation and troubleshooting. Figure 6 is a photograph of the completed prototype.

The inverter efficiency was measured during the test at ORNL. There were two types of loads—an RL load and a dynamometer. For the RL load in normal operation mode without boost, the modulation index of the inverter is kept constant, and the output voltage increases with the increase of the input voltage. During boost mode, the output voltage is controlled by a potentiometer controlling the modulation index and shoot-through duty ratio. Figure 7(a) shows the measured efficiency with the RL

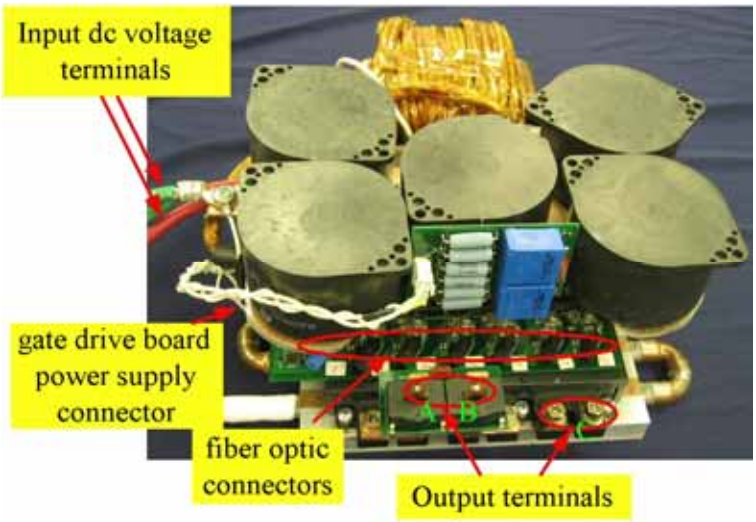

Figure 6. Final Z-source inverter prototype as tested.

load. The point marked with a dark cross is the test point during boost; others are all during normal mode without shoot-through. For the test using the dynamometer as the load, the output voltage is always kept proportional to the output frequency to keep the magnetizing current constant (or constant V/F control); thus, the output power can be changed by adjusting the load torque, adjusting the input voltage, or adjusting the boost factor during boost mode. The inverter efficiency with different input voltages and different power levels is shown in Figure 7(b). Note that the inverter efficiency is defined against the output apparent power of the inverter. The points with dark marks are the testing points with boost, and the others are in normal operation modes without shoot-through. The efficiency was above 97% for most operation points, which achieved the 97% efficiency goal. More noticeably, the efficiency became much higher than 97% at medium and low power, which is extremely beneficial to vehicles, according to most driving cycles.

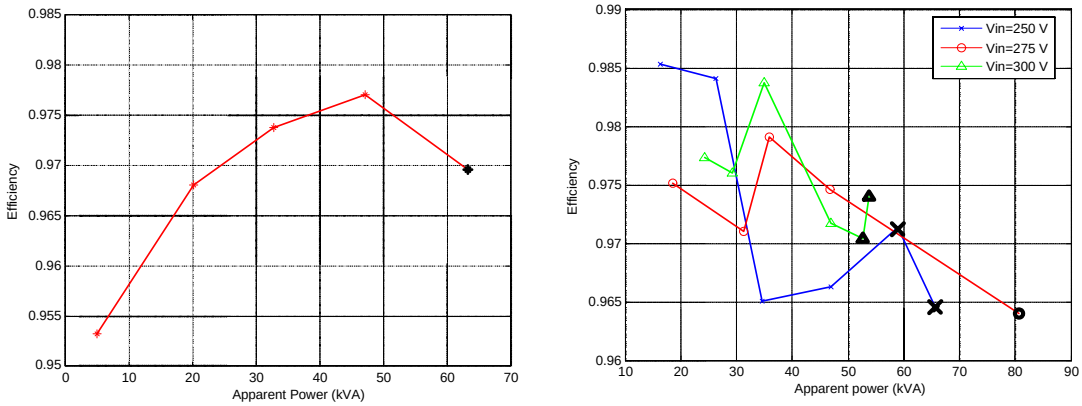

(a) Inductive load (b) Dyno load

Figure 7. Measured inverter efficiency.

FreedomCAR has a set of specifications and goals for the traction drive inverter to meet. However, it should be noted that the FreedomCAR has not yet set up clear goals for the dc-dc boost converter that are used for FCVs and HEVs. The Z-source inverter prototype has both inverter and dc-dc boost converter functions (i.e., equivalent to the traditional two stages of power conversion: inverter plus dc-dc boost converter), thus making comparison difficult. A comparison of the prototype to the initial goals of FreedomCAR is shown in Table 5. The numbers in the parentheses of the "FreedomCAR goals" column are the corresponding goals for the combined total system of inverter and dc-dc boost converter, assuming that the goals for the dc-dc boost converter are the same as the inverter. The power density numbers in the parentheses of the "Prototype" column are based on the actual peak power capacity of 80 kW that was successfully tested at ORNL, while the outside numbers are based on the design value of 55 kW.

As can be seen from the table, the most important goals—the efficiency, power, and current ratings—are all well met and exceeded. The power density goals are well met by the prototype based on the actual peak power capacity of 80 kW for the combined dc-dc boost converter and inverter system goals. The only problem is the coolant temperature goal of 105°C, which was not possible for this prototype with the semiconductor device's maximum junction temperature limit of 125°C. Future higher-temperature devices and more advanced circuit topology may make this goal possible. A commercially available heatsink is used in the prototype for cost consideration, which contributes almost half of the inverter weight and a significant portion of the inverter volume. The capacitors used are commercial products, which have a cylinder shape with legs that are difficult for packaging. Significant void space exists in the prototype, thus making the volume unnecessarily larger. The size and the weight of the prototype can be further reduced with custom-designed heatsink and capacitor shapes. Once again, all the goals (efficiency,

Table 5. Comparison of the prototype and the FreedomCAR goals

Requirement	FreedomCAR goals Inverter (inverter+dc-dc)	Prototype
Specific power @ peak load (kW/kg)	>12 (6)*	4.7 (6.8)†
Volumetric power density (kW/l)	>12 ()*	4.7 (6.8)†
Efficiency, 10–100% speed, 20% rated torque (%)	>97 (93)*	>97%
Peak power (kW)	55 (5)*	80
Continuous power (kW)	30 (3)*	30
Maximum current, rms (A)	300 (30)*	300
Coolant inlet temperature	105 (10)*	77

* Indicates the goals for the total combined system of inverter and dc-dc boost converter assuming the dc-dc boost converter has the same goals as the inverter.

† Shows the prototype power density values based on the actual peak power capacity of 80 kW that was tested, while the value of 4.7 is based on the designed peak power of 55 kW.

power, and current) that are related to the technology are well met and exceeded. The volume and weight goals that are strongly related to engineering aspects can be met through better engineering and custom-designed parts for full utilization of the space.

Conclusion

This report has summarized the results and findings of the work conducted on the Z-source inverter for FCVs. The major work completed in this project includes (1) development of a low-cost, high-efficiency traction drive Z-source inverter for FCVs; (2) a detailed comparison of the Z-source inverter with traditional inverter topologies; (3) the design and fabrication of a 55-kW Z-source inverter; and (4) testing and demonstration of the Z-source inverter prototype.

First, a unique Z-source inverter was developed for FCVs. This inverter is especially suited for a fuel cell that requires unidirectional current/power flow and has a wide voltage range. At present, there are two existing topologies for FCVs: the traditional PWM inverter and the dc/dc–boosted PWM inverter. The traditional PWM inverter topology uses the fuel cell voltage directly, which results in a limited CPSR for the motor and a freeze-start problem for the fuel cell. The dc/dc–boosted PWM inverter topology suffers from high cost, low converter efficiency, and complexity. The specially developed Z-source inverter can solve these problems.

Second, a comprehensive comparison was conducted of the Z-source inverter and the two existing inverter topologies mentioned. The comparison results showed that the Z-source inverter is highly suitable for FCVs, having a lower cost (20% lower semiconductor ratings), higher conversion efficiency (1% higher), a wider CPSR (1.68 times that of the traditional PWM inverter), and greater reliability (no need for dead time).

A 55-kW Z-source inverter was designed and fabricated. The detailed design process included circuit design, 3-D design, and thermal design. To reduce the switching loss of the inverter, a new PWM scheme for shoot-through was introduced.

Finally, lab testing was conducted at MSU and ORNL separately. Testing results confirmed the theoretical analysis and comparison results obtained and showed that the inverter had higher efficiency (up to more than 98%) and low harmonic distortion (i.e., low current and torque ripples).

A self-boost phenomenon of the Z-source inverter when the traction motor was operating at low speed, low power, and low power factor was observed during the test. This self-boost function was initially deemed a problem; however, it turned out to be a needed function for successful fuel cell startup, especially for freeze-starts. In addition, this self-boost can be totally controllable when a battery is incorporated into the inverter system. A detailed analysis of the self-boost phenomenon and a control method using a battery was provided and confirmed by simulation.

In summary, the results of the project have shown high feasibility and many unique features of Z-source inverter for FCVs.

Future Direction

This project is complete. Follow-on work has been recommended to address the issues and possibilities of using the Z-source inverter in more near-term bridging technologies such as in more conventional HEVs with a combination of an internal combustion engine and batteries rather than a fuel cell.

Publications

Fang Z. Peng, "Z-Source Inverter," pp.775–781 in *Proc. of IEEE IAS 2002*.

Fang Z. Peng, "Z-Source Inverter," *IEEE Transactions on Industry Applications*, **39**(2), March–April 2003, pp. 504–510.

Fang Z. Peng, Xiaoming Yuan, Xupeng Fang, and Zhaoming Qian, "Z-Source Inverter for Adjustable Speed Drives," *IEEE Power Electronics Letters*, **1**(2), June 2003, pp. 33–35.

Fang Z. Peng, "Z-Source Inverter for Adjustable Speed Drives," IEEE/PESC Aachen, 2004, pp. 249–254.

Fang Z. Peng, Miaosen Shen, and Zhaoming Qian, "Maximum Boost Control of the Z-Source Inverter," IEEE/PESC Aachen, 2004, pp. 255–260.

Xupeng Fang, Zhaoming Qian, Qi Gao, Bin Gu, Fang. Z. Peng, and Xiaoming Yuan, "Current Mode Z-Source Inverter-Fed ASD system," IEEE/PESC Aachen, 2004, pp. 2805–2809.

Miaosen Shen, Jin Wang, Alan Joseph, Fang Z. Peng, Leon M. Tolbert, and Donald J. Adams, "Maximum Constant Boost Control of the Z-Source Inverter," IEEE/IAS, Seattle 2004, pp. 142–147.

Miaosen Shen, Alan Joseph, Jin Wang, Fang Z. Peng, and Donald J. Adams, "Comparison of Traditional Inverter and Z-Source Inverter for Fuel Cell Vehicles," IEEE WPET 2004, pp. 125–132.

Fang Z. Peng, "Z-Source Converters and Their Motor Drive Applications," International Conference on Electric Machines and Systems, invited paper, no. 630-M08-052, Jeju, Korea, Nov. 1–3, 2004.

F. Z. Peng, M. Shen, and A. Joseph, "Z-Source Inverters, Controls, and Motor Drive Applications," *KIEE International Transactions on Electrical Machinery and Energy Conversion Systems*, vol. 5-B 2005, pp. 6–12.

Yi Huang, Miaosen Shen, and Fang Z. Peng, "A Z-source Inverter for Residential Photovoltaic Systems," International Power Electronics Conference, Niigata, Japan, 2005.

Fang Z. Peng, Alan Joseph, Jin Wang, Miaosen Shen, Lihua Chen, Zhiguo Pan, Eduardo Ortiz, and Yi Huang, "Z-Source Inverter for Motor Drives," to be published in *IEEE Transactions on Power Electronics*, 20(4), 2005.

Fang Z. Peng, Miaosen Shen, and Zhaoming Qian, "Maximum Boost Control of the Z-Source Inverter," to be published in *IEEE transactions on Power Electronics*, 20(4), 2005.

Miaosen Shen, Alan Joseph, Jin Wang, Fang Z. Peng, and Donald J. Adams, "Comparison of Traditional Inverters and Z-Source Inverter," to be presented at IEEE PESC 2005.

Miaosen Shen, Fang Z. Peng, "Study of the Z-Source Inverter," to be presented at IEEE IAS 2005.

Kent Holland, Miaosen Shen, and Fang Z. Peng, "Z-Source Inverter Control for Traction Drive of Fuel Cell–Battery Hybrid Vehicles," to be presented at IEEE IAS 2005.

Kent Holland and Fang Z. Peng, "Control Strategy for Fuel Cell Vehicle Traction Drive Systems Using the Z-Source Inverter," to be presented at IEEE VPPC 2005.

Yi Huang, Miaosen Shen, and Fang Z. Peng, "A Z-Source Inverter for Residential Photovoltaic Systems," submitted to *IEEE Transactions on Power Electronics*.

Miaosen Shen, Jin Wang, Alan Joseph, Fang Z. Peng, Leon M. Tolbert, and Donald J. Adams, "Constant Boost Control of the Z-Source Inverter to Minimize Current Ripple and Voltage Stress," submitted to *IEEE Transactions on Industry Applications*.

Xu Peng Fang, Zhao Ming Qian, Qi Gao, Bin Gu, Miaosen Shen, and Fang Zheng Peng, "Z Source PWM AC/AC Converters," submitted to *IEEE Power Electronics Letters*.

Patents

The Z-Source converter intellectual property pre-dates this project and is owned by MSU. The patent application was filed on June 10, 2003, assigned application number 10/458,564, and is titled "Impedance Source Power Converter."

References

1. F. Z. Peng, Li Hui, Su Gui-Jia, and J. S. Lawler, "A New ZVS Bidirectional DC-DC Converter for Fuel Cell and Battery Application," IEEE Transactions on Power Electronics, 19(1), Jan. 2004, pp. 54–65.
2. S. E. Gay, Gao Hongwei, and M. Ehsani, "Fuel Cell Hybrid Drive Train Configurations and Motor Drive Selection," presented at Vehicular Technology Conference, 2002, 2(24–28), Sept. 2002, pp. 007–1010.
3. Tadaichi Matsumoto, Nobuo Watanabe, Hiroshi Sugiura, and Tetsuhiro Ishikawa, "Development of Fuel-Cell Hybrid Vehicle," presented at Fuel Cell Power for Transportation 2002 Conference, SAE 2002 World Congress, March 2000, ref: 2002-01-0096.
4. B. D'Souza, H. Rawlins, J. Machuca, C. Larson, M. Shuck, B. Shaffer, T. Maxwell, M. Parten, D. Vines, and J. Jones, "Texas Tech University Develops Fuel Cell Powered Hybrid Electric Vehicle for FutureCar Challenge 1998," presented at International Congress & Exposition, March 1999, Detroit, MI, SAE 1999, Ref: 1999-01-0612.
5. J. Adams, W. Yang, K. Oglesby, and K. Osborne, "The Development of Ford's P2000 Fuel Cell Vehicle," presented at Society of Automotive Engineers 2000 World Congress, March 2000, Detroit, MI, SAE 2000, Ref: 2000-01-1061.
6. D. Tran and M. Cummins, "Development of the Jeep Commander 2 Fuel Cell Hybrid Electric Vehicle," presented at Future Transportation Technology Conference & Exposition, August 2001, Costa Mesa, CA, SAE 2001, Ref: 2001-01-2508.
7. Kent Holland, "Z-Source Inverter Control for Traction Drive of Fuel Cell—Battery Hybrid Vehicles," Masters Thesis, Michigan State University, August 2005.
8. F. Z. Peng, "Z-Source Inverter," IEEE Transactions on Industry Applications, 39(2), pp. 504–510, March/April 2003.
9. Kent Holland, Miaosen Shen, and Fang Z. Peng, "Z-Source Inverter Control for Traction Drive of Fuel Cell—Battery Hybrid Vehicles," in Proceedings *of* IEEE IAS, 2005.
10. Miaosen Shen, Jin Wang, Alan Joseph, Fang Z. Peng, Leon M. Tolbert, and Donald J. Adams, "Maximum Constant Boost Control of the Z source Inverter," in Proceedings of IEEE IAS '04, 2004.
11. "General Considerations: IGBT & IPM Modules," Powerex Application Notes for IPM PM600CLA060, A10–A27, Powerex Corporation.
12. Fang Z. Peng, Miaosen Shen, Zhaoming Qian, "Maximum Boost Control of the Z-Source Inverter," IEEE Transactions on Power Electronics, 20(4), July 2005.

4.5 dc-dc Converter for Fuel Cell and Hybrid Vehicle

Principal Investigator: Laura Marlino
Oak Ridge National Laboratory
National Transportation Research Center
2360 Cherahala Boulevard
Knoxville, TN 37932
Voice: 865-946-1245; Fax: 865-946-1262; E-mail: marlinold@ornl.gov

DOE Technology Development Manager: Susan A. Rogers
Voice:202-586-8997; Fax:202-586-1600; E-mail: susan.rogers@ee.doe.gov

ORNL Program Manager:Mitch Olszewski
Voice:865-946-1350; Fax: 865-946-1262; E-mail: olszewskim@ornl.gov

---

Objectives

- Develop and fabricate a 5-kW dc-dc converter with a baseline 14-V output capability for fuel cell and
  — hybrid vehicles to satisfy the following requirements:
  — Higher efficiency (92%)
  — High coolant temperature capability (105°C)
  — High reliability (15 years/150,000miles)
  — Smaller volume (5 l)
  — Lower weight (6 kg)
  — Lower cost ($75/kW)

Approach

The key technical challenge for these converters is the 105°C coolant temperature requirement. The power switches and magnetics must be designed to sustain high operating temperatures reliably, without a large cost/mass/volume penalty. During FY 2005, a 5-kW prototype was developed by Ballard Power Systems and initial testing was performed.

The following key technologies are being used to break through technical barriers to achieve a high-temperature, high-power-density, and lower-cost design.

1. Converter topology

A novel interleaved dc-dc converter topology (Figure 1) was proposed for this high power conversion. The key merits of the converter are

- Lower RMS current stresses on components due to interleaving
- Reduced ripple current on capacitors due to interleaving
- Lower power losses due to low Rds_on and soft-switching
- Smaller magnetics due to high switching frequency
- Low electromagnetic interference as a result of integrated power devices and magnetics

2. Integrated module-based dc-dc converter

The project uses Ballard's Class 10,000 clean-room power semiconductor packaging facility to develop and apply custom packaging processes and materials that address size, heat, and inductance-related burdens while reducing component cost. The custom packaging process reduces size by increasing the density of the electronic assemblies. Custom packaging materials will lower heat generation by reducing thermal interface layers and facilitating the integration of advanced cooling methods.

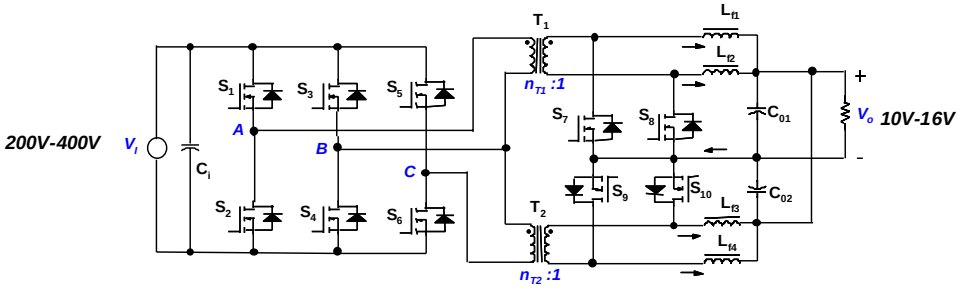

Figure 1. The novel interleaved dc-dc converter topology.

The major advantages of the power module based dc-dc converter are

- Enhanced thermal performance
- Reduced number of devices
- Increased reliability
- Higher level of integration

3. Planar magnetics with enhanced cooling

This converter has also been designed using planar magnetics, a technology that Ballard believes is critical for reliable and cost-effective high-volume production of such products. The benefits from this technology are

- Lower leakage inductance as a result of shorter winding termination and smaller circuit paths
- Elimination of discrete contacts' ohmic loss
- Reduction of ohmic loss as a result of shorter conduction paths
- Lower ac loss due to flat winding structure
- Higher core window utilization ratio
- Smaller core volume and weight
- Higher surface-to-volume ratio for improved heat conduction
- Direct cooling of core by direct contact to heat sink
- Higher power density

Major Accomplishments

The project is divided into four major phases: Phase 1: key technologies prove-out; Phase 2: full-function alpha design and test; Phase 3: final beta prototype design; Phase 4: final build, DV test, delivery and report. Ballard Power Systems has achieved the following during FY 2005.

1. Key technologies proved out

A 2.5-kW segmented dc-dc power module was developed at the beginning of FY 2005 to verify key technologies adopted in this project. Figures 2, 3, and 4 show the preliminary power module and the test results. Through this first design iteration, the following technologies have been verified and implemented:

- DBC transformer winding design and manufacture feasibility
- Key variables affecting the performance
- Wirebond diagram and Rds_on packaging efficiency
- Non-interleave planar transformer vs interleaved planar transformer
- Metal oxide semiconductor field effect transistor die selection with low Qrr
- Snubber circuit optimization
- Transformer ratio
- Power module fabrication process with larger DBCs and lead frames

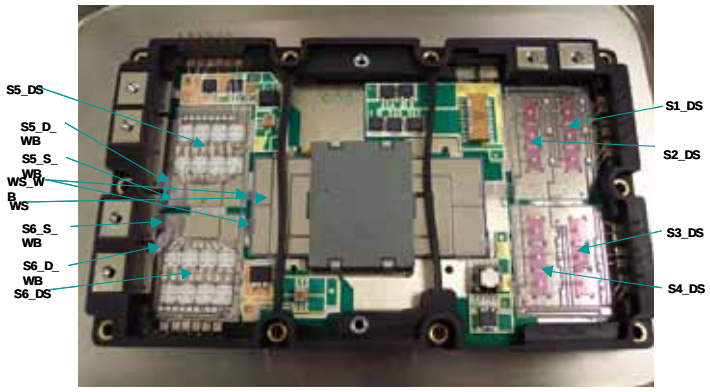

Figure 2. A segmented preliminary 2.5-kW dc-dc power module.

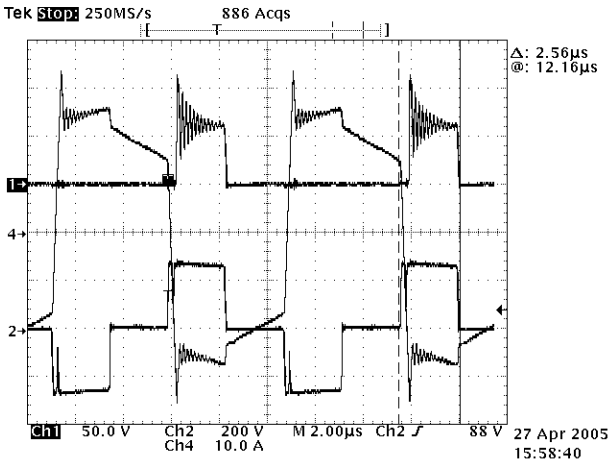

Figure 3. Tested waveforms at Vi=300V, Vo=13.35V/197A, Po=2627W, I_rr=35A.

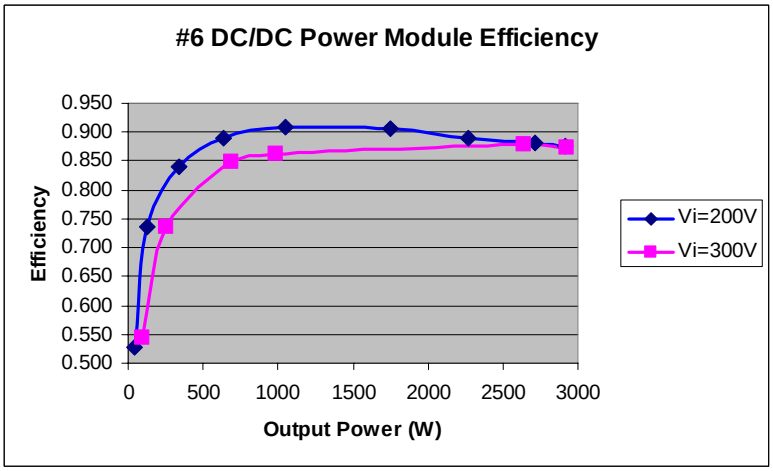

Figure 4. Efficiency mapping of the segmented dc-dc power module.

2. Fully-functional, alpha unit prototype design and fabrication:

A 5-kW converter with the selected topology (Figure 1)was designed during this phase. The following major tasks were accomplished:

- Power module design, including DBC, lead frame, and module baseplate
- dc/dc converter packaging: housing plate, seal, busbar, etc
- Control board, erasable programmable logic device program, and simulation
- High-temperature components selection
- Design release and components purchasing
- Power module process development
- Fabrication and assembly

Figures 5 and 6 show the designed alpha 5-kW power module and completed dc-dc converter. This design level incorporated the lesson learned from the 2.5-kW segmented power module (described earlier), with the goal to verify full electrical function against the specification. To reduce prototyping time, the lead frame was made from urethane and the baseplate was made from aluminum. The final design will use plastic and AlSiC, respectively.

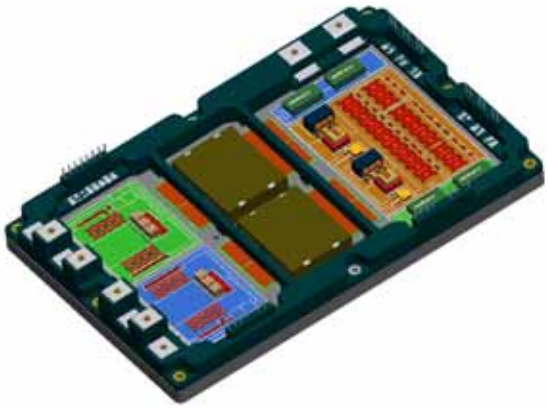

Figure 5. A 5-kW full functional dc-dc power module—alpha design.

Figure 6. A completed 5-kW dc-dcconverter—alpha design.

3. High-volume cost estimation

Based on the bill of material generated in the alpha version dc-dc converter design, a unit cost at high volume has been estimated, as illustrated in Table 1. The current cost estimate for this module is $545/per unit, 45% higher than the DOE target of $375/per unit. The power module is the major cost in the dc-dc converter, composing 59% of the total cost. Table 2 and Figure 7 contain a detailed study of the power module cost.

Table 1. Alpha dc-dc converter bill of material and cost estimation at 1000 K volume.

#	Level	Part Description	Tooling Cost	Tooling Type	Part Unit Price (@1KK)	# Per Uint	Part Cost
1	1	ORNL 5kW DC-DC Power Module	$166,000		$320	1	$320
2	1	LV Busbar Positive	$15,000	Stamping die	$2	1	$2
3	1	LV Busbar Positive	$15,000	Stamping die	$2	1	$2
4	1	Converter Housing	$80,000	Die cast	$15	1	$15
5	1	Housing Cover	$50,000	Stamping die	$8	1	$8
6	1	LV Studs	$30,000	Insert mold	$5	2	$10
7	1	HV Connector			$20	1	$20
8	1	Inductor	$10,000		$9	4	$35
9	1	LV Capacitor Board Assembly			$10	1	$10
10	1	Signal Connector			$8	1	$8
11	1	Control Board	5000		$80	1	$80
12	1	Current Sensor			$8	2	$16
13	X	MFG, F&T					$18

Tooling Cost	$371,000

Part Cost Per Unit @1000K	$545	145%
DOE Target	$375	

Table 2. dc-dc power module cost spreadsheet

1	Lead Frame	$10.00	3%
2	AlSic Baseplate	$50.00	17%
3	DBC Substrates	$57.86	20%
4	DBC XFMR Wingding	$36.50	13%
5	HV mosfets	$22.00	8%
6	LV mosfets	$32.00	11%
7	Chip Resistors	$10.80	4%
8	HV Caps	$32.00	11%
9	LV Caps	$12.00	4%
	Sub Total	$263.16	90%
	Total Cost	$291.00	100%

4. Alpha prototype test results

Figure 8 shows the ORNL alpha dc-dc converter test setup. The tests are still ongoing. Currently the converter attains 5.0-kW output (full power) and achieves a peak efficiency of 95%. From the test waveform shown in Figure 9, the Irr loss is eliminated compared with the segmented dc-dc converter tested earlier this year. The alpha unit efficiency map is shown in Figure 10. Comparing these results with the segmented dc-dc converter efficiencies found in Figure 4, overall efficiency in the alpha design has been improved by 5%.

The measured volume of the alpha unit approaches 6.5 L, approximately 1.5 L over the DOE target of 5 L. The measured pressure drop of this module is approximately 2.3 psi, exceeding the DOE target by 1.57 psi.

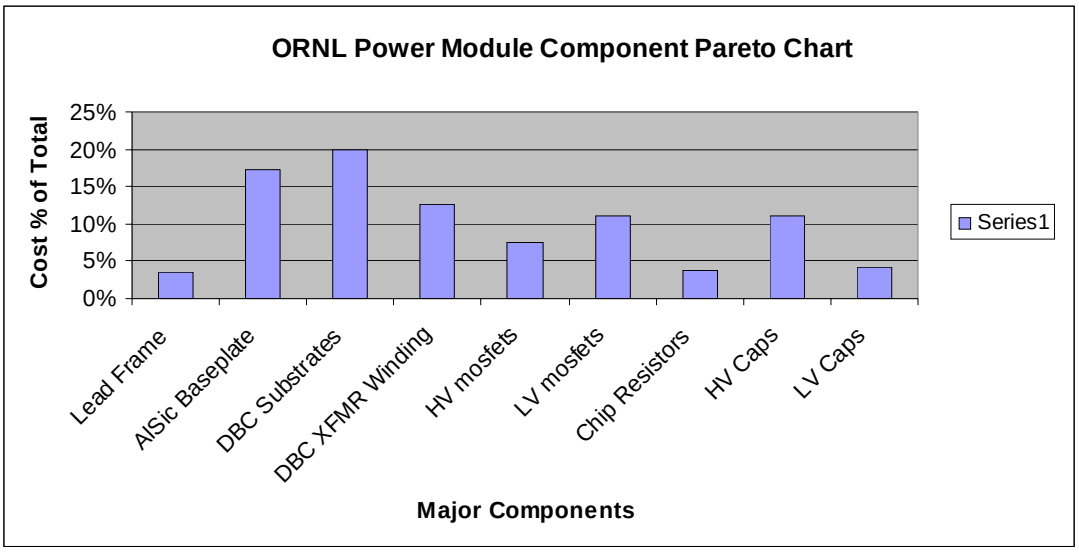

Figure 7. dc-dc power module cost distribution.

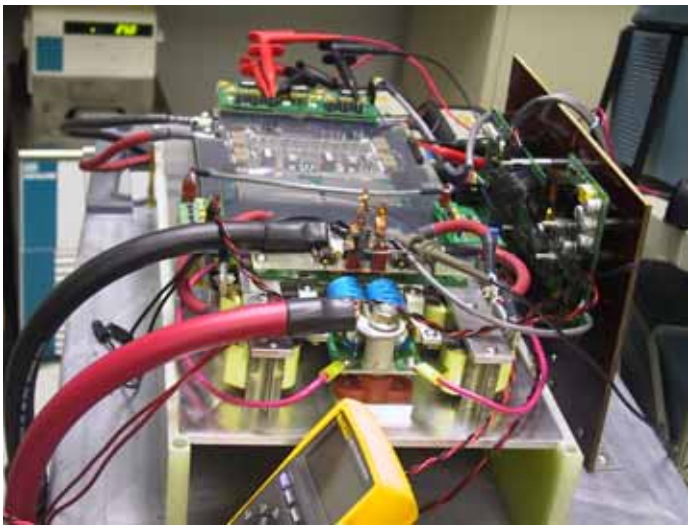

Figure 8. Alpha dc-dc converter under test.

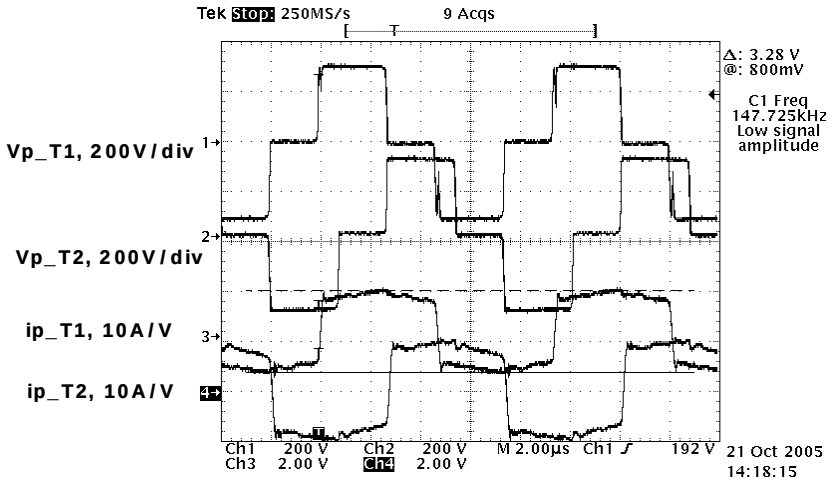

Figure 9. Alpha unit tested waveforms at Vi=300.6V, Vo=13.31V, Po=5.1kW, η=93.3%.

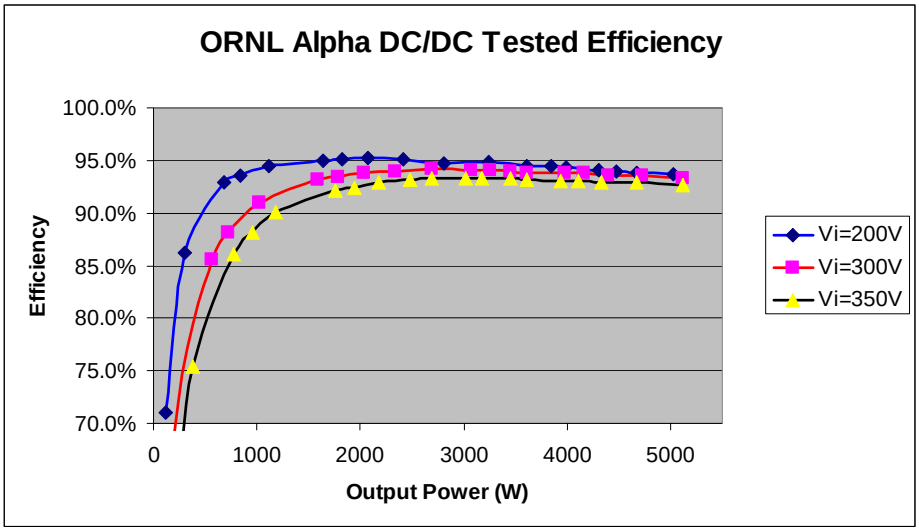

Figure 10. Alpha unit tested efficiency at Vi=200 V, 300 V, 350 V and up to 5 kW.

Technical Discussion

The alpha-level prototype of the 5-kW dc-dc converter successfully verified the operation of the proposed topology and the improvement of the power module layout. The efficiency was improved by 5% compared with the preliminary design and achieved a peak efficiency of 95%, exceeding the DOE target of 92%. However, several issues require further improvement for the final beta level design:

- High-volume cost target must be met.
- Power density needs improvement, toward the DOE target.
- Large DBC size (87 ×112 mm) exceeds the supplier's zone of comfort and has reliability implications (thermal cycling).
- Large lead frame results in excessive tooling costs.
- Large module baseplate approaches the limit of production facility capabilities.
- Pressure drop is higher than the target.

Conclusions

- The key technologies have been proven.
- Alpha converter prototype has been designed.
- All components have been received and the system has been assembled.
- High-volume cost estimates have been developed.
- Testing has achieved full power output (5 kW).
- Efficiency has been improved by 5% compared with the preliminary design.
- Volume and pressure drop of the alpha design have been tested.
- The up-to-date status from the alpha design is summarized in Table 3.

Table 3. Up-to-date status summary from the alpha design

	Alpha Design	DOE Goal	% Target
Output Power	5.1kW	5kW	102%
Efficiency	93%	92%	101%
Cost Estimation	$545	$375 total, ($75/kW)	69%
Coolant Temperature	90 Deg C	105 Deg C	86%
Volume	6.5 Liter	5 Liter	77%
Weight	7.6kg	6kg	79%
Coolant Pressure Drop	2.3 PSI	0.73PSI (5kPa)	32%

Future Direction

This project will conclude in FY 2006. In order to finalize the beta level (final) design, the following steps will be completed during FY 2006:

- Perform beta design addressing gap areas toward the final targets.
- Reduce costs by further simplifying design and fabrication requirements.
- Reduce DBC size to improve reliability.
- Reduce module baseplate size to improve manufacturability.
- Reduce converter packaging volume.
- Reduce pressure drop through baseplate flow channel optimization.
- Develop/refine DV test plan.

Patents

"A Interleaved High Power DC/DC Converter," PAT0589-01US, filed June 4, 2004.

"Integration of Planar Magnetics Transformer and Power Switching Devices in a Liquid-cooled High Power DC/DC Converter," PAT0588-02US, filed October 12, 2004.

4.6 Semikron Automotive Integrated Power Module Testing

Principal Investigator: Sam Nelson
Oak Ridge National Laboratory
National Transportation Research Center
2360 Cherahala Boulevard
Knoxville, TN 37932
Voice: 865-946-1327; Fax: 865-946-1262; E-mail:neslonsscjr@ornl.gov

DOE Technology Development Manager: Susan A. Rogers
Voice: 202-586-8997; Fax: 202-586-1600; E-mail: Susan.Rogers@ee.doe.gov

ORNL Program Manager: Mitch Olszewski
Voice: 865-946-1350; Fax: 865-946-1262; E-mail: olszewskim@ornl.gov

---

Objectives

The objective of the Semikron Automotive Integrated Power Module (AIPM) testing task is to evaluate the electrical performance of the high-voltage Semikron AIPM. Electrical tests were performed on the unit at Oak Ridge National Laboratory (ORNL) during January, 2005. The objective of the electrical tests includes the determination of continuous power capability, peak power capability, and efficiency at various power levels.

Approach

The approach used in this task was to perform standard electrical tests on the Semikron unit. The unit was tested with an inductive load to evaluate its performance across a range of input voltages (i.e., minimal, nominal, and maximum), output power levels, and output frequencies. The unit was also tested while driving a load motor (Solectria motor) in a dynamometer test cell at the National Transportation Research Center (NTRC).

Major Accomplishments

The Semikron AIPM unit was successfully tested during January 2005 at ORNL. The Semikron AIPM inverter demonstrated the ability to operate at the continuous (i.e., 30-kW) and peak (i.e., 55-kW) power levels with an efficiency of 0.97 when supplied with 70ºC coolant at 2.5 gpm during induction load testing. The inverter operated at the continuous power level for 60 min during the induction load tests with an average efficiency of 0.972. During dynamometer testing, driving a load motor, the inverter had efficiencies that ranged from 0.94 to 0.97 when operated at continuous power levels.

Technical Discussion

The Semikron inverter was tested during January 2005 at ORNL. The initial testing of the inverter was performed in room L101 of the NTRC with an inductive/resistive load. The load was connected in a Y-arrangement with an inductor and a resistor connected in series for each phase leg. Figure 1 shows a top view of the Semikron AIPM unit being load tested. Figure 2 shows the notebook computer containing the controller area network (CAN) bus controller program, the Yokogawa power meter, and the power supply for the Semikron controller. The Semikron inverter is in the background in Figure 2. Figure 3 shows a more detailed view of the CAN bus display.

Figure 1. Top view of Semikron AIPM unit.

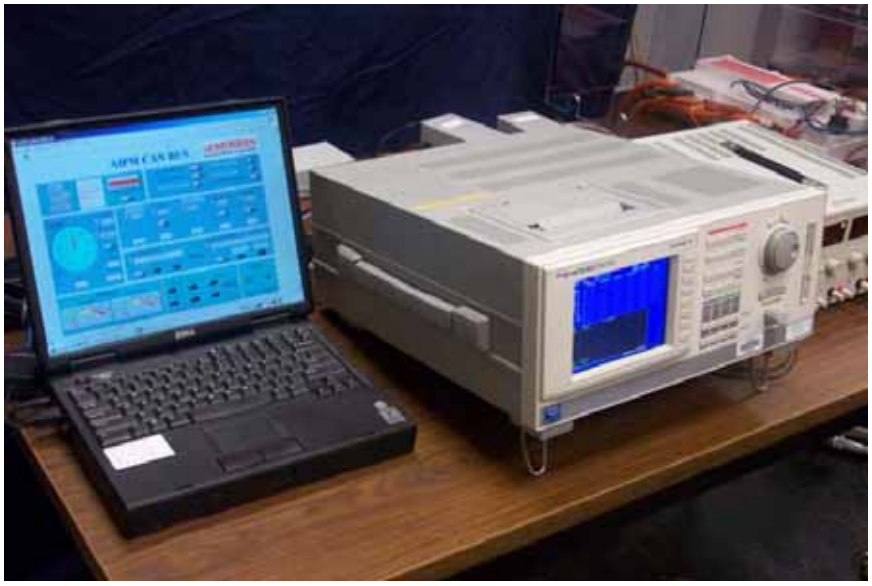

Figure 2. Control computer, power meter, power supply, and Semikron unit.

Table 1 lists the test results when the inverter was operated at 50 Hz at six different power levels with a 200-Vdc link for short-duration testing. The unit was operated at each test point for about 1 min with 20ºC coolant at a flow rate of 2.5 gpm. The average efficiency for the six data points is 0.966, and the efficiency increased with increased power levels.

Table 2 displays the test results when the inverter was operated with a 250-Vdc link for short-duration testing with 20ºC coolant at a 2.5-gpm flow. The unit had an average efficiency of 0.962 when operated with an output frequency of 10 Hz at seven different power levels. The inverter had an average efficiency of 0.976 when operated at five different output frequencies (i.e., 10, 20, 30, 50, and 60 Hz) with a requested dc link current of 80 A. The average efficiency during the load testing with a 250-Vdc link was 0.968.

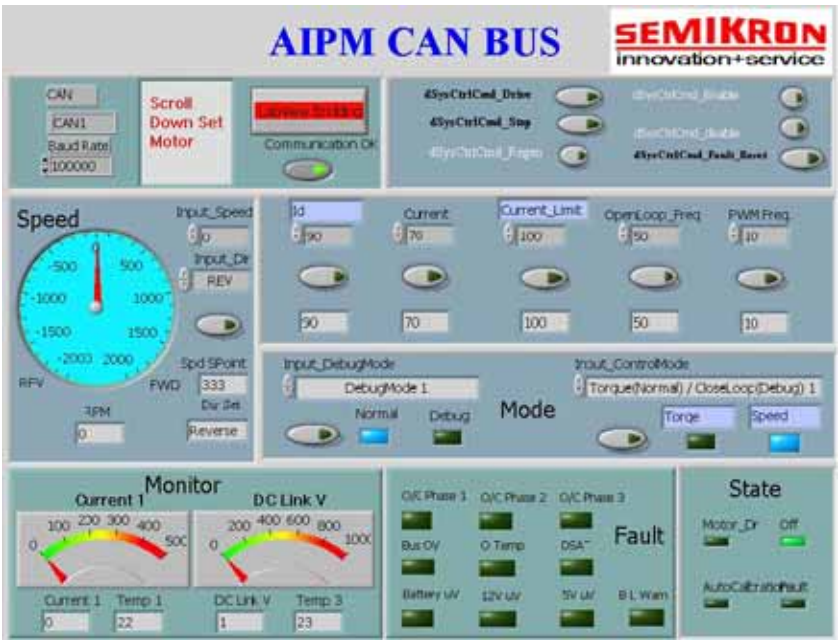

Figure 3. CAN bus display.

Table 1. Short-duration testing of Semikron inverter with 200-Vdc link

dc link	Freq	Idc	Vac	Iac	Pin	Pout	Effic.	Cool.	Flow
(Vdc)	(Hz)	(A)	(V_{LL})	(A_{rms})	(kW)	(kW)		(C)	(gpm)
200	50	7.5	87.5	24.9	1.51	1.43	0.947	20	2.5
200	50	16.5	106.3	34.0	3.3	3.15	0.955	20	2.5
200	50	28.1	123.1	43.3	5.71	5.54	0.970	20	2.5
200	50	43.3	137.0	53.6	8.79	8.56	0.974	20	2.5
200	50	61.5	149.4	64.5	12.46	12.14	0.974	20	2.5
200	50	74.9	156.8	70.8	15.13	14.8	0.978	20	2.5

Table 2. Short-duration testing of Semikron inverter with 250-Vdc link

dc link	Freq	Idc	Vac	Iac	Pin	Pout	Effic.	Cool.	Flow
(Vdc)	(Hz)	(A)	(V_{LL})	(A_{rms})	(kW)	(kW)		(C)	(gpm)
250	10	6.09	94.18	22.7	1.53	1.44	0.941	20	2.5
250	10	13.19	114	33.7	3.3	3.13	0.948	20	2.5
250	10	22.99	131.3	44.4	5.75	5.54	0.963	20	2.5
250	10	35.19	146	54.2	8.79	8.5	0.967	20	2.5
250	10	50.32	159.4	64.0	12.56	12.21	0.972	20	2.5
250	10	67.62	171.7	74.0	16.88	16.45	0.975	20	2.5
250	10	89.51	183.6	84.8	22.35	21.61	0.967	20	2.5
250	20	89.99	184.9	85.5	22.47	21.84	0.972	20	2.5
250	30	90.7	107.5	86.4	22.66	22.28	0.983	20	2.5
250	50	87.08	190.4	84.7	21.71	21.21	0.977	20	2.5
250	60	86.56	194.6	84.7	21.67	21.26	0.981	20	2.5

Table 3 shows the test results when the unit was operated with a 400- and 450-Vdc link for short-duration testing. With a 400-Vdc link, the unit was operated with an output frequency of 10 and 50 Hz with the same requested output current. The unit had a higher efficiency (0.986) when operated at 50 Hz. The unit was tested with a 450-Vdc link with an output frequency of 10, 50, and 70 Hz and the same requested output current. The efficiency exceeded the efficiency goal (i.e., 0.97) at 50 and 70 Hz but was below specification at 10 Hz (0.939).

Table 3. Short-duration testing of Semikron inverter with 400- and 450-Vdc link

dc link	Freq	Idc	Vac	Iac	Pin	Pout	Effic.	Cool.	Flow
(Vdc)	(Hz)	(A)	(V_{LL})	(A_{rms})	(kW)	(kW)		(C)	(gpm)
400	10	35.6	294.7	37.7	14.22	13.95	0.981	20	2.5
400	50	35.8	295.9	36.7	14.3	14.1	0.986	20	2.5
450	10	40.5	331.6	40.5	18.34	17.22	0.939	20	2.5
450	50	40.9	335.4	41.4	18.53	18.09	0.976	20	2.5
450	70	45.5	337.1	42.5	18.66	18.36	0.984	20	2.5

Table 4 displays the test results when the unit was operated with a 325-Vdc link for short-duration testing with 70ºC coolant and a flow rate of 2.5 gpm. The unit was operated at output frequencies of 10, 20, 50, 75, and 100 Hz with the same requested dc link currents of 20, 40, 60, 80, and 100 A during the test. The Semikron inverter demonstrated efficiencies near or above the target efficiency (i.e., 0.97) when operated at a reasonable load. In general, the higher efficiencies were demonstrated when the unit was operated with an output frequency of 20 Hz. Figure 4 plots efficiency vs output power for the inverter based on the test results in Table 4.

The inverter was tested at continuous output power levels (i.e., 30 kW) for 60 min with 70ºC coolant at a flow rate of 2.5 gpm. Figure 5 shows the test data from the power meter and the current waveforms for the inverter. The inverter was operating with an efficiency of 0.972 at the end of the 60-min test. Phase A, phase B, and the dc link currents are displayed in the Figure 5 plot. The two-wattmeter method was used to measure the inverter's output per the Blondel theorem. Element 1 measured the input; elements 2 and 3 measured the output of phases A and B. Element 4 was not used in the test. Sum A and B are the summations of the dc input and the output of the inverter, respectively. Table 5 displays test data from the continuous power test.

The inverter was operated at power levels greater than the continuous power level for short durations with 70ºC coolant. The inverter demonstrated a peak power capability of 57.7 kW with an efficiency of 0.976 when operated with a dc link of 400 V. The inverter produced 38.6 kW of output power when operated with a 325-Vdc link and 41.2 kW when operated with a 335 Vdc link. Figure 6 shows the power meter readings and the current waveforms at peak power conditions. The inverter's input and output power was 59.17 kW and 57.74 kW, respectively, which provides an efficiency of 0.976. Table 6 summarizes the test results for short-duration testing at power levels greater than 30 kW.

Table 4. Short-duration testing of Semikron inverter with 325-Vdc link

dc link	Freq	Idc	Vac	Iac	Pin	Pout	Effic.	Cool.	Flow
(Vdc)	(Hz)	(A)	(V_{LL})	(A_{rms})	(kW)	(kW)		(C)	(gpm)
325	10	5.4	108.2	27.0	1.8	1.6	0.892	70	2.5
325	10	18.6	150.3	45.5	6.0	5.7	0.944	70	2.5
325	10	40.1	182.4	65.2	13.0	12.4	0.957	70	2.5
325	10	69.4	209.6	85.3	22.5	21.8	0.971	70	2.5
325	10	104.4	232.6	104.0	33.7	32.8	0.973	70	2.5
325	20	5.5	107.9	27.7	1.8	1.6	0.898	70	2.5
325	20	18.7	150.3	45.9	6.0	5.8	0.957	70	2.5
325	20	39.37	183.8	65.1	12.81	12.4	0.968	70	2.5
325	20	69.7	210.1	85.7	22.4	22.0	0.983	70	2.5
325	20	104.7	232.9	104.1	33.7	32.9	0.976	70	2.5
325	50	5.1	110.9	26.9	1.6	1.5	0.909	70	2.5
325	50	18.2	155.6	45.4	5.9	5.6	0.956	70	2.5
325	50	39.8	188.9	65.3	12.8	12.3	0.964	70	2.5
325	50	69.3	217.6	85.3	22.3	21.6	0.969	70	2.5
325	50	105.9	242.2	105.5	34.0	33.2	0.976	70	2.5
325	75	5.2	110.8	27.2	1.7	1.5	0.873	70	2.5
325	75	18.3	163.3	45.5	5.9	5.6	0.959	70	2.5
325	75	39.6	198.1	65.3	12.7	12.3	0.972	70	2.5
325	75	68.9	228.5	85.4	22.1	21.4	0.970	70	2.5
325	75	105.1	253.5	104.7	33.7	32.8	0.973	70	2.5
325	100	5.0	122.5	26.4	1.6	1.4	0.894	70	2.5
325	100	18.3	172.2	45.1	5.9	5.6	0.949	70	2.5
325	100	39.4	209.8	64.8	12.6	12.3	0.969	70	2.5
325	100	68.3	241.0	84.5	21.9	21.3	0.974	70	2.5
325	100	84.2	257.2	94.0	27.4	26.7	0.974	70	2.5

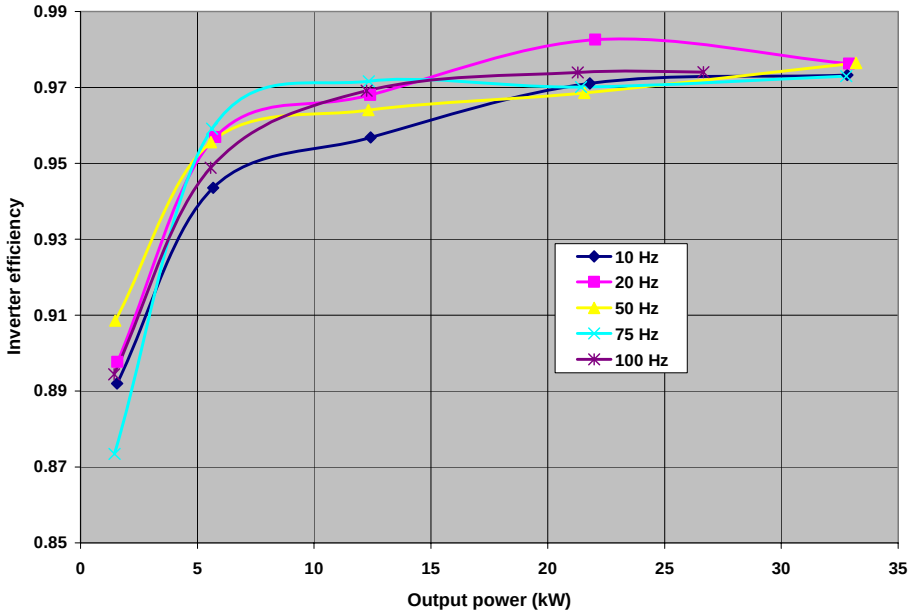

Figure 4. Inverter efficiency vs output power with 70°C coolant.

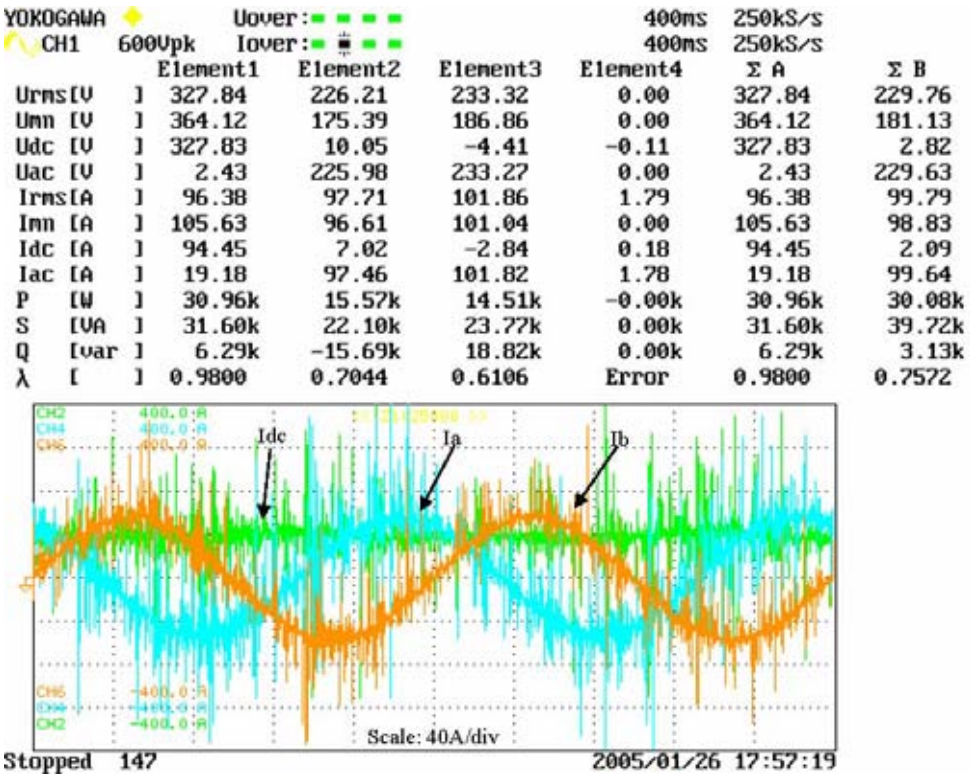

Figure 5. Power meter readings and current waveforms at end of continuous power test with 70°C coolant.

Table 5. Continuous power testing of Semikron inverter with 325-Vdc link

dc link	Freq	Idc	Vac	Iac	Pin	Pout	Effic.	Cool.	Flow	Time
(Vdc)	(Hz)	(A)	(V_{LL})	(A_{rms})	(kW)	(kW)		(C)	(gpm)	(m)
325	20	94.99	229.6	99.4	30.9	30.1	0.975	70	2.5	5
325	20	95.79	228.8	99.9	31.0	30.2	0.976	70	2.5	30
325	20	94.47	229.8	99.5	31.0	30.0	0.967	70	2.5	45
325	20	94.45	229.8	99.8	31.0	30.1	0.972	70	2.5	60

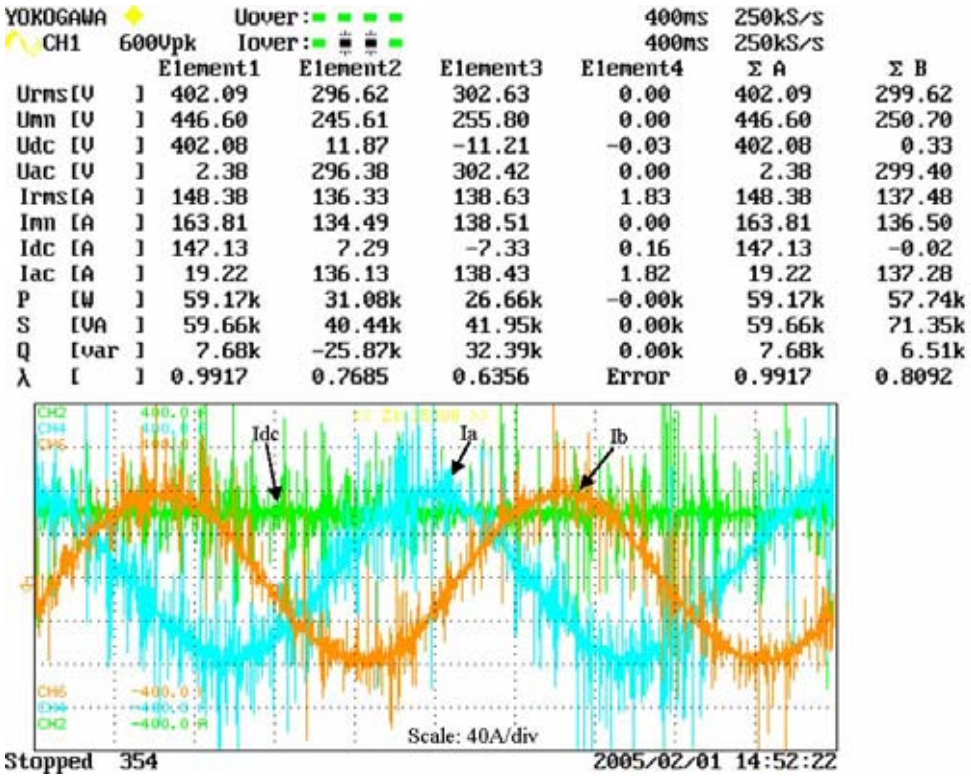

Figure 6. Power meter readings and current waveforms at end of peak power test with 70°C coolant.

Table 6. Testing of Semikron inverter at greater than continuous power levels

dc link	Freq	Idc	Vac	Iac	Pin	Pout	Effic.	Cool.	Flow
(Vdc)	(Hz)	(A)	(V_{LL})	(A_{rms})	(kW)	(kW)		(C)	(gpm)
325	20	118.7	242.1	111.2	38.6	37.7	0.977	70	2.5
335	30	122.5	122.7	114.9	41.2	40.0	0.970	70	2.5
400	20	147.1	299.6	137.5	59.2	57.7	0.976	70	2.5

Dynamometer testing

The inverter was tested while driving a Solectria motor in the 100-HP dynamometer cell at ORNL. The Solectria motor is a four-pole induction motor with a base speed of 2500 rpm. Dynamometer testing was performed with a dc link voltage of 325 V and with the inverter being supplied with 70ºC coolant at a flow rate of 2.5 gpm. The inverter supplied electrical energy to drive the induction motor from 750 to 2500 rpm with a torque load of 100, 150, and 200 Nm.

Figure 7 plots the inverter efficiency vs motor speed during the test. The highest efficiency (0.97) was obtained at 2500 rpm with a load of 150 Nm on the Solectria motor. Table 7 presents the test data for the tests at 100, 150, and 200 Nm. The higher inverter efficiency was obtained near the base speed on the motor at the higher torque loads. The inverter meets the efficiency goal at a speed of 2500 rpm.

The inverter was tested at continuous power (30-kW) conditions with the load motor speed ranging from 1000 to 2400 rpm. Figure 8 shows the tests results at seven different motor speeds with the inverter supplying 30 kW of electrical power. The inverter had an efficiency of 0.97 at 2400 rpm with an output of 30 kW. Figure 9 shows the power meter readings and current waveforms during the continuous power test on the dyne.

Table 8 summarizes weight and volume measurements, power density measurements, and goals for the Semikron AIPM. The unit has a peak power requirement of 55 kW. At that value the unit had a peak specific power density of 7.1 peak kW/kg, exceeding the goal of 5 peak kW/kg. The unit had a peak volumetric power density of 8 peak kW/L, which failed to meet the goal of 12 peak kW/L.

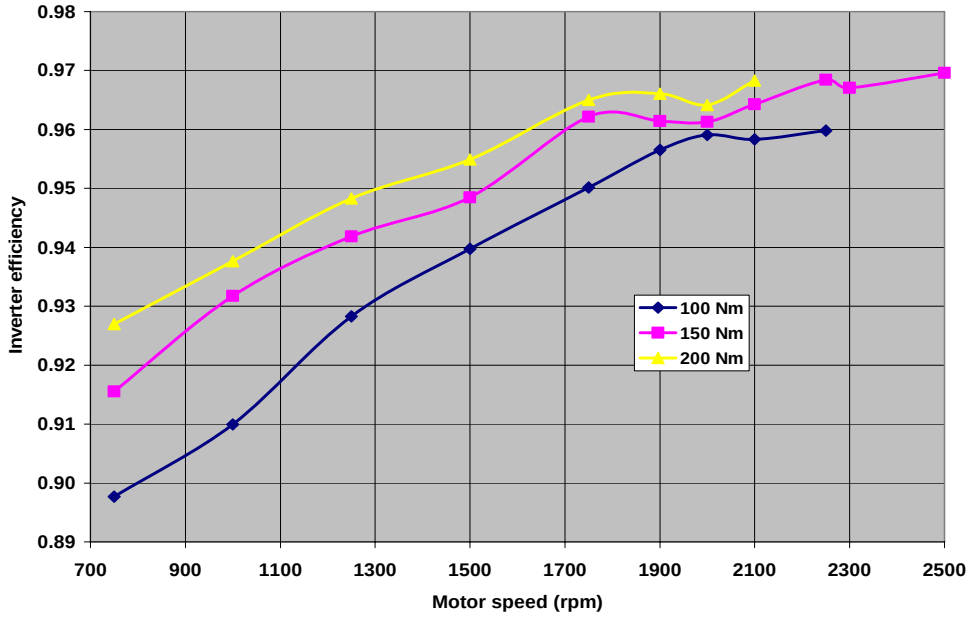

Figure 7. Inverter efficiency vs motor speed with 70ºC coolant.

Table 7. Dynamometer testing of Semikron inverter—speed vs inverter efficiency

dc link	Speed	Torq	Idc	Vac	Iac	Pin	Pout	Mech	AIPM
(Vdc)	(rpm)	(Nm)	(A)	(V_{LL})	(A_{rms})	(kW)	(kW)	(kW)	Effic.
325	750	100	34.3	145.7	155.0	11.2	10.1	7.8	0.898
325	1000	100	43.7	167.9	166.6	14.3	13.0	10.4	0.910
325	1250	100	49.5	104.4	157.2	16.3	15.1	13.1	0.928
325	1500	100	58.4	202.4	162.2	19.3	18.1	15.6	0.940
325	1750	100	65.2	211.7	134.5	21.5	20.4	18.3	0.950
325	1900	100	70.6	222.5	140.5	23.2	22.2	19.9	0.957
325	2000	100	72.7	222.6	130.0	23.9	23.0	20.9	0.959
325	2100	100	78.0	235.3	144.3	25.7	24.6	21.9	0.958
325	2250	100	82.5	241.3	142.7	27.1	26.0	23.5	0.960
325	750	150	49.5	147.5	178.0	16.2	14.9	11.8	0.916
325	1000	150	62.0	169.8	189.1	20.7	19.2	15.7	0.932
325	1250	150	72.1	184.9	180.5	23.7	22.4	19.6	0.942
325	1500	150	85.5	203.0	184.4	28.2	26.7	23.5	0.948
325	1750	150	97.2	208.7	161.3	32.0	30.8	27.4	0.962
325	1900	150	105.7	223.7	169.6	34.7	33.4	31.4	0.961
325	2000	150	109.2	211.1	165.6	35.9	34.5	31.4	0.961
325	2100	150	115.9	234.3	170.1	38.1	36.7	33.0	0.964
325	2250	150	121.5	233.7	162.4	39.9	38.6	35.2	0.968
325	2300	150	127.2	251.2	190.3	41.9	40.5	36.1	0.967
325	2500	150	140.5	232.1	178.1	46.1	44.7	40.0	0.970
325	750	200	19.2	149.3	206.5	21.8	20.2	15.7	0.927
325	1000	200	83.7	170.8	215.8	27.4	25.7	20.9	0.938
325	1250	200	96.5	185.8	209.9	31.7	30.1	26.1	0.948
325	1500	200	114.0	204.0	215.6	37.5	35.8	31.4	0.955
325	1750	200	132.2	212.9	204.1	43.4	41.9	36.7	0.965
325	1900	200	141.9	221.9	205.0	46.6	45.0	39.8	0.966
325	2000	200	147.8	217.2	210.2	48.5	46.8	42.0	0.964
325	2100	200	155.9	234.0	206.0	51.1	49.5	43.9	0.968

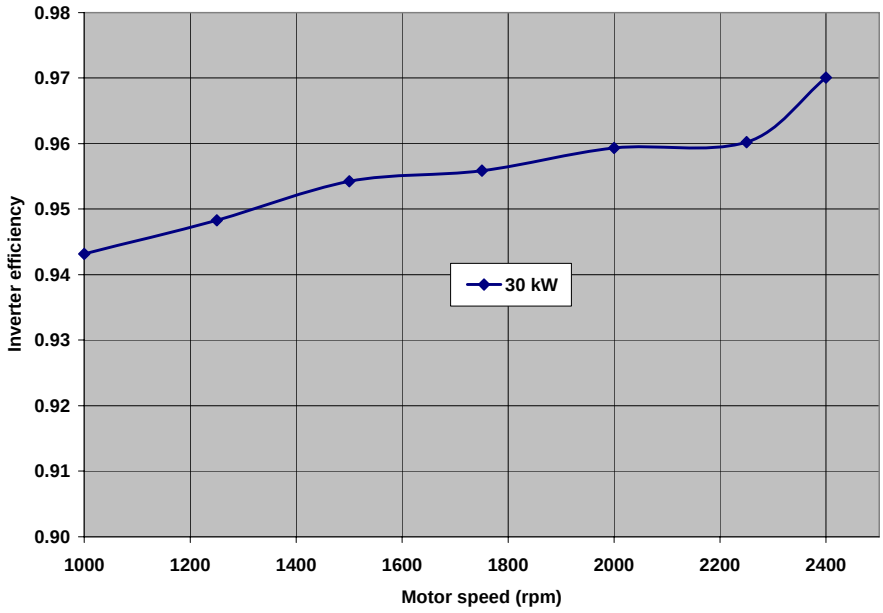

Figure 8. Semikron inverter efficiency vs speed at continuous power with 70ºC coolant.

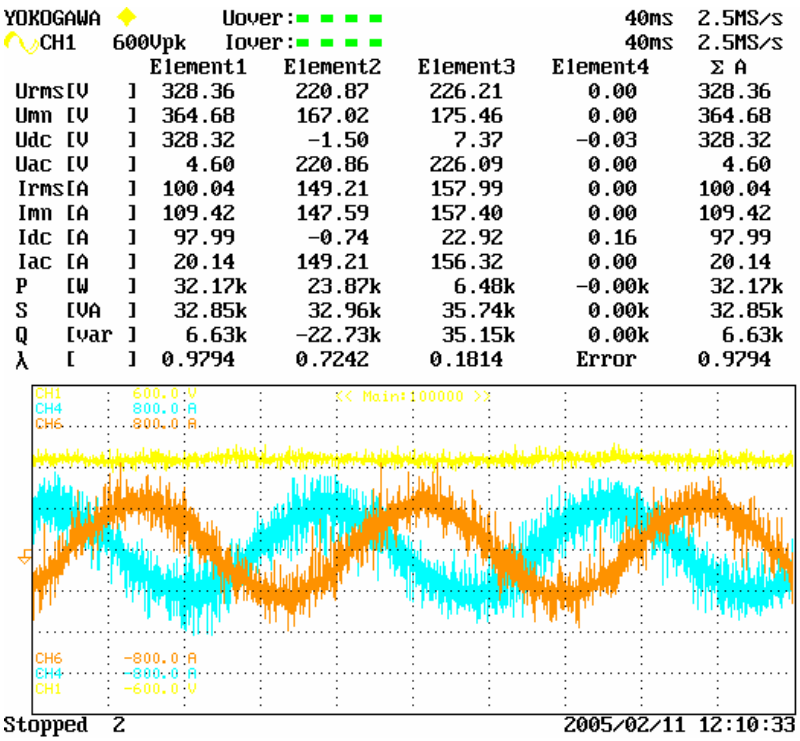

Figure 9. Power meter readings and current waveforms during continuous power test on dyne with 70ºC coolant.

Table 8. Specific power density summary

Characteristic	Semikron measurement	FreedomCAR Goal
Weight (kg)	7.7	NA
Volume (L)	6.9	NA
Peak power (kW)	55	55
Peak specific power density (peak kW/kg)	7.1	5
Peak volumetric power density (peak kW/L)	8	12

Conclusion

The AIPM unit demonstrated the ability to operate at continuous and peak power levels with an efficiency of 0.97. The unit had a specific power density of 7.1 kW/kg, exceeding the goal of 5 kW/kg, based upon the FreedomCAR-specified 55-kW peak power rating. The unit had a volumetric power density of 8 peak kW/L, failing to meet the FreedomCAR goal of 12 kW/L.

The Semikron AIPM has a capability of operation at a peak power rating of 160 kW with coolant supplied at 25ºC. At that rating the unit has a volumetric power density of 23 peak kW/L and a power density of 21 peak kW/kg.

Future Direction

Testing of the Semikron unit in January 2005 completes this task. Other inverter development and/or test activity will continue as needed.

Publications

Testing of the Semikron Validation AIPM Unit at ORNL—January 2005, ORNL/TM-2005/44.

4.7 High Performance Embedded Film-on-Foil Capacitors for HEV Power Electronics

D.Y. Kaufman, S. Saha, and K. Uprety
Energy Technology Division
Argonne National Laboratory
9700 S. Cass Ave.
Argonne, IL 60439
Voice: (630)252-4250 Fax: (630)-252-4289 E-mail: david.kaufman@anl.gov

DOE Technology Development Manager: Susan A. Rogers
Voice: 202-586-8997; Fax: 202-586-1600; E-mail: Susan.Rogers@ee.doe.gov

---

Objectives

This R&D program is developing high performance and economical DC bus capacitor technologies that will achieve APEEM specifications for HEV power electronic systems. Current DC bus capacitors occupy a large fraction of the volume and weight of the inverter module, cannot tolerate temperatures >120°C, and suffer from poor packaging, reliability, and deleterious failure modes. Traditional capacitor architectures with conventional dielectrics cannot adequately satisfy all of the performance goals. Key stumbling blocks include capacitance density, high temperature operation, and fail-safe operation, as well as manufacturability and cost. Achieving APEEM goals for capacitance density, weight, volume, and cost requires a high permittivity, high temperature rated dielectric packaged in a high volumetric efficiency architecture with benign failure features.

Approach

Argonne National Lab's (ANL) capacitor R&D program addresses these needs in an innovative manner by developing high performance low cost capacitors embedded into the printed wire board. In these "embedded film-on-foil capacitors" a base-metal foil (Nickel or Copper) is coated with a high permittivity ferroelectric material, $(Pb,La)(Zr,Ti)O_3$ (abbreviated as PLZT). Ferroelectrics possess high permittivity, breakdown electric field and insulation resistance. They can withstand high temperatures such that high ripple currents can be tolerated at under hood temperatures. Use of base-metals and chemical solution deposition reduce cost. An embedded capacitors approach significantly reduces component footprint, improves device performance, provides greater design flexibility, and offers an economic advantage. This technology will achieve the highest degree of packaging weight and volume efficiency.

Our R&D efforts focus on examining the underpinning issues of film-on-foil embedded capacitor performance, developing low cost capacitor designs, establishing robust commercially and economically viable fabrication protocols, and transferring the technology to industry for manufacturing.

Major Accomplishments

- Refined $LaNiO_3$ (LNO) buffer layers to avoid deleterious effects of a parasitic low capacitance interfacial oxide layer.
- Developed a core technology of PLZT/ LNO/ Ni capacitor foils with dielectric constants of 1200 (1.5 $\mu F/cm^2$) and loss ≤ 0.06.
- Developed PLZT/LNO/Ni capacitor foils reaching 580 V with breakdown fields ≥ 1.2 MV/cm.
- Designed electrode architectures to achieve benign failure via self-clearing. In such a mode evolving faulted areas become removed from the larger structure and the capacitor continues to operate with a

nearly undetectable loss in performance. This mechanism parallels fail-safe designs hailed in certain polymer capacitors.

- Identified manufacturers and OEM providers for commercial partnering and initiated R&D collaborations.

Technical Discussion

The replacement of bulky inefficient discreet capacitors with capacitors embedded within the layers of a printed wire board is an innovative solution to high capacitance density and high volumetric efficiency capacitors. Embedded capacitors can be located directly underneath the active devices, greatly reducing component footprint and improving reliability. While this technology has primarily received attention for high frequency decoupling capacitors, it can be extended to the higher voltages of HEV systems. The vision of embedded DC bus capacitors is compelling and offers US automotive companies a substantial technological advantage over their foreign counterparts. Gone will be the bulky coke-can-like banks of capacitors, replaced instead by lengths of capacitors tucked flat and neatly underneath the active components and bus structure.

The key provision is the integration of high-k ferroelectric dielectric layers within the printed wire board. Since high temperature processing (~600-800 °C) is required to obtain crystalline ferroelectric materials, direct deposition on the polymeric printed wire board is not possible. Instead, a pre-fabricated 'film-on-foil' approach is adopted whereby the ferroelectric is first deposited via chemical solution deposition (CSD) on a thin base metal foil, crystallized at high temperatures, and the coated foil subsequently embedded within the printed wire board.

A principal concern in the fabrication of 'film-on-foil' capacitors is eliminating the deleterious effects of a low-k parasitic oxide at the metal-ferroelectric interface that acts as a series capacitor and reduces the overall capacitance. To negate the influence of the interfacial oxide a conductive oxide buffer layer is interposed between the ferroelectric and the metal foil. The buffer layer acts as the bottom electrode and any secondary oxide formed below it at the metal interface is inconsequential to the parallel plate capacitor.

We have developed a core technology for CSD PLZT on Ni film-on-foil capacitors with $LaNiO_3$ [LNO] buffer layers. CSD solutions were synthesized at ANL and films deposited by spin coating. All annealing and pyrolosis were done in air and repeated to build up layers of sufficient thickness.

Even a single layer of LNO (~0.15 microns) is sufficient to obviate the parasitic influence of interfacial NiO formation. LNO film metrology exerts a pronounced influence on dielectric loss and breakdown strength. Three layers of LNO are required to completely cover and ameliorate the roughness of the Ni substrate. The planarizing influence of the LNO layer is highlighted in the cross sectional SEM image of a 3.5 micron PLZT/ 0.45 micron LNO/Ni foil heterostructure shown in Figure 1. Besides obviating any NiO formation along the Ni interface, the LNO provides a smooth interface for PLZT nucleation and growth. The PLZT is dense as no discernable porosity can be observed. These PLZT/LNO/Ni capacitors achieved capacitance densities of 1.5 microfarads/cm^2 nearly equivalent to the 1.7 microfarad/cm^2 obtained using inert platinized Si substrates. The smooth interfaces and dense microstructure both contribute to high breakdown strengths ≥12.MV/cm.

We are developing an understanding of processing-property relationships and core technologies for film-on-foil capacitor sheets and embedding of those sheets. The processing libraries will be then transferred to manufacturers. Together we will develop low cost high throughput manufacturing processes while scaling the technology to commercial production. This will involve assessing the interrelationship between fabrication processes, materials, and capital investment. US microelectronics and auto electronics companies are very interested in embedded passives technologies. We have collaborated with a number of companies on issues of mutual concern and capitalize on their engineering solutions towards embedding. This also ensures that our technology can easily be ported to industry for manufacturing.

We have developed film-on-foil capacitors that exhibit graceful failure – a gradual loss in capacitance upon localized breakdown events. Following a discreet breakdown the capacitor continues to function and is only considered to have failed at such time that a defined leakage current or dielectric loss is reached. At sufficiently high voltages dielectric breakdown occurs in a discreet localized area and leads to the discharge of the stored energy in that localized area of the dielectric. In a matter of microseconds the discharge causes heating of the immediate area such that the dielectric is physically "cleared" away from the defect site and the metal top electrode is vaporized a nominal distance from the defect. By this process the breakdown site becomes electrically isolated and removed from the remainder of the capacitor structure, while the capacitor continues to operate and can obtain even higher voltages. A small loss in capacitance is only observed after several breakdown/clearing events have occurred. Indeed, it usually takes hundred to thousands of such clearings to cause a few percent loss in capacitance. In such a manner, instead of shorting, the capacitor has effectively repaired itself ("self-healed") and failure occurs gracefully. Self-clearing capacitors can sustain many breakdown events during their lifetime and can tolerate higher voltages. Such self-clearing failure modes are the same as those in polymer capacitors

Conclusion

We have developed a core technology for high capacitance density, high breakdown strength film-on-foil capacitors exhibiting graceful failure. PLZT film-on-foil capacitors have been fabricating with LNO buffer layers interposed on top the Ni foils. The LNO layers allow the film-on-foil capacitors to be processed in air and compensates the roughness of the Ni foil and provides a smooth interface for the PLZT films, resulting in higher breakdown strengths. Top electrode metallization enables self-clearing of faults and graceful failure. This core technology is a first step in embedded DC bus capacitors with significant size and weight reduction and improved performance and reliability.

Future Directions

In FY06 we will elucidate processing-microstructure-dielectric property relationships to provide strategies for device manufacturing. We will evaluate the high voltage and high temperature behavior of ferroelectric films on metal foils with a perspective on reliability. Processing protocols will be developed for high capacitance density ferroelectric films on Cu and eliminate the need for interlayers, thereby increasing the engineering capacitance density. We will investigate the microstructural aspects of dielectric breakdown and degradation and tailor devices based on those findings.

Significant effort will be directed towards fabricating embedded film-on-foil capacitors prototypes. We will evaluate device performance including reliability and benchmark against APEEM goals. These initial prototypes will be evaluated by ORNL as well.

The laboratory work is focused on developing a proven qualified technology that can be transferred to industry for commercial device manufacturing. As such we continue to work in concert with our industrial contacts to advance embedded passive technology and maintain our technology in alignment with industrial directions

Publications

"Scaling Effects in PLZT/Ni Film-on-Foil-Capacitors for Embedded and Discreet Capacitors", D. Y. Kaufman, S. Saha and S. K. Streiffer, Presented at the Fall Mtg. of the Materials Research Society.

"PLZT Film-on-Foil Capacitors For Embedded Passives", D. Y. Kaufman, S. Saha, and K. Uprety, Proceedings of the 12th US-Japan Seminar on Dielectric & Piezoelectric Ceramics

"Chemical solution deposition of $LaNiO_3$ on Ni metallic substrate", K. Uprety, D. Kaufman, in preparation.

"Dielectric Performance of PLZT/LNO/Ni Film-on-Foil Capacitors for Embedded Passives", K. Uprety and D.Y. Kaufman, in preparation.

Patents

"Ceramic Capacitor Exhibiting Graceful Failure by Self-Clearing", D.Y. Kaufman and S. Saha, filed with U.S. Patent Office, June 2005.

Figures

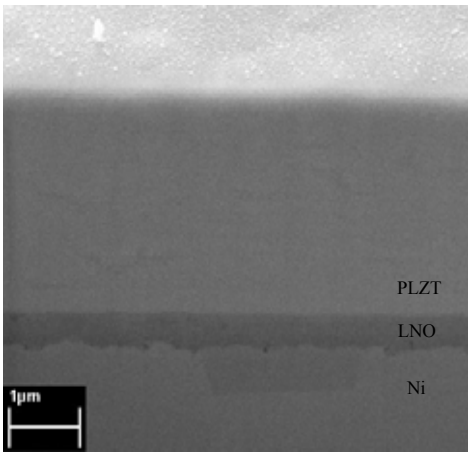

Fig. 1. Cross sectional SEM micrograph of a PLZT/LNO/Ni film-on-foil heterostructure.

4.8 Glass Ceramic Dielectrics for DC Bus Capacitors

Principal Investigator: Mike Lanagan
280 Materials Research Laboratory
Penn State University
University Park, PA 16802
e-mail: MLanagan@psu.edu
Phone: 814-865-6992

DOE Technology Development Manager: Susan A. Rogers
Voice: 202-586-8997; Fax: 202-586-1600; E-mail: Susan.Rogers@ee.doe.gov

---

Objectives: Power converters play a major role by converting energy stored in electrochemical batteries and fuel cells from direct current (DC) into alternating current (AC) for electric and hybrid vehicles. The conversion from DC into AC is not ideal; however, and the operation of a typical switch mode inverter leads to alternating currents on the DC bus at harmonics associated with the switching frequency. DC bus capacitors are required to reduce ripple current. The overall goal of this program is to reduce the cost, volume, and weight of power electronic inverter modules by focusing research efforts on capacitor components and dielectric materials for capacitors

Targets are tied to the FC R&D Plan and EE Tech Team Roadmap: Recently, U.S. capacitor manufacturers are focusing on high voltage high power capacitors. These companies see increased demand from the medical, telecommunication, and automotive industries for high voltage capacitors. Major manufacturers include: AVX, Kemet, Taiyo Yuden, Murata, TDK and EPCOS. The comparison of Multilayer Ceramic Capacitors (MLCCs) with EE tech team specifications is shown in Figure 1.

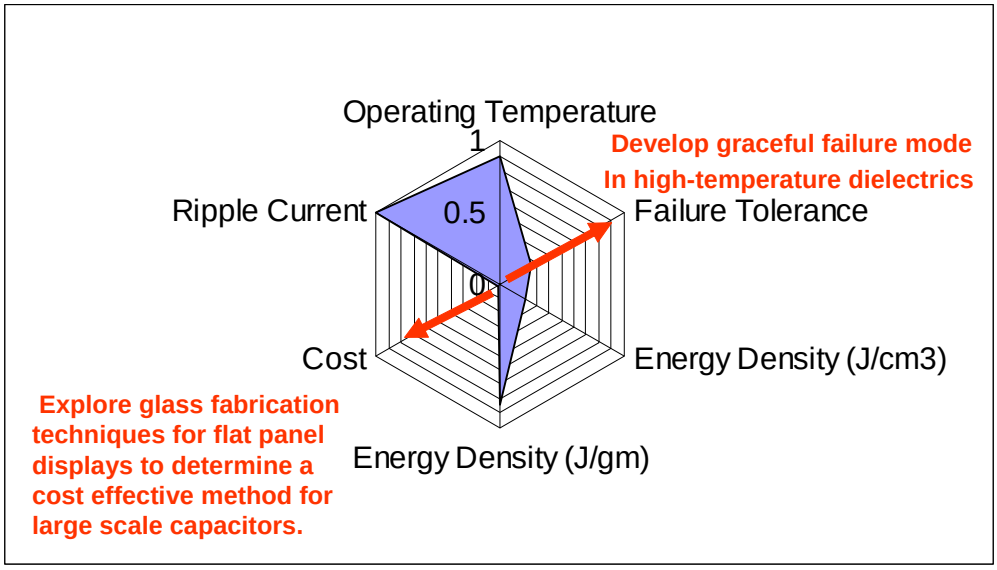

Figure 1: Comparison of MLCC Capacitor Parameters with EE Tech Team specifications.

As shown in Figure 1, the ripple current and operating temperature specification are close to meeting the EE tech team inverter specifications; however, failure tolerance, energy density and cost targets are

substantially below than what is required for hybrid vehicles. The multilayer ceramic capacitor temperature specification is generally limited by the dependence of dielectric constant on temperatures. One of the major drawbacks of MLCCs is the failure mode, which often results in a short circuit. Generally, the fabrication process involves deposition of thick electrode layers which melt and fuse together at high temperature. For this reason, the voltage ratings for MLCCs substantially below the failure voltage, which limits the energy density and increases cost. Future research and development activities need to focus on graceful failure mechanisms in multilayer ceramic capacitors. The ripple current capability of MLCCs, especially at high temperature, is superior to all of the other capacitor types. Figure 1 shows that these capacitors are very close to satisfying the DOE freedom car specifications on operation temperature and ripple current.

Approach: In order to address the critical gaps shown in Figure 1, the major focus is on developing graceful failure mechanisms in glass-ceramic based capacitors and finding a large-scale manufacturing process for D.C bus capacitors. We have had several fruitful interactions with Corning, a flat-panel display manufacturer to determine if their materials are appropriate for capacitors. As shown in Figure 2, very large glass sheets can be manufactured.

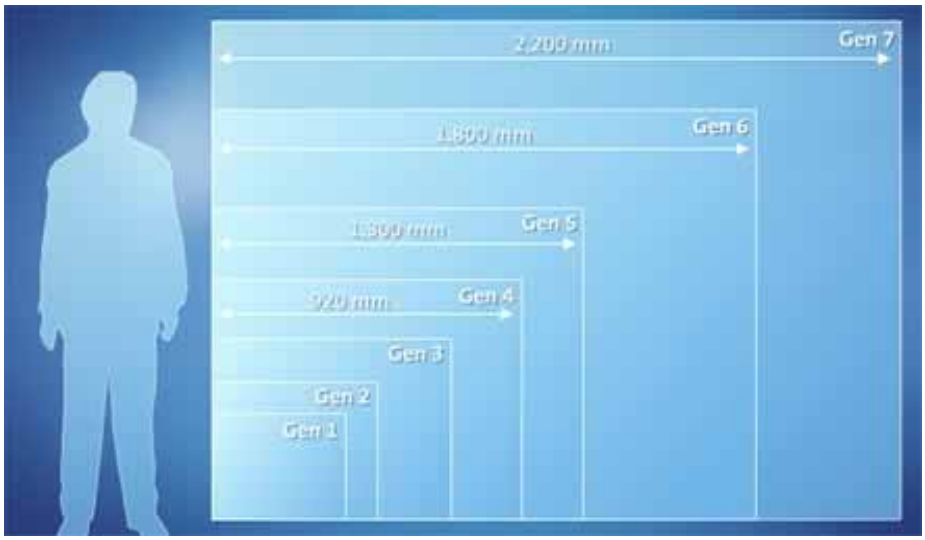

Figure 2: Large area glass panels for flat panel displays will be studied for high temperature D.C. bus capacitors for hybrid electric vehicles. This project explores the electrical properties of display glass at high temperatures.

The first task is to characterize dielectric material and capacitor performance (capacitance, loss, ESR) as a function of frequency, temperature, and voltage. These properties are directly related to reducing capacitor volume in the inverter.

Task two is to identify capacitor failure mechanisms and develop new ways in which capacitors fail in the "open mode" instead of a short circuit.

Task three is to develop a low cost glass process for manufacturing recrystallized-glass capacitors which can operate at high temperatures in automotive applications.

Major Accomplishments:

- We have successfully characterized the dielectric properties of Corning display glass at high temperature. Figures 3 and 4 show that these materials are very promising for operating temperatures over 250°C.

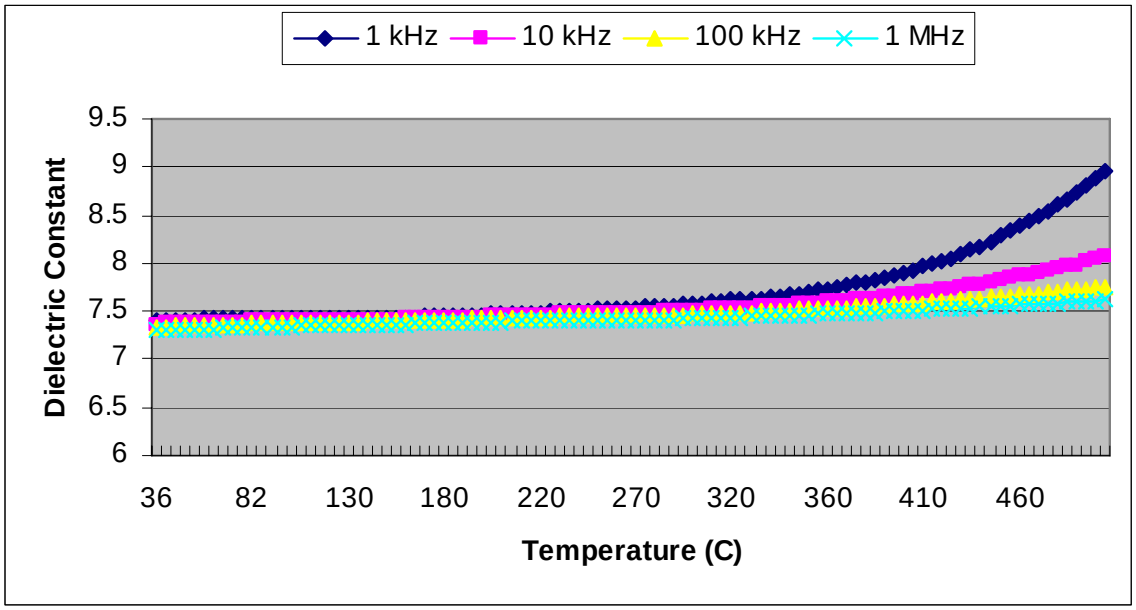

Figure 3: The dielectric constant of Corning Eagle 2000 glass as a function of temperature and frequency. The materials were characterized in the typical frequency range for a DC bus inverter (1 kHz to 1 MHz). The dielectric constant of 7.5 is double that of conventional polymers, which will decrease the capacitor size by 50%.

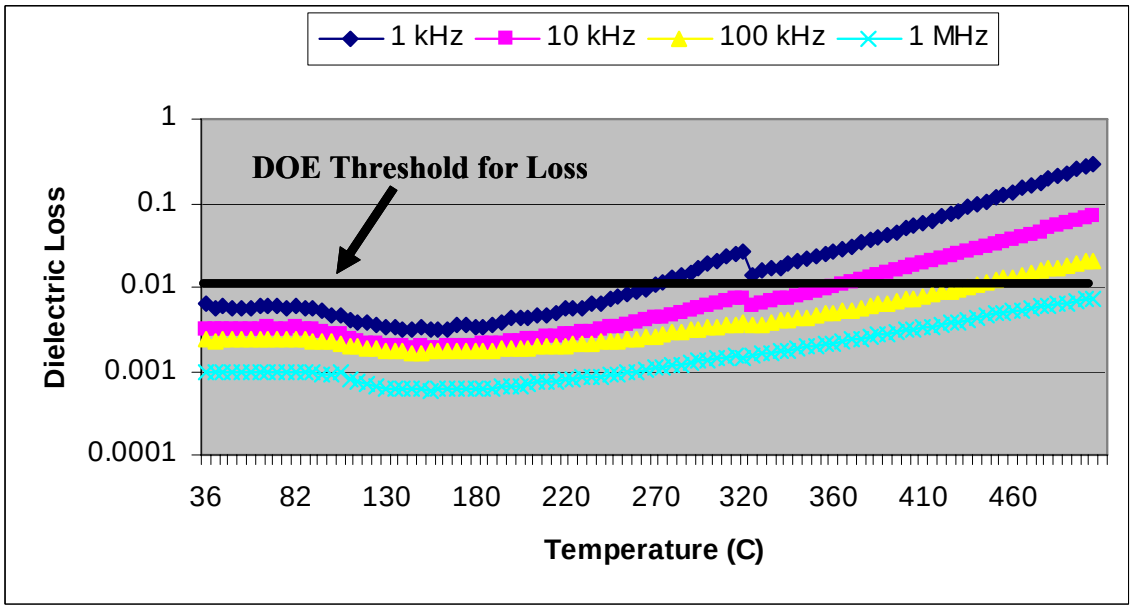

Figure 4: The dielectric loss of Corning Eagle 2000 glass as a function of temperature and frequency. The dielectric loss is within DOE Freedom Car specifications up to a temperature of 270°C.

.

- We completed an upgrade to our glass casting process in which a motor was added to roll quench system (see Figure 5), which will allow us to fabricate larger glass sheets for scaling-up the process.

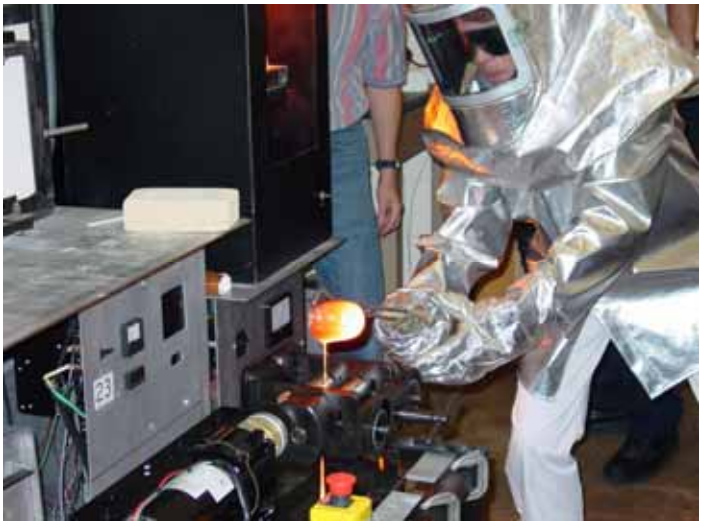

Figure 5: New glass quenching apparatus developed at Penn State University for fabricating glass sheet for DC bus capacitors.

- We developed a series of glass compositions to optimize the energy density and process tractability, and we found that increased silica in the starting batch will assist in developing large glass sheets. However, there will be trade-offs between energy density (DOE-Tech team goal = 0.9 J/cm^3) and the ability to form large glass sheets. A capacitor sample was sent to Oak Ridge for testing. Several publications from this work are shown in the Publications section of this report.

Technical Discussion : We have demonstrated that glass and glass-ceramic materials are promising for high temperature DC Bus capacitors for hybrid electric vehicles. In order to determine the reliability of glass ceramic materials at high temperature we will carry out Highly Accelerated Life Tests (HALT). These tests will be used to project capacitor life during use in a hybrid vehicle. The long-term failure mechanisms are associated with electrochemical phenomena, electromigration, and electromechanical effects. To quantify the capacitor reliability, we will explore HALT, which utilizes temperatures and voltages that are well above the operational conditions of the capacitors. HALT testing is carried out between 100 and 200 ° C for conventional capacitors that operate near room temperature. In order to predict long-term capacitor reliability, component manufacturers have developed an empirical relationship between capacitor failure time, applied DC voltage, and temperature.

Equation 1:

$$\frac{t_1}{t_2} = \left(\frac{V_2}{V_1}\right)^N \exp\left[\frac{E_s}{k_b}\left(\frac{1}{T_1} - \frac{1}{T_2}\right)\right]$$

The mean time to failure (t_1) under operating conditions (V_1 and T_1) can be estimated from an accelerated life test time (t_2) at higher voltage and temperature (V_2 and T_2).The HALT activation energy (E_s) and the empirically-derived exponential (N) have been obtained for capacitors by several manufacturers.

Typically, thousands of samples are used at several temperature and bias levels. Activation energy levels range from 0.9 to 1.2 eV and N values are often 2 to 3.
The next step is to carry out highly accelerated life tests (HALT) on these materials to determine if they degrade under a DC bias.

Conclusion: This project has two major thrusts: 1) Explore commercial glass as a dielectric material for high temperature DC bus capacitors and 2) Synthesize new glass-ceramic materials for capacitor miniaturization. What is needed to greatly improve energy storage capacitor technology beyond the current state-of-the-art is a robust, high permittivity dielectric material. Ferroelectric glass-ceramics offer a solution to this problem. Researchers at PSU have demonstrated a material with an energy density of ~ 5 J/cm^3, which exceeds the Freedom Car goal. Capacitors made from glass-ceramic would have the energy density, reliability, and the low-loss needed for high frequency power conditioning and filtering. In addition this material is expected to exhibit high temperature capability (> 200°C) that will be required for next generation power converters based on silicon carbide (SiC). For this program Penn State and its industrial partner, TRS Ceramics, will investigate a variety of techniques for fabricating glass-ceramic into high energy density capacitors. Our specific goals will be to demonstrate 1 to10 μF capacitors with packaged energy densities of 3 to 5 J/cm^3 at AC ripple frequencies in excess of 50 kHz. Secondary goals will be to demonstrate operation to temperatures in excess of 200°C and achieving a graceful failure mechanism.

Future Directions: Future research activities for DC bus capacitors should focus on polymer and glass-ceramic dielectrics with high dielectric constant and high temperature operation. Current work at Sandia National Laboratories on hydroxylated polystyrene (PVOH) has demonstrated dielectric constants between 4.5 and 6 and excellent high temperature properties. Glass Ceramic research at Penn State University has shown that high dielectric constant (ε_r=800) can be achieved. Research at Argonne National Laboratory on $(Ba_xSr_{1-x})Ti\ O_3$ films has demonstrated the possibility of operating these films up to 150ºC. Critical Issues will be in achieving the energy density and temperature goals set forth by the EE Tech Team, and in the scale-up of the processes being developed under the current program.

Publications:

Cheng CT, **Lanagan M**, Jones B, et al., Crystallization kinetics and phase development of PbO-BaO-SrO-Nb2O5-B2O3-SiO2-based glass-ceramics, JOURNAL OF THE AMERICAN CERAMIC SOCIETY 88 (11): 3037-3042 NOV 2005.

Du J, Jones B, **Lanagan M**, Preparation and characterization of dielectric glass-ceramics in Na2O-PbO-Nb2O5-SiO2 system, MATERIALS LETTERS 59 (22): 2821-2826 SEP 2005.

Cheng CT, **Lanagan M**, Lin JT, et al., Crystallization kinetics and dielectric properties of nanocrystalline lead strontium barium niobates, JOURNAL OF MATERIALS RESEARCH 20 (2): 438-446 FEB 2005.

Kwon DK, **Lanagan MT**, Shrout TR., Synthesis of BaTiTe3O9 ceramics for LTCC application and its dielectric properties, JOURNAL OF THE CERAMIC SOCIETY OF JAPAN 113 (1315): 216-219 MAR 2005.

Pan Ming-Jen, **Lanagan M.**, Bender B., Cheng CT, High Energy Density Ferroelectric Glass Ceramics, CERAMIC TRANSACTIONS, 169, 187-193, 2005.

4.9 High Temperature Film Capacitors

Principal Investigator: Bruce Tuttle
Sandia National Laboratories
P.O. Box 5800, MS 1411
Albuquerque, NM 87185-1411
Voice : (505) 845-8026, Fax: (505) 844-9781; E-mail: batuttl@sandia.gov

DOE Technology Development Manager: Susan A. Rogers
Voice: 202-586-8997; Fax: 202-586-1600; E-mail: Susan.Rogers@ee.doe.gov

Contractor: Sandia National Laboratories, Albuquerque, New Mexico
Prime Contract No.: 04-94AL85000

Objectives

- Develop a replacement technology for aluminum electrolytic dc bus capacitors currently used for fuel cell/electric hybrid vehicles.
- Develop a high-temperature polymer dielectric film technology that has dielectric properties technically superior to those of aluminum electrolytic dc bus capacitors and will result in comparable or smaller size.
- Perform extensive high field and high temperature testing of polymer film dielectrics
- Scale up cost-competitive polymer film dielectric technology.
- Fabricate prototype capacitors.

Approach

- Contact DOE program managers, automobile design and component engineers, dielectric powder and polymer film suppliers, and capacitor manufacturers to determine state-of-the-art capabilities and to define market-enabling technical goals.
- Develop a project plan with DOE Program Managers, automobile manufacturers and large and small capacitor companies to fabricate polymer dielectric sheets suitable for FreedomCAR capacitor manufacturing.
- Synthesize unique conjugated polyaromatic chemical solution precursors that result in dielectric films with low dissipation factors (DFs) and excellent high-temperature dielectric properties.
- Develop polymer film processes and technologies that will lower costs to permit competitive high-volume capacitor manufacturing.
- Develop chemically prepared nanoceramic powders and high density layers of two classes of dielectrics: 1) High K PLZT materials and 2) lower K, High breakdown field TiO_2 materials
- Interact with Oak Ridge National Laboratory (ORNL) with regard to mechanical characterization of films.

Major Accomplishments

- Invented chemical synthesis procedures that resulted in lower cost polyphenylated polyphenylene product that should reduce cost of these polymer films with excellent low loss properties (@150^{o}C) by a factor of ten.
- Invented chemical synthesis procedures for both sulfonamide functionalized and low cost processed hydroxylated phenylated polyphenylene films
- Developed synthesis procedures for novolac resins with cross-link iso-cyanate elastomer chemistries and polyaeryl ether based polymers
- Developed direct write aerosol spray deposition process to fabricate high quality chem-prep PLZT layers of 50 micrometer thickness that could withstand 220 kV/cm fields – a potential factor of two reduction in volume compared to state of the art barium titanate capacitors.
- Improved direct write aerosol spray deposition process such that 6 layer PLZT multilayer capacitors could be fabricated in a single firing.
- Synthesized chem-prep TiO_2 powders and fabricated capacitors using aerosol spray deposition that could withstand 600 kV/cm fields.
- Characterized dielectric constant, dissipation factor and leakage current behavior for both polymer and nanoceramic dielectrics.
- Collaborated with ORNL to develop new metric for polymer film mechanical properties, specifically the strain to failure rather than the mechanical strength was shown to be a better metric for the efficient winding of polymer film capacitors.

Technical Discussion

Strategy and Interactions

SNL has interacted with DOE program managers and a number of representatives from the automobile industry to obtain their perspective on what is needed for 2010 automobiles. In FY 2005, SNL continued its primary emphasis on the development of polymer film dielectrics for two reasons. First, DOE and EE tech team members have retained their position that soft breakdown dielectric film technology is highly desired. Soft breakdown is a phenomenon that large volume manufactured polymer film capacitors inherently possess. Second, emphasis on polymer dielectrics provides greater balance of the DOE effort between polyfilm and ceramic technologies, as requested by DOE and the Electrical and Electronics Tech Team. SNL also began a new technical start in FY05 in the area of nanoceramic capacitors. The investigation of this new technology was due to the 2010 high temperature requirement of 140^{o}C and Sandia's long standing expertise in chemically prepared ceramic powders for electronic ceramic applications. In FY05, the synthesis of high energy storage density nanoceramic dielectric powders of TiO_2 and lead lanthanum zirconate lead titanate (PLZT) was begun. SNL has consulted with the Advanced Technology Vehicles Division of GM, Custom Electronics, AVX, TPL, Hydrosize, Inc., and Brady Corporation about these technologies and future scale up operations.

These interactions led us to the conclusion that the most viable replacement technology for electrolytic dc bus capacitors by 2010 is either multilayer polymer film or multilayer ceramic capacitors. Reducing the size of the polymer capacitors was most often cited by automobile design engineers and capacitor manufacturers as a needed technology-enabling breakthrough. In addition, it is necessary to improve high-temperature (140^{o}C) performance while keeping the technology cost-competitive.

An individual dielectric layer thickness of approximately 3 μm for polyfilm capacitors is projected to reduce capacitor size. These thickness values are based on operating field strengths of 2 MV/cm for the newly developed polyfilm capacitors. Based on these assumptions and on measurement of presently

available commercial capacitors, size comparisons and capacitance densities were obtained for 500 μF dc bus capacitors for different technologies. The projected polymer film capacitor volume was calculated assuming that there is 40% non-active capacitor space and 200-nm thick electrodes are used. Note that the volumetric capacitance efficiency for a K = 4.5 polyfilm capacitor of 2.4 $\mu F/cm^3$ exceeds the near-term commercialization goal of 2 $\mu F/cm^3$. In order to meet the 2010 EE Tech team specification of 5$\mu F/cm^3$, a polymer with dielectric constant of 6 and operating field of 2.7 MV/cm will be required. From recent discussions, it is expected that DOE program managers and the EE Tech team will support SNL scale up of dielectric film technology that is more volumetrically efficient than present state of the art commercial technologies.

Polymer Film Dielectric Development

SNL polymer film dielectric development has been based on the request from manufacturers that the new polyfilm dielectrics have voltage and temperature stability equivalent to that of present polyphenylene sulfide (PPS) technology. Thus a structural family of polymer dielectrics has been designed and synthesized to meet two of the most stringent FreedomCAR requirements: (1) low dielectric loss and (2) extremely good temperature stability. Very low dissipation factors on the order of 0.003 were measured at 150°C for these SNL fabricated films. A patent disclosure has been initiated covering the design and synthesis techniques for this polymeric family [1,2] based on phenylated polyphenylene (PPP). A previous drawback to this technology was the high cost synthesis costs of these materials. In FY 2005, our team developed procedures that substantially lowered the cost of synthesis of scale up quantities. Lower cost was achieved by developing new procedures that eliminated two chemical synthesis steps and the identification of less expensive raw materials.

A total of seven different polymer film chemistries were investigated in FY05. These chemistries included polyaryl ethers (tenax), hydroxylated polyphenylene, modified polyphenylene sulfide and sulfonamide functionalized low cost phenylated polyphenylene. In order to keep a clear view of technical progress an EXCEL table (Figure 1) was created at the request of Raymond Fessler. Our metrics were synthesis, film fabrication, mechanical properties and electrical properties. The progress table was color coded. Green indicated a completed task, yellow a task in progress, red a major technical hurdle and white a task not yet begun.

Polymer Name		Synthesis	Film Fabrication	Mechanical Properties	Electrical Properties
Polyphenylene Sulfide (PPS)		Purchased commercially state of the art	Toray 3 micron sheet	good strain to failure properties	K = 3.1, DF = 0.006 to 140C
High Cost Phenylated Polyphenylene (PPP); O,S and F side groups		SNL Patented Process, little change in K, DF with heteroatom bridging or F side group modifications	Spin Deposited Films on Al coated Si Only	not tested due to high cost of scale up	K=3.8, DF =0.002, very stable to 130C, (highest temp measured)

Figure 1. A Small Portion of the EXCEL Table of SNL Polymer Film Development Progress

A large number of film chemistries were attempted that led to successful development of purified monomers of film chemistries. Fabrication into large area films was difficult for some polymer chemistries. An example of one of these chemistries was hydroxylated phenylated polyaryl ether.

Although difficult to fabricate into films of large area, encouragingly initial small area films passed the SNL engineering flexibility tests. Further, this material had a dielectric constant of 4.7 and a dissipation factor of 0.01 at 25°C. Unfortunately, the dissipation factor was too high at temperatures of 140°C. A second example of film chemistry explored was hydroxylated low cost process polystyrene. A good film was obtained and dielectric measurements indicated a dielectric constant of 3.35 and a dissipation factor of 0.011. SNL scientists decided to concentrate the majority of their efforts in FY05 into the fabrication of low cost phenylated polyphenylene. There were several reasons for this program strategy. First PPP has a demonstrated low dielectric loss and high breakdown strength at elevated temperatures (Figure 2). Further, scale up of the process appears quite straight forward. SNL scientists interacted with Hydrosize, Inc. Raleigh, NC to fabricate 50 grams of low cost PPP precursor in FY05. While these precursors were acceptable for permeable membrane fabrication for fuel cells, they were not acceptable for low loss dielectric applications such as DC bus capacitors. SNL scientists are now working on adjusting the chemistry procedures and molecular weight to produce high quality thin films. Initial results from the new SNL PPP monomer synthesis are promising, dense, pore free films have been fabricated and are in the process of being electrically characterized.

Excellent high temperature dielectric properties are shown in Figure 2 for the high cost (PPP) films developed by SNL. Dissipation factors measured to 140°C were exceedingly low, on the order of 0.005. This result is promising for high temperature inverter operation. Unfortunately, these films are very expensive to synthesize and they are extremely brittle in nature. Dielectric constants for these films are greater than 4, compared to 3 for commercial state of the art polyphenylene sulfide films. When these results are coupled with the 4 MV/cm breakdown fields measured, then a factor of 4 improvement in energy density and thus capacitor volume is projected compared to SOA PPS films.

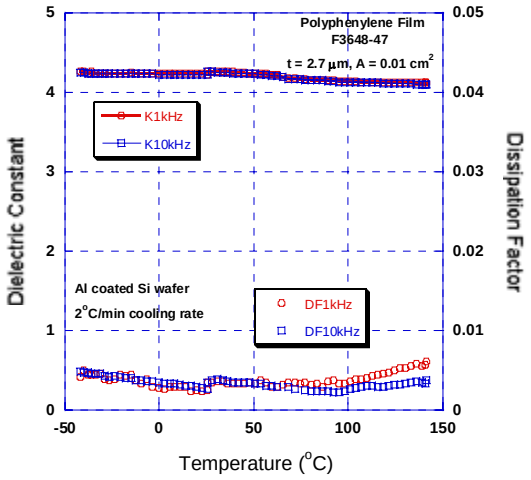

Figure 2. Dielectric constant and dissipation factor for PPP films using initial SNL chemistry

High quality nanoceramic powders of PLZT and TiO_2 were fabricated in FYO5 by SNL scientists of TiO_2 and PLZT. Powder synthesis procedures are shown in Figure 3. The SNL patented process consists of an acetic acid solution of Pb acetate, Zr butoxide and Ti isopropoxide precursors precipitated with oxalic acid using high shear rate mixing. Extremely homogenous, fine particles are created with a crystallite size on the order of 90 nm. A variety of PLZT compositions were synthesized including PLZT 12/70/30, PLZT 1.5/96/4 and PLZT 5/87/13 in FY05. Figure 3 shows the powder synthesis precipitation step and SNL lab facilities for 1.5 kg batches. Ten kilogram PZT batches can be fabricated at SNL facilities. In addition, the nozzle head for direct write aerosol spray deposition is shown. Six layer

multilayer PLZT capacitors have been fabricated by the direct write process. Aerosol spray deposited PLZT films of 50 micrometer thickness have breakdown strengths that exceed 200 kV/cm.

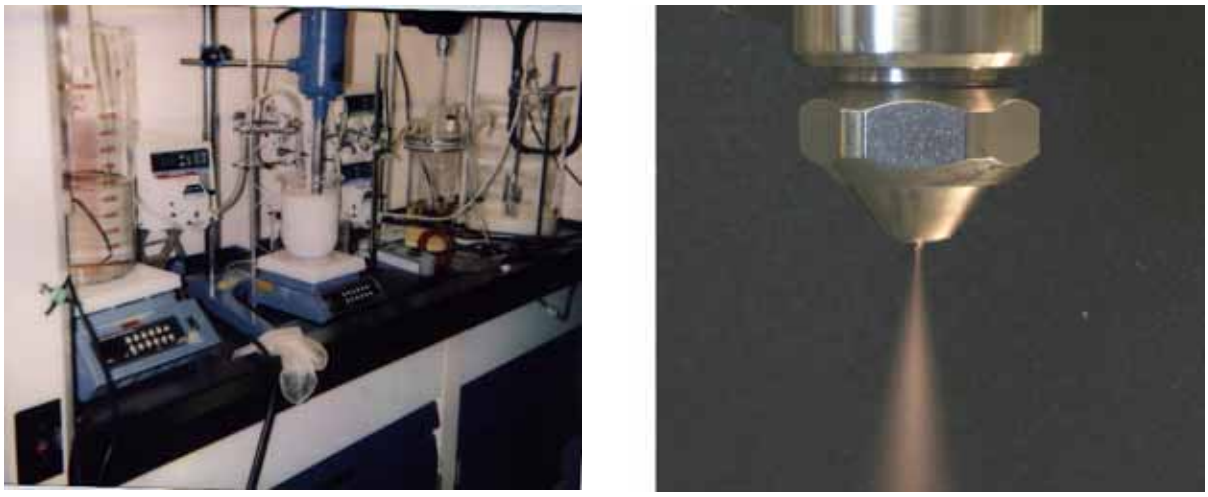

Figure 3: Chemical synthesis facility and aerosol spray deposition nozzle for nanoceramics.

SNL scientists also investigated lower dielectric constant, higher breakdown strength nanoceramic dielectrics in FY05. TiO_2 was chosen as the first higher breakdown strength dielectric to investigate. Powders of titania with less than 20 nm size were synthesized (Figure 4). These were fabricated using a Ti-n butoxide based synthesis. The solution was pumped/sheared at 6000 RPM to create a homogeneous mixture of fine particles. In-situ densification studies were performed to determine optimum firing conditions for densification. Films of 50 micrometer thickness were fabricated using aerosol spray deposition. These films withstood fields of 600 kV/cm or 3000 volts. Ideally, prototype capacitors could be made from films that are less than 10 micrometers thick, resulting in volumetrically efficient DC bus capacitors for FreedomCAR applications.

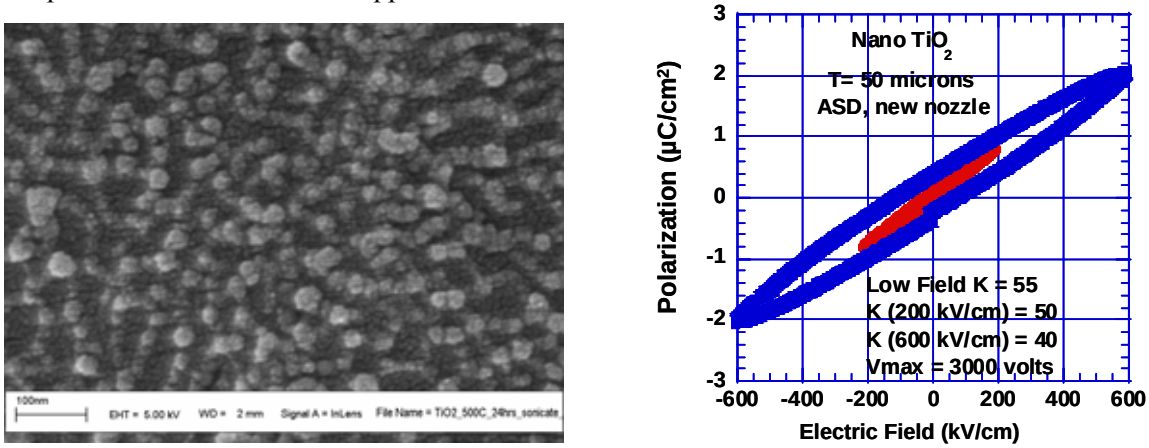

Figure 4. SNL Sub-20 nm TiO_2 Particles and Polarization versus Field Characteristics of Aerosol Spray Deposited TiO_2 Layer

Conclusion

Discussions with DOE program managers, DOE consultants, automotive engineers and capacitor industry representatives reinforced the importance of high temperature polymer film dielectric development. The 2010 temperature specifications put forth by DOE and the EE TECH team of –40°C to 140°C will not be met by recently developed state of the art polyethylene dielectrics. Thus development of high temperature polymer and nanoceramic dielectric materials is necessary to reduce volume and improve temperature performance of DC bus capacitor dielectrics. In FY05, SNL launched a multifaceted program of chemical synthesis, electrical characterization, film processing, and mechanical characterization for development of low volume, high temperature DC bus capacitors. Among the accomplishments was the identification and development of a low cost phenylated polyphenylene synthesis procedure. Capacitors fabricated on aluminum coated silicon wafers exhibited low loss and had dielectric constant that exceeded that of state of the art polyphenylene sulfide. Further, we synthesized high quality nanoceramic dielectric powders of PLZT and TiO_2. Both bulk specimens and aerosol spray deposited films were fabricated from these materials. A thorough mechanical characterization of these films headed by Andrew Wereszczak of ORNL indicated that the chemical modifications resulted in marginal improvement in mechanical properties.

Future Directions

In FY 2006, we will develop the processes necessary for the development of high quality films of low cost polyphenylated polyphenylene dielectric and for the fabrication nanoceramic dielectric multilayer capacitors. Specific tasks for our FY06 efforts are shown below.

- Invent synthesis procedures for low cost phenylated polyphenylene (PPP) films that will meet FreedomCAR requirements for breakdown field and DF for temperatures from –40°C to 140°C.
- Fabricate and characterize spin deposited PPP films on Al coated Si and on Mylar coated Si wafers and characterize electrical and mechanical properties of these films.
- If these film properties are acceptable to DOE program managers initiate scale up to 1 to 5 liter batches of solution (Hydrosize, Inc) and have polymer sheets fabricated of 500 foot length for fabricating wound polymer capacitors.
- If these measurements are successful, then have large-value (20- to 200-μF) capacitors fabricated by vendor(s) and evaluated by SNL, ORNL and auto manufacturers in simulated electric hybrid vehicle environments.
- Synthesize chemically prepared powders for nanoceramic dielectric fabrication.
- Fabricate multilayer high quality 20 to 50 micrometer nanoceramic dielectric layers using either an automated aerosol spray deposition process or conventional tape casting.
- Evaluate electrical properties at temperatures up to 140°C for FreedomCAR applications.

Publications / Presentations

1. D. Wheeler and G. Jamison, "Novel Polymer Film Synthesis Routes of Voltage and Temperature Stable Dielectrics," October 5, 1999.
2. B. A. Tuttle, J. Wheeler, G. Jamison, D. Williams and D. Dimos, "FY03 Annual Report, High Temperature Film Capacitors," *2003 Annual Progress Report*, October, 2003.
3. B.A. Tuttle, D.P. Williams, J.A, Voigt and J. Wheeler, Comparison of Bulk and Thin Film High Zr Content PLZT films, Extended Abstracts 107th Annual American Ceramic Society Meeting (April 27-30, 2005).
4. D.P. Williams, B.A. Tuttle, J.A. Voigt, D. Moore and J. Wheeler, "Aerosol Spray Deposited PLZT Films, Extended Abstracts 107th Annual Meeting of the American Ceramic Society, April 27-30, 2005.
5. Bruce Tuttle, Jill Wheeler, David Williams, and Greg Jamison, "Capacitor Technologies: A Comparison of Competing Options," DOE Hi-Tec Inverter Meeting, Baltimore, MD October 13, 2004 (Invited Presentation)
6. Bruce Tuttle, David Williams and Jill Wheeler, "Capacitor Development for Next Generation Pulse Discharge Applications," TCG X Meeting Los Alamos, NM November 3, 2004.
7. D.P. Williams, B.A. Tuttle, D. Moore, J. Voigt, P. Clem, Sandia National Laboratories, "Integrated High Zirconia Content PLZT Capacitors" The 29th International Conference on Advanced Ceramics and Composites, Cocoa Beach, January 23-18, 2005.
8. D. P. Williams, B. A. Tuttle, J. A. Voigt and D. L. Moore, "Thick Film Multilayer PLZT Capacitors formed via Aerosol Deposition," 107th Annual Meeting of the American Ceramic Society, Baltimore, MD, April 10-13, 2005.
9. B.A. Tuttle*, D. P. Williams, J.A. Voigt, D. L. Moore, T. Headley, L. Brewer, M. Rodriguez, P. G. Clem, and J.S. Wheeler, "Chemically Prepared PLZT Films and Layers for High Energy Density Applications," Sandia National Laboratories, Albuquerque, NM; G. Brennecka, University of Illinois, Urbana, IL, 107th Annual Meeting of the American Ceramic Society, Baltimore, MD, April 10-13, 2005. (Invited Presentation).
10. B. Tuttle, D. Williams, J. Wheeler and P. Mahoney, "Chemically Prepared PLZST Thin Films for High Energy Density Capacitor Applications", the 6th Pacific Rim Conference on Ceramic and Glass Technology. September 11 – 16, 2005.
11.D. Williams, B. Tuttle, P. Clem, D. Moore, J. Cesarano, M. Niehaus and J. Voigt, " Integrated High Energy Density Capacitors Formed Via Aerosol Deposition," the 6th Pacific Rim Conference on Ceramic and Glass Technology. September 11 – 16, 2005.
12 J. Voigt, D. Moore, D. Williams, J. Richardson, P. Clem and B. Tuttle, "Solution Synthesis of Ferroelectric Precursor Powders - A General Approach, " the 6th Pacific Rim Conference on Ceramic and Glass Technology. September 11 – 16, 2005.